Journal of METALS

FEBRUARY 1956

TRANSACTIONS SECTION

VOL. 8, NO. 2, IN TWO SECTIONS — SECTION TWO

Diffusion and Marker Movements in Beta Brass	U. S. Landergren, C. E. Birchenall, R. F. Mehl	73
X-Ray Diffraction Study of the Nitrides of Uranium	D. A. Vaughan	78
Preferred Orientations in Rolled and Annealed Titanium	J. H. Keeler, A. H. Geisler	80
Thermodynamic Properties of Solid Fe-Au Alloys	L. L. Seigle	91
New Intermediate Phase in Burnt Tungsten Steels	Kehsin Kuo	97
System Zirconium-Nitrogen	R. F. Domagala, D. J. McPherson, M. Hansen	98
Creep-Rupture by Vacancy Condensation	E. S. Machlin	106
Tensile Deformation of Germanium Single Crystals	R. P. Carreker, Jr.	111
Hot-Rolled Textures of Titanium Alloys	C. J. McHargue, J. R. Holland, J. P. Hammond	113
Mechanism of Plastic Flow in Titanium At Low and High Temperatures	F. D. Rosi, F. C. Perkins, L. L. Seigle	115
Preferred Orientations in a Meta-Stable Body-Centered-Cubic Zr-Cb Alloy	J. H. Keeler	122
Heterogeneous Nucleation of the Martensite Transformation	R. E. Cech, D. Turnbull	124
Thorium-Columbium and Thorium-Titanium Alloy Systems	O. N. Carlson, J. M. Dickinson, H. E. Lunt, H. A. Wilhelm	132
Comparison of Techniques in a Study of Zinc Self-Diffusion	F. E. Jaumot, Jr., R. L. Smith	137
Strain Rate Effects in Tungsten	J. H. Bechtold	142
Interaction of Precipitation and Creep in Mg-Al Alloys	C. S. Roberts	146
Occurrence of CsCl-Type Ordered Structures in Certain Binary Systems of Transition Elements	P. A. Beck, J. B. Darby, Jr., O. P. Arora	148

Table of Contents Continued

Effects of Oxygen, Nitrogen, and Carbon on the Ductility of Cast Molybdenum — L. E. Olds, G. W. P. Rengstorff — 150

Creep of Copper at Intermediate Temperatures — T. E. Tietz, J. E. Dorn — 156

Allotropic Transformations in Titanium, Zirconium, and Uranium Alloys — A. E. Dwight — 162

Self-Diffusion in Single and Polycrystals of Zinc at Low Temperatures — F. E. Jaumot, Jr., R. L. Smith — 164

Mechanism of Grain Boundary Sliding — H. C. Chang, N. J. Grant — 169

Search for Oxidation-Resistant Alloys of Molybdenum — G. W. P. Rengstorff — 171

Crystallographic Angles for Bismuth and Antimony — E. I. Salkovitz — 176

Tensile Deformation of Molybdenum as a Function of Temperature and Strain Rate — R. P. Carreker, Jr., R. W. Guard — 178

Transformation of the TiO Phase — C. C. Wang, N. J. Grant — 184

Internal Friction in Zirconium — W. J. Bratina, W. C. Winegard — 186

Experimental Observations Concerning the Collapse of Dislocation Loops During Annealing — J. Washburn — 189

High Speed Quenching Dilatometer — F. E. Martin, R. H. Ryerg — 191

Tensile Creep of High Purity Aluminum — R. W. Guard, W. R. Hibbard, Jr. — 195

Diffusion in Liquid Lead — S. J. Rothman, L. D. Hall — 199

Effects of Alloying Elements on the Electrical Properties of Manganin-Type Alloys — D. D. Pollock, D. E. Finch — 203

Occurrence of Chi Phase in a 16 Pct Cr-15 Pct Ni-7 Pct Mn-6 Pct Mo Alloy — J. Birtalan, R. A. Bloom — 210

Titanium-Rich Corner of the Ti-Al-V System — J. J. Rausch, F. A. Crowley, H. D. Kessler — 211

Density Distribution in Metal Powder Compacts — S. C. Kuczynski, I. Zapiorowsky — 215

Production of High Nitrogen Steels — V. F. Zackay, E. R. Morgan, J. C. Shyne — 216

The Transactions papers appearing in the Journal of Metals *during 1956 will subsequently appear in* AIME Transactions *Volume* 206, *and may be permanently referenced to that volume.*

Diffusion and Marker Movements in Beta Brass

Diffusion coefficients and marker movements have been determined in β brass using welded couples. Three different concentration ranges were employed at 750°C, while a fourth concentration range was measured at 500°, 600°, 700°, and 800°C. Marker displacements toward and porosity development in the high zinc side of the couple were observed in all cases. The results were interpreted as favoring a vacancy diffusion mechanism.

by Ulf S. Landergren, C. Ernest Birchenall, and Robert F. Mehl

IN the large amount of diffusion literature which has accumulated during the past half century, very few experimental data have been presented on body-centered-cubic metallic phases. The impressive combination of experimental and theoretical studies which has given the vacancy mechanism a fairly secure position as the preferred mechanism for most face-centered-cubic metals has no counterpart for body-centered-cubic phases, although the theoretical picture seems to be in a better state than the experimental work.

The attempts to select diffusion mechanisms by the theoretical calculation of the activation energy for the various conceivable unit diffusion processes and the energy of formation of the type of lattice defect required have been based on models of two kinds. The first kind utilizes potential functions fitted for certain properties of pure crystalline copper; the second kind is fitted for sodium. The latter is an example of an *open* metal in which the metallic ion is small compared with interatomic distance,[1] while the former is characteristic of the larger class of metals in which the ions have diameters about as large as the interatomic distance. β brass should resemble copper in this fundamental property. It should be evident that results on the mechanism of diffusion obtained for one of these classes need not necessarily apply to the other.

Huntington and Seitz,[2] using a model of the copper type, showed that the activation energies to be expected for interstitial migration or a two-atom direct interchange were much higher than that for vacancy diffusion. Zener[3] pointed out that a four-atom ring rotation would involve an activation energy considerably lower than the two unlikely mechanisms although still higher than the vacancy mechanism in the face-centered-cubic structure. Furthermore, he argued, the four-atom rotation would be relatively easier in a body-centered-cubic lattice and might be competitive with the vacancy mechanism.

Paneth[4] showed that a body-centered-cubic crystal-like sodium could form interstitial defects of special type, called a *crowdion*, by crowding an extra atom into <111> directions where the defects would affect a line of about eight atoms. The defect was constrained to move along the defining line.

Unlike the face-centered-cubic case, therefore, the theoretical calculations for the body-centered-cubic mechanism do not provide a very clear-cut answer, and the absence of adequate experimental studies is the more serious.

This investigation was undertaken for the purpose of obtaining useful information on diffusion in body-centered-cubic phases. β brass was chosen for several reasons: 1—the phase field is sufficiently wide at high temperatures to permit the use of diffusion couples with adequate concentration ranges for satisfactory chemical analysis, 2—thermodynamic activity data are available for the calculation of mobilities from diffusion coefficients, 3—the phase is as close to the theoretical model of the copper type on which the calculations have been done as any body-centered-cubic metallic phase is likely to be.

Measurements of the movements (if found) of inert markers during the diffusion process would indicate that a vacancy or interstitial mechanism played a major role in diffusion in β brass. If no marker movement should be found, a ring mechanism would be indicated but not assured.

Experimental Procedure

The alloys used in these experiments, listed in Table I with analyses, were supplied by the Naval Research Laboratory. They were from ingots of 3x3 in. cross-section, heated to 760°C, reduced under a

U. S. LANDERGREN, formerly Graduate Student, Dept. of Metallurgical Engineering, Carnegie Institute of Technology, is associated with SKF Industries Inc., Gottenburgh, Sweden, C. E. BIRCHENALL, Associate Member AIME, is associated with Dept. of Chemistry, Princeton University, Princeton, N. J., and R. F. MEHL, Member AIME, is associated with Dept. of Metallurgical Engineering, Carnegie Institute of Technology, Pittsburgh.

Discussion of this paper, TP 4023E, may be sent, 2 copies, to AIME by Apr. 1, 1956. Manuscript, Oct. 13, 1954. Philadelphia Meeting, October 1955.

This paper is based on a portion of a thesis by U. S. Landergren submitted, in partial fulfillment of the requirements for the degree of Doctor of Science, to Dept. of Metallurgical Engineering, Carnegie Institute of Technology.

Copyright 1956 by American Institute of Mining and Metallurgical Engineers, Inc.
Printed in U. S. A.

forging hammer until the temperature dropped to about 480°C, and then reheated and reforged three more times to give finished bars about 1½x1½ in. cross-section. The bars were annealed for 2 hr at 425°C and furnace-cooled. Cylindrical disks 1¼ in. diam and ¼ to ½ in. thick were cut from the bars. The opposite faces of the disks were carefully ground parallel within 0.005 mm. The average grain diameters were about 0.1 mm, but recrystallization during welding produced grain diameters ranging between 0.1 and 10 mm.

Table I. Analyses of Alloys Used

Alloy No.	Cu Wt Pct	Zn Wt Pct	Zn Atomic Pct	Impurities, Wt Pct
1	59.0	40.8	40.2	0.2
2	50.0	49.7	48.9	0.3
3	46.4	53.4	52.6	0.2
4	56.0	43.7	43.0	0.3
5	49.7	50.0	49.2	0.3

Marker wires, 2 mil W, were supplied by Sylvania Electric Products Inc.

Sandwich-type couples were prepared by welding two disks of one alloy to each face of an alloy of lower zinc content with tungsten wire markers crossing the weld interfaces. Thus, a couple designated 3/1/3 would consist of a disk of alloy No. 1, Table I, welded between two disks of alloy No. 3, Table I. Couples of type 3/1/3, 2/1/2, and 3/2/3 were run at 750°C, some for the determination of diffusion penetration curves, others for the direct determination of marker displacements. Couples of type 5/4/5 were run at 500°, 600°, 700°, and 800°C for the determination of penetration curves.

The cylindrical disks were given a metallographic polish, thoroughly cleaned with soap and alcohol, and etched lightly in a 50 pct aqueous solution of HNO_3. The wire was wound around the central disk, the outer disks placed on it, and the unit subjected to 10,000 psi in a hydraulic press. The pressed couple was held for 10 min at 650°C in an atmosphere of flowing hydrogen, with light pressure applied to prevent loss of alignment. Heating times ranged from 15 to 20 min. After welding, the specimens were removed from the furnace and air-cooled. Corrections for diffusion during welding were applied by converting the time at welding temperature to an equivalent time at diffusion temperature. Corrections were always small compared with the actual diffusion time.

Table II. Diffusion Couples and Their Annealing Treatment

Type of Couple	No.	Diffusion Temperature, °C	Diffusion Time, Hr
For Determination of Penetration Curves			
3/1/3	47	750	0.9
	59	750	2.0
	60	750	3.9
2/1/2	62	750	0.8
	66	750	3.7
	67	750	8.4
	68	750	11.8
3/2/3	56	750	4.5
	57	750	7.0
5/4/5	50	800	1.0
	51	800	1.7
	38	800	4.2
	53	700	5.3
	39	700	9.3
	24	600	21.4
	27	600	25.9
	26	600	29.5
	21	500	72.0
For Direct Measurement of Marker Displacements			
3/1/3	32	750	0.9
	33	750	2.0
	45	750	3.9
	46	750	8.8
2/1/2	31	750	0.8
	40	750	2.2
	41	750	3.7
	30	750	8.4
	58	750	9.1
	61	750	11.8
3/2/3	44	750	1.1
	42	750	4.5
	43	750	9.1

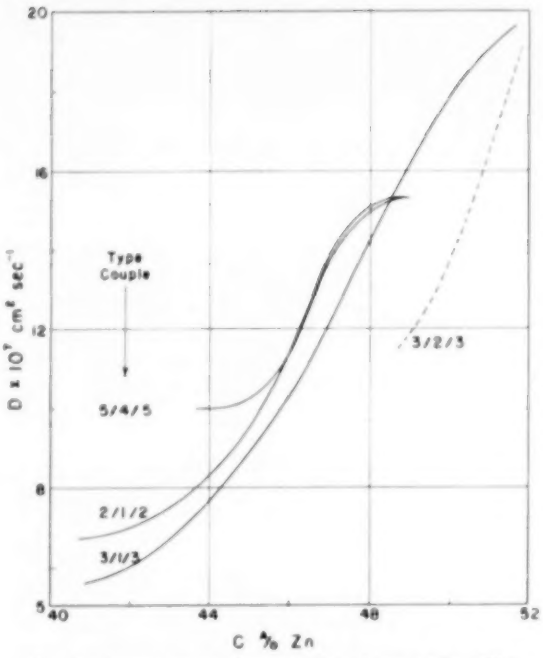

Fig. 1—Average curves show the dependence of the diffusion coefficient of β brass on the concentration at 750°C. Concentration is given in atomic pct Zn.

Two plane and parallel surfaces were then machined perpendicular to the weld interfaces, and small cuts made to avoid excessive cold work. After metallographic polishing, the interfaces were examined microscopically and unsound welds rejected. Because of smearing during polishing, some faulty welds escaped detection but later failed during machining for analysis. These specimens were also discarded.

For determining marker displacements by the direct measurement of distances between the markers in the two parallel interfaces, a Kodak contour projector made available by the East Pittsburgh plant of Westinghouse Electric Corp. was employed. This comparator was capable of measuring distances to ±0.00005 in. Reference marks were made at the ends of the couples, which were always placed in the same position in the comparator. Changes in distance were determined for pairs of markers and averages were taken over all pairs in the two interfaces, resulting in slightly better accuracy than the procedure of da Silva and Mehl.[6]

One or two diffusion couples were placed in a bomb constructed of 1½ in. ID black iron pipe and fitted at the ends with screw caps. The dead space in the bomb was packed with a mixture of β brass chips to decrease vaporization losses of zinc from the couple and lampblack to prevent the couple from sticking to the bomb.

Two tube furnaces with a 6 in. constant temperature zone were used for the diffusion anneals. Each had one winding that operated continuously and another controlled automatically to maintain the temperature within ±2°C during the diffusion runs. To minimize heating time, the furnace was brought to temperature and stabilized before the bomb was inserted. The couple temperature was measured by a chromel-alumel thermocouple placed against the end of the bomb which contained the specimen. The thermocouple was checked frequently against a Bureau of Standards Pt—90 pct Pt-10 pct Rh thermocouple. An atmosphere of flowing nitrogen was maintained in the furnace tube. At the completion of the run, the bomb was removed from the furnace and cooled in air.

Specimens were carefully machined to produce new flat surfaces parallel to the old surfaces but beyond the layer which had gained or lost zinc through the surface. The new flat regions were ground, polished, and etched. For some couples, the distances between markers were measured on the comparator. The remaining couples were aligned in a lathe, sighting the markers with a telescope to assure that cuts would be taken parallel to the weld interfaces. The outer surface was turned off in order to eliminate any material affected by the gain or loss of zinc through the surface. Outside the diffusion zone, 4 to 6 mil cuts were begun. In the diffusion zone the cuts were 2 to 3 mil with 2 mil or smaller cuts being taken in the steep part of the penetration curve. The distances as measured on the feed micrometer on the lathe were checked after every tenth cut with a portable micrometer.

Traces of the wires were usually found in two to four cuts, never more than five. This indicates that the weld interfaces were reasonably plane and the alignment for machining satisfactory. The uncertainty in locating the marker interface by this method is estimated to average less than 1 mil.

Near the weld interface, every second sample was analyzed; away from the interface, every third sample was chosen. Each penetration curve had about 30 analyses. If a particular value was doubtful, samples from the adjoining cuts were run. On the 0.1 g samples available, electrodeposition of copper gave a mean deviation of only ±0.2 pct Cu. This precision was satisfactory for all except two couples of type 3/2/3 in which the concentration range was only 3.7 atomic pct. As a result, the diffusion coefficients are determined with lower precision for these couples than for the others.

Table IV. Diffusion Coefficients at 750°C

Atomic Pct Zn	Couple No., $Dx10^5$ Cm² per Sec								
	047	059	060	062	066	067	068	056	057
40.5	4.6	8.2	5.2	6.0	6.1	5.8	7.0		
41	4.8	7.6	5.8	6.7	7.1	6.4	7.4		
41.5	5.1	8.3	6.3	6.9	7.3	6.5	7.6		
42	5.4	9.0	6.3	6.8	6.9	6.0	7.6		
42.5	5.5	9.3	6.3	6.7	6.7	6.5	7.9		
43	5.6	9.2	6.6	6.8	6.6	6.7	8.1		
43.5	6.2	9.2	7.0	7.2	6.9	7.1	8.6		
44	6.9	9.1	7.8	8.0	7.8	7.5	9.0		
44.5	7.4	9.1	8.5	9.2	8.6	8.0	10.0		
45	7.9	9.1	9.3	10.6	9.5	8.5	11.2		
45.5	9.2	9.2	10.0	11.4	10.2	9.6	13.1		
46	10.0	10.3	11.0	12.0	11.2	10.4	14.6		
46.5	10.6	11.7	12.0	12.7	11.3	12.0	15.0		
47	11.4	12.6	12.8	13.5	12.1	13.2	15.4		
47.5	12.5	12.4	14.0	13.5	12.5	13.8	15.0		
48	13.7	14.5	15.1	12.5	12.7	15.2	14.7		
48.5	14.4	15.5	16.1	12.6	12.6	15.1	14.6		
49	15.8	16.3	16.0					10.8	13.1
49.5	17.8	17.8	16.4					13.0	14.1
50	19.4	18.4	17.4					12.0	15.4
50.5	20.4	18.9	18.9					13.5	15.7
51	20.5	19.1	18.8					15.2	17.6
51.5	20.9	18.7	19.5					16.7	20.5
52	18.5	20.5	19.8					16.5	23.1
52.5	—	—	—					18.6	21.2

Experimental Results

Diffusivities—Table II lists the couples used in this investigation, the identifying numbers, type, temperature, and time of diffusion anneal. Table III, copies of which are available,* gives the results of chemical analysis for the group for which penetration curves were determined. The distances are taken from the marker interface to the center of the machined layer; the analyses are in terms of atomic percent zinc. These data were plotted on probability paper, and the smoothed curve from this plot was used to calculate the diffusion coefficient as a function of concentration by the Boltzmann-Matano[6] procedure. The results are given for all couples at 750°C in Table IV and for all 5/4/5 couples at 500°, 600°, 700°, and 800°C in Table V.

* Table III, which gives the results of chemical analysis for the group for which penetration curves were determined, has been deposited as Document No. 4515 with ADI Auxiliary Publications Project, Photoduplication Service, Library of Congress, Washington 25, D. C. A copy may be secured by citing Document No. 4515 and by remitting $1.25 for photoprints or $1.25 for 35 mm microfilm. Advance payment is required and checks or money orders should be made payable to: Chief, Photoduplication Service, Library of Congress.

Table V. Diffusion Coefficients for Type 5/4/5 Couples

Atomic Pct Zn	Couple No., Temperature °C, $Dx10^5$ Cm² per Sec								
	800			700		600			500
	050	051	038	053	039	024	037	026	021
43.5	10.3	16.8	16.2	5.5	5.3	1.7	2.1	1.9	0.38
44	10.4	17.3	16.2	5.9	5.6	1.9	2.1	1.9	0.43
44.5	12.1	17.8	16.2	6.0	5.9	1.9	2.2	2.0	0.41
45	14.0	17.4	16.2	5.8	5.8	1.9	2.1	2.1	0.42
45.5	16.1	17.5	17.1	5.9	5.9	2.0	2.1	2.0	0.45
46	18.4	18.2	17.9	5.9	6.3	2.3	2.3	2.6	0.49
46.5	20.5	19.7	18.4	6.3	7.3	2.6	2.4	2.3	0.58
47	22.2	21.3	19.7	7.2	8.4	2.9	2.6	2.8	0.65
47.5	24.6	22.2	22.0	8.1	9.5	2.9	2.7	3.1	0.71
48	25.4	22.0	21.6	9.6	9.5	3.0	2.8	3.4	0.78
48.5	24.8	21.8	22.2	10.7	9.2	2.9	3.0	3.6	0.77
49	23.4	20.9	21.9	10.4	8.9	3.4	2.9	3.4	0.77

The averaged curves for the three types of couples employed at 750°C and interpolated values for the same temperature from the 5/4/5 couples are plotted in Fig. 1. Since the data within each type of couple exhibit a considerable amount of scatter, it cannot be concluded from these results that the diffusivity depends upon the concentration range as well as the concentration itself. However, the diffusivities for the low zinc end of the 3/2/3 type couples lie appreciably below the other results for couples which are losing zinc at the same concentration. Unfortunately, the experimental uncertainty associated with this type couple is rather large.

Fitting the 5/4/5 couple data to the equation $D = D_o e^{-Q/RT}$ yields values for D_o which run from about 1.8×10^{-2} cm² per sec at the low zinc end to about 1.3×10^{-1} at the high zinc end, while the activation energy also appears to vary from 19.9 kcal per mol to about 18.2. Fitting these same data to the expression introduced by da Silva and Mehl[7]

$$M = K_u t^{1/2} e^{-Q_u/RT}$$

where M is the Matano area, K_u is a constant, and Q_u is the average heat of activation for the diffusion process over the specified concentration range, leads

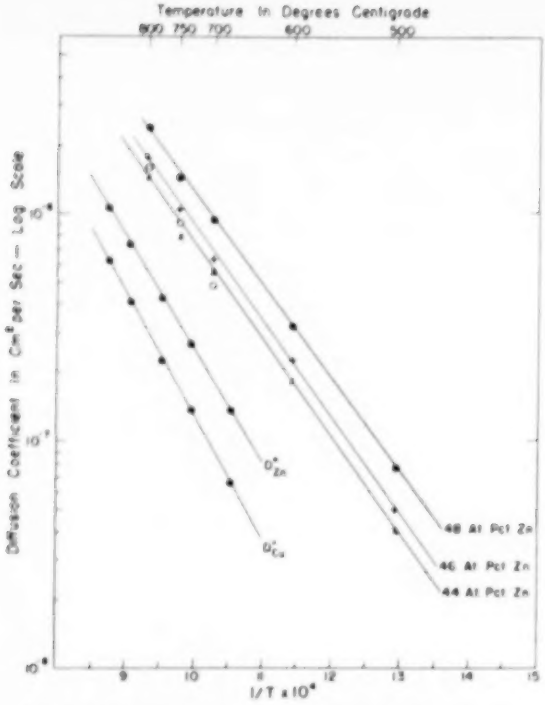

Fig. 2—Curves and data points illustrate the temperature dependence of β brass diffusion coefficients. Open circle represents D, calculated from self-diffusion data of Inman.[12]

to the values: $Q_u = 19.2$ kcal per mol and $K_u = 25.7$ atomic pct times cm per hr.

Marker Shifts—The results of the direct measurement of marker shifts[7] are listed in Table VI. Table VII gives values of the shift attained by comparing the location of the markers observed during machining of analytical specimens with the Matano interface determined on the penetration curves. Although the latter show much greater consistency than the former, reasons will be given in the discussion for believing that the former are more nearly correct. However, the compositions and slope of the penetration curve at the marker interface are taken as nearly correct. It seems likely that there is a systematic error in the location of the Matano interface, probably arising from the fact that the high zinc end of the couple tails off very gradually and may be seriously shortened due to normal scatter in the chemical analyses. It is found that arbitrarily shifting the Matano interface by small amounts produces little change in the diffusion coefficients calculated for the middle of the concentration range. However, if the curve is adjusted at the ends to keep the area balanced as required, the diffusion coefficients calculated at the concentration extremes vary widely.

The amount of shift to be expected on the basis of lattice parameter changes[8] is of the order of 10^{-4} cm, which is only about 10 pct of the observed values. No correction for this effect has been included because of its small magnitude.

An undetermined amount of porosity was found in the high zinc side of each couple near the marker interface. Quantitative measurements were not satisfactory due to distortion in metallographic preparation. No attempt has been made to correct for this porosity.

The scatter in the direct marker shift measurements may be partially due to one or more of the following conceivable sources: 1—failure of the same fraction of vacancies to remain as porosity in each specimen, 2—relief of welding stresses which may not have been uniform from sample to sample, 3—absorption or evolution of gases (hydrogen was used for welding, nitrogen for diffusion, and lampblack for packing the bombs), and 4—distortion of the surface in machining, grinding, and polishing of the flat face. These things should affect all specimens so that an additional systematic source is required to account for the much larger *indirect* shifts recorded.

Discussion

Errors in Diffusion Coefficients—The errors from nonsystematic sources are those of distance, time, temperature, and chemical analysis. The uncertainty in distance was of the order of 10 pct of the thickness of a cut, therefore causing the largest error for diffusion at short times and low temperatures. The uncertainty in time measurement due to welding and heating and cooling may approach 50 pct on the very short runs while accounting for only a few percent on the long runs. Control of temperatures to ± 2°C should assure comparatively small error from this source. The ± 0.2 pct Cu uncertainty in chemical analysis together with the large number of samples analyzed per couple enabled penetration curves to be located precisely in the middle of the concentration range for most couples. However, at the extremes of the penetration curves and for the whole range of the 3/2/3 couples which had a small total concentration difference the true penetration curve was difficult to draw. The uncertainty may have been close to 50 pct in these instances.

Since none of the 3/2/3 type couples were run for very short times, it seems likely that the uncertainty in these couples, in other couples run for very short times, and at the extremes of the concentration range in all couples is about 50 pct, with a decided improvement for the median concentrations of wide range couples run for relatively long times. The overall uncertainty for composite curves such as those recorded in Fig. 1 is probably about 25 pct for the diffusion coefficients.

Systematic errors due to the failure of Fick's law to hold precisely when porosity develops or to variations in the bulk concentration at the ends of the couples must be added. Balluffi and Seigle[9] obtained diffusion coefficients in α brass in the absence of porosity that agreed well with da Silva and Mehl's[5] couples which developed pores.

Table VI. Marker Displacements by Direct Method

Couple No.	Type Couple	Diffusion Time, Hr	Diffusion Time$^{1/2}$	Shift x 10^{4} Cm
032	3/1/3	0.9	0.95	0.14
033	3/1/3	2.0	1.41	0.57
045	3/1/3	3.9	1.98	0.53
046	3/1/3	8.8	2.96	0.92
031	2/1/2	0.8	0.89	0.29
040	2/1/2	2.2	1.48	0.17
041	2/1/2	3.7	1.92	0.21
039	2/1/2	8.4	2.90	0.83
058	2/1/2	9.1	3.02	0.65
061	2/1/2	11.8	3.44	0.84
044	3/2/3	1.1	1.05	0.05
042	3/2/3	4.5	2.12	0.52
043	3/2/3	9.1	3.02	0.94

Comparison of Diffusion Coefficients and Marker Displacements with Other Measurements—The

Table VII. Marker Displacements by Indirect Method

Diffusion Couple No.	Type Couple	Diffusion Temperature, °C	Diffusion Time, Hr	Diffusion Time$^{1/2}$, Hr$^{1/2}$	Matano Area, Atomic Pct x Cm	C_{Matano}, Atomic Pct Zn	$C_{Metzger}$, Atomic Pct Zn	Shift x 10^3, Cm	$\frac{\partial N_{Zn}}{\partial x}$, Cm^{-1}
047	3/1/3	750	0.9	0.95	0.43	47.35	48.05	1.26	0.489
059	3/1/3	750	2.0	1.41	0.66	47.20	47.90	2.00	0.318
060	3/1/3	750	3.9	1.98	0.91	47.25	47.85	2.50	0.217
062	2/1/2	750	0.8	0.89	0.26	45.00	45.35	0.77	0.404
066	2/1/2	750	3.7	1.92	0.54	45.00	45.25	1.34	0.203
067	2/1/2	750	8.4	2.90	0.81	45.10	45.35	1.78	0.145
068	2/1/2	750	11.8	3.44	1.06	45.05	45.30	2.11	0.101
056	3/2/3	750	4.5	2.12	0.32	50.85	50.90	0.87	0.0657
057	3/2/3	750	7.0	2.65	0.44	50.85	50.95	1.12	0.0506
050	5/4/5	800	1.0	1.00	0.24	46.45	46.60	0.90	0.189
051	5/4/5	800	1.7	1.30	0.38	46.25	46.55	1.74	0.155
038	5/4/5	800	4.2	2.05	0.58	46.25	46.45	1.95	0.102
053	5/4/5	700	5.3	2.30	0.40	46.35	46.55	1.35	0.160
039	5/4/5	700	9.3	3.05	0.54	46.40	46.60	1.66	0.101
024	5/4/5	600	21.4	4.63	0.48	46.35	46.60	2.06	0.117
037	5/4/5	600	25.9	5.09	0.52	46.25	46.50	2.00	0.113
026	5/4/5	600	29.5	5.43	0.56	46.40	46.60	1.58	0.111
021	5/4/5	500	72.0	8.48	0.42	46.45	46.60	1.03	0.576

earlier measurements of Seith and Krauss[10] lie about an order of magnitude below those reported here. Since their α brass measurements obtained in the same investigation by the questionable vapor loss method also differ considerably from the accepted values, it seems likely that their results are in error.

Better agreement exists with data reported by Petrenko and Rubinstein[11] which were also obtained by a vaporization method. Their heat of activation of 18.5 kcal per mol for diffusion in β brass is close to the average value of 19.2 for this investigation.

A value of D at 46 atomic pct Zn obtained by da Silva (unpublished) in a couple containing a moving α-β phase boundary is in good agreement with the authors' results.

The results of this investigation accord with the observation made earlier by Petrenko and Rubinstein that diffusion in β phases in Ag-Zn, Ag-Cd, and Cu-Zn is much more rapid than in the α phases of the same systems. This is generally attributed to the less dense packing in the body-centered-cubic structure. The activation energy for β brass diffusion is almost exactly half that for α brass diffusion.

Inman[12] has reported self-diffusion coefficients for both copper and zinc in a 45 pct Zn β brass at five temperatures between 678° and 870°C. Over this range, the ratio of zinc to copper mobility drops steadily from 2.08 to 1.75. His data are plotted in Fig. 2. Utilizing Darken's[13] analysis of the Kirkendall effect, chemical diffusion coefficients are calculated from Inman's mobilities and Hargreaves'[14] vapor pressure data.

$$D = (N_{Cu} D^*_{Zn} + N_{Zn} D^*_{Cu}) \left(1 + N_{Zn} \frac{\partial \ln \gamma_{Zn}}{\partial N_{Zn}}\right) \quad [1]$$

where the N's are atom fractions, D^*'s are self-diffusion coefficients and γ is the thermodynamic activity coefficient.

$\frac{\partial \ln \gamma_{Zn}}{\partial N_{Zn}}$ is found to be about 5.30, nearly independent of both temperature and composition within the precision of Hargreaves' data. It is seen from Fig. 3 that the calculated D's are in reasonably good agreement with the present results although they lie somewhat lower.

The expected marker shift may be calculated from the observation of Inman that $D^*_{Zn} \simeq 2\ D^*_{Cu}$ and from Darken's equations

$$X = 2t \frac{(D_{Zn} - D)}{N_{Zn}} \frac{\partial N_{Zn}}{\partial x} \quad [2]$$

$$D = N_{Zn} D_{Cu} + N_{Cu} D_{Zn} \quad [3]$$

where t is the diffusion time, X is the marker displacement, and x is distance.

The values of N_{Zn} and $\frac{\partial N_{Zn}}{\partial x}$ at the marker are given in Table VII as obtained from the penetration curves. Average values of D for the concentration and temperature appropriate to each marker interface were taken from the data reported herein. The displacements are plotted against the square root of time in Fig. 3. Direct measurements of the displacement are plotted on the same figure. It is evident that, in spite of the large scatter in the direct measurements, the two sets of data are in substantial

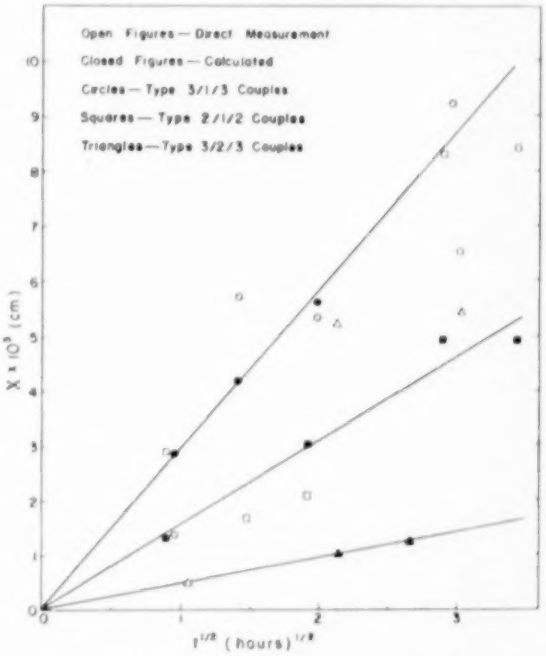

Fig. 3—Dependence of marker displacements in β brass on time at 750°C is illustrated by lines and data points. Note: The calculated shifts for type 3/2/3 couples are too low by a factor of 2.5. The filled triangles and the lowest line which they define should be raised by this factor. The open triangle at longest time should also be raised to a displacement of 9.4×10^{-3} cm.

agreement. It is just as evident that the indirect measurements are much higher and must be incorrect due to some systematic error. In fact, if individual mobilities are calculated from these marker movements by equations of types 2 and 3, negative values for D^*_{Cu} are obtained, as has been pointed out by Heumann.[16]

Thus marker displacements toward the high zinc side of the couple are present in magnitude expected from the differences in mobility of the individual components. As in most other systems showing this behavior, porosity develops in the couple on the side rich in the faster diffusing component, in this case the high zinc side. Therefore, it seems probable that a vacancy mechanism of diffusion also applies in β brass, although an interstitial mechanism remains possible. A ring-type mechanism seems to be ruled out as a major contributor.

Summary

1—The chemical diffusion coefficients for β brass have been determined as a function of composition at temperatures from 500° to 800°C. Within the precision of the data, the diffusion coefficient was found to be a single valued function of concentration, sigmoid in shape, without regard to the concentration range of the diffusion couple.

2—The activation energy appeared to decrease slightly with increasing zinc content showing an average value of 19.2 kcal per mol, about half that generally accepted for α brass.

3—A displacement of tungsten wire markers toward the high zinc side of the couple was observed by the so-called direct method. In spite of considerable experimental scatter, the magnitude of the displacement was in agreement with the values calculated from Inman's self-diffusion measurements using Darken's equations.

4—Porosity in undetermined amount was found to form near the marker interface on the high zinc side of each couple.

5—The composition at the marker interface was found to be independent of time and temperature but dependent upon the range of concentration.

6—It was concluded that the evidence favors a vacancy mechanism of diffusion although it does not exclude an interstitial mechanism.

Acknowledgment

The authors wish to acknowledge the support afforded this work by the Office of Naval Research.

Discussion of this paper, if any, will appear in JOURNAL OF METALS, November 1956, and in AIME Metals Branch *Transactions*, Vol. **206**, 1956.

References

[1] W. Hume-Rothery: *Atomic Theory for Students of Metallurgy* (1952) 2nd Ed., pp. 235, 236. London. Inst. of Metals.
[2] H. B. Huntington and F. Seitz: *Physical Review* (1942) **61**, p. 315.
[3] C. Zener: *Acta Crystallographica* (1950) **3**, p. 346.
[4] H. R. Paneth: *Physical Review* (1950) **80**, p. 708.
[5] L. C. C. da Silva and R. F. Mehl: *Trans.* AIME (1951) **191**, p. 155; JOURNAL OF METALS (February 1951).
[6] C. Wells: *Atom Movements* (1951), p. 26. Cleveland. ASM.
[7] A. D. Smigelskas and E. O. Kirkendall: *Trans.* AIME (1947) **171**, p. 130; METALS TECHNOLOGY (October 1946).
[8] L. H. Beck and C. S. Smith: *Trans.* AIME (1952) **194**, p. 1079; JOURNAL OF METALS (October 1952).
[9] R. W. Balluffi and L. L. Seigle: *Journal of Applied Physics* (1954) **25**, p. 607.
[10] W. Seith and W. Krauss: *Ztsch. für Elektrochemie* (1938) **44**, p. 98.
[11] B. G. Petrenko and R. E. Rubinstein: *Journal of Physical Chemistry* USSR (1939) **13**, p. 508.
[12] M. C. Inman: *Journal* Inst. of Metals, London (1953) **81**, p. 744.
[13] L. S. Darken: *Trans.* AIME (1948) **175**, p. 184; METALS TECHNOLOGY (January 1948).
[14] R. Hargreaves: *Journal* Inst. of Metals, London (1939) **64**, p. 115.
[15] T. Heumann: *Naturwissenschaften* (1953) **40**, p. 164.

Technical Note

X-Ray Diffraction Study of the Nitrides of Uranium

by D. A. Vaughan

COMPOUNDS in the U-N system have received little attention since the work of Rundle, Baenziger, Wilson, and McDonald in 1948.[1] They described the three nitrides UN_3, U_2N_3, and UN as the only phases in this system. The region between UN and U_2N_3 was reported to consist of the two phases while the region between U_2N_3 and UN_3 is a homogeneous solid solution in which the U_2N_3 structure transforms with increasing nitrogen content into the UN_3 structure. This report presents the results of an X-ray diffraction study of the phases present in the region of the diffusion gradient on uranium reacted with nitrogen at several temperatures between 500° and 915°C.

Several samples of uranium used in U-N gas-metal reactions by Mallett and Gerds[2] were available for X-ray diffraction study of phase composition through the diffusion gradient. X-ray diffraction data were obtained using filtered iron radiation at intervals through the diffusion layer of the several samples on filings or turnings at approximately 0.001 in. increments down to the base metal.

Representative X-ray diffraction patterns from various layers through the case on uranium after nitriding at 850°C are shown in Fig. 1. These data show that three different phases are present in the

D. A. VAUGHAN is Principal Physicist, Structural Chemistry Div., Battelle Memorial Institute, Columbus, Ohio.

TN 313E. Manuscript, June 6, 1955.

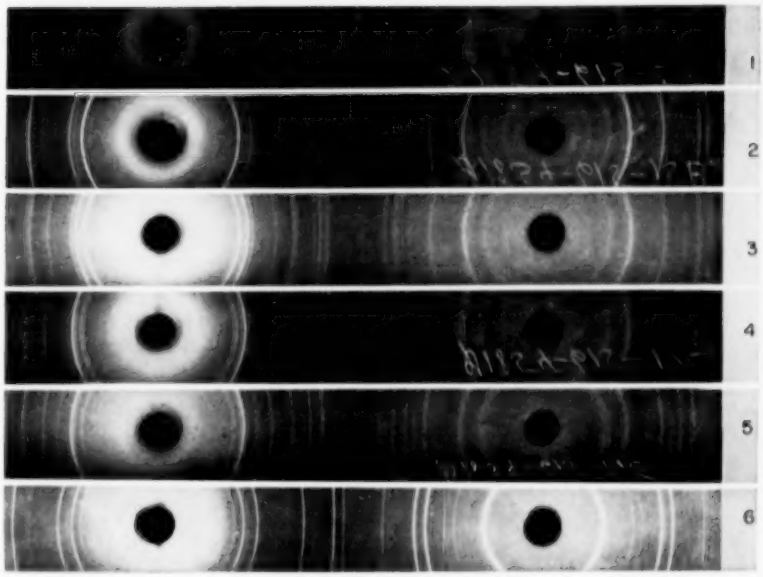

Fig. 1—Representative X-ray diffraction patterns from various layers through the case on uranium after nitriding at 850°C are shown in the composite figure. Nos. 1 through 6 are various phase patterns which are described in the text.

nitride layer. Similar data were obtained over the temperature range 650° to 900°C. X-ray study of layers on uranium nitrided at 500°C gave the pattern of one nitride phase, UN_2.

Pattern 1 of Fig. 1 is that of UN_2 and was obtained from the loose powder lightly brushed off the surface. Patterns 2 through 6 show the change in phase composition with depth from the surface. Additional data were obtained at greater depths but are not shown here since no other nitride phases were observed. Pattern 6 is that of UN and was found as a thin layer adjacent to the base metal. Faint lines of UN_2 and FeKβ lines of UN are present in pattern 6. A number of diffraction lines of the same relative intensity which do not belong to the UN_2 or UN patterns are present in patterns 2 through 5. Furthermore, the layer which gave the highest intensity of these lines lies between UN_2 and UN, suggesting an intermediate nitride phase. The diffraction patterns of the various uranium nitride phases observed in the present study are shown in Fig. 2, along with the pattern of U_2N_3 reported by Rundle.[1] It can be seen that the pattern of the new uranium nitride does not correspond to any of the previously known nitride phases of uranium.

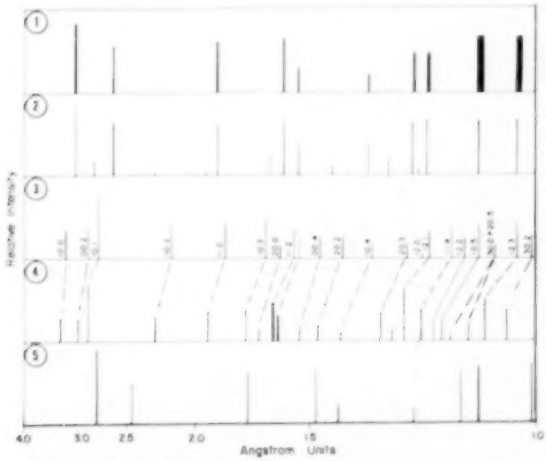

Fig. 2—Five-part drawing shows the diffraction patterns of the various uranium nitride phases that were observed in the present study and/or by other investigators. No. 1 is the pattern for UN_2; No. 2, U_2N_3, observed by Rundle et al.[1] but not observed in this study; No. 3, the new uranium nitride; No. 4, Th_2N_3, observed by Zachariasen and included for comparison;[3] and No. 5, UN.

The spacing of the diffraction lines of the new phase indicated a hexagonal-close-packed structure. A good match of lines on a hexagonal-close-packed net was found for an axial ratio of 1.58 with $a_o = 3.69 \pm 0.01$A and $c_o = 5.83 \pm 0.01$A. Consideration of possible structures revealed that the new uranium nitride has the same structure as that proposed by Zachariasen[3] for Th_2N_3 (the La_2O_3 type of structure). A comparison of the diffraction patterns of Th_2N_3 and the new uranium nitride is shown in Fig. 2. The agreement in the relative intensities of the diffraction lines is seen to be very good, and the two structures are apparently isomorphous.

The present investigation has shown the existence of a new nitride phase in the U-N system. The occurrence of this phase indicates a nitrogen composition less than UN_2 and greater than UN. The isostructural relationship between this phase and Th_2N_3 suggests a composition of U_2N_3 for the new nitride phase. Since the X-ray diffraction pattern does not agree with Rundle's pattern for U_2N_3, further proof of the nitrogen content of the new phase is needed to resolve the difference between Rundle's U_2N_3 and the new nitride phase. It is possible, however, that this and Rundle's U_2N_3 structures are polymorphic modifications of the same compound. No study has been made of the thermal stability of the new phase.

Acknowledgments

This work was performed under AEC Contract No. W-7405-eng-92. The author wishes to express his appreciation also to C. M. Schwartz and A. F. Gerds for their interest and discussions during the course of this work.

References

[1] R. F. Rundle, N. C. Baenziger, A. S. Wilson, and R. A. McDonald: *Journal Amer. Chemical Soc.* (1948) 70, pp. 99-105.
[2] M. W. Mallett and A. F. Gerds: *Journal Electrochemical Soc.* (1955) 102, No. 6, pp. 292-296.
[3] W. F. Zachariasen: The Crystal Structure of Th_2N_3. *AECD Report No. 2999* (Jan. 17, 1948) 2 pp.

Preferred Orientations in Rolled And Annealed Titanium

by J. H. Keeler and A. H. Geisler

Preferred orientations in rolled and annealed titanium sheets were determined by the Geiger counter spectrometer X-ray diffraction technique. Five annealing textures dependent upon the temperature range of annealing were found, and in order of increasing annealing temperature are: 1—a deformationlike texture, 2—a rotated α-recrystallization texture, 3—a retained α-recrystallization texture on annealing at lower temperatures of the β-region, 4—a transformation texture based on recrystallized α and predicted by the Burgers' relationship, and 5—a β-cube texture. These results are examined in terms of current theories of recrystallization textures.

NUMEROUS investigators have described the texture obtained by cold rolling the hexagonal metals, titanium, zirconium, and beryllium, which have c/a ratios less than that of ideal packing, 1.633. The basal planes are rotated out of the rolling plane, about the rolling direction, so that the basal poles are tilted toward the transverse direction as shown schematically in Fig. 1a. In all instances but one,[1] it was also reported that the [1010] direction was parallel to the rolling direction (see Fig. 1b).

Hot rolling has been reported[2-6] as causing a similar tilt of the basal poles in the transverse direction (see Fig. 1a) and causing the [1010] direction also to be parallel to the rolling direction as shown schematically in Fig. 1b.

Annealing after deformation does not appreciably change the tilt of the basal poles in the transverse direction.[2,3] Beryllium[2] continues to have the [1010] direction in the rolling direction after annealing, and similar observations for titanium[3] and zirconium[5,7] have been reported for annealing at fairly low temperatures, again as in Fig. 1b.

At higher annealing temperatures, however, the recrystallized grains of titanium[3] and zirconium[4,5,7] have an orientation such that the [1120] direction is approximately in the rolling direction, although the basal poles are still inclined in the transverse direction. Figs. 1a and 1c show the resulting orientations schematically. This change in orientation has been described as a nominally $\pm 30°$ rotation of the hexagonal crystallites about the basal poles of the cold rolled texture and is apparent from the results which are summarized in Table I for investigations with the X-ray diffraction technique employing film. The angles γ, δ, and β are indicated in Fig. 2 which represents the stereographic projection of $(10\bar{1}0)$ poles for the mean orientation of a pole figure.

Texture determinations for titanium using the Geiger counter spectrometer[5,7] have provided similar results except that in some instances additional components of the texture were proposed, as shown by the summary of data in the upper half of Table II.

On the other hand, the spectrometer technique, when applied to zirconium,* has revealed a splitting of the intense areas of the pole figure for samples annealed at 600°C. This splitting could be described by a 7° rotation of the tilt axis about the normal to the rolling plane.[5,7] Such a splitting for the annealed texture relative to the cold rolled texture was not observed in other determinations for either zirconium or titanium using the less sensitive film X-ray method[2-6,8] and makes the relationship between the two types of texture more complex than the simple rotation about the (0001) pole based on film work. The more precise investigations on zirconium[5,7] permit the descriptions in the lower part of Table II, which show that the texture depends quantitatively on the temperature of annealing. When zirconium is annealed at temperatures up to 400°C, the texture is similar to the cold rolled texture, while annealing in the range 500° to 900°C produces a texture which is only approximately described as $[11\bar{2}0]$ in the rolling direction. More precisely described results for zirconium show that the two types of splitting (1—about an axis in the rolling plane through an angle given in the second column in Table II and 2—about the normal to the rolling plane through an angle given in the third column of Table II) depend on annealing temperature. The [1120] is the rolling direction only when the annealing temperature is in the vicinity of 900°C

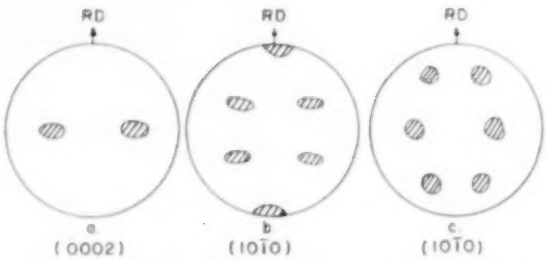

Fig. 1—Shown are schematic pole figures of basal poles (*a*) and prism poles (*b* and *c*) for previously reported sheet orientations of hexagonal metals with c/a ratios less than 1.633.

* Recently completed studies of the textures of annealed zirconium[10] show zirconium to possess textures very similar to those reported here for titanium. Therefore, much of this discussion will include zirconium by virtue of its close similarity to titanium in preferred orientations.

J. H. KEELER, Member AIME, is Research Associate, and A. H. GEISLER, Member AIME, deceased, was Research Associate, Research Laboratory, General Electric Co., Schenectady.

Discussion of this paper, TP 3999E, may be sent, 2 copies, to AIME by Apr. 1, 1956. Manuscript, Nov. 17, 1954. Philadelphia Meeting, October 1955.

and only the split about an axis in the rolling plane (in the rolling direction) remains.

In two investigations, annealing above the allotropic transformation temperature did not appreciably change the texture obtained by annealing somewhat below the transformation temperature for titanium[4] and zirconium,[5] although, in another instance,[6] coarse grained zirconium was reported as showing more scatter in the transformation texture than in the recrystallization texture.

In this study, the spectrogoniometer method of pole figure determination was used with the objective of procuring more detailed and more precise information for titanium than had been available.

Experimental Procedure

The material used in this investigation was high purity titanium prepared by the iodide process. The crystal bar titanium was consolidated by arc melting under argon in a multihearth furnace containing a number of water cooled copper crucibles and a tungsten-tipped electrode. In order to minimize contamination of the titanium by the traces of oxygen and nitrogen remaining in the furnace after evacuation and flushing with argon, 50 g of zirconium were melted to act as a getter before the titanium was melted. After the first melting, the 50 g Ti ingot was inverted and melted a second time.

Cold rolled specimens were prepared from the ingot by a series of reductions of approximately 0.010 in. until the sheet reached a thickness of 0.010 in. From this dimension, it was further reduced to a thickness of 0.001 in. by cold rolling between sheets of alloy steel. The total cold reduction amounted to about 99.7 pct. Specimens were annealed for a fixed time of 1 hr in an evacuated Vycor or quartz tube. Annealing temperature was investigated extensively, but other factors such as annealing time and amount of prior deformation were not included as variables.

An X-ray spectrogoniometer with CuKα radiation was used to obtain transmission pole figures by the quantitative method of Decker, Asp, and Harker[11] modified by Geisler.[12] Also used in this investigation was the automatic pole figure recorder reported recently by Geisler.[13] All four quadrants were examined with 5° increments along the radius of the pole figure. The inner 40° of the pole figure was not determined because the specimen holder interfered with the passage of the X-ray beam. It was not necessary to examine this area, since consistent pole figures of [10$\bar{1}$0] poles, which were confirmed by making (0002) pole figures for most samples, were obtained in the outer 50°, thus defining the textures. Absorption corrections were made for changes in length of the X-ray path through the sample as inclination of the sample to the beam changed. During examination, the specimen was translated back and forth in its plane through a 1 in. distance in order to increase the total number of grains contributing to the measured X-ray intensity. The intensity contours were expressed in multiplicities of the intensity of a comparable sample, but with randomly oriented crystallites.

A 3° source slit has been used frequently in the determination of pole figures by the X-ray spectrogoniometer technique. However, spurious areas in (0002) pole figures were found which were caused by lack of resolution of the (0002) and (10$\bar{1}$1) reflections only 2° apart in 2θ. This difficulty, encountered when a determination of the pole figure for (0002) planes for the cold rolled sheet was made in this investigation, should be recognized before attempting to rationalize pole figures in general which have been determined by the spectrogoniometer technique.[14] It would be expected that the (0002) pole figure would only show nodes in the transverse direction as in Fig. 1a, since the basal plane is tipped about the rolling direction. On the other hand, the first observed pole figure which is reproduced in Fig. 3a exhibited additional intense areas which could not be attributed to (0002) poles of the expected texture. These spurious areas, indicated by triangles in Fig. 3a, occurred at orientations which correspond to (10$\bar{1}$1) reflections of the basic texture. Improving the resolution of the spectrometer by substituting a 1° source slit for the normally used 3° source slit caused the spurious areas to disappear almost completely, as shown in Fig. 3b. They also were removed when a cobalt filter was used to remove the Kα component from the copper radiation, thus showing that they were reflections of Kα radiation in contrast to components of the white radiation which have produced similar spurious areas in pole figures of iron and nickel alloys.[14]

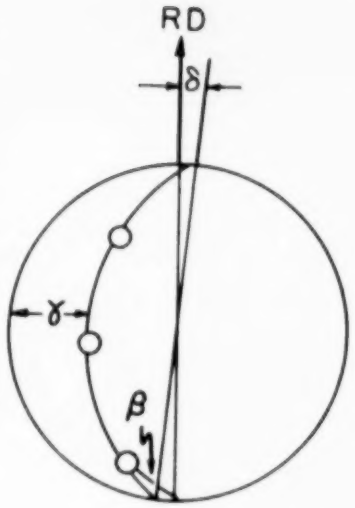

Fig. 2—Represented is the stereographic projection of (10$\bar{1}$0) poles for the mean orientation of a pole figure showing the angles γ, δ, and β used in describing the preferred orientation. γ is the angle between the rolling plane and (0001), δ is the angle between the axis of tilt and the rolling direction, and β is the angle between the rolling direction and [10$\bar{1}$0].

Table I. Previous Results of Texture Analyses Using Film Techniques

Metal	Treatment	Angle Between Rolling Plane and (0001), γ	Angle Between Axis of Tilt and Rolling Direction, δ	Angle Between Rolling Direction and [10$\bar{1}$0], β	References
Be	Cold rolled	0 to 65°	0	0	2
	Annealed at 700°C	0 to 40°	0	0	2
Zr	Cold rolled	0 to ~35°	0	30°*	1
	Cold rolled	0 to 30°	0	0	4
	Annealed at 650°C	30°	0	30°*	4
	Annealed at 800° to 860°C	30°	0	30°*	4
Ti	Cold rolled	30°	0	0	6
	Cold rolled	27°	0	0	3
	Annealed at 500°C	30°	0	?	6
	Annealed at 535°C	27°	0	0	3
	Annealed at 705°C	27°	0	0	3
		27°	0	30°*	
	Annealed at 815°C	27°	0	30°*	3
	Through transformation	27°	0	30°*	3

* [11$\bar{2}$0] appeared to be in rolling direction.

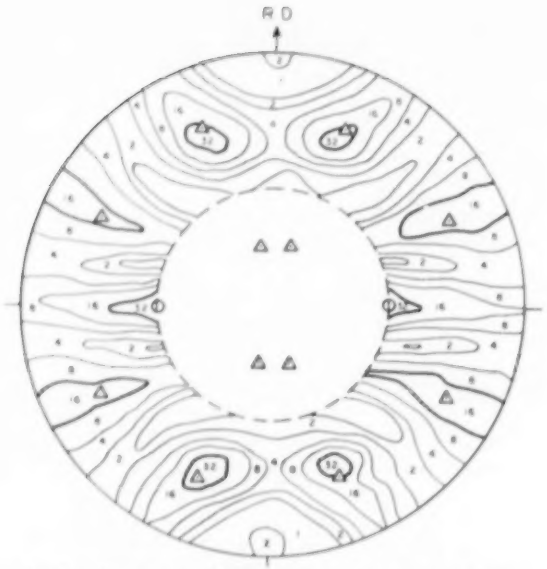

Fig. 3a—Shown is the (0002) pole figure for the same specimen as Fig. 4. The use of a 3° slit allowed (10$\bar{1}$1) reflections indicated by the triangles to be picked up by the counter. The real (0002) poles are those indicated by the circles.

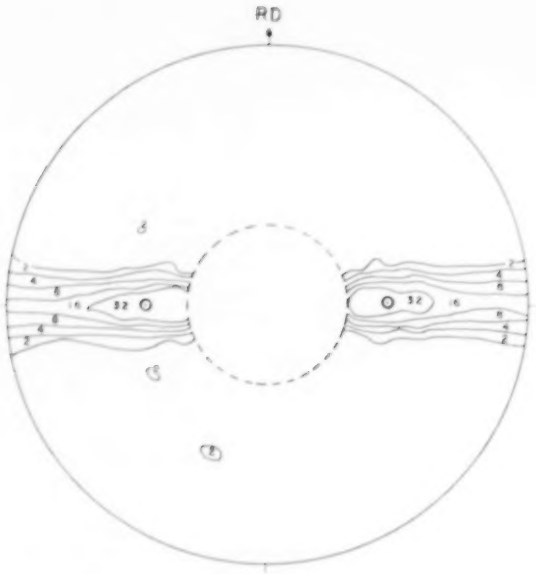

Fig. 3b—Drawn is the (0002) pole figure for the same specimen as Figs. 3a and 4. Use of a 1° slit eliminated all but a few traces of the (10$\bar{1}$1) reflections found in Fig. 2. The (0002) reflections are indicated by the circles.

Areas of all the pole figures to be presented subsequently have been verified for authenticity.

Results

The Cold Rolled Texture—The pole figure for the 99.7 pct cold reduced sheet shown in Fig. 4 indicates that the [10$\bar{1}$0] direction is in the rolling direction and that there is a tilt of the hexagonal unit cells in such a manner that the basal planes are rotated 50 ± 10° out of the rolling plane about the rolling direction. This amount of tilt, confirmed by the (0002) pole figure in Fig. 3b with the peak at about 49°, is greater than that reported by earlier investigators.[5, 6] This result may be due to the greater cold reduction in the present investigation.

Recent investigations using the Geiger counter technique rather than the film technique have shown that for zirconium[5, 7] the spread in the transverse direction did not extend all the way across the pole figure. Williams and Eppelsheimer[5] failed to observe a strong segregation of (10$\bar{1}$0) poles at 60° to the rolling direction of titanium as in Fig. 4 although their pole figure for the (0001) planes showed distinct nodes. No evidence of the double rolling texture observed by Williams and Eppelsheimer[5] was found in this investigation.

Recrystallization Textures—As in the case of zirconium, the annealing textures of titanium were found to depend both qualitatively and quantitatively on the temperature of annealing.

Deformationlike Annealing Texture: The texture for annealing at 400°C shown in Fig. 5 is similar to the rolling texture, but the tilt of the basal planes about the rolling direction is approximately 7° less, as shown in Table III. A similar change in tilt had been observed for zirconium annealed at 300° or 400°C; see Table II.

Rotated α Annealing Textures: For annealing at 500°, 700°, and 950°C, a texture different in kind from the rolled texture was developed, as shown by Figs. 6, 7, and 8. The general feature of this type of texture is that two intense areas now replace each of the intense areas of the cold rolled texture. This type of splitting had not previously been reported for titanium and had been observed only in spectrogoniometer determinations of the textures for zirconium. The annealing texture is characterized by a [10$\bar{1}$0] direction being parallel to the rolling plane and 14° to 20° away from the rolling direction (depending on temperature, as shown in Table III), with the basal planes rotated approximately ±35° out of the rolling plane about the [10$\bar{1}$0] directions in the rolling plane. The orientations are illustrated in Fig. 9.

Inspection of the pole figures in Figs. 6 to 8 discloses that the reorientation after recrystallization does not correspond to a simple rotation about the basal poles, as has been suggested for titanium[5] and for zirconium.[5, 6, 7] This feature is seen from the observations that: 1—high intensity areas of (10$\bar{1}$0) poles remain on the basic great circle, i.e., in the plane of rolling, 2—high intensity regions located 45° from the rolling direction are tilted 40° out of the rolling plane about an axis in the rolling direction, and 3—high intensity regions located 75° from the rolling direction are tilted about 30° out of the rolling plane about an axis in the rolling direction. Thus, it is apparent that all prism poles are not 90° away from a basal pole tilted in the transverse direction (which would have to be true if only rotation about the basal poles occurred during annealing after cold deformation). A rotation about a perpendicular to the rolling plane combined with a rotation about the rolling direction more easily describes the change in orientation from the deformation texture to the recrystallization texture, as shown in Fig. 10. A similar type of rotation about a normal to the rolling plane was mentioned as being able to describe the texture change in the 500°C annealing of zirconium,[5] as seen from Table

Fig. 4—Drawing shows (10$\bar{1}$0) pole figure for 99.7 pct cold reduced titanium sheet. The orientations of (10$\bar{1}$0) poles for the deformation texture (0001) [10$\bar{1}$0] with a tilt of ±49° about the rolling direction as an axis are indicated by the squares.

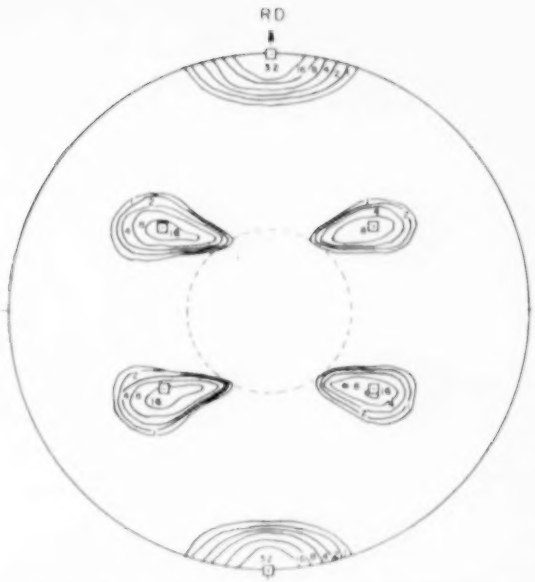

Fig. 5—Drawing shows (10$\bar{1}$0) pole figure for 99.7 pct cold reduced titanium sheet annealed 1 hr at 400°C. The orientations for a 42° tilt of the basal planes in the transverse direction with (10$\bar{1}$0) poles in the rolling direction are indicated by the squares.

II; but on annealing at 600° to 900°C, the [10$\bar{1}$0] direction no longer remained in the rolling plane, and a rotation about the basal poles was a more fitting rationalization.

β Annealed α-Like Textures: In the current investigation, annealing at 950°C, which is about 70°C above the allotropic transformation temperature, produced a texture which also conformed to a rotation about a normal to the rolling plane, as is seen by the comparison of Fig. 8 with Fig. 7. The texture after this heat treatment is the same in type as that of titanium annealed below the α-to-β transformation temperature. This finding of the return to the sheet texture of α-annealed material after being transformed to the body-centered-cubic modification is in agreement with earlier investigations for titanium[7] and zirconium.[5] On the other hand, annealing at temperatures further above the transformation temperature promoted the development of new textures which are described in the next section of the paper.

Transformation Textures—*Texture Based on Recrystallized α:* When the low temperature hexagonal modification of titanium is heated to transform it to the body-centered-cubic form and the latter is subsequently cooled to retransform it back to the hexagonal form, many new orientations would be expected to appear. This behavior is based on the observed orientation relationship[15, 16] in which the (0001) plane of the hexagonal modification forms parallel to one of the {110} cubic planes with a [1120] hexagonal direction parallel to one of the <111> cubic directions. Although this orientation relationship was observed for the cubic to hexagonal transformations, it would also be expected to obtain for the hexagonal to cubic transformation. Thus, the effect on room temperature texture of annealing rolled titanium at temperatures above the transformation temperature would reside in the behavior whereby each hexagonal orientation on heating would produce six cubic orientations with a (110) plane parallel to the original (0001) hexagonal plane and with the six possible combinations of parallel directions (two <111> directions in the (110) plane and three <1120> directions in the (0001) plane). On cooling each of the six cubic orientations would provide 12 orientations of the hexagonal product (two different combinations of the parallel directions for each of the six (110) cubic planes). A four orientation recrystallization texture of the type in Figs. 6 to 8 thus would be replaced by a texture with 288 orientations on heating to above the transformation temperature followed by cooling to room temperature.

Annealing at 1000° and 1050°C produced textures which could be related as previously to the recrystallized-type hexagonal texture found at 500° to 950°C. The (10$\bar{1}$0) pole figure in Fig. 11a for the 1050° anneal was not strikingly different from that for the 950°C anneal (Fig. 8), but six major new maxima appeared adjacent to the base great circle of the pole figure and the four internal areas near the rolling direction were displaced away from the base great circle. The latter behavior suggested a rotation in a manner that would place a <1120> direction in the rolling direction. The predicted orientations for the (10$\bar{1}$0) poles for material that had been heated above the transformation temperature is shown in Fig. 11b.† Although the many new orientations tended to produce a general flattening of the texture, the density of poles at areas corresponding to the nodes of Fig. 11a was generally greater than average. This correlation was especially evident for the six major nodes of Fig. 11a,

† The split about the normal to the rolling plane was neglected in drawing the stereographic projection of predicted poles. When considered, this split would cause an additional minor spread in the locations of the predicted poles.

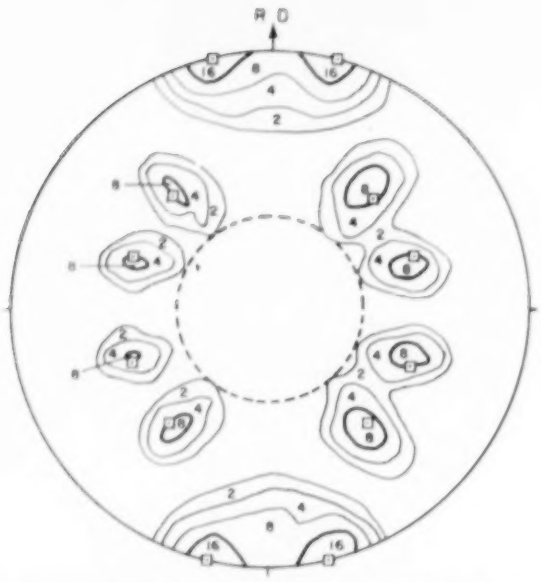

Fig. 6—Drawing shows (10$\bar{1}$0) pole figure for 99.7 pct cold reduced titanium sheet annealed 1 hr at 500°C. The orientations for a 35° angle between the rolling plane and the (0001) planes, a 14° angle between the axis of tilt and the rolling direction, and an angle of 14° between the rolling direction and the [1010] direction are indicated by the squares.

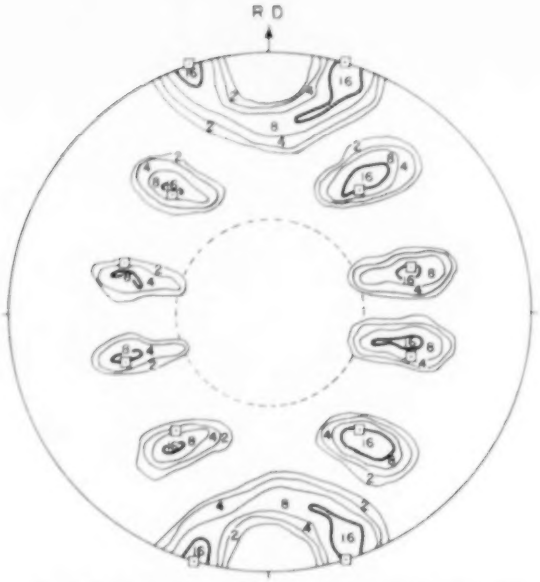

Fig. 7—Drawing is of (10$\bar{1}$0) pole figure for 99.7 pct cold reduced titanium sheet annealed 1 hr at 700°C. The orientations for a 35° angle between the rolling plane and the (0001) planes, a 17° angle between the axis of tilt and the rolling direction, and an angle of 17° between the rolling direction and the [1010] direction are indicated by the squares.

and the encircled areas of Fig. 11b. On the other hand, a more pronounced difference was observed for the (0002) pole figure shown in Fig. 12a, since the recrystallized-type texture showed only intense areas 35° from the rolling plane towards the transverse direction, and a more satisfying correlation existed between the observed texture and the predicted orientations; see Fig. 12b. In view of the good correlations, the cold rolled hexagonal sheet evidently recrystallized during heating before transforming. The recrystallized texture evidently was somewhat different from that for annealing at 950°C and lower temperatures, according to the measurements in Table III for the base texture.

β-Cube Texture: On annealing at 1125° and 1200°C, a second type of transformation texture, shown in Figs. 13a and 14a‡ was observed. The striking feature of this texture which was apparent in both the (10$\bar{1}$0) and (0002) pole figures was the fourfold symmetry which at once suggested that the high temperature form of titanium with its cubic symmetry played a preponderant role in the development of the texture. The fourfold symmetry of a cubic material is evident only when a (100) plane is parallel to the rolling plane and such would occur if a cube texture could be developed in the high temperature modification by secondary recrystallization. Predicted poles for hexagonal product formed from the cubic form with a cube texture are given in Figs. 13b and 14b for comparison with the observed pole figures. The agreement is very good and permits the conclusion that annealing at 1125° and 1200°C developed a cube texture in the body-centered-cubic phase. Since the (0001) plane forms parallel to the {110} planes, the presence of nodes in the (0002) pole figure at 45° positions readily shows that a cube texture must have existed in the high temperature phase. This texture predominately controlled the transformation texture for 1125° and 1200°C annealing; not a recrystallization texture of the hexagonal modification.

‡ The individual intense areas and the irregular contours of Fig. 14a are due to the large grain size produced in the 1200°C anneal.

Table II. Previous Results of Texture Analyses Using Geiger Counter Spectrometer

Treatment	Angle Between Rolling Plane and (0001), γ	Angle Between Axis of Tilt and Rolling Direction, δ	Smallest Angle Between Rolling Direction and [10$\bar{1}$0], β	References
Cold rolled	30°	0	0	8
Cold rolled	30°	0	0	8
	20°	90°	?	
Commercial titanium, ½ hr, 650°, 800°, or 850°C	30°	0	0	9
	30°	0	30°	
	30°	20°	20°	
Iodide titanium, 5 min, 800°C	30°	0	0	9
	30°	0	30°	
Zirconium, cold rolled	36°	0	0	7
Cold rolled	40°	0	0	5
Annealed 1 hr, 300°C	38°	0	0	5
Annealed 1 hr, 400°C	45°	0	0	5
Annealed 1 hr, 500°C	38°	14°	14°	5
Annealed 1 hr, 600°C	36°	7°	20°*	7
Annealed ½ hr, 600°C	35°	7°	20°*	5
Annealed ½ hr, 900°C	40°	2°	24°*	5
Annealed ½ hr, 600°C and 900°C	40°	0	30°*	5

* [10$\bar{1}$0] not in rolling plane. For the case when this angle is 30°, the [11$\bar{2}$0] is in the rolling direction.

Discussion of Results

The present results taken together with recent results for zirconium[5, 10] provide the most complete survey yet available for the textures of the two

Fig. 8—Drawing shows (10$\bar{1}$0) pole figure for 99.7 pct cold reduced titanium sheet annealed 1 hr at 950°C. The orientations for a 35° angle between the rolling plane and the (0001) planes, a 20° angle between the axis of tilt and the rolling direction, and an angle of 20° between the rolling direction and the [1010] direction are indicated by the squares.

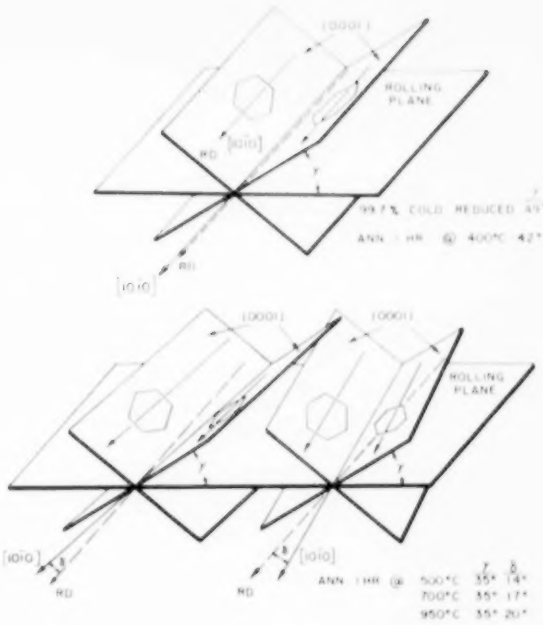

Fig. 9—Diagrams give schematic representation of deformation and recrystallization textures found in titanium sheet.

hexagonal metals, titanium and zirconium. The observed behaviors are similar to the extent that there are five temperature ranges of annealing which in order of increasing temperature correspond to: 1-the deformationlike texture, 2-the rotated α-recrystallization texture, 3-the retained α-recrystallization texture on annealing at lower temperatures of the β-region, 4-the transformation texture based on recrystallized α, and 5-the β-cube texture. This discussion will be devoted to interpreting the origin of the textures associated with the five temperature ranges and any conclusions would appear to be equally applicable to either titanium or zirconium because of the similarity of their behaviors.

One interesting general aspect is the fashion in which the texture depends primarily on annealing temperature. A dependence of texture on annealing temperature has been observed for other metals and must be given due consideration in any theory of the origin of annealing textures.[17, 18] With zirconium and titanium, the recrystallization texture tends to appear on the periphery of intense areas of the cold rolled texture, and it departs more and more from the areas of maximum intensity in the cold rolled texture as the annealing temperature is increased. Quantitative measurements of the departure are plotted for various annealing temperatures in Fig. 15 where the angle between the location of (1010) maxima in the rolled texture and in the annealed texture are plotted. The initial part of the curve with low slope corresponds to the region of the deformationlike texture, the sharply increasing branch to the α-recrystallization textures and the upper flat part corresponds to the transformation textures. Each of these should be considered separately, since different phenomena are involved.

Deformationlike Annealing Texture—The deformationlike texture persists on annealing at tem-

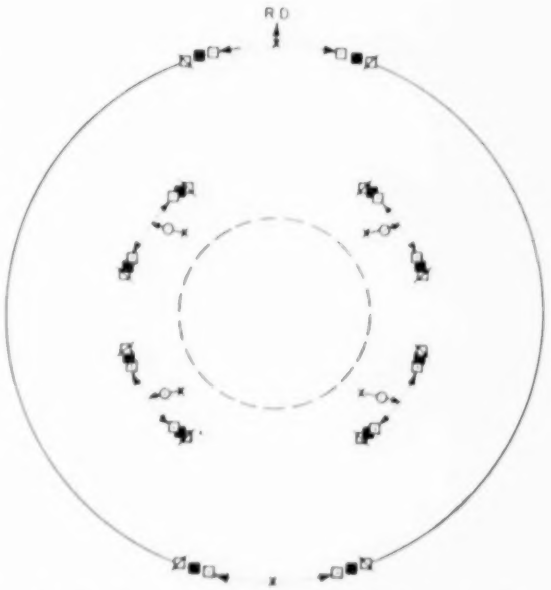

Fig. 10—Illustrated is the stereographic projection describing changes in position of (1010) poles with successively higher annealing temperatures. Solid arrow represents the rotation about the rolling direction and dotted arrow, the rotation about the normal to rolling plane. Symbols represent: cross, location of (1010) poles in the deformation texture; circle, annealed at 400°C; open square, annealed at 500°C; filled square, annealed at 700°C; and bisected square, annealed at 950°C.

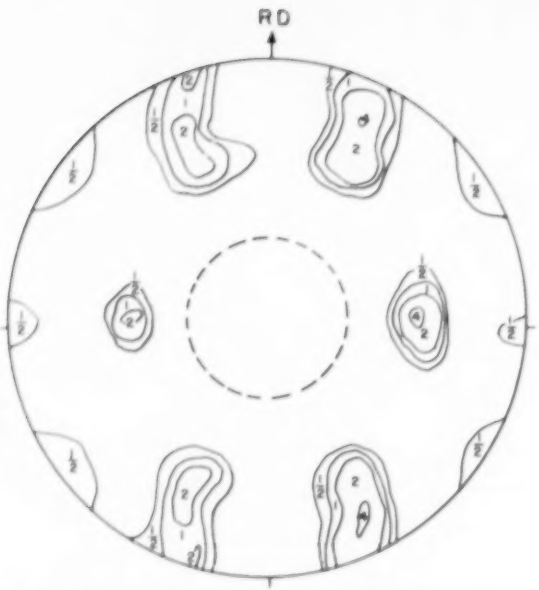

Fig. 11a—Drawing is of (1010) pole figure of 99.7 pct cold reduced titanium sheet annealed 1 hr at 1050°C.

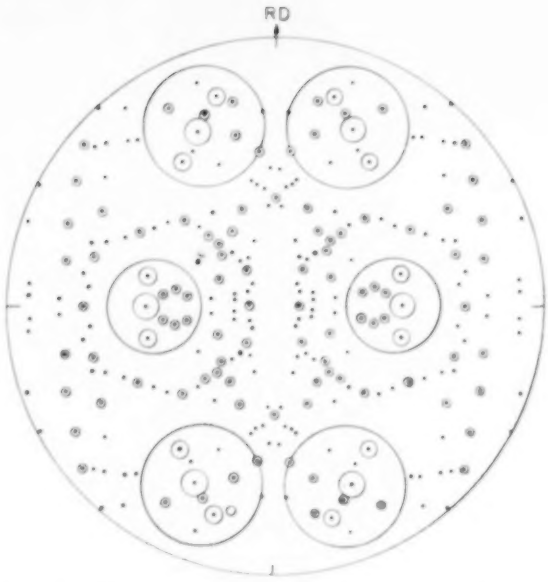

Fig. 11b—Drawing shows predicted orientations for (10$\bar{1}$0) poles for titanium heated above the transformation with the initial orientation (0001) 40° to rolling plane and [11$\bar{2}$0] in rolling direction. The encircled points indicate superposition of 2, 3, or 6 poles with the number increasing with size of circle.

peratures of 400°C or less. The significant differences relative to the cold rolled texture include first, a slight rotation about the [10$\bar{1}$0] which is in the rolling direction and second, a general sharpening of the texture. The observed rotation for titanium was about 7° whereas that for zirconium was 2° to 5° (Table II). Sharpening of the texture is clearly evident from the more closely spaced contours of 400°C annealed sample, Fig. 5, compared with that for the cold rolled sample, Fig. 4. McGeary and Lustman[1] have determined the kinetics for this reaction by determining the change in intensity of the [10$\bar{1}$0] reflection in the rolling direction and have shown that the intensity increased during the annealing at the lower temperatures. According to the data for zirconium the process was complete in 1 hr at temperatures from 350° to 400°C. Thus observations presented for 1 hr at 400°C (Tables II and III) would be expected to represent the end state of this particular process, providing there are not significant differences in composition of materials investigated. Measurements made in the rolling direction do not form sufficient basis on which to decide whether the intensity increase was due to the appearance of more crystallites with the [10$\bar{1}$0] aligned in the rolling direction (texture sharpening) or to recovery from diffraction line broadening.§ In view of the slight rotation apparent—only the (10$\bar{1}$0) reflections that are remote from the rolling direction—it can be concluded that the process involved crystallite reorientation. Analysis of the data of McGeary and Lustman has shown that the activation energy for the process is in the range of 36,000 to 44,000 cal.[10] The process has been referred to as *recrystallization in situ*[1] and *recrystallization into the [1010] annealing texture*.[10] Its nature appears to be adequately described by a rearrangement of imperfections into a subgrain structure, i.e., *polygonization* probably followed by the favored growth of some of the slightly disoriented regions to account for the observed rotation. The kinetics of annealing clearly indicate that the formation of the [10$\bar{1}$0] annealing texture is the first stage of recrystallization which is followed by the process in which a more significantly rotated texture is evolved.

§ Line broadening would result in abnormally low intensity mainly when conditions for maximum resolution were used in the X-ray diffraction spectrogoniometer.

Table III. Summary of Preferred Orientations for Titanium

Treatment	Angle Between Rolling Plane and (0001), γ	Angle Between Axis of Tilt and Rolling Direction, δ	Angle Between Rolling Direction and [10$\bar{1}$0], β
Cold rolled	49°	0	0
Annealed 1 hr, 400°C	42°	0	0
Annealed 1 hr, 500°C	35°	14°	14°
Annealed 1 hr, 700°C	35°	17°	17°
Annealed 1 hr, 950°C	35°	20°	20°
Annealed 1 hr, 1000°C	37°	5°	24°
	Plus other components of transformation texture from this recrystallized α texture.		
Annealed 1 hr, 1050°C	38°	8°	25°
	Plus other components of transformation texture from this recrystallized α texture.		
Annealed 1 hr, 1125°C	45°	0, 90°	25°
	90°	45°	45°
Annealed 1 hr, 1200°C	Transformation from β cube texture same as 1125°C.		

Rotated α-Annealing Textures—The α-recrystallization textures formed in the region of 500° to 950°C cannot be described precisely on a 30° rotation about the pole of the basal plane but include a component around the normal to the sheet surface. Thus, including these metals in any generalization that describes the recrystallization texture by a rotation of the deformation texture around the normal of the closest packed plane[28] is an oversimplification of the texture change. Instead, the axis

Fig. 12a—Drawn is (0002) pole figure of 99.7 pct cold reduced titanium sheet annealed 1 hr at 1050°C.

Fig. 12b—Shown are predicted orientations for (0002) poles for titanium heated above the transformation with the initial orientation (0001) rotated 30° from rolling plane about [1120] axis at 8° to rolling direction. The encircled points indicate superposition of 2 or 3 poles with the number increasing with size of the circle.

normal to the sheet surface for the one component of titanium is about 3° from the pole of the (1125) plane. When the component for the additional tilt about the rolling direction is included, the axis which describes the whole process becomes even more complex. The kinetics of the process for annealing zirconium at 600°C have been adequately followed by determining the increase in diffracted intensity at a position in the 600°C pole figure which corresponds to the nominal location of (1010) poles.[7] The results suggest that the process is 75 to 85 pct complete in ½ to 1 hr, thus showing that the annealing time periods used in this and previous work[4] were sufficient for substantially complete recrystallization. On the other hand, the variations in orientation of the texture with annealing temperature reported here for titanium (Table III) and zirconium (Table II) show the inadequacy of exploring the kinetics at various temperatures using the assumption that only a single type of recrystallization texture obtains. For example, in a sample annealed for 1 hr at 500°C, McGeary and Lustman found that the 600° annealing texture was present to the extent of only 35 pct whereas the deformation texture had disappeared to the extent of 65 pct. Since the peak intensity where measurements should be made is at a different location for the 500°C annealing texture than for the 600°C texture, a greater percentage of recrystallized texture consistent with the disappearance of the deformation texture would be expected if the proper location in the pole figure had been explored.¶

¶ Another example of an inconsistency which may be clarified by considering temperature dependence of texture appears in Fig. 8 of the paper by McGeary and Lustman. The illustration is a micrograph of a 97 pct cold rolled sample that had been annealed 96 hr at 395°C. It shows an equiaxed grain structure which is clearly a substantially recrystallized structure but X-ray diffraction measurements showed that only 55 pct of the material had reoriented from the rolled texture with 35 pct appearing in the 600°C annealing texture. Analysis of the complete pole figure undoubtedly would have shown that a texture with maxima at locations between those for the cold rolled texture and those for the 600°C anneal would have been completely developed but that the rotation had been an amount less than that for 600°C annealing.

Previously the suggestion was made that three types of annealing textures should be distinguished for zirconium.[10] The results of the type shown in Fig. 15 suggest that there is a continuous change of the texture in the α-recrystallization range. Each different annealing temperature would require measurements at a different location relative to the rolling direction and rolling plane. Such would be required for any accurate evaluation of the activation energy of the recrystallization process.

Each of the textures which have been determined for annealing in the range from 500° to 950°C appears to be distinctive rather than a combination of more basic components such as would be the case if recrystallization had not been substantially complete in the annealing interval used. The relation of the recrystallization textures to the deformation texture is such that the proportion of original grains contributing their orientation to the recrystallization texture decreases with annealing temperature. That is, the component of the deformation texture which develops into the recrystallization texture is of a decreasing minority. Possibly the favored orientation has less competition for growth as temperature increases until the recrystallization texture is the ideal one which satisfies the relation of 30° rotation about the pole of the basal plane. This condition is attained during a 900°C anneal (following a 600°C anneal) for zirconium but apparently requires a much higher temperature, well into the β-region, for titanium, which then is complicated by the transformation texture. A further consideration on the quantitative variation of the annealing texture with temperature supposes that, if interfacial energy for nucleation or growth of certain orientations is the controlling factor, then the dependence of interfacial energy on orientation is a function of tempera-

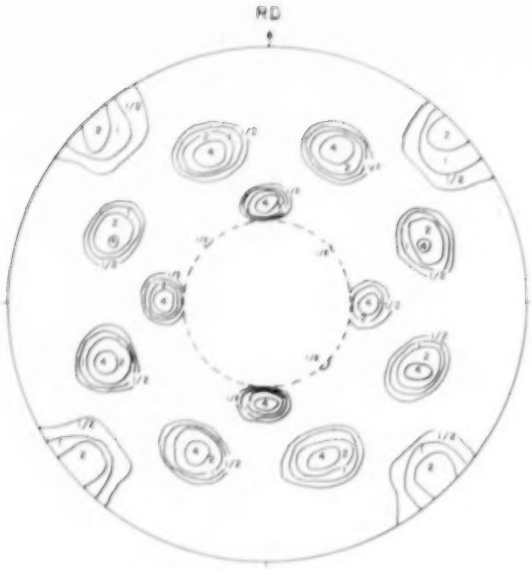

Fig. 13a—Drawing is of (10$\bar{1}$0) pole figure of 99.7 pct cold reduced titanium sheet annealed 1 hr at 1125°C.

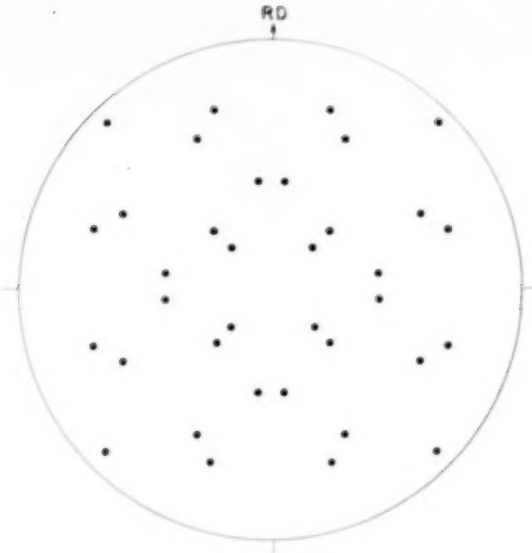

Fig. 13b—Drawn are (1010) poles for α-titanium transformed from a cube texture of β.

ture. There appears to be agreement between the proponents of the various theories for recrystallization textures that the driving energy of *recrystallization* is interface energy associated with boundaries between lattice regions of different orientation.[17] Considerable variation of anisotropy of growth rates alone with annealing temperature during primary recrystallization does not seem likely.[17, 18] Thus, a variation with temperature of the orientation dependence of nucleation is suggested by these results for explaining the textures which are observed. As annealing temperature is increased, those nuclei which depart more and more from the major orientation of the deformation texture are activated and grow to dominate the recrystallization texture.

The thought that the textures observed in the range 500° to 950°C are grain coarsening textures rather than primary recrystallization textures cannot be readily dismissed. This premise is supported by the conclusion that the recrystallization texture of beryllium was the same as the rolling texture[9]**

** A detailed investigation on the annealing textures of beryllium has not yet been made but might well be expected to provide results similar to those reported here for titanium.

which might also be the case for zirconium and titanium. McHargue and Hammond[3] have proposed that the deformation texture of titanium is retained by the material just recrystallized, and as the tempera-

Fig. 14a—Shown is (0002) pole figure of 99.7 pct cold reduced titanium sheet annealed 1 hr at 1200°C.

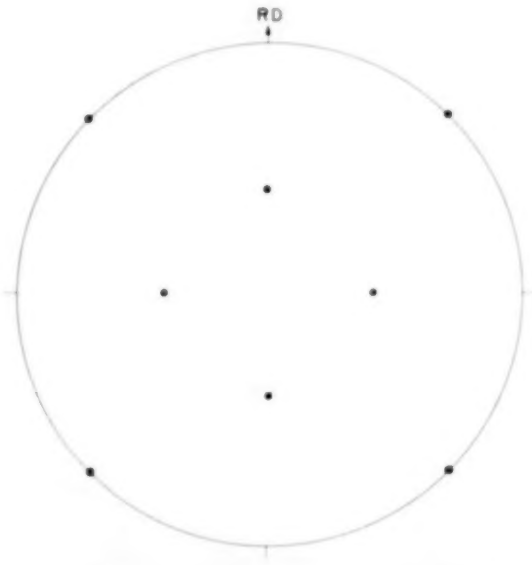

Fig. 14b—Shown are (0001) poles for α-titanium transformed from a cube texture of β.

ture is increased and grain growth and secondary recrystallization take place, a new texture is produced. Furthermore, the metallographic observations of McGeary and Lustman[1] for zirconium have shown that annealing in the range 500° to 600°C is accompanied by grain coarsening after an induction period. If the process is one of secondary recrystallization, the variation in texture with temperature could then be attributed to a temperature dependence of growth rates in various directions. On the other hand, McGeary and Lustman were unable to find evidence that discontinuous grain growth typical of secondary recrystallization had occurred. They found that about 40 pct reorientation had occurred before the start of grain coarsening. In addition, formation of the [1010] annealing texture was associated with only a small fraction of the softening rather than the substantial amount which is normally associated with primary recrystallization. In view of those various features of the process, a clear distinction between primary and secondary recrystallization cannot be made for annealing in the temperature range of 500° to 900°C.††

†† Additional work is now in progress for annealing in this temperature range in order to explore the effect of time on the annealing texture.

β-Annealed, α-Like Textures—Proceeding to the textures formed on annealing in the β-temperature region, the failure to detect an appreciable change in the recrystallization α-texture on heat treating at temperatures 40° to 70°C above the transformation[5,6] can be interpreted as the result of either the failure of the transformation to occur or the reversion of material to the original orientation of the α phase rather than to the many orientations suggested by the Burgers' orientation relationship. The latter seems more likely, since similar observations, mainly on single crystals which had been subjected to transformation cycles, have been made by Newkirk and Geisler[15] for titanium, for zirconium by Burgers,[21] for thallium by Dehlinger,[22] and for cobalt by Dehlinger, Osswald, and Bumm.[23] Each β-orientation formed on heating from the original α-phase should be capable of providing 12 orientations of crystallites of the α-phase on cooling. It is improbable that an α-grain would favor any one of these orientations without the influence of some nucleating agent. Such an agent may be a crystalline inclusion, an oriented overgrowth, or a special condition of residual stress.‡‡ Increasing the β-annealing temperature to 1000°C and above would reduce the influence of the nucleating agent by allowing greater solution of impurities and by relief of lattice strain. In this way all the orientations of the family would have equal probability of occurrence and the modified α-textures would be expected as observed.

‡‡ In a very recent study[24] Glen and Pugh discuss the possible orientations which can arise from several transformations. They suggest that dislocations in the parent phase may be responsible for a reversion to the original texture after a transformation cycle.

Transformation Textures Based on Recrystallized α—The texture formed at intermediate temperatures in β-temperature range has been clearly rationalized on the basis of an α-recrystallization texture modified by the transformation cycle $\alpha \rightarrow \beta \rightarrow \alpha$. Two conclusions apparently are permitted by the interpretation of this texture: 1—the deformed α-phase had recrystallized prior to the transformation and 2—the orientation relationship which has been determined for the β-to-α transformation also serves for the α-to-β transformation.

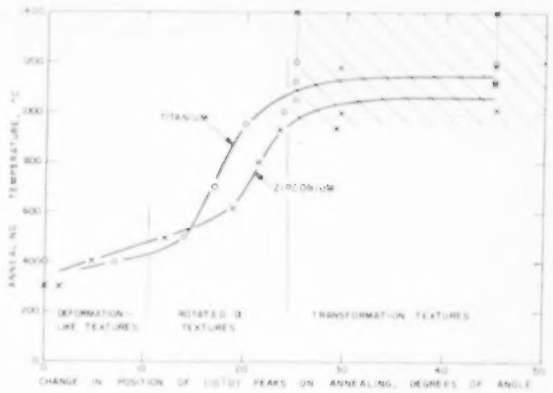

Fig. 15—Annealing temperature vs angular change in position of (1010) peaks from position in deformation texture is charted.

β-Cube Texture—The cube texture in zirconium and titanium apparently is a product of secondary recrystallization, for, when cold worked sheet is annealed at 1000° to 1100°C, the transformation texture is derived from the primary recrystallization texture of α. Consequently, the heating rate presumably had been such that α recrystallized before the transformation temperature had been reached. At the higher annealing temperatures, the primary β-texture from which the cube texture is derived thus may be regarded as the transformation texture of β derived from the recrystallization texture of α. The predicted locations of cube poles in the transformation texture (Fig. 16) show that a minor component indicated by circles in Fig. 16 approximates the cube orientation. The nominal orientation for the recrystallized hexagonal phase

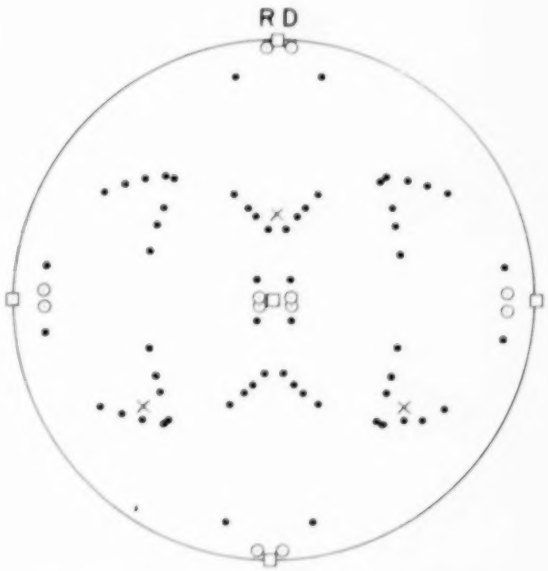

Fig. 16—Drawing shows location of (100) poles of cubic β form of titanium after transformation from recrystallized hexagonal α in the orientations (0001) ±38° to rolling plane tilted about axis 8° to rolling direction. Cube texture is indicated by squares.

of (0001) tilted 38° to the rolling plane about an axis 8° to the rolling direction provides four β-orientations (of 24) which are 7° to 8° away from the cube position. On the other hand, material which departs slightly from the nominal orientation of the recrystallized α-texture to the extent that the basal plane is tilted 45° to the rolling plane about an axis about 5° to the rolling direction would provide four orientations which are precisely in the cube orientation. These orientations, which represent about 17 pct of the total, deviate appreciably from the balance, which tend to cluster about other areas of the pole future. Thus, one of the requirements proposed by Dunn[20]—that secondary grains arise from growth of primary grains, which deviate in orientation from the major percentage of the primary grains—tends to be fulfilled. The second requirement—that a number of primary grains in the deviating orientation be larger than the average size of the primary grains by a factor of two or three—cannot readily be verified but could reasonably be expected to obtain. Such would happen if the primary β-grains of cube orientation were the first to form in the hexagonal to cube transformation and thus had the opportunity to grow before transformation to β-grains of other orientations occurred. Stimulation of one orientation in a transformation at the expense of other crystallographically equivalent orientations is a common phenomenon in phase transformations. Although the details have not yet been determined, the stimulation might well involve the same factors that account for the return to the same α-orientations when lower annealing temperatures in the β-temperature range were used.

The origin of the cube texture in titanium and zirconium does not seem to reside in a 30° to 40° rotation about the pole of the close packed (110) plane away from a major component of the original texture as has been proposed for the primary recrystallization texture of iron[20] or the cube texture of face-centered-cubic metals.[21] The two major components in Fig. 16 might be regarded as those of the type approximated by crosses which correspond to (112) [111]. The relation of this orientation to the cube texture can be described by a 35° rotation about a (110) pole, but a 45° rotation about [001] is also required. Thus, the process cannot be described as a simple rotation of the intense areas about the pole of a close-packed plane. It more readily meets the requirements for secondary recrystallization specified by Dunn as described in the previous paragraph. Regardless of the specific mechanism which produces the cube texture, the development of this single sharp texture from a multicomponent matrix is noteworthy.

Summary

1—The deformation texture of cold reduced sheet titanium discloses a symmetrical orientation characterized by an average tilt of the basal plane 50° ± 10° out of the rolling plane toward the transverse direction and about the rolling direction. There are two orientations corresponding to the two directions of tilt of the basal plane. Annealing at 400°C produced a similar type of texture, but the basal planes were somewhat less tilted.

2—The texture for annealing at 500° to 950°C is also a symmetrical orientation with a $[10\bar{1}0]$ direction lying in the rolling plane 14° to 20° away from the rolling direction and the basal poles at an angle of 35° from the rolling plane. There are four such orientations.

3—The relation between the α-recrystallization texture and the deformation texture can be described as a 14° change in the amount of tilt of the basal planes followed by a rotation of ±14° to 20° about a normal to the rolling plane. This analysis does not agree with earlier results for both titanium and zirconium, wherein a rotation about the basal pole described the final relation.

4—Annealing at 950°C, above the allotropic transformation temperature, produces a texture very similar to that obtained by recrystallization below the allotropic transformation temperature.

5—Annealing at higher temperatures in the β-temperature region, at temperatures of 1000° and 1050°C, produced additional texture components that could be predicted by the Burgers' relationship from the α-recrystallized texture.

6—Annealing at 1125° and 1200°C, in the β-temperature region, produced α-titanium textures that could be shown to have transformed from a cube texture of β-titanium.

7—The behavior for titanium was found to be similar to that for zirconium, according to recently obtained data on the latter. These results were examined in terms of current theories of recrystallization textures.

Acknowledgments

The authors wish to thank Anne S. Cooper, who obtained the X-ray data, and other members of the Metallurgy Research Department who assisted in the experimental portions of this study. The authors are also grateful to J. E. Burke for helpful comments on the manuscript.

Discussion of this paper, if any, will appear in JOURNAL OF METALS, November 1956, and in AIME Metals Branch *Transactions*, Vol. **206**, 1956.

References

[1] W. G. Burgers and F. M. Jacobs: *Metallwirtschaft* (1935) **14**, p. 285.
[2] A. Smigelskas and C. S. Barrett: *Trans.* AIME (1949) **185**, p. 145; JOURNAL OF METALS (February 1949).
[3] C. J. McHargue and J. P. Hammond: *Trans.* AIME (1953) **197**, p. 57; JOURNAL OF METALS (January 1953).
[4] R. K. McGeary and B. Lustman: *Trans.* AIME (1951) **191**, p. 994; JOURNAL OF METALS (November 1951).
[5] J. H. Keeler, W. R. Hibbard, Jr., and B. F. Decker: *Trans.* AIME (1953) **197**, p. 932; JOURNAL OF METALS (July 1953).
[6] H. T. Clark, Jr.: *Trans.* AIME (1950) **188**, pp. 1154-1156; JOURNAL OF METALS (September 1950).
[7] R. K. McGeary and B. Lustman: *Trans.* AIME (1953) **197**, p. 284; JOURNAL OF METALS (February 1953).
[8] D. N. Williams and D. S. Eppelsheimer: *Trans.* AIME (1953) **197**, p. 1378; JOURNAL OF METALS (October 1953).
[9] D. N. Williams and D. S. Eppelsheimer: *Ztsch. für Metallkunde* (1953) **44**, p. 360.
[10] J. H. Keeler and A. H. Geisler: *Trans.* AIME (1955) **203**, p. 395; JOURNAL OF METALS (February 1955).
[11] B. F. Decker, E. T. Asp, and D. Harker: *Journal of Applied Physics* (1948) **19**, p. 388.
[12] A. H. Geisler: *Modern Research Techniques of Physical Metallurgy* (1953) pp. 131. Cleveland. ASM.
[13] A. H. Geisler: *Review of Scientific Instruments* (1954) **25**, p. 727.
[14] A. H. Geisler: *Journal of Applied Physics* (1954) **25**, p. 1245.
[15] J. B. Newkirk and A. H. Geisler: *Acta Metallurgica* (1953) **1**, p. 370.
[16] A. J. Williams, R. W. Cahn, and C. S. Barrett: *Acta Metallurgica* (1954) **2**, p. 117.
[17] W. G. Burgers and T. J. Tiedema: *Acta Metallurgica* (1953), **1**, p. 234.
[18] J. J. Becker: *Trans.* AIME (1951) **191**, p. 115; JOURNAL OF METALS (February 1951).
[19] A. H. Geisler, J. H. Keeler, and W. R. Hibbard, Jr.: Discussion of ref. 7. *Trans.* AIME (1953) **197**, p. 1574; JOURNAL OF METALS (November 1953).
[20] P. A. Beck: *Acta Metallurgica* (1953), **1**, p. 230.
[21] W. G. Burgers: *Physica* (1933-1934) **1**, p. 561.
[22] U. Dehlinger: *Metallwirtschaft* (1932) **11**, p. 223.
[23] U. Dehlinger, E. Osswald, and H. Bumm: *Ztsch. für Metallkunde* (1933) **25**, p. 62.
[24] J. W. Glen and S. F. Pugh: *Acta Metallurgica* (1954) **2**, p. 520.
[25] C. G. Dunn: *Acta Metallurgica* (1953) **1**, p. 163.
[26] C. G. Dunn: *Acta Metallurgica* (1954) **2**, p. 173.
[27] A. Merlini and P. A. Beck: *Acta Metallurgica* (1953) **1**, p. 598.

Thermodynamic Properties of Solid Fe-Au Alloys

Free energies, heats, and entropies of mixing of solid Fe-Au alloys have been measured by the galvanic cell method between 800° and 900°C. A positive deviation from Raoult's law and a large excess entropy of mixing were observed, both attributable to lattice distortion caused by the disparity in component atom sizes. Since the terminal solid solutions are not *regular*, thermodynamic properties computed from the location of the miscibility gap do not agree well with measured quantities. The electromotive force data suggest some changes in the existing Fe-Au phase diagram.

by L. L. Seigle

ALTHOUGH a considerable amount of information has been accumulated about the thermodynamic properties of metal solid solutions which exhibit negative deviation from Raoult's law, particularly those in which ordering occurs, relatively few experimental measurements have been made on solutions with positive deviation. This is due to the infrequency of broad homogeneous regions suitable for experimental measurement in solutions of this type, since any marked positive deviations from ideality lead to restricted solubility and the formation of miscibility gaps. Thermodynamic data reported in the literature for such systems have usually been calculated from the location of the miscibility gap boundaries under the assumption that the entropies of mixing are ideal, i.e., the terminal solutions are *regular*.[1]

One of the few binary systems with both positive deviation and a wide homogeneous range in the solid is the Ni-Au system. A recent investigation of solid Ni-Au alloys[2] revealed that the entropies of mixing were much larger than ideal and consequently thermal data computed from the phase boundaries assuming regular solutions were seriously in error. Theoretical considerations put forward by Zener[3, 4] indicated that high entropy values should generally be associated with systems possessing a miscibility gap in the solid, when this is due to differences in the size of component atoms. These facts suggest that the regular solution assumption is a poor approximation for many solid solutions with positive deviation and that reliable thermodynamic data generally cannot be obtained by conventional methods from the location of miscibility gap boundaries.

The Fe-Au system, Fig. 1, resembles the Ni-Au system in certain respects. The presence of a miscibility gap in the solid indicates a large positive deviation from ideality, but there is nevertheless an extensive single phase region suitable for experimental measurement. The following investigation of solid Fe-Au alloys was carried out in order to obtain additional data on the thermodynamic properties of metal solid solutions with positive deviation from Raoult's law and to further compare thermodynamic data computed from miscibility gap boundaries with those measured experimentally.

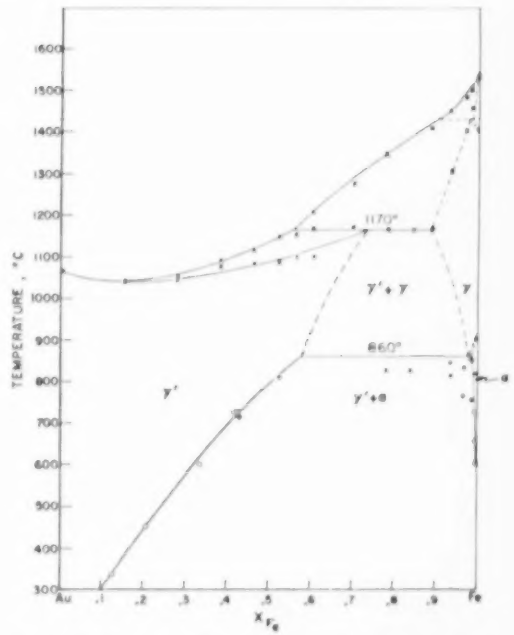

Fig. 1—Fe-Au phase diagram is presented. Symbols represent: cross, data of Isaac and Tammann;[7] circle, data of Jette et al.;[6] and plus, data from the present investigation.

Experimental Method

The thermodynamic properties were derived from measurements of the potential developed between pure solid iron and Fe-Au alloys in a high temperature galvanic cell. The experimental apparatus and technique were the same as those used for the Ni-Au alloys and described in a previous report.[2] Cell electrodes were 1/16 in. diam rods swaged from chill-cast ingots and annealed for one week at 850°C. The alloys were prepared by melting fine gold granules under argon with pure iron obtained from the National Research Co. The cell electrolyte was

L. L. SEIGLE, Member AIME, is Head, Fundamental Metallurgy Section, Sylvania Electric Products Inc., Bayside, N. Y.

Discussion of this paper, TP 4029E, may be sent, 2 copies, to AIME by Apr. 1, 1956. Manuscript, Nov. 24, 1954. Philadelphia Meeting, October 1955.

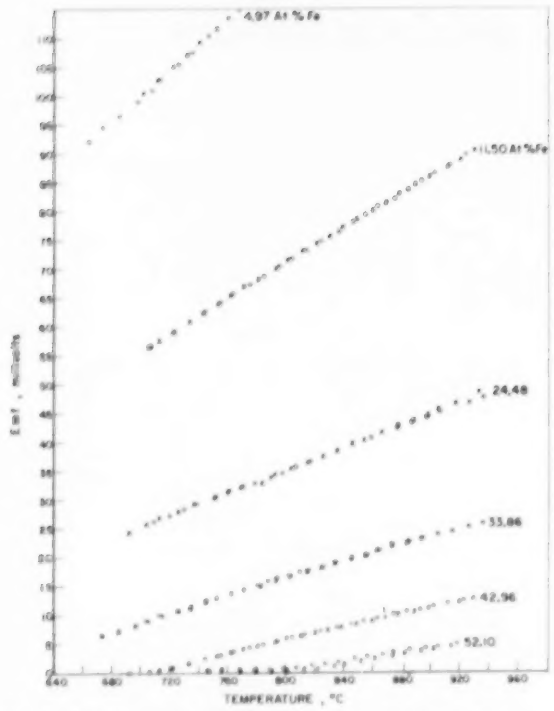

Fig. 2—Plot of experimental potential vs temperature curves shows that cell potentials were the same on heating and cooling. Equilibrium was evidently attained in the homogeneous alloys. Crosses represent cooling and circles, heating.

an equimolar mixture of KCl and NaCl to which was added 0.2 mol pct $FeCl_2$ and 0.5 mol pct NH_4Cl. Traces of $FeCl_2$ were removed by evaporation at temperatures well below the cell operating temperatures (boiling point of Fe_2Cl_6 = 319°C). The cell was heated under purified argon from 700° to 900°C in 10° steps, allowing 1 hr before measuring the final potential difference at each temperature.

Experimental Results

Shortly after reaching temperature, a steady potential was developed in the galvanic cells which remained constant within a few tenths of a millivolt for a period of days. The slight tendency for potentials to drift noticed in the Ni-Au cells[2] was almost completely absent. Chemical analysis revealed changes in alloy electrode compositions amounting to no more than a few tenths of an atomic percent after immersion for about one week in the molten electrolyte. Furthermore, the amount of gold picked up by the pure iron electrode varied from 0 to 0.02 atomic pct, and evidently a smaller transport of gold through the electrolyte in the Fe-Au than in the Ni-Au cells was responsible for the increased cell stability.

As shown in Fig. 2, cell potentials were the same on heating and cooling, and equilibrium was evidently attained in the homogeneous alloys. The variation of cell potential was very nearly linear with temperature, but for all of the alloys a slight negative curvature was observed whose significance becomes clear when it is recalled that the pure α-iron electrode passes through its Curie point at 770°C. Since the pure iron electrode undergoes a change of state involving a heat effect within the temperature range studied, it is to be expected that

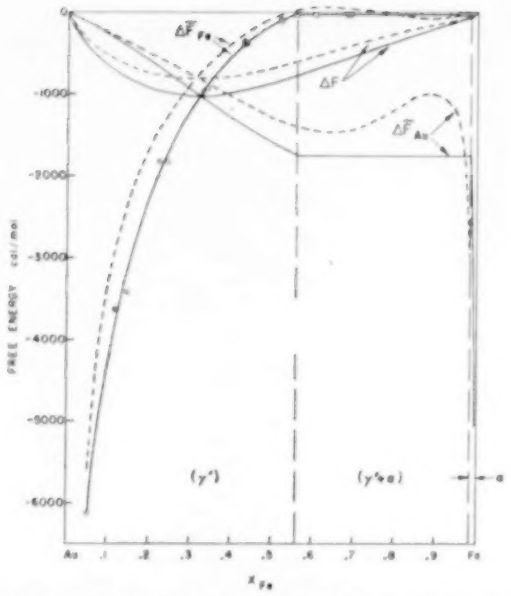

Fig. 3—Free energies of solid Fe-Au alloys are plotted at 850°C relative to α-iron. Solid lines represent experimental data and dashed lines, data calculated from the phase diagram.

the partial heats of mixing and therefore the slopes of the curves will vary with temperature. Partial heats and entropies of mixing were obtained from the slopes of the curves between 800° and 900°C and therefore represent the values of these quantities in the paramagnetic face-centered-cubic alloys relative to paramagnetic body-centered-cubic iron.

Free Energies of Mixing and Activities

Values of these quantities determined from the experimental data at 850°C are compared in Figs. 3 through 5 with values calculated from the position of the miscibility gap. A direct application of the Borelius method[5] for calculating thermodynamic properties from the equilibrium diagram is not possible in this system, since the phases in equilibrium have different crystal structures. However, a variation of this method was devised for deriving these properties from the location of the phase boundaries between 400° and 700°C (see Appendix) which takes advantage of the facts that the solubility of gold in α-iron is very low and the free energy differences between α and γ-iron well known, and which makes the usual regular solution assumption for the γ' phase.[6]

The values of thermodynamic constants shown in Figs. 3 through 5 and throughout the manuscript are values relative to pure solid α-iron, and for this reason the free energy and activity calculated for the face-centered-cubic phase from the equilibrium diagram do not go to zero and unity, respectively, for $X_{Fe} = 1$, since $\Delta F_{\alpha\text{-}\gamma}$ at 850°C is 14 cal per mol. This quantity is so small, however, that the free energy and activity curves at 850°C are practically identical whether referred to pure α or γ-iron as a standard state. Calculation of free energies and activities from the potential data was carried out by the usual methods (see ref. 2). Graphical integration of the Gibbs-Duhem equation yielded partial molar free energies and activities for the homogeneous gold-rich alloys. In the heterogeneous alloys, these quantities are shown as constants in

accordance with well known principles. The values of $\Delta\bar{F}_{Au}$ and a_{Au} for the α-phase shown in Figs. 3 and 5 are estimated values.

As expected from the appearance of the phase diagram, the free energy and activity values for iron indicate a positive deviation from Raoult's law. However, throughout most of the homogeneous range, the deviation for gold is negative. This negative deviation is, formally, a consequence of the fact that the iron activity curve starts out with a positive curvature. If the Gibbs-Duhem equation is written in the form $X_{Fe}\, d \ln \gamma_{Fe} + X_{Au}\, d \ln \gamma_{Au} = 0$, then

$$\frac{d\gamma_{Au}}{dX_{Fe}} = -\left(\frac{X_{Fe}\,\gamma_{Au}}{X_{Au}\,\gamma_{Fe}}\right)\left(\frac{d\gamma_{Fe}}{dX_{Fe}}\right).$$

Since $\left(\frac{X_{Fe}\,\gamma_{Au}}{X_{Au}\,\gamma_{Fe}}\right)$ is always positive, the sign of $\frac{d\gamma_{Au}}{dX_{Fe}}$ is opposite to that of $\frac{d\gamma_{Fe}}{dX_{Fe}}$. It is obvious from the positive curvature of the iron activity curve throughout the region $X_{Fe} = 0$ to 0.2 that $\frac{d\gamma_{Fe}}{dX_{Fe}}$ is positive and hence $\frac{d\gamma_{Au}}{dX_{Fe}}$ negative, which means that γ_{Au} must be less than unity throughout this region. Peculiarities in the gold-rich solutions are also indicated by the occurrence of maxima and minima in the partial excess free energies of iron and gold (Fig. 4); however, the integral excess free energy is positive throughout.

The free energies and activities computed from the phase diagram do not coincide with the experimental values, but there are some parallels in the calculated and experimental curves. For example, in Fig. 4 the calculated values of $\Delta\bar{F}_{Au}^{ex}$ remain close to zero throughout the range of compositions in which the experimental values are negative. The calculated $\Delta\bar{F}_{Fe}^{ex}$ curve begins to level off at about the same point that the experimental curve goes through a maximum. Similarly, the calculated and experimental activity curves in Fig. 5 remain approximately parallel throughout the homogeneous range, although there are no inflections in the calculated curves. Within the two phase region, the dotted lines represent calculated values for the metastable face-centered-cubic solid solution.

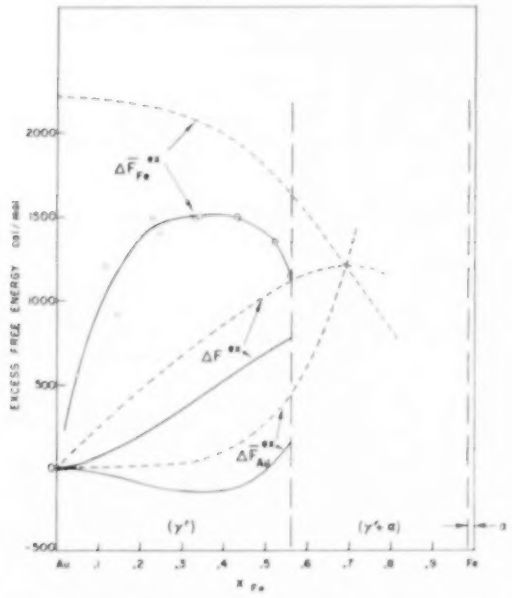

Fig. 4—Excess free energies of solid Fe-Au alloys are plotted at 850°C relative to α-iron. Solid lines represent experimental data and dashed lines, data calculated from the phase diagram.

Heats of Mixing

Heats of mixing for the homogeneous alloys were calculated from the potential data using standard methods already described.[5] Values of the slopes of the potential temperature curves at 850°C were obtained from a straight line drawn through the points between 800° and 900°C, since these temperatures are above the Curie point of iron. Experimental curves within the heterogeneous region of Fig. 6 were constructed by first evaluating $\Delta\bar{H}_{Fe}^{het}$ from the potential temperature curves for a series of heterogeneous alloys, using the Gibbs-Helmholtz equation. As shown in Fig. 6, the value of ΔH_{Fe}^{het} is constant within the heterogeneous region and different from the relative partial molar heats of mixing of the homogeneous phases.* Having established the value of $\Delta\bar{H}_{Fe}^{het}$ from the experimental data, the values of ΔH in the heterogeneous region were obtained graphically by extending the $\Delta\bar{H}_{Fe}^{het}$ horizontal until it intersected the vertical axis $X_{Fe} = 1$ and connecting this point with the point of intersection of the ΔH curve for the homogeneous alloys and the vertical line representing the left-hand phase boundary, $X_{Fe} = 0.562$. The value of $\Delta\bar{H}_{Au}^{het}$ was then determined by extending this line to the vertical axis, $X_{Au} = 1$.

In Fig. 6 the values for the heats of mixing for the face-centered-cubic phase calculated from the

* If ΔH is the relative integral molar heat of mixing, then $\Delta\bar{H}_{Fe} = \Delta H + (1 - X_{Fe}) \frac{d\Delta H}{dX_{Fe}}$. Since the proportions of the two phases vary linearly with composition in the heterogeneous region, ΔH^{het} is a linear function of X, $\Delta H^{het} = MX_{Fe} + b$, $\Delta\bar{H}_{Fe}^{het} = MX_{Fe} + b + (1 - X_{Fe})M = M + b$ = constant. This fact is readily seen from a plot of the heat of mixing vs mol fraction, as pointed out by Wagner (chap. 1, ref. 1).

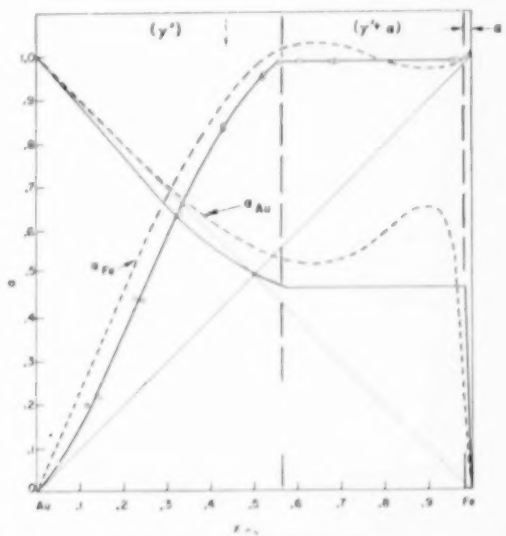

Fig. 5—Activity curves are given for solid Fe-Au alloys at 850°C and refer to α-iron as the standard state. Solid lines represent experimental data and dashed lines, data calculated from the phase diagram.

phase diagram are shown as dotted lines. These values are referred to pure α-iron as a standard state and, therefore, the calculated and experimental heats of mixing for the homogeneous alloys are directly comparable. The calculated curves intersect the pure iron line at a value of 340 cal per mol corresponding to the heat of transformation from γ to α-iron at 850°C. It is immediately apparent that there is a much greater discrepancy between experimental and calculated enthalpies than between experimental and calculated free energies (Fig. 3); and in this system, as in the Ni-Au system, calculations from the phase diagram do not yield reliable values for the heats of mixing. This is true, again, because the entropies of mixing (Figs. 7 and 8) are considerably higher than the ideal entropy, and the regular solution assumption does not hold. The leveling off of the calculated $\Delta\bar{H}_{Fe}$ curve, and near zero values of $\Delta\bar{H}_{Au}$ occurring between $X_{Fe} = 0.4$ to 0 are not borne out by the experimental data and it is evidently not safe to draw conclusions from the shapes of the calculated curves as has been done for very similar examples in the Au-Pt system.[1] From its shape throughout the homogeneous region, the integral heat of mixing curve is clearly quite asymmetric.

Entropies of Mixing

Relative partial and integral molar entropies, presented in Figs. 7 and 8, were calculated from the slopes of the potential temperature curves between 800° and 900°C. Construction of the curves for the heterogeneous region was accomplished as already described for the ΔH values. A large excess entropy of mixing was found in the solid FeAu alloys which are, therefore, similar in this respect to the Ni-Au alloys.

It appears from a consideration of the enthalpy and entropy curves in Figs. 6 through 8 that the odd shape of the excess free energy curves of iron and the negative deviation of gold are due to an exceptionally rapid increase in the excess entropy with addition of iron to the high gold solid solutions. Thus the negative deviation of gold is not due to an energy effect, since the addition of gold to these alloys is accompanied by the absorption of heat but is associated, seemingly, with the exceptionally large entropy of mixing in the gold-rich alloys.

Fe-Au Phase Diagram

The potential temperature curves of alloys containing 95 to 100 pct Fe were not in agreement with the accepted phase diagram for the Fe-Au system in the neighborhood of the α-γ transformation, and some consideration was given to redrawing the diagram in this region. Fig. 1 shows all of the experimental data reported in the literature for this system. The lattice parameter measurements of Jette, Bruner, and Foote[6] precisely establish the miscibility gap boundaries between 300° and 750°C, but the antiquated data of Isaac and Tammann[7] form a very poor basis for the involved configuration in the region around the α-γ transformation shown in the *Metals Handbook*. These data, for example, give the α-γ transformation temperature for pure iron as 827°C. In addition to the foregoing, the phase diagram in *Metals Handbook* has been copied to some extent from a paper of Nowack[8] who based his version on data by Wever that was apparently unpublished.

The experimental potential temperature curves for alloys containing 95.9, 97.0, 98.3, and 98.9 atomic pct Fe all possessed an inflection which occurred at about 855° to 865°C, suggesting the existence of an isothermal reaction at this temperature level, in disagreement with the minimum shown in the accepted phase diagram. Moreover, the activity of iron in the two phase alloys at 850°C varied from 0.986 to 0.990. Since Raoult's law is probably obeyed in these dilute solutions, the solubility of gold in α-iron at this temperature must be less than 1.5 atomic pct which is considerably less than that indicated in the current diagram and makes the appearance of a minimum all the more unlikely.

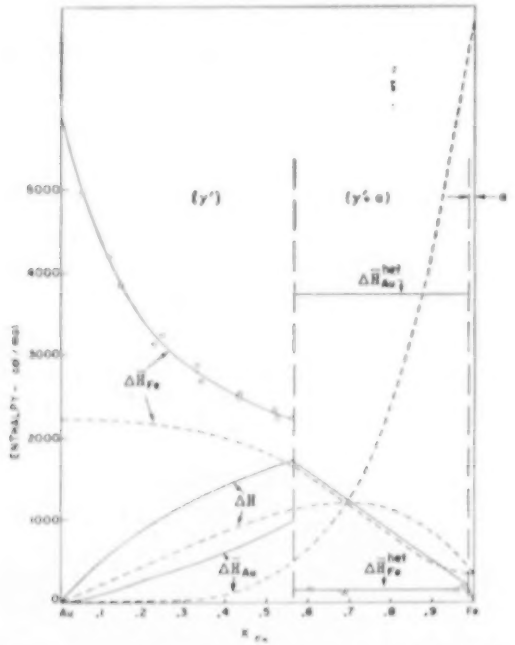

Fig. 6—Enthalpies of solid Fe-Au alloys are plotted at 850°C relative to α-iron. Solid lines represent experimental data and dashed lines, data calculated from the phase diagram.

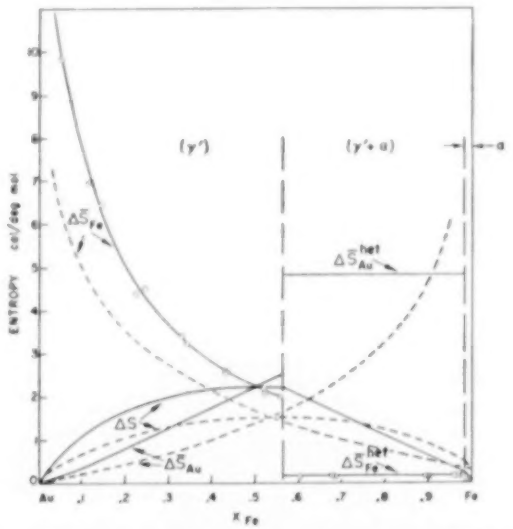

Fig. 7—Entropies of solid Fe-Au alloys are plotted at 850°C relative to α-iron. Solid lines represent experimental data and dashed lines, data calculated from the phase diagram.

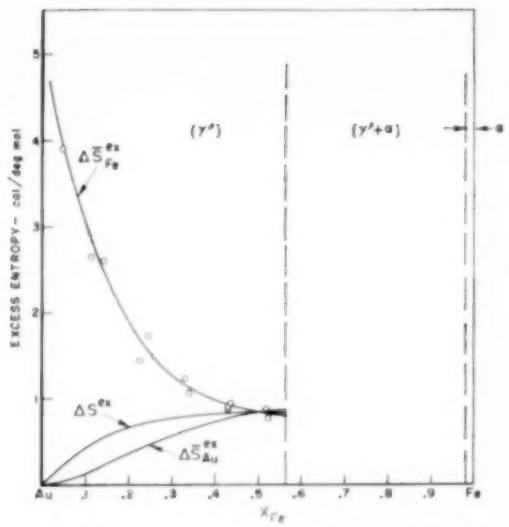

Fig. 8—Excess entropy of solid Fe-Au alloys is plotted at 850°C relative to α-iron.

These experimental data are in accord with the occurrence of a eutectoid reaction at 855° to 865°C and an attempt was made to construct the phase diagram assuming a eutectoid horizontal at 860°C. The eutectoid composition was calculated from the thermodynamic data to be $X_{Fe} = 0.978$ and the peak of the miscibility gap to lie at 1172°C, $X_{Fe} = 0.793$ (see Appendix). The calculated height of the miscibility gap relative to the solidus confirms the existence of a peritectic transformation in this system. Using these facts as a guide, the diagram was drawn as shown in Fig. 1.

Discussion of Results

As expected from the appearance of the phase diagram, solid solutions in the Fe-Au system exhibit a positive deviation from ideality. This statement is made on the basis that the excess free energy of mixing is positive throughout, although the partial values for gold are negative in most of the homogeneous region. In addition, the heat of mixing of the solid alloys is positive.

It seems likely that this positive deviation in the Fe-Au, as in the Ni-Au alloys, is a consequence of the atomic size factor, since the gold atom is about 14 pct larger than the iron atom, using Pauling's metallic radii for coordination No. 12.[9] The magnitude of the distortional energy term may be calculated on the basis of the model suggested by Lawson,[10] modified to take into account the fact that the atoms are compressible and therefore do not occupy the same volume in solid solution as in the pure solid.[11] It is assumed that the addition of an off-size atom to the solid solution lattice results in a primarily shear distortion of the lattice and volume expansion or contraction of the solute atom. Based upon a simple elasticity picture, therefore, the total strain energy is the sum of the shear-strain energy of the lattice, plus the hydrostatic work of expansion or compression of the solute atom, and can be written as

$$E_{total} = \frac{2\,G_m}{3\,V_m}(V-V_m)^2 + \frac{K_s}{2\,V_s}(V-V_s)^2 \quad [1]$$

where V_m and V_s are molar volumes of matrix and solute, respectively, G_m is the shear modulus of matrix, K_s is the bulk modulus of pure solute, and V is the molar volume of solute in solution.

It is considered that the molar volume of the solute in the solid solution will be that which minimizes the total elastic strain energy and is given by

$$\frac{dE_{total}}{dV} = \frac{4\,G_m}{3\,V_m}(V-V_m) + \frac{K_s}{V_s}(V-V_s) = 0 \quad [2]$$

or

$$V = \frac{V_m V_s (4\,G_m + K_s)}{4\,G_m V_s + 3\,V_m K_s}. \quad [3]$$

Substituting this value of V in Eq. 1, an expression is obtained for the strain energy increment upon adding one mol of solute of molar volume V_s to an infinite matrix of molar volume V_m; in other words, the partial molar free energy of the solute due to elastic distortion, $\Delta\bar{F}_D$,

$$\Delta\bar{F}_D = \frac{2\,G_m K_s (V_s-V_m)^2}{4\,G_m V_s + 3\,V_m K_s}.$$

Setting $V_m = X_1 V_1 + X_2 V_2$, $G_m = X_1 G_1 + X_2 G_2$ and $\Delta E_D = X_1 \Delta\bar{F}_{D_1} + X_2 \Delta\bar{F}_{D_2}$, the following expression is obtained for the distortional energy term

$$\Delta E_D = 2\,X_1 X_2 (V_2 - V_1)^2 \left\{ \frac{K_1 X_2}{4\,V_1 + 3\,K_1 A} + \frac{K_2 X_1}{4\,V_2 + 3\,K_2 A} \right\} \quad [4]$$

where $A = (X_1 V_1 + X_2 V_2)/(X_1 G_1 + X_2 G_2)$, X_1 and X_2 are mol fractions of constituents, V_1 and V_2 are molar volumes of constituents, G_1 and G_2 are shear moduli of constituents, and K_1 and K_2 are bulk moduli of constituents.

Substituting appropriate values for molar volumes and elastic constants† in the foregoing, ΔE_D for $X = 0.5$ is computed to be 1500 cal per mol for Ni-Au and 850 cal per mol for Fe-Au solid solutions at 900°C. As Machlin has pointed out in a recent note,[12] the strain energy computed by such an isothermal work calculation is free energy and not internal energy. Therefore, ΔE_D should be compared with the excess free energy and not with enthalpy as done previously.[2] Experimentally measured values of excess free energy at $X = 0.5$ and 900°C are 1100 cal per mol in the Ni-Au and 680 cal per mol in the Fe-Au solutions. The magnitude of strain energy given by the foregoing expression is in better agreement with the experimental data than that given by previous formulas (see refs. 2 and 11).

An important feature of the thermodynamic data for both the Fe-Au and Ni-Au solid solutions is the existence of an entropy of mixing which is considerably in excess of that for an ideal solution. For this reason, heats of mixing computed from the miscibility gap boundaries, assuming regular solution behavior, are seriously in error for both of these systems. In addition, the usual statistical treatments of solid solutions, which ignore vibrational entropy changes, are probably not applicable.

It appears from an examination of the literature that large positive excess entropies are not excep-

† Appropriate values for molar volumes and elastic constants are:
V_{Ni} (900°C) = 6.63 cu cm per mol
V_{Fe_γ} (900°C) = 7.26 cu cm per mol
V_{Au} (900°C) = 10.33 cu cm per mol
K_{Ni} (900°C) = 1.60×10^{12} dynes per sq cm
K_{Fe_γ} (900°C) = 1.21×10^{12} dynes per sq cm
K_{Au} (900°C) = 4.90×10^{11} dynes per sq cm
G_{Ni} (900°C) = 6.00×10^{11} dynes per sq cm
G_{Fe_γ} (900°C) = 4.54×10^{11} dynes per sq cm
G_{Au} (900°C) = 1.84×10^{11} dynes per sq cm
Values of bulk and shear moduli were estimated from Köster's data,[13] assuming $\nu = 1/3$.

tional in metal solutions. In addition to the results for the Ni-Au and Fe-Au systems, positive excess entropies have been measured in solid solutions of Cu-Pt ($\Delta S^{ex} = 1.1$)[14] and Co-Pt ($\Delta S^{ex} = 0.8$).[16] Computations based upon the solubility of various elements in the terminal solid solutions of aluminum indicate the existence of large partial excess entropies for the solute elements.[4] Similar results have been obtained for the Cd-Zn system.[16] The data collected by Chipman and Elliott (p. 102, ref. 4) show that many liquid metal solutions also possess excess entropies ranging up to 0.6 E.U. More recently, Kleppa[17] has measured positive excess entropies in liquid Ti-Au, Sn-Au, Pb-Au, and Bi-Au varying from a few tenths to about 1.0 E.U.

In solid solutions, the excess entropy can be attributed to an increase in vibrational specific heat, and correspondingly vibrational entropy, as a result of lattice distortion arising from the disparity in atom radii. Such an increase in vibrational entropy was predicted on thermodynamical and statistical mechanical grounds by Zener[4] and Lumsden (p. 343, ref. 16) and recently confirmed by direct experimental measurement of the heat capacity of a 50-50 Ni-Au alloy by DeSorbo and Oriani.[18] Although it does not appear that the excess entropy of liquid solutions can be explained in terms of lattice distortions, Kleppa[17] has observed that there is a qualitative relationship between the magnitude of ΔH in liquid solutions with positive deviation and difference in the size of the component atoms. He believes that the excess entropies are related to these size differences and that the size factor plays a role in liquid solutions similar to that in solid solutions.

As already mentioned, the predicted and observed large deviations from ideal entropy of mixing in solid solutions of atoms of different size invalidate the usual methods of computing thermodynamic data from phase boundaries, which depend upon the regular solution assumption. These methods have naturally been applied mainly to systems possessing a miscibility gap, but it is just such systems in which large excess entropies are to be expected. It appears, therefore, that thermal data for solid solutions computed from the location of phase boundaries by the usual schemes are not generally reliable.

Conclusions

1—Measurements of the thermodynamic properties of solid Fe-Au alloys between 800° and 900°C indicate, in agreement with the phase diagram, that the solid solutions deviate positively from ideal behavior. This positive deviation is apparently due to lattice distortion arising from the difference in size of the component atoms.

2—In Fe-Au as well as Ni-Au solid solutions, a large excess entropy of mixing occurs which is apparently a consequence of the disparity in component atom sizes as predicted by Zener. Since the size factor is frequently responsible for limited solid solubility, it appears that abnormally high mixing entropies may often be associated with the presence of a miscibility gap in the solid. Therefore, the usual methods of calculating thermal data from the position of the miscibility gap are not accurate because they assume that the entropy of mixing is ideal.

3—The currently accepted phase diagram of the Fe-Au system may be in error in the region near the α-γ transformation of iron. The present data are consistent with the occurrence of a simple eutectoid reaction rather than the involved picture transcribed from ancient documents.

Appendix

Following Borelius,[5] it is assumed that the relative integral molar free energy of the γ' phase can be represented as a function of composition and temperature as follows

$$\Delta F = a_1 X(1-X)^4 + a_2 X^2(1-X)^3 + a_3 X^3(1-X)^2 + a_4 X^4(1-X) + RT[X \ln X + (1-X)\ln(1-X)]. \quad [5]$$

The partial molar free energy of iron in the γ' phase relative to pure γ-iron may then be written

$$\Delta\bar{F}_{Fe} = \bar{F}_{Fe} - F^{\circ}_{\gamma} = a_1 + (2a_2 - 8a_1)X + (3a_3 - 10a_2 + 22a_1)X^2 + (4a_4 - 10a_3 + 18a_2 - 28a_1)X^3 + (-8a_4 + 11a_3 - 14a_2 + 17a_1)X^4 + (4a_4 - 4a_3 + 4a_2 - 4a_1)X^5 + RT\ln X. \quad [6]$$

The partial molar free energy of iron in the γ' phase referred to pure α-iron as a standard state is given by $\Delta\bar{F}'_{Fe} = \Delta\bar{F}_{Fe} + (F^{\circ}_{\gamma} - F^{\circ}_{\alpha})$.

Accordingly

$$\Delta\bar{F}'_{Fe} = RT\ln a'_{Fe} = a_1 + (2a_2 - 8a_1)X + \ldots + RT\ln X + (F^{\circ}_{\gamma} - F^{\circ}_{\alpha}). \quad [7]$$

To evaluate the unknown coefficients a_1 to a_5, values of a'_{Fe} were obtained from the solubility of gold in the α phase at 400°, 500°, 600°, and 700°C, assuming that Raoult's law applies to iron as the solvent in this dilute solution. The positions of the phase boundaries are accurately known in this temperature range from the work of Jette et al.[5] Values of $F^{\circ}_{\gamma} - F^{\circ}_{\alpha}$ were obtained from the tabulations of Zener[19] and Darken.[20] Having evaluated a_1 to a_5, it was possible to compute the thermodynamic functions for the γ' phase at any temperature. Values for the coefficients are as follows: $a_1 = 7016$, $a_2 = 11243$, $a_3 = 7309$, and $a_4 = 1909$.

The peak of the miscibility gap was located at 1172°C and $X_{Fe} = 0.793$ by making use of the fact that at this point

$$\frac{d^2\Delta F}{dX^2} = 0$$

and

$$\frac{d^3\Delta F}{dX^3} = 0.$$

Since 1172°C is above the solidus temperature for this composition, the calculations bear out the existence of a peritectic reaction in this system.

Finally, the eutectoid composition was calculated by inserting the experimental value of $\Delta\bar{F}_{Fe} = \bar{F}_{Fe} - F^{\circ}_{\gamma}$ at 860°C in Eq. 6 and solving for X. The value obtained was $X_{Fe} = 0.978$ and represents the composition of iron-rich γ-phase which is in equilibrium with α at 860°C.

Acknowledgments

The author wishes to express his appreciation to Ben Howell for carrying out the experimental measurements and to Harry Fara for help in performing the calculations. This work was carried out in the Dept. of Metallurgy, Massachusetts Institute of Technology, under sponsorship of the AEC.

Discussion of this paper, if any, will appear in JOURNAL OF METALS, November 1956, and in AIME Metals Branch *Transactions*, Vol. **206**, 1956.

References

[1] C. Wagner: *Thermodynamics of Alloys*. (1952) Cambridge, Addison-Wesley Press. See, for example, Chap. 4.
[2] L. Seigle, B. L. Averbach, and M. Cohen: *Trans.* AIME (1952) **194**, p. 1329; JOURNAL OF METALS (December 1952).
[3] C. Zener: *Acta Crystallographica* (1949) **2**, p. 163.
[4] C. Zener: *Thermodynamics in Physical Metallurgy*. (1950) p. 16. Cleveland, ASM.

[5] G. Borelius: *Annalen der Physik* (1937) 28, p. 507.
[6] E. R. Jette, W. L. Bruner, and F. Foote: *Trans.* AIME (1934) 111, p. 354.
[7] E. Isaac and G. Tammann: *Ztsch. für Anorg. Allgem. Chemie* (1907) 53, p. 291.
[8] L. Nowack: *Ztsch. für Metallkunde* (1930) 22, p. 97.
[9] L. Pauling: *Journal* Amer. Chemical Soc. (1947) 69, p. 542.
[10] A. W. Lawson: *Journal of Chemical Physics* (1947) 15, p. 831.
[11] B. L. Averbach, P. A. Flinn, and M. Cohen: *Acta Metallurgica* (1954) 2, p. 92.
[12] W. Köster: *Ztsch. für Metallkunde* (1948) 39, p. 1.
[13] E. S. Machlin: *Trans.* AIME (1954) 200, p. 592; JOURNAL OF METALS (May 1954).
[14] F. Weibke and H. Matthes: *Ztsch. für Elektrochemie* (1941) 47, p. 421.
[15] R. A. Oriani: *Acta Metallurgica* (1953) 1, p. 144.
[16] J. Lumsden: *Thermodynamics of Alloys* (1952) pp. 225-234. London, Institute of Metals.
[17] O. J. Kleppa: *Journal* Amer. Chemical Soc. (1949) 71, p. 3275; (1950) 72, p. 3346; (1951) 73, p. 385.
[18] W. DeSorbo and R. A. Oriani: *Acta Metallurgica* (1955) 3, pp. 227, 232.
[19] C. Zener: *Trans.* AIME (1946) 167, p. 513; METALS TECHNOLOGY (January 1946).
[20] L. S. Darken and R. P. Smith: *Industrial and Engineering Chemistry* (1951) 43, p. 1815.

Technical Note

New Intermediate Phase in Burnt Tungsten Steels

by Kehsin Kuo

DIE steel with 1.47 pct C, 0.42 pct Mn, and 8.22 pct W contains Fe_3C and WC in the annealed state and WC embedded in a martensitic matrix in the hardened state (quenched from 800°C). The presence of a large amount of undissolved angular WC carbide particles makes this steel extremely wear-resistant.

However, the WC carbide begins to dissolve in the austenite when the heating temperature is raised above 1000°C, but this solution process is still not complete at 1250°C although partial melting has already taken place at the austenite grain boundaries. At 1325°C, this steel contains austenite and liquid metal but no WC carbide, Fig. 1. On quenching into brine, the liquid metal solidifies into a constituent which etches differently from the austenite-martensite matrix. This constituent appears lighter than the matrix at the 1250°C stage when etched with 2 pct nital but darker in Fig. 1 when etched with Murakami's reagent. Such a constituent has also been found in burnt tungsten high speed steels.

This constituent has been isolated from the matrix by anodic dissolution in a 5 pct HCl electrolyte and was found by the X-ray powder method to be isomorphous with β-manganese, Table I. The agreement in line intensity between these two phases indicates that there is no ordering in this new phase. The calculated cube edge of this phase is 6.395A, somewhat larger than that of β-manganese (6.30A).

Besides this phase, the anodic residue also contains free carbon from the matrix and amorphous WO_3, although the X-ray powder pattern of the residue shows the presence of only this phase. This makes it impossible to determine directly the composition of this phase from the residue. Attempts to prepare an alloy containing only this phase have hitherto been fruitless. The following experiments serve to show that this phase can only be obtained by drastic quenching from the liquid state and that its tungsten and carbon contents must be lower than those in the Fe_3W_3C carbide.

On air cooling from 1325°C, the liquid metal solidifies into a eutectic consisting of austenite and the Fe_3W_3C carbide. The nature of this dark-etching Fe_3W_3C has also been ascertained by X-rays. This eutectic becomes coarser on furnace cooling. The solidification of a specimen cooled for 5 min from 1325° to 1200°C and water quenched is still not complete and the fine eutectic is formed during the quenching. Since this new phase can be replaced by a eutectic of austenite and the Fe_3W_3C carbide, its composition must lie somewhere between the latter two phases. The special features of this phase are: 1—it can only form directly from the liquid state by drastic quenching and 2—it is a ternary phase of iron, tungsten, and carbon.

The β-manganese structure of this phase is also interesting. In the Periodic Table, iron and tungsten lie on opposite sides of manganese; a certain combination of these two elements, in the presence of carbon, may have average properties similar to those of manganese. It has already been established that the χ phase, a ternary one of iron, chromium, and molybdenum, has the α-manganese structure.[3,4] A similar phase has also been found in the ternary system Fe-Cr-W[5] and in the following binary systems: Re-Cb, Re-Ta, Re-Mo, and Re-W.[6]

Table I. X-Ray Diffraction Data for the New Phase*

HKL	$\sin^2\theta_{obs}$	$\sin^2\theta_{calc}$	I_{obs} †	$I_{\beta\text{-Mn}}$ †
111	0.0432	0.0436	VW	2.7
210	0.0724	0.0727	W	9.1
211	0.0877	0.0872	VW	1.6
300, 221	0.1307	0.1308	VS	272
310	0.1454	0.1453	S	163
311	0.1599	0.1598	MS	89.6
321	0.2036	0.2034	M	28.8
411, 330	0.2621	0.2615	M	30.5
420	0.2900	0.2906	M	28.6
332	0.3194	0.3197	W	5.1
510, 431	0.3783	0.3778	S	142.2
511, 333	0.3922	0.3923	W	25.3
520, 432	0.4217	0.4214	S	127.2

* CuKα radiation.
† Letters represent: VS, very strong; S, strong; MS, medium strong; M, medium; W, weak; and VW, very weak.

K. KUO, Junior Member AIME, is associated with Institute of Chemistry, Uppsala University, Uppsala, Sweden.
TN 288E. Manuscript, Apr. 25, 1955.

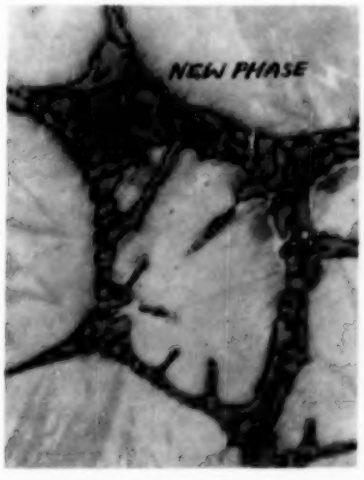

Fig. 1 — Die steel containing 1.47 pct C, 0.42 pct Mn, and 8.22 pct W was heated at 1325°C for 5 min and water quenched. Micrograph shows new phase into which the liquid metal solidified on quenching. Etched with Murakami's reagent. X1200. Area reduced approximately 10 pct for reproduction.

References

[1] G. D. Preston: *Philosophical Magazine* (1928) 5, 7th Series, p. 1207.
[2] K. W. Andrew: *Nature* (1949) 164, p. 1015.
[3] J. G. McMullin, S. F. Reiter, and D. G. Eberling: *Trans.* ASM (1954) 46, p. 799.
[4] J. S. Kasper: *Acta Metallurgica* (1954) 2, p. 456.
[5] H. J. Goldschmidt: *Trans.* ASM (1954) 46, p. 807.
[6] P. Greenfield and P. A. Beck: Private communication.

System Zirconium-Nitrogen

Iodide zirconium was combined with calculated amounts of nitrided zirconium sponge and arc melted to prepare alloys in the 0 to 6 wt pct N region. Annealing treatments were carried out at 21 temperature levels. Metallographic examination of the heat-treated specimens permitted construction of the binary phase diagram from 0 to 6 pct N. Features of the diagram include the peritectic formation of both α and β solid solutions. The maximum solubility of nitrogen is 0.8 pct in β zirconium and 4.8 pct in α zirconium. An X-ray study of nitrided materials was made in the range 6 to 13 wt pct N region because serious nitrogen losses were experienced when attempts were made to arc melt these high nitrogen alloys.

by R. F. Domagala, D. J. McPherson, and M. Hansen

PHASE relationships in the Zr-N system have been determined. Due to the inability to retain nitrogen in nitrogen-rich alloys subjected to arc melting, definitive work was possible only in the range 0 to 6 wt pct (0 to 30 atomic pct) N. Sufficient complementary X-ray work was done to permit construction of the binary phase diagram up to 13.3 wt pct (50 atomic pct) N (ZrN).

Small ingots were prepared by arc melting master alloys with enough zirconium to produce an alloy of the desired composition. Following pretreatment, alloys were annealed at temperature levels between 600° and 2020°C. Determination of the phase boundaries was then accomplished by metallographic evaluation of specimens quenched from the various temperatures. Incipient melting techniques were used to corroborate solidus curves, and X-ray diffraction was employed to study the nitrogen-rich region of the α + ZrN phase field.

Materials

Westinghouse Grade 1 iodide zirconium crystal bar served as the base material for this investigation. The as-received bars were lightly sandblasted, pickled in a 20 pct HNO_3-5 pct HF aqueous solution, rinsed in water and acetone, and dried. They were rolled to about 1/32 in. strip and acid-pickled, followed by water and then acetone rinses. The material was sheared to approximately ¼ in. squares, cleaned with acetone, and stored for use.

Pure zirconium nitride is not commercially available, according to correspondence with possible suppliers. A literature survey indicated that nitrogen may be introduced into zirconium metal by passing nitrogen or ammonia gas over zirconium at an elevated temperature.[1-3] After considerable experimentation, a train was devised whereby high quality nitrogen was passed through a series of bubblers to remove the last traces of oxygen, through an H_2SO_4 bubbler and a cold trap to remove moisture, and finally over zirconium within a resistance furnace.

Hand-picked Bureau of Mines magnesium-reduced zirconium sponge proved more amenable to nitriding than the crystal bar. The nitrogen used was *extra pure* gas purchased from Linde Air Products Co. The first two bubblers through which the gas was passed contained a solution suggested by L. F. Fieser[4] as being ideal for removing the last traces of oxygen from nitrogen. The solution contains 20 g KOH, 2 g sodium-anthraquinone β-sulphonate, and 15 g $NaHSO_3$ dissolved in 100 ml water. It is blood-red and turns brown when contaminated with oxygen.

A saturated lead acetate solution, next in the series of bubblers, removed any H_2S which might have formed in the O_2 removal stage. An H_2SO_4 bubbler and cold trap removed moisture before the nitrogen was passed over the zirconium. The zirconium was contained in a stainless steel screen within a Vycor or quartz tube in a resistance furnace. Unreacted nitrogen passed out of the system through a mercury bubbler.

A nitriding run was performed in the following manner: Zirconium was placed in the screen within the furnace tube. The unit was assembled, suitably clamped off, and evacuated to remove the air and moisture within the tube and that trapped by the zirconium sponge. The unit was flushed with nitrogen and evacuated twice. After nitrogen was allowed to pass over the zirconium for about 30 min, the furnace was turned on; several hours were required to reach temperature. The reaction was allowed to continue at temperature for about 4 hr and the screen was then withdrawn from the hot zone of the furnace by means of a Nichrome or Kanthal rod. The screen and its contents were allowed to cool at the end of the tube and were then removed.

At 800°C no more than about 5 pct N could be introduced into the sponge zirconium. This material was designated *M*-1 (master alloy No. 1) and reserved for the preparation of alloys in the dilute nitrogen region. A second set of experiments was conducted at 1000°C; no more than 7.2 pct N could be introduced into the zirconium at this temperature. Enough material (*M*-2) of this nitrogen content was prepared to produce a second set of alloys to complement the first and to provide alloys in the 0 to 6 wt pct N range.

It was hoped that a diffusion anneal plus a renitriding might yield a material of higher nitrogen content. The material containing about 7 pct N was therefore given a *homogenization* treatment at 1000°C for 6 hr under an argon atmosphere. It was

R. F. DOMAGALA, D. J. MCPHERSON, Junior Members AIME, are Associate Metallurgist and Assistant Manager, respectively, Metals Research Dept., Armour Research Foundation of Illinois Institute of Technology, Chicago, and M. HANSEN, Member AIME, formerly Manager, Metals Research Dept., Armour Research Foundation, is Vice President, Metallgesellschaft A. G., Frankfurt/Main, West Germany.

Discussion of this paper, TP 3993E, may be sent, 2 copies, to AIME by Apr. 1, 1956. Manuscript, Oct. 18, 1954. Philadelphia Meeting, October 1955.

This paper is based on a portion of a thesis by R. F. Domagala submitted, in partial fulfillment of the requirements for the degree of Master of Science, to Metallurgy Dept., Illinois Institute of Technology.

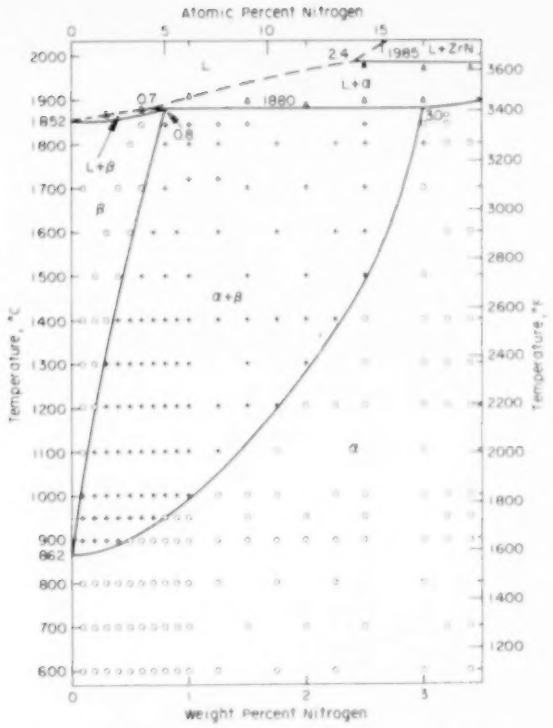

Fig. 1—In this expanded diagram of the zirconium-rich region of the Zr-N system, the circle represents one phase; plus, two phases; the open triangle, melting, α and/or β; closed triangle represents melting in which ZrN appears.

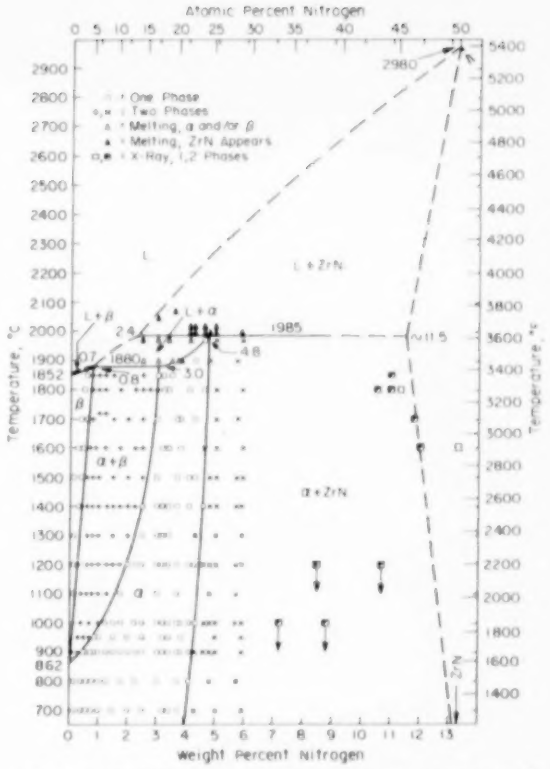

Fig. 2—Partial diagram of the Zr-N system shows phase relationships up to ZrN.

then exposed to nitrogen for an additional 4 hr treatment at the same temperature. Analyses conducted on samples of these materials showed no nitrogen increase. This experiment was repeated a second time and the same results were experienced.

It appeared necessary to investigate the results of nitriding at higher temperatures. In order to accomplish this a new unit was constructed, utilizing a small globar heated tube furnace and a quartz tube. Following the same technique employed at lower temperatures, a small quantity of *M*-2 (7 pct N) was exposed to nitrogen at 1200°C for 4, 8, and 12 hr. After 4 hr there was an initial nitrogen increase to about 9 pct; after 8 hr the nitrogen content was 10.4 pct and seemed to level off at about this value. An X-ray powder pattern was made using material containing 10.6 pct N. The nitrided sponge was then arc melted and a small quantity of the melted button was submitted for X-ray diffraction study and chemical analysis. Analytical data showed the nitrogen content to drop from 10.6 to 5.6 pct and the X-ray patterns showed that, while the as-nitrided material contained only a very few faint lines of α solid solution, the arc melted material clearly contained many α lines. Some loss of nitrogen on arc melting was experienced whenever the nominal nitrogen content of an alloy exceeded about 4 pct. It was not possible to retain more than about 6 pct N in any of the arc melted alloys.

A third batch of sponge zirconium was nitrided for 4 hr at 1000°C and 8 hr at 1200°C prior to runs at higher temperatures. This material was analyzed and found to contain about 8.5 pct N. It was designated *M*-3 and divided into five equal parts, each weighing about 50 g. Each small lot was exposed to nitrogen for 4 hr at temperatures from 1200° to 1400°C, the limit of the apparatus. Analytical data from samples of each lot indicate that it is not readily possible to produce an appreciable quantity of stoichiometric ZrN (13.3 pct N) even at relatively high temperatures. The highest average nitrogen content reached was about 11 pct. Accordingly, it was decided to cease nitriding experiments at this point and attempt to equilibrate the nitrided sponge and to subject such material to X-ray studies to supplement the metallographic work.

Equipment and Procedures

A nonconsumable electrode arc melting furnace was used to prepare alloys. Details of operation, including drawings of this type furnace, may be found in the literature.[7]

Twenty gram alloy ingots containing 0 to 3 wt pct N were prepared by combining calculated amounts of iodide zirconium and *M*-1 master alloy, which after consolidation by arc melting was found to contain 5 pct N. Alloys in the nominal composition range 3.25 to 7.0 wt pct N were prepared by utilizing the *M*-2 master alloy containing 7.2 pct N. No attempt was made to consolidate this second master alloy by arc melting. Although such a pretreatment would have been desirable, it was deemed inadvisable due to the nitrogen losses experienced previously. During arc melting operations, current levels were kept below 300 amp to minimize losses.

Before the regular isothermal annealing treatments were carried out, all alloys were homogenized for 48 hr at 1200°C and certain alloys were cold worked to hasten the approach to equilibrium during the anneals. Samples were sealed in either Vycor

or quartz bulbs for isothermal annealing treatments up to 1400°C, where resistance-type porcelain tube furnaces were employed. Vycor bulbs were employed for temperatures up to 1100°C and quartz was used from 1100° to 1400°C. The bulbs were evacuated before sealing for treatments up to 950°C. For anneals above this temperature, a reduced pressure of

Table I. Analyses of Zr-N Alloys

Alloy No.*	Analyzed Nitrogen, Pct	Alloy No.*	Analyzed Nitrogen, Pct
ZN 0.1		ZN 2.75	
ZN 0.2	0.21	ZN 3.0	3.08
ZN 0.3		ZN 3.25	3.2
ZN 0.4	0.33	ZN 3.5	3.7
ZN 0.5		ZN 3.75	3.4
ZN 0.6	0.62	ZN 4.0	3.6
ZN 0.7		ZN 4.25	3.8
ZN 0.8	0.86	ZN 4.5	4.2
ZN 0.9		ZN 4.75	4.2
ZN 1.0	0.91	ZN 5.0	4.3
ZN 1.25		ZN 5.25	4.6
ZN 1.5	1.63	ZN 5.5	4.8
ZN 1.75		ZN 5.75	4.8
ZN 2.0	2.05	ZN 6.0	5.6
ZN 2.25		ZN 6.5	5.7
ZN 2.5	2.63	ZN 7.0	5.9

* The alloy number is divided in two parts: ZN refers to a Zr-N alloy and the digits following denote the nominal nitrogen content.

argon was admitted to the bulb before sealing. Temperature control in general was ±3°C. Specimens were quenched at the conclusion of an anneal by rapidly withdrawing the bulb from the furnace and breaking it under water.

Inasmuch as nitrogen additions to zirconium raise its melting point as well as its transformation temperature, important phase boundaries had to be delineated at temperatures well above the maximum operating temperature of the furnaces normally employed for annealing treatments. A complete description, including a drawing, of the furnace constructed for very high temperature use may be found in an earlier paper on the Zr-O binary phase diagram.[7] Briefly, a split cylindrical resistor of molybdenum sheet serves as a heater. Extremely high temperatures are obtained when a low voltage high current source is applied. Temperatures are measured optically, and temperature corrections are applied according to a calibration curve based on the observed melting points of high purity metals. Although very rapid heating rates are possible in this furnace, specimens were brought to temperature in about 15 min and held there from 2 to 6 min before quenching onto a water-cooled brass bottom plate. Pressure less than 0.1μ (1×10^{-4} mm Hg) was maintained during annealing runs. Temperature control during treatments was held within ±10°C.

The vacuum induction furnace used to aid in outlining the solidus curves for this system has been described in detail.[7] Specimens supported on wolfram wire are rapidly heated until visible melting occurs; then samples of the same alloy content are quenched from successively lower temperatures. By metallographic evaluation of the resulting structures, the solidus curve is determined.

A Debye-Scherrer powder camera was used for all X-ray work on this system. A copper target was used and a nickel filter permitted only $CuK\alpha$ radiation to reach the specimen. The powder specimen, passed through a 200 mesh screen, was placed in a Pyrex capillary at the center of a 14 cm diam camera.

Nitrogen analyses for this study were obtained by a modified Kjeldahl method which provided reproducible results for the Zr-N alloys.

Results and Discussion

Thirty-two alloys were arc melted for a study of the phase relationships in this system in the 0 to 6 wt pct N region. All alloys were prepared, utilizing nitrided sponge zirconium as the alloy addition and iodide zirconium as the diluent. A complete tabulation of these alloys together with analytical data is given in Table I. Alloys up to about 3.25 pct N were found to contain the intended nitrogen content within ±0.1 pct. Beyond 4.0 pct N, serious nitrogen losses were experienced, apparently due to the arc melting. Regardless of the nitrogen content of the master alloy, it was not possible to prepare alloys containing more than 6 pct N by arc melting. Many unsuccessful attempts were made to produce such ingots. The diagrams were constructed on a basis of analyzed compositions of alloys.

All as-cast alloys were given a homogenization anneal at 1200°C for 48 hr. Ingots in the very dilute alloy region were amenable to a slight amount of cold work by rolling; alloys containing more than 0.3 pct N could not be cold worked.

Subsequent to homogenization and cold rolling, specimens were sawed or broken up to provide specimens suitable for isothermal annealing treatment.

In addition to the data collected through the metallographic study of the arc melted alloys, additional information was acquired by an X-ray study of selected portions of nitrided sponge. Such data were carefully evaluated and used in completing the partial diagram up to ZrN. A discussion of this study is given later.

A complete list of the number of alloy compositions treated at each temperature level is given in Table II. Except at temperatures above 1800°C, a control sample of unalloyed zirconium was included

Table II. Annealing Schedule of Zr-N Alloys

Temperature, °C	Time, Hr	No. of Compositions Treated
2020	~0.1	5
2000	~0.1	6
1975	0.1	6
1900	0.1	7
1850	0.1	4
1840	0.1	5
1800	0.1	14
1720	0.1	2
1700	0.1	13
1600	0.1	14
1500	0.1	16
1408	1	27
1300	3	20
1205	5	28
1100	30	17
998	70	27
952	75	19
896	100	27
801	150	18
700	305	19
598	500	19

with each annealing treatment. The anneals at all temperatures above 1400°C were carried out in the high temperature vacuum resistance furnace, while treatments at or below this temperature were made in the regular annealing furnaces.

Alloys containing nominally 0.5, 1.0, 3.0, and 7.0 pct N were treated for three times at 800°, 1000°, and 1200°C. The ingots previously had been given a homogenization anneal at 1200°C for 48 hr. A metallographic study of these alloys showed no change in the relative amounts of phases after 150, 50, and 5 hr at 800°, 1000°, and 1200°C, respectively.

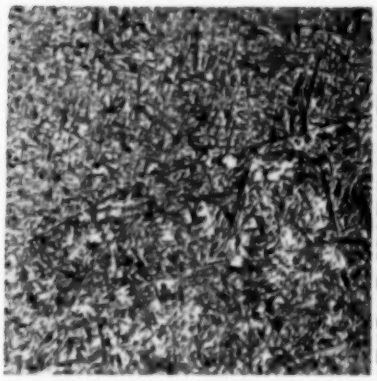

Fig. 3—Transformed β phase appears in micrograph of 0.6 pct N alloy, as-cast. Sample was etched. X150. Area reduced approximately 25 pct for reproduction.

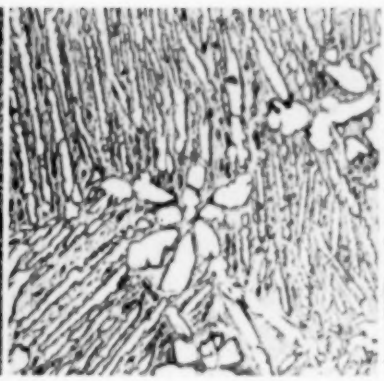

Fig. 4—In 0.8 pct N alloy, as-cast, primary α dendrites appear in a matrix of transformed β. Sample was etched. X250. Area reduced approximately 25 pct for reproduction.

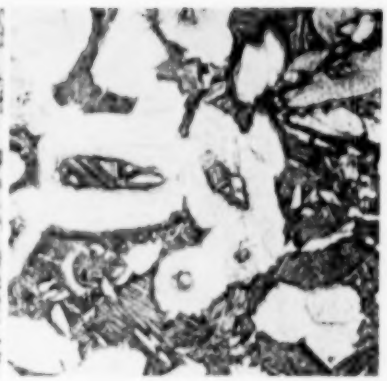

Fig. 5—In 2.5 pct N alloy, as-cast, primary particles of ZrN appear within α grains in a transformed β matrix. Specimen was etched. X250. Area reduced approximately 25 pct for reproduction.

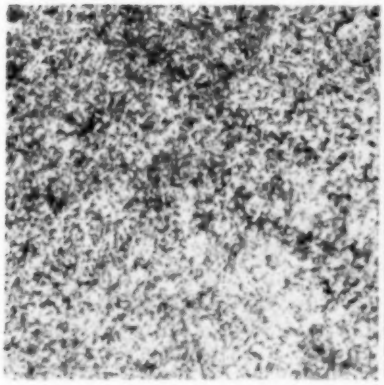

Fig. 6—Transformed β solid solution appears in micrograph of 0.2 pct N alloy quenched from 1205°C. Sample was etched. X250. Area reduced approximately 25 pct for reproduction.

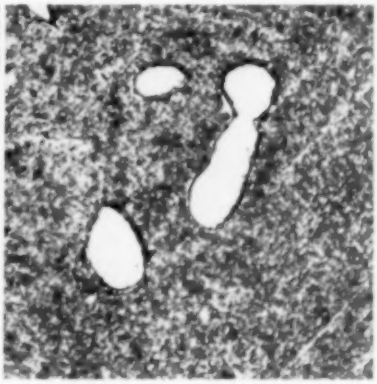

Fig. 7—Isothermal α plus transformed β appear in 0.3 pct N alloy quenched from 1205°C. Sample was etched. X250. Area reduced approximately 25 pct for reproduction.

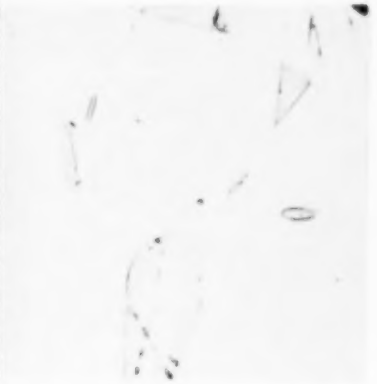

Fig. 8—Micrograph shows α plus last traces of transformed β in 1.75 pct N alloy quenched from 1205°C. Sample was etched. X500. Area reduced approximately 25 pct for reproduction.

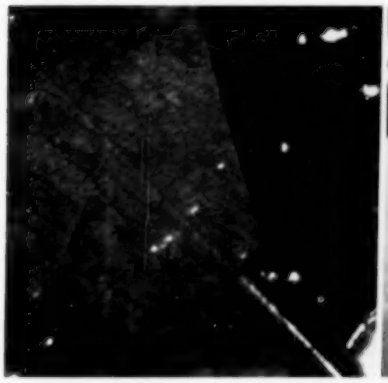

Fig. 9—All-α structure appears in 2.0 pct N alloy quenched from 1205°C. Sample, taken in polarized light, is unetched. X500. Area reduced approximately 25 pct for reproduction.

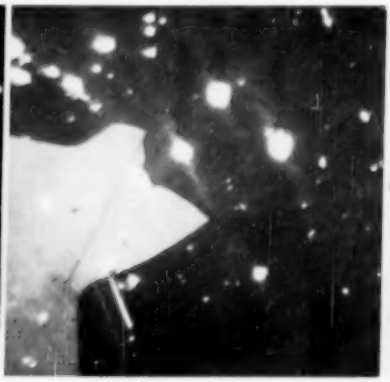

Fig. 10—All-α structure appears in 4.3 pct N alloy quenched from 1205°C. Unetched sample was taken in polarized light. X500. Area reduced approximately 25 pct for reproduction.

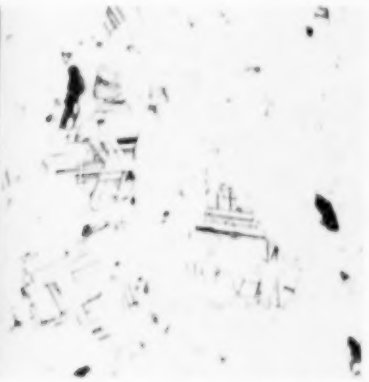

Fig. 11—Micrograph shows α plus ZrN structure appearing in 4.6 pct N alloy quenched from 1205°C. Sample was etched. X500. Area reduced approximately 25 pct for reproduction.

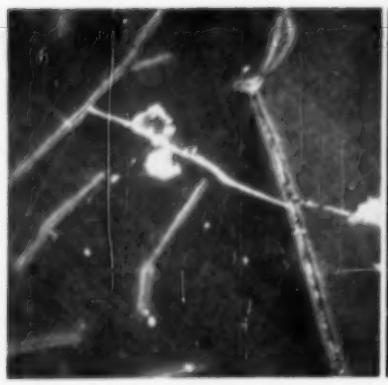

Fig. 12—Micrograph shows α plus last traces of transformed β in 3.0 pct N alloy quenched from 1800°C. Unetched sample was taken in polarized light. X500. Area reduced approximately 25 pct for reproduction.

Fig. 13—Micrograph shows all-α structure in 3.2 pct N alloy quenched from 1800°C. Unetched sample was photographed in polarized light. X500. Area reduced approximately 25 pct for reproduction.

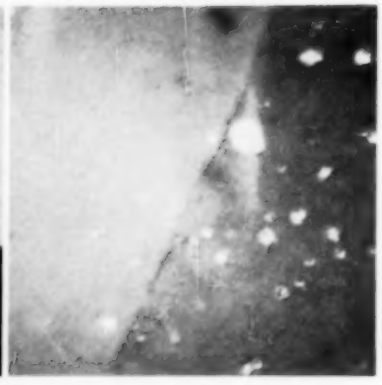

Fig. 14—Micrograph of 4.6 pct N alloy quenched from 1800°C shows all-α structure. Unetched sample was photographed in polarized light. X500. Area reduced approximately 25 pct for reproduction.

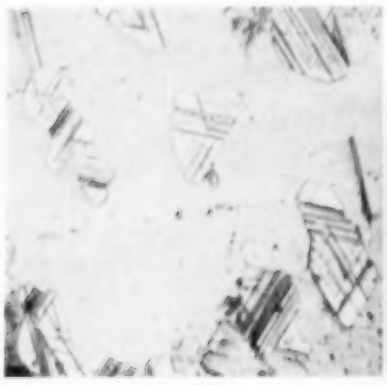

Fig. 15—Micrograph of 5.0 pct N alloy quenched from 1800°C shows α plus particles of isothermal ZrN. Sample was etched. X500. Area reduced approximately 25 pct for reproduction.

Fig. 16—Micrograph of 3.0 pct N alloy quenched from 1840°C shows α. Unetched sample was photographed in polarized light. X250. Area reduced approximately 25 pct for reproduction.

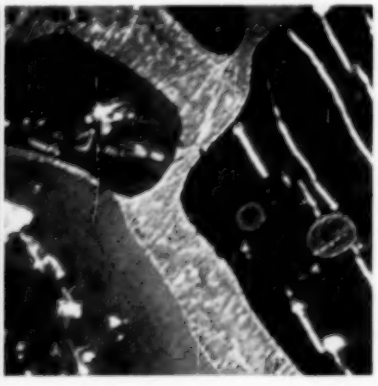

Fig. 17—Micrograph of 3.0 pct N alloy quenched from 1900°C shows α plus signs of melt. Compare with Fig. 16. Unetched sample was photographed in polarized light. X500. Area reduced approximately 25 pct for reproduction.

The results of this work were extrapolated to predict proper annealing times at all levels employed for the study of this system.

Partial diagrams of the Zr-N binary system are presented in Figs. 1 and 2. The former figure is an expanded diagram of the zirconium-rich region, while the latter presents the phase relationships up to ZrN. These two diagrams are documented with most of the data points necessary for the construction of the diagram.

Important features of the diagram include:

1—β solid solution forms on cooling by the peritectic reaction: liquid (0.7 wt pct, 4.4 atomic pct N) + α (3.0 wt pct, 16.8 atomic pct) → β (0.8 wt pct, 5.0 atomic pct N), at 1880±10°C.

2—Nitrogen additions stabilize α zirconium, raising the transformation temperature and resulting in the peritectic reaction: liquid (2.4 wt pct, 13.5 atomic pct N) + ZrN solid solution (~11.5 wt pct, ~46 atomic pct N) → α (4.8 wt pct, 25 atomic pct N), at 1985±15°C.

3—The maximum solubility of nitrogen in β zirconium is 0.8 wt pct (5.0 atomic pct) at the peritectic reaction and decreases to 0 at the transformation temperature, 862°C.

4—The α modification of zirconium can dissolve 4.8 wt pct (25 atomic pct) N at the temperature of the peritectic formation of α, and the solubility decreases with decrease in temperature to about 4 wt pct (21 atomic pct) N at 600°C.

5—The intermediate phase ZrN has a reported maximum melting point at approximately 2980°C and has a range of homogeneity on the zirconium side of the stoichiometric composition (13.3 wt pct, 50 atomic pct N). It was not possible to determine this boundary accurately but it is believed to extend from about 11.5 wt pct (~46 atomic pct) N at 1985°C down to nearly stoichiometric ZrN at temperatures below 600°C. No attempt was made to determine the possible extent of the field on the nitrogen side of ZrN.

6—There are no additional singular phases between zirconium and ZrN.

The melting point of zirconium, 1852°C, used in the construction of the diagram was experimentally determined in previous phase diagram work[9] and was corroborated in this study. The temperature of the allotropic transformation, $\alpha \leftrightarrows \beta$, was positioned at 862±5°C. This corresponds to the value given by Vogel and Tonn[10] and was checked in the present

Fig. 18—Melting in an all-α structure appears in micrograph of 4.1 pct N alloy quenched from 1975°C. Unetched sample was photographed in polarized light. X500. Area reduced approximately 25 pct for reproduction.

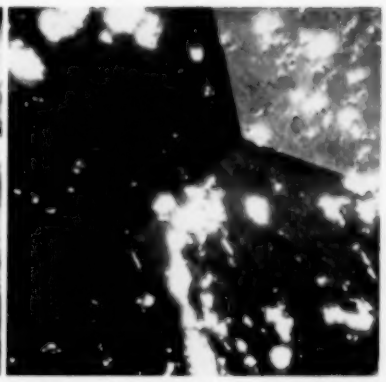

Fig. 19—All-α structure with no signs of melting appears in micrograph of 4.6 pct N alloy quenched from 1975°C. Unetched sample was photographed in polarized light. X500. Area reduced approximately 25 pct for reproduction.

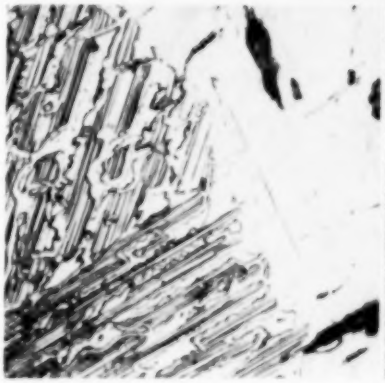

Fig. 20—ZrN crystals appear in the melted region of 4.1 pct N alloy quenched from 2000°C. Compare with Fig. 18. Sample was etched. X250. Area reduced approximately 25 pct for reproduction.

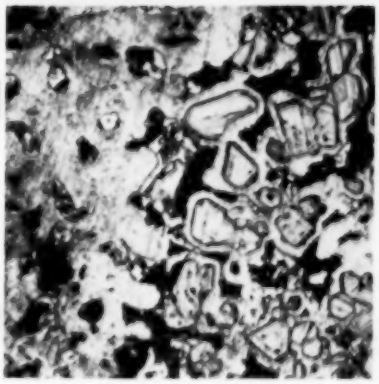

Fig. 21—Micrograph shows 2.5 pct N alloy quenched from 1975°C in the incipient melting furnace. Figs. 19 to 21 position the peritectic formation of α at 1985±15°C. Sample was etched. X250. Area reduced approximately 25 pct for reproduction.

work by a metallographic investigation of structures in unalloyed arc melted zirconium annealed at five temperature levels between 845° and 885°C. As in past work, a transformation *range* was indicated in the vicinity of the value given previously.

The compositions noted and the positions of the phase boundaries in the diagrams are considered to be accurate within ±0.2 pct in the 0 to 6 pct N region, while the α + ZrN/ZrN boundary is believed to be within ±0.5 pct N of the equilibrium value. Evidence substantiating the placement of various phase boundaries and temperature horizontals is presented in the micrographs.*

* The composition values given in the discussion of structures refer to weight percent. The etchant employed was 20 pct HF and 20 pct HNO_3 in glycerine.

A series of as-cast structures, which clarifies the solidification history of Zr-N alloys, is shown in the first few micrographs. An 0.6 pct N alloy is shown in Fig. 3 and a single phase, transformed β structure, is seen. At 0.8 pct N, Fig. 4, primary crystals of α form on solidification and are contained in a transformed β matrix. These two structures position the composition of the liquid involved in the peritectic formation of β at about 0.7 pct N. With increasing nitrogen contents, more primary α crystals appear. Primary crystals of ZrN make their initial appearance at 2.5 pct N as shown in Fig. 5. The primary ZrN particles are surrounded by α in a matrix of transformed β. Fig. 5 confirms the peritectic formation of α; the composition of the liquid entering into the reaction was positioned at 2.4 pct N. Increasing amounts of ZrN primary crystals were observed in as-cast alloys containing more nitrogen.

Micrographs of specimens quenched from 1205°C are presented in the next set of figures. Here an alloy containing 0.2 pct N (Fig. 6) is seen to consist of transformed β, while at 0.3 pct N (Fig. 7) an α plus transformed β structure is observed. Samples containing 1.75 and 2.0 pct N are shown in Figs. 8 and 9. The 1.75 pct composition is mostly α with residual particles of β, while at 2.0 pct N the structure is 100 pct α. The α/α + ZrN boundary is positioned at 1205°C by the micrographs of Figs. 10 and 11, 4.3 and 4.6 pct N alloys, respectively. The former is all α, while the latter is two phase, α + ZrN. The markings which appear in the ZrN in Fig. 11, as well as in other structures, have been identified as anisothermal α, rejected from the compound during the quench. These markings have been observed to blend without interface into the α matrix.

Table III. Results of Combined X-Ray and Analytical Study

Composition, Pct N	Quenching Temperature, °C	Phase Lines Present	Parameter ZrN,* kX
10.5	1800	ZrN + weak α	4.567
11.0	1850	ZrN + very faint α	4.569
11.0	1800	ZrN + very faint α	4.567
11.3	1800	ZrN	4.567
11.7	1700	ZrN + faint α	4.567
12.0	1600	ZrN + faint α	4.567
13.5	1600	ZrN	4.567

* The parameter of ZrN was calculated on a basis of the (331), (420), (422), (511), and (440) lines, plotted vs $\sin^2\theta$ and extrapolated to $\sin^2\theta = 1$. ZrN has a cubic NaCl-type structure.

An alloy containing 0.5 pct N quenched from 1800°C consisted of a coarsened transformed β structure, while at 0.8 pct N an α plus transformed β structure was present. With increasing nitrogen content, the amount of α increases until at 3.0 pct N (Fig. 12) only residual β particles remain. At 3.2

pct N (Fig. 13), a 100 pct α structure is seen. Alloys containing 4.6 and 5.0 pct N, also quenched from 1800°C, are shown in Figs. 14 and 15. The former figure shows an all-α structure, while the latter manifests ZrN particles in an α matrix. Markings in ZrN appear as before.

It was found that the presence of holes and cracks in the very brittle α structures was unavoidable. Particular care during the metallographic preparation of samples provided some improvement in the final appearance, but since the α alloys containing more than 2 pct N are inherently brittle, they are very susceptible to cracking.

The next series of structures positions important diagram features in the vicinity of the two peritectic reactions. A 3.0 pct N alloy quenched from 1840°C is shown in Fig. 16. The all-α structure positions the maximum extent of the $\alpha + \beta/\alpha$ boundary at about 3.0 pct N. The same alloy quenched from 1900°C is shown in Fig. 17. The appearance of melting in this structure places the temperature of the peritectic formation of β at some temperature below 1900°C. Since the melting point of zirconium is 1852°C and is raised by nitrogen additions, the peritectic formation of β must occur between 1852° and 1900°C; with the aid of other metallographic and incipient melting data, this level was positioned at 1880 ± 10°C.

The next two micrographs present structures observed in alloys quenched from 1975°C. At 4.1 pct N, signs of melt appear in an α structure as shown in Fig. 18. At 4.6 pct N only α, with no signs of melt, may be seen, as indicated by Fig. 19. The maximum solubility of nitrogen in α zirconium was therefore placed at 4.8 pct N, since the next alloy in the series, 5.0 pct N, had an α + ZrN structure with no signs of melting.

The position of the peritectic formation of α at 1985 ± 15°C is confirmed by the structures of Figs. 20 and 21. The former figure is a 4.1 pct N alloy quenched from 2000°C, and particles of ZrN are seen to appear in the melted region. These ZrN particles did not appear in this alloy when quenched from 1975°C, as was shown in Fig. 18. The last figure is that of a 2.5 pct N alloy quenched from 1975°C in the incipient melting furnace. As in Fig. 20, ZrN particles have formed in the melted regions. Although this represents the only case of ZrN appearing in α or $\alpha + \beta$ alloys quenched from 1975°C, it helps position rather accurately the temperature level at which the reaction, $L + ZrN \rightarrow \alpha$, occurs.

Inasmuch as nitrogen losses were experienced during the arc melting of some compositions, it was considered possible that annealing treatments, especially at elevated temperatures, might result in composition changes in the alloys treated. Accordingly, four alloy compositions (0.2, 2.0, 3.25, and 5.0 pct N) were slowly heated to 1600°, 1850°, and 2000°C in the incipient melting furnace. After holding for about 1 min at these high temperatures, the specimens were quenched and submitted for chemical analysis. The results showed that no nitrogen losses had occurred.

A cursory incipient melting study confirmed the solidus curves determined from a metallographic study of specimens heat treated at elevated temperatures. The results of the incipient melting work are plotted on the diagrams.

Since it was not possible to retain more than about 6 pct N in alloys prepared by arc melting, other experimental techniques were necessarily applied to determine the position of the α + ZrN/ZrN phase boundary, and to make at least a cursory examination of the α + ZrN field. A combined X-ray analytical study with complementary metallographic work was used. Materials subjected to this study consisted of as-nitrided and nitrided and homogenized sponge zirconium. Data points determined by these methods are indicated by squares on the diagrams; arrows attached to data points indicate as-nitrided specimens, while the absence of an arrow means that the specimen was heat treated at the temperature indicated prior to examination.

Slight surface contamination of all metallographic specimens annealed between about 900° and 1400°C was visible. It was therefore deemed advisable not to perform any *bulb anneals* of nitrided sponge due to the small particle size involved. Even a slight layer of contamination on small specimens could easily lead to spurious X-ray data. Consequently, data for this study were collected on specimens taken directly from the nitriding unit or on samples given a heat treatment in the high temperature vacuum resistance furnace where neither contamination nor nitrogen losses were experienced.

In connection with the initial nitriding experiments, conducted at temperatures not exceeding 1200°C, various materials were submitted for X-ray diffraction and analysis. Without exception, these materials yielded α + ZrN patterns and are indicated in Fig. 2 by a half-filled square with an arrow attached. The arrow is intended to mean that, although the cooling rate was not known, the two phase structure is characteristic of that composition at some lower temperature.

Subsequently, a comprehensive study of nitrided materials prepared at 1200° to 1400°C was made. Small quantities of nitrided sponge from each of these batches were annealed at temperatures between 1600° and 1850°C for from 0.1 to 0.2 hr in the high temperature resistance furnace. After quenching, particles of about 20 mesh material were ground to 200 mesh and submitted for X-ray diffraction and chemical analysis. Exposure times in the powder camera were held constant and all films were developed simultaneously. Analyses were conducted on the powders from which the X-ray sample was taken. The results of this study are presented in Table III. It may be seen that in only two instances were α solid solution lines absent from the X-ray films. In one case, an analysis showed the material to be of the stoichiometric ZrN composition within analytical error. However, the absence of α lines in the case of the sample containing 11.3 pct N may not necessarily mean that no α existed in the specimen, since lines may not be detected when the quantity of a phase is small. A metallographic study of these nitrided and annealed particles has shown that complete homogeneity was not attained, even after annealing at 1850°C. At the center of the specimens ZrN and α were present, while the exterior generally consisted of single phase ZrN. It is interesting that whenever ZrN existed in the form of a layer on the nitrided particles it was entirely free of the markings observed in ZrN in the interior of the metallographic specimen. The markings were identified as anisothermal α in the metallographic work. This positive evidence of a decreasing solubility of zirconium in ZrN with decreasing temperature was applied in the construction of the α + ZrN/ZrN boundary. Because of the extreme difficulty of preparing samples approaching

the stoichiometric composition, it was not possible to *bracket* the boundary, but the position indicated on the drawings is believed to be accurate to about ±0.5 wt pct N.

The fact that the parameter values for ZrN were always the same, regardless of the thermal history of the specimen, means either that the change in parameter within the ZrN field is small and could not be measured or, alternatively, that all α was rejected by an unsuppressible precipitation, resulting in stoichiometric ZrN in every case. It seems more likely, considering the metallographic evidence, that α was rejected.

Table IV. Parameter Data for ZrN

Parameter Value, kX	Reference
4.63	14, 15
4.59	16
4.56	2
4.61	14
4.567	17 and present investigation

Some material, after nitriding and homogenization, was subjected to a second nitriding and homogenization cycle. Analyses indicated that practically no increase in nitrogen content was realized as a result of this treatment. The X-ray and metallographic study of such specimens provided no new information. These data are included in Table III.

Summarizing the results of this phase of the study, the following facts were established:

1—It is very difficult to produce an appreciable quantity of ZrN even by exposures to nitrogen at temperatures as high as 1400°C.

2—The decreasing solubility of zirconium in ZrN with decreasing temperature was confirmed and a semiquantitative placement of the α + ZrN/ZrN boundary was possible.

3—Complete equilibration of nitrided sponge is difficult even when such treatment is conducted at temperatures as high as 1850°C.

4—No nitrogen losses were experienced in this phase of study, and it may be inferred that the loss of nitrogen on arc melting is a direct result of the dissociation of ZrN at temperatures above 1850°C, and very likely at temperatures above its melting point, 2980°C.

Comparisons with the Literature

A survey of unclassified literature on ZrN alloys has disclosed limited data for comparison with the present investigation. Several authors[11, 12] have reported that the $\alpha \leftrightarrows \beta$ transformation temperature is raised by the addition of nitrogen to zirconium. One group of investigators[11] presented data on the solubility of nitrogen in β zirconium from the transformation temperature up to 1600°C. The data herein presented coincide with their line within 0.1 pct N. DeBoer and Fast[12] reported the solubility of nitrogen in α zirconium to be about 20 atomic pct, which is in good agreement with the value determined in this work.

The melting point of ZrN, not determined in this investigation, has been variously reported as 2930°C[13] and 2980±50°C;[14] the latter value represents the most recent work and was used in constructing the binary phase diagram. Various lattice parameters have been reported for ZrN. All investigators agree that the phase is yellow in color and has an NaCl-type structure. The various parameter data are summarized in Table IV.

No direct data were found in the literature suggesting the peritectic formation of either α or β, nor was there any mention of a homogeneity range for the phase ZrN.

Summary

Metallographic analysis of as-cast and annealed specimens of arc melted alloys, plus a combined X-ray and analytical study of nitrided sponge, yielded the partial Zr-N binary phase diagram.

Features of the diagram include:

1—A peritectic reaction between liquid (0.7 wt pct, 4.4 atomic pct N) and α (3.0 wt pct, 16.8 atomic pct N) occurs at 1880°C. The product of the reaction is β solid solution (0.8 wt pct, 5.0 atomic pct N).

2—α solid solution is stabilized to increasing temperatures by nitrogen additions. At 1985°C, α solid solution (4.8 wt pct, 25 atomic pct N) enters into a peritectic reaction with liquid (2.4 wt pct, 13.5 atomic pct N) and ZrN solid solution (~11.5 wt pct, 46 atomic pct N).

3—At the temperature of the peritectic formation of β, 0.8 wt pct (5.0 atomic pct) N is soluble in the β phase. This solubility decreases to 0 at the transformation temperature.

4—α zirconium has a maximum solubility for nitrogen of 4.8 wt pct (25 atomic pct) N at 1985°C, which decreases to about 4 wt pct (21 atomic pct) N at 600°C.

5—The intermediate phase ZrN has a reported maximum melting point of 2980°C. There is a range of homogeneity for this phase extending from about 11.5 wt pct (46 atomic pct) N at 1985°C to nearly stoichiometric ZrN (13.3 wt pct, 50 atomic pct N), at temperatures below 600°C.

Acknowledgments

The authors wish to thank the AEC, sponsors of this work under supplement No. 3 of Contract No. AT(11-1)-149 *Phase Diagrams of Zirconium-Base Alloys* for permission to publish this paper. Special thanks are due to J. R. Dvorak, who was responsible for the metallographic work, W. Rostoker, who supervised the X-ray work, W. A. Dupraw and H. M. Manasevit for chemical analyses, and to J. W. Lenke for his untiring efforts to produce ZrN.

Discussion of this paper, if any, will appear in JOURNAL OF METALS, November 1956, and in AIME Metals Branch *Transactions*, Vol. **206**, 1956.

References

[1] C. Agte and K. Moers: *Ztsch. für Anorg. Allgem. Chemie* (1931) **198**, p. 231.
[2] E. Friedrich and L. Sittig: *Ztsch. für Anorg. Allgem. Chemie* (1925) **143**, p. 293.
[3] E. Wedekind: *Annalen der Chemie* (1913) **395**, p. 149.
[4] J. F. Mudd and J. Milwee: *Report No. TIP-U-11983* Inst. of Industrial Research, University of Louisville (July, August 1956).
[5] R. Kieffer and F. Benesovsky: *Metallgesellschaft* (1952) **6**, p. 174.
[6] L. F. Fieser: *Experiments in Organic Chemistry* (1941) p. 395. Boston, D. C. Heath Co.
[7] M. Hansen, H. D. Kessler, and D. J. McPherson: *Trans.* ASM (1952) **44**, p. 518.
[8] R. F. Domagala and D. J. McPherson: *Trans.* AIME (1954) **200**, p. 238; JOURNAL OF METALS (February 1954).
[9] D. J. McPherson and M. Hansen: *Trans.* ASM (1953) **45**, p. 915.
[10] R. Vogel and W. Tonn: *Ztsch. für Anorg. Allgem. Chemie* (1931) **202**, p. 293.
[11] M. W. Mallett, E. M. Baroody, H. R. Nelson, and C. A. Papp: *Journal* Electrochemical Soc. (1953) **100**, No. 3, p. 103.
[12] J. H. DeBoer and J. D. Fast: *Recueil des travaux chimiques* (1936) **55**, p. 459.
[13] C. A. Phalinker and W. M. Baldwin, Jr.: *Proceedings* Amer. Soc. for Testing Materials (1951) **51**, p. 1038.
[14] G. B. Hall: *AECD No. 2971* (Nov. 11, 1947).
[15] K. Becker and F. Ebert: *Ztsch. für Physik* (1925) **31**, p. 268.
[16] A. E. Van Arkel: *Physica* (1924) **4**, p. 286.
[17] P. Duwez and F. Odell: *Journal* Electrochemical Soc. (1950) **97**, p. 299.

Creep-Rupture by Vacancy Condensation

The possibility that formation of voids under creep-rupture conditions may take place by the condensation of vacancies has been investigated theoretically. It has been concluded that nucleation of voids under creep-rupture conditions by vacancy condensation is highly improbable. However, growth of pre-existant voids by vacancy condensation is probable. A number of predictions made in this theory have been verified by the data. It has been predicted and checked that the product of rupture life and steady-state creep rate for *preannealed* metals and single phase alloys is an approximately invariant quantity, independent of stress, temperature, and atomic number for a given type structure. The direction of the effect of cold work on this product has been predicted and found in agreement with experiment. A number of experiments to evaluate the vacancy condensation mechanism further are described.

by E. S. Machlin

SEVERAL papers have appeared recently which speculate on the origin of voids formed at grain boundaries under stress.[1, 2] The object of this paper is to examine quantitatively the proposition that the voids produced in a creep test are a result of vacancy condensation. A result of this paper is a theory of creep-rupture.

Void Nucleation

Application of standard nucleation theory[3] to the problem of void nucleation leads to the following conclusions:

1—Homogeneous nucleation of voids requires a supersaturation ratio (concentration of vacancies in supersaturated to that in saturated solution) of 400 for a reasonable surface energy of 1000 erg per cm^2 and 1.4 for the improbably low surface energy of 10 erg per cm^2.

2—Heterogeneous nucleation of voids at plane interfaces between two phases requires a supersaturation ratio of 2.5 for a typical contact angle of 145°.[4]

3—Void nucleation about a solid particle may be accomplished at a supersaturation ratio of 1.17 for a typical value of work of adhesion† of 60 erg per cm^2 [5] between an oxide and a metal in the presence of a surface active element such as sulphur.

† The work of adhesion is the surface work to replace two solid-vapor surfaces by a solid-solid interface.

Estimates of the supersaturation ratio at which voids are produced in diffusion experiments yield a maximum of 1.01.[2] Inasmuch as the foregoing mechanisms of void nucleation probably will not operate at this level—too low a surface energy is required—the investigator is led to the conclusion that voids must already exist. That is, nucleation of voids probably does not occur. Rather, existing submicroscopic voids grow out to visible size. Already existing voids might be produced during solidification or working. Supercritical sized particles which contain cracks may act as heterogeneous void nuclei. Gas pockets may act as void nuclei. Experiments are desired to determine the nature of the heterogeneous void nuclei which grow out to voids in both diffusion and creep experiments.

E. S. MACHLIN, Member AIME, is Associate Professor of Metallurgy, Columbia University, New York City.

Discussion of this paper, TP 4062E, may be sent, 2 copies, to AIME by Apr. 1, 1956. Manuscript, Oct. 26, 1954. Philadelphia Meeting, October 1955.

Void Growth

Void growth might occur in at least two possible ways, depending upon whether the already existing void nuclei are at grain boundaries or within the grains. In the case of a spherical void far from a crystal boundary, vacancies are generated during creep as a consequence of the migration of suitable dislocation jogs[1] and are also annihilated at sinks. Under these conditions, a steady-state concentration of vacancies is built up in the crystal, defined by the condition that for any differential volume the rate of generation of vacancies in that volume equals the rate of annihilation of those vacancies.[6]

This equality would lead to the development of a gradient of vacancy concentration radially outward from the void surface up to a radius where the vacancy lifetime becomes equal for all directions of vacancy migration. The distance over which this vacancy concentration gradient extends equals about $2\sqrt{D_v T^v}$[6] where D_v is the vacancy diffusivity and T^v the vacancy lifetime in a crystal outside the gradient in a zone of constant vacancy concentration.

The vacancies generated in the region over which the gradient exists will annihilate more often at the void than elsewhere. Approximately a little over one-half the vacancies generated in the gradient zone will annihilate at the void. Hence, the growth rate of the void is given by

$$\frac{dV}{dt} = 4\pi R^2 \frac{dR}{dt} = \frac{1}{2}\,\Omega\, R_v\, 4\pi R^2\, 2\sqrt{D_v T^v} \qquad [1]$$

or

$$G = \frac{dR}{dt} = \Omega\, R_v \sqrt{D_v T^v} \qquad [2]$$

where R is the radius of void in centimeters, Ω is the atomic volume, and R_v is the rate of generation of vacancies, number per centimeter^3 per second.

R_v, D_v and T^v may be estimated in terms of other physical parameters.[6] In particular,

$$R_v = n_v \dot{e}/b^2 \qquad [3]$$

where n_v is the average number of vacancy produc-

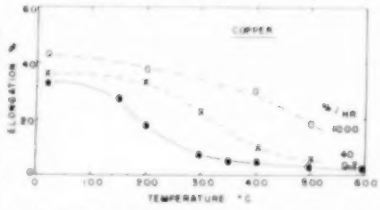

Fig. 1—Elongation vs temperature. Note: transcrystalline rupture (lower temperature region) characterized by higher elongation values than intercrystalline rupture (higher temperature region). Inflection points are close to boundary between transcrystalline, intercrystalline rupture. Greenwood et al.[1]

ing jogs per centimeter length of dislocation, $\dot{e}$ is the creep rate, inches per inch per second, and b is the Burgers' vector in centimeters.

The value of n_j, the average number of vacancy producing jogs per centimeter length of dislocation contributing to the creep strain, can be estimated on the basis of a number of models. The result is

$$n_j = f N_s L \qquad [4]$$

where L is the average half-distance moved by a dislocation from source to barrier either during creep or during the previous working history of the specimen, N_s is the number of dislocations per unit area, and f is the fraction of jogs which generate vacancies. The product $D_v T^*$ has been shown by Seitz[5] to be given by

$$D_v T^* = m b^2 \qquad [5]$$

where m is the average number of atomic jumps a vacancy will take between source and sink, and b is the Burgers' vector (as given previously).

Estimates of m, assuming the absence of interstitialcies, depend upon whether a dislocation is an effective trap or only dislocation jogs are effective traps for vacancies. The former is believed to be applicable in the temperature range in which a Cottrell atmosphere of vacancies can be formed,[6] the latter only at higher temperatures.[6] The two cases are then described by

$$m = \frac{1}{\alpha N_s b^2} \quad (\textit{low} \text{ temperature region}) \qquad [6]$$

or

$$m = \frac{1}{\alpha' N_s n_j b^2} \quad (\textit{high} \text{ temperature region}) \qquad [7]$$

where α and α' are the *sticking* coefficients: fraction of number of collisions between vacancy and dislocation (dislocation jog) that do not result in reevaporation of vacancy and

$$1 - \alpha = \exp\,(-V/kT) \qquad [8]$$

where V is the interaction energy between vacancy and dislocation.

Table I. Effect of Cold Work on Elongation for Transcrystalline Rupture of Monel*

State	Elongation, Pct
Cold Worked	10 to 20
Annealed	40 to 55

* Data are from Grant and Bucklin.[7]

If the application of the equations is carried through to the relatively low temperature region, interesting results are predicted. Eq. 8 indicates that α will be appreciable for most values of T (assuming $V \geq 0.1$ E.V.).

Substituting Eqs. 6, 5, 4, and 3 in Eq. 2 yields

$$G = K b \sqrt{N_s \dot{e}} \qquad [9]$$

where

$$K = fL/\sqrt{\alpha} \qquad [10]$$

will be treated as a disposable parameter. Eq. 9 is basic to a calculation of elongation at rupture and to the development of a relation between creep rate and rupture life, as will be shown.

Elongation at Rupture—Transcrystalline Rupture

For the sake of simplicity, it will be assumed that transcrystalline rupture occurs when the area resisting rupture approaches zero. Hence, for a *constant stress* test the following relation is obtained as defining the rupture condition

$$N_v \frac{4}{3} \pi \left(\int_0^{t^*} G\, dt\right)^3 = 1 \qquad [11]$$

where N_v is the number of void nuclei per centimeter[3] and t^* is the rupture life.

Table II. Effect of Mode of Rupture on Elongation of Annealed Monel*

Mode of Rupture	Elongation, Pct	Creep Rate, Pct per Hr
Transcrystalline	43.5	<20,000
Transcrystalline	54.8	< 1,400
Transcrystalline	56.5	63
Intercrystalline	44.8	14
Intercrystalline	35.5	1.4
Intercrystalline	29.7	0.21
Intercrystalline	31.7	0.094
Intercrystalline	32.2	0.0075

* Data are from Grant and Bucklin.[7]

Substituting Eq. 9 and changing the integration variable from time to strain

$$N_v \frac{4}{3} \pi \left(\int_0^{e^*} K b \sqrt{N_s}\, de\right)^3 = 1 \qquad [12]$$

is obtained. In this equation e^* is the value of the uniform elongation at rupture. Assuming N_s is constant during the creep test, integration of Eq. 12 and solving for e^* yields

$$e^* = \left[K b \sqrt{N_s} \left(\frac{4}{3} \pi N_v\right)^{1/3} \right]^{-1}. \qquad [13]$$

The prediction contained in Eq. 13 is that an increase in the density of dislocations and the number of void nuclei per unit volume should decrease the uniform elongation at rupture in the region of transcrystalline rupture. Cold working a recrystallized specimen should increase the dislocation density.[8] Thus, cold working should decrease the uniform elongation at rupture. This prediction is verified by the data of Grant and Bucklin[7] summarized in Table I, which compares the total elongation at rupture of cold worked and annealed specimens. It would be desirable, of course, to have further verification of this relation, which was derived to apply to the case of transcrystalline rupture at low temperature.

Elongation at Rupture—Intercrystalline Rupture

The previous discussion applied to the case of transcrystalline rupture. It is desirable to consider intercrystalline rupture as well. It is possible that the density of void nuclei along the grain boundaries is higher than along any imaginary plane surface in the matrix because of the tendency of the boundary to cling to particles and adsorb impurities. Also,

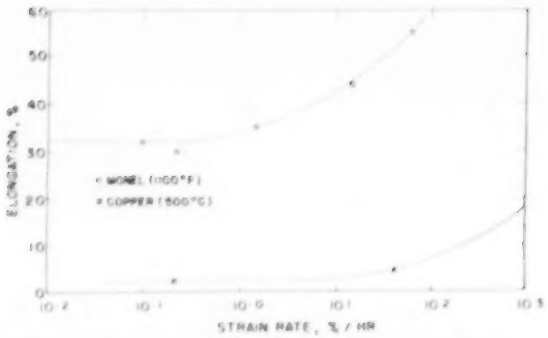

Fig. 2—Data, from refs. 1 and 7, are plotted to show limiting elongation at low stresses in intercrystalline rupture.

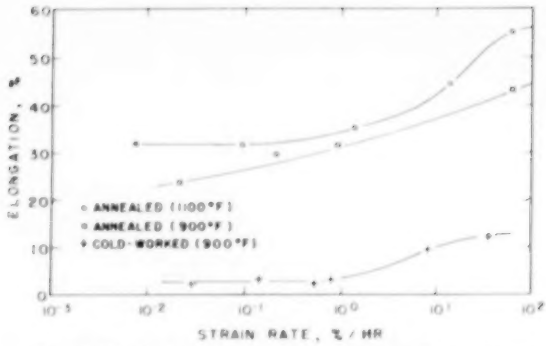

Fig. 3—Effect of cold work on limiting elongation in intercrystalline rupture is plotted from data taken from ref. 7.

it is possible that the creep rate in the vicinity of the boundary may be higher than in the matrix because of the tendency to set up stress concentrations with boundary sliding. For these reasons, the boundaries may be expected to become preferential sites for void formation. The very process of localized void formation at the boundaries will lead to an enhanced creep rate in these regions and to preferential intercrystalline failure. Thus, for intercrystalline rupture the *measured total elongation* does not correspond to the local elongation at the boundaries. It might be expected that there be about the same critical elongation at the boundaries with intercrystalline rupture as occurs throughout the matrix at the moment of transcrystalline rupture. Because the volume in which this same critical strain exists is less in intercrystalline than transcrystalline rupture, the total elongation values for intercrystalline rupture should be less than those obtained during transcrystalline rupture. The data of Grant and Bucklin[7] shown in Table II check this interpretation as do the data of Greenwood,[7] Fig. 1.

Table III. Values of the $\dot{\epsilon}^{*}\epsilon$ Product for Thoroughly Annealed Metals and Alloys

Metal or Alloy	$\dot{\epsilon}^{*}\epsilon$	Reference
Al (99.99+ pct)	0.316	10
Al (99.3 pct)	0.360	10
Cu (99.98 pct)	0.32	11
Cu (OFHC)	0.12	12
Sn	0.20	13
Pb	0.12	14
Ti	0.35	15
Mg	0.05	1
Be	0.08	16
Monel	0.1 to 0.32	7
18-8 stainless steels	0.02 to 0.20†	17

† The value in this range was constant for a given type of steel, i.e., type 316 L had a value of about 0.2, whereas type 347 had a value of about 0.025.

A number of other predictions based on this model are possible. For example, it would be expected, other things being equal, that an increase in grain size should decrease the measured elongation (less regions of high elongation contribute to the total value). Also, the lower the creep rate or stress, the less the contribution of the matrix elongation to the total elongation, until some stress or creep rate is reached below which the total elongation will be due only to that at the boundaries. It should then remain approximately constant in this range providing that the grain size, dislocation density, and void nuclei density remain constant. The effect is illustrated by the results of Grant and Bucklin and Greenwood et al. that are reproduced in Fig. 2. This behavior of grain boundary elongation relative to total elongation has recently been demonstrated extremely well by the experiments of McLean.[5] In this range, where the elongation is almost wholly due to creep at the boundaries, the total elongation is given by

$$e_t = \left(\frac{h}{D}\right) e^{*+} \qquad [14]$$

where e_t is the total elongation due to creep in the vicinity of the grain boundaries, D is the grain diameter, e^{*+} is the value of e^{*} with the values appropriate to the neighborhood of a grain boundary, and h is the thickness of boundary region over which creep occurs. Hence,

$$e_t = \frac{h}{D}\left[K\, b \sqrt{N_v^{+}}\left(\frac{4}{3}\pi N_v^{+}\right)^{1/3}\right]^{-1} \qquad [15]$$

where the plus symbol denotes the value of the quantity in the vicinity of the grain boundaries.

Consequently, cold work prior to the rupture test should increase N_v^{+} and decrease the measured e_t. As shown in Fig. 3, the data of Bucklin and Grant are consistent with this prediction. That is, the limiting elongation—the elongation corresponding to grain boundary creep alone—is decreased by an increase in the dislocation density. It should be apparent that comparison of the foregoing relations, Eqs. 13 and 15, between elongation and dislocation density with experiment is based on the assumption that the total elongation is due to either the uniform elongation alone, Eq. 13, or to the grain boundary elongation alone, Eq. 15. If the actual experimental setup involves other sources of elongation, Eqs. 13 and 15 do not apply. Applications of Eqs. 13 and 15 are limited to single phase alloys, or structurally stable two phase alloys, where the measurements refer to uniform elongation and total elongation, respectively.

Some additional data in the literature relate to the effect of oxidation on elongation at rupture. The data of Bleakney[6] on the effect of oxygen partial pressure on the total elongation of copper are reproduced in Fig. 4. These data, together with similar data on silver which show a nil effect of oxygen pressure on the total elongation, may be interpreted in terms of Eq. 15—that the value of N_v^{+}, the number of void nuclei, is markedly increased in copper, but

Table IV. Comparison of $t^*\dot{e}$ Values for Cold Worked and Annealed Metals and Alloys

Metal	$t^*\dot{e}$ Cold Worked	Cold Worked and Recrystallized During Test	Pre-annealed
Monel	0.0075 to 0.037	0.25 to 0.30	0.1 to 0.32
Beryllium	0.007	0.08	—

not in silver, during exposure to an oxygen atmosphere. Inasmuch as copper forms oxides at these pressures and temperatures and silver does not, it is further implied that the additional void nuclei are associated with oxide particles. However, other interpretations are possible and further experimentation to pinpoint the real effect of oxidation on elongation and rupture life is highly desirable.

Rupture Life

The remaining observable that this theory should describe is the rupture life. Inasmuch as a critical elongation supposedly exists for a given specimen and testing condition, it will be necessary to know the creep rate as a function of time in order to describe the rupture life. For simplicity, the concept of a steady-state creep rate in preference to more exact relations will be used. In this case

$$\ln \dot{e} = \ln A + B \ln \sigma \qquad [16]$$

where $\dot{e}$ is the creep rate, A and B are the constants, and σ is the stress. Inasmuch as the stress now changes because of a decrease in cross-sectional area, in a constant stress test‡

‡ The corresponding term in a constant load test is $\sigma_o e^{-(1 - e/e^*)^2}$.

$$\sigma = \sigma_o/[1 - (e/e^*)^2] \qquad [17]$$

where σ_o is the original stress (load per area), e is the strain, and e^* is $\left[K\, b \sqrt{N_s} \left(\frac{4}{3}\pi N_v\right)^{1/3}\right]^{-1}$ or with plus superscripts if rupture is intercrystalline (see Eqs. 13 and 15). Substituting Eq. 17 in Eq. 16 and solving for the strain rate yields

$$\dot{e} = \dot{e}_o/[1 - (e/e^*)^2]^B \qquad [18]$$

where $\dot{e}_o$ is the minimum or steady-state creep rate and $B = (d \ln \dot{e})/(d \ln \sigma)$, (the slope of log creep rate-log stress plot). Integrating Eq. 18, the following is obtained

$$\int_o^{e^*} [1 - (e/e^*)^2]^B \, de = \dot{e}_o \int_o^{t^*} dt \qquad [19]$$

where t^* is the rupture life corresponding to the critical elongation e^*. The integral can be solved to yield

$$t^*\dot{e}_o = e^*\, g\,(B) \qquad [20]$$

where

$$g\,(B) = 1 - \frac{B}{4} + \frac{B\,(B-1)}{14} - \ldots \frac{(-1)^{n-1} B\,(B-1)\ldots(B-(n-2))}{(n-1)!\,[3\,(n-1)+1]} \qquad [21]$$

and e^* is given by Eqs. 13 or 15 as the case may be.

A search of the literature reveals that typical values of B lie between the limits 5 to 15. For this

Fig. 4—Data of Bleakney[7] on effect of partial pressure of oxygen on ductility in creep-rupture of copper are reproduced. Open circles represent 5×10^{-1} mm Hg; filled circles, 3×10^{-2} mm Hg; and plus signs, 760 mm Hg.

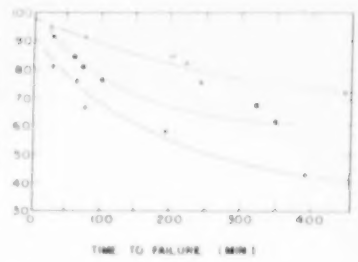

variation Eq. 21 yields a maximum variation in $g(B)$ of from 0.5025 to 0.362, respectively. Hence, $g(B)$ can be considered *constant* to within about 30 pct. Using the average value of 0.4 for $g(B)$

$$t^*\dot{e}_o = 0.4 \left[K\, b \sqrt{N_s} \left(\frac{4}{3}\pi N_v\right)^{1/3}\right]^{-1}. \qquad [22]$$

This relation implies that for a given previous history the dimensionless product of rupture life and minimum creep rate should be a constant, within a factor of 30 pct, independent of the stress and temperature. This relation should apply, however, only to the cases where the measured creep rate and the creep rate producing vacancies for the voids are the same. Figs. 5 and 6, which are compilations of data from refs. 10 and 7, provide checks of Eq. 22 and, as shown, the agreement is excellent. This result provides strong support for the theory.

Another check of Eq. 22 can be made on the basis that for annealed metals and single phase alloys of the same structure, N_s would not be expected to vary by more than a factor of 10, nor $t^*\dot{e}_o$ by more than a factor of about three. If the impurity content is not varied by more than a factor of ten, $t^*\dot{e}_o$ should not vary by more than about 2.2. Hence, the maximum variation in $t^*\dot{e}_o$ expected from annealed metals or single phase alloys of the same structure and having an impurity variation of less than tenfold is itself less than ten. A compilation of $t^*\dot{e}_o$ values from the literature[7, 9, 10, 11] is given in Table

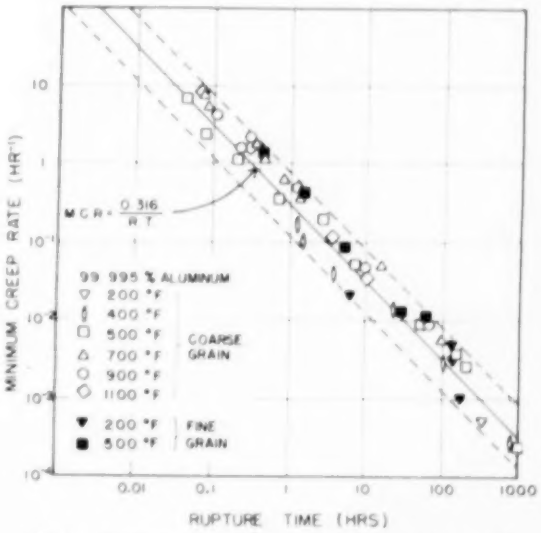

Fig. 5—Invariance of the $t^*\dot{e}$ product for preannealed metals is demonstrated from data after Servi and Grant.[10]

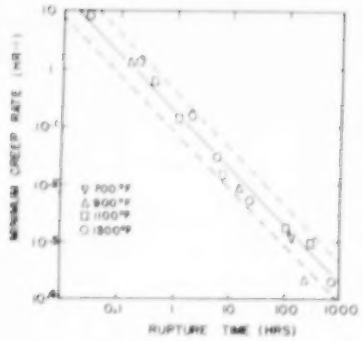

Fig. 6—Data taken from ref. 7 demonstrate the invariance of the $t^*\dot{e}$ product for preannealed single phase alloys.

III and, as shown, the variation found is within a factor of about five for alloys having the same structure.

Still another check of Eq. 22 is the effect of cold work (a variation in N_z) upon the $t^*\dot{e}_s$ product. This effect is demonstrated experimentally by the data in Table IV taken from refs. 7 and 16 and is qualitatively in agreement with theory, i.e., as indicated by Eq. 22, an increase in N_z should decrease the $t^*\dot{e}_s$ product.

Discussion of Results

There is no doubt that the model of rupture based on void growth through vacancy condensation is consistent with experiment. It has been possible to predict the trend of the effect of cold work on the critical local elongation for rupture and from a knowledge of the steady-state creep rate on the rupture life as well. An inverse relation for annealed metals and single phase alloys has been predicted between steady-state creep rate and rupture life independent of stress and temperature which has been found to exist experimentally. On the basis of this agreement between theory and experiment, it may be concluded that the theory is probably valid. However, it is by no means proven. To obtain a greater degree of confidence in the validity of the theory, it would be desirable to compare predictions of the theory with the results of critical experiments. In particular, there are two quantitative predictions of the theory which should be checked. The dimensionless product of the steady-state creep rate and rupture life should vary inversely as the one-third power of the number of void nuclei per centimeter^3 and inversely as the square root of the dislocation density at rupture. Creep specimens can be prepared with known densities of voids either by powder metallurgical techniques or by diffusion techniques involving pore formation (dezincification or the like). Known dislocation densities can be introduced by twisting. A check of the dislocation density in silver can be obtained by measuring thermally etched dislocation pits according to the technique of Hendrickson and Machlin.[18]

Other critical experiments checking the basic assumptions of the theory can be performed as follows:

Vacancy Condensation into Voids—1—Stop a test in the transcrystalline range of rupture before failure. It should be possible to observe voids within the grains just as Greenwood et al.[1] have observed them at grain boundaries. These voids should tend to be spherical if they are brought about by vacancy condensation.

2—In creep tests with single crystals, it should be possible to develop voids at creep rates equal to those at which voids are developed within the grains of a polycrystal. Also, as the creep rate in a single crystal is decreased, it should be possible to find a limiting creep rate below which voids are not formed. This creep rate would correspond to the one yielding a vacancy supersaturation that itself corresponds to a critical void nucleus size just larger than the size of those available.

3—It should be possible to form visible voids by vacancy condensation in specimens undergoing compression creep.

Rate of Vacancy Generation—1—The decrease in density of specimens tested in tension should be larger for specimens pretwisted around the tension axis than for an *originally* annealed metal.

2—A particular type of dependence of dislocation density during creep has been assumed. It should be verifiable by direct measurement using the thermal etch technique[18] to reveal dislocations.

Existence of Voids Larger than Critical Size—If voids exist as a consequence of solidification, cold working, and the like, it should be possible to remove these voids in a pure metal by a long time high temperature anneal (about 100 hr near the melting point) under zero stress. It should then be possible to conduct a creep test in situ at the same temperature at a high enough rate to grow out voids but not high enough to nucleate voids heterogeneously. With another specimen similarly annealed, it should then be possible to quench to a lower temperature such that the supersaturation ratio of vacancies is enough to nucleate voids of the desired critical size homogeneously. A simultaneous creep test at the same creep rate should then produce visible voids. Along with this experiment, both density and resistance should be measured at the liquid nitrogen temperature of specimens which have been annealed as described and quenched to a lower temperature, held there for a sequence of times, and quenched to liquid nitrogen. If the density does not change with time at the lower temperature, but resistance does, the interpretation is that voids have been formed and vacancy concentration has decreased by condensation into voids rather than into dislocation sinks. On the other hand, if neither the density nor resistance change with time at the lower temperature, it must be concluded that the vacancy lifetime is much less than the experimental times involved. The results of the latter experiment will aid the interpretation of the former experimental results.

Void Nuclei at Boundaries—Tests such as Bleakney[7] has conducted should be repeated except that rupture life, steady-state creep rate, and elongation should be simultaneously determined in oxygen and in vacuum on specimens comprising controlled variation of surface active elements. All these data are required to be able to interpret the results in terms of the theory. A prediction may be made on the basis of the theory that the creep-rupture behavior of silver should be independent of the oxygen composition of the surrounding atmosphere because, at elevated temperatures, silver oxide vaporizes and does not form void nuclei. On the other hand, the presence of a surface active element in silver, such as zinc, which does tend to form an oxide, should markedly change the creep-rupture response of silver to the oxygen content of the surrounding atmosphere.

The foregoing are only a few of the experiments that should be conducted to aid in the evaluation

of the rupture theory developed in this paper.

Acknowledgment

The author gratefully acknowledges the support of the Office of Scientific Research, Air Research and Development Command, under Contract No. AF-18-600-899.

Discussion of this paper, if any, will appear in JOURNAL OF METALS, November 1956, and in AIME Metals Branch *Transactions*, Vol. **206**, 1956.

References

[1] J. N. Greenwood, D. R. Miller, and J. W. Suiter: Intergranular Cavitation in Stressed Metals. *Acta Metallurgica* (1954) **2**, p. 250.

[2] R. Balluffi and L. Seigle: Effect of Grain Boundaries upon Pore Formation and Dimensional Changes during Diffusion. *Acta Metallurgica* (1955) **3**, p. 170.

[3] J. H. Hollomon and D. Turnbull: Nucleation. *Progress in Metal Physics*. (1953) **4**. New York. Interscience Publishers Inc.

[4] C. F. Baes, Jr. and H. H. Kellogg: Effect of Dissolved Sulfur on the Surface Tension of Liquid Copper. *Trans.* AIME (1953) **197**, p. 643; JOURNAL OF METALS (May 1953).

[5] A. H. Cottrell: *Dislocations and Plastic Flow in Crystals*. (1953). Oxford. Clarendon Press.

[6] F. Seitz: On the Porosity Observed in the Kirkendall Effect. *Acta Metallurgica* (1953) **1**, p. 355.

[7] N. J. Grant and A. G. Bucklin: Creep-Rupture and Recrystallization of Monel from 700 to 1700°F. *Trans.* ASM (1953) **45**, p. 151.

[8] D. McLean: *Journal* Institute of Metals (1953) **81**, p. 293.

[9] H. H. Bleakney: *Canadian Journal of Technology* (1952) **30**, p. 340.

[10] I. S. Servi and N. J. Grant: *Trans.* AIME (1951) **191**, p. 909; JOURNAL OF METALS (October 1951).

[11] D. L. Martin and E. R. Parker: *Trans.* AIME (1944) **156**, p. 126; METALS TECHNOLOGY (December 1943).

[12] E. R. Parker and C. F. Ritsness: *Trans.* AIME (1944) **156**, p. 117; METALS TECHNOLOGY (February 1944).

[13] D. Hanson and E. J. Sandford: *Journal* Institute of Metals (1938) **62**, No. 1, p. 215.

[14] J. N. Greenwood and H. K. Worner: *Journal* Institute of Metals (1939) **64**, p. 135.

[15] F. B. Cuff, Jr. and N. J. Grant: *Iron Age* (1952) **70**, p. 134.

[16] A. R. Kaufman, P. Gordon, and D. W. Lillie: *Trans.* ASM (1950) **42**, p. 785.

[17] E. J. Dulis, G. V. Smith, and E. G. Houston: *Trans.* ASM (1953) **45**, p. 42.

[18] A. A. Hendrickson and E. S. Machlin: *Acta Metallurgica* (1955) **3**, p. 64.

Tensile Deformation of Germanium Single Crystals

by R. P. Carreker, Jr.

Six germanium single crystals were tested in tension in the temperature range 550° to 670°C. Plastic extension of 35 pct was obtained at 670°C. The flow stress of germanium is particularly sensitive to rate of straining.

GERMANIUM is a member of that group of elements—carbon, silicon, germanium, and tin—that are currently of particular interest because of their interesting electrical properties. Near room temperature these materials of diamond cubic crystal structure are characteristically brittle. However, there have been several recent reports that germanium is not brittle at elevated temperatures.[1-3] These observations may be summarized as follows:

1—Germanium single crystals were observed to creep in bending under a maximum fiber stress of 6 kg per mm² (8500 psi) at 500°C and above.[1] The creep curves were sigmoidal, with an induction period that decreased with increasing temperature.

2—Germanium crystal bars have been bent 90° about radii ten times the bar thickness at 550°C.[1]

R. P. CARREKER, JR., Junior Member AIME, is Research Associate, Research Laboratory, General Electric Co., Schenectady.

Discussion of this paper, TP 4014E, may be sent, 2 copies, to AIME by Apr. 1, 1956. Manuscript, Dec. 1, 1954. Philadelphia Meeting, October 1955.

3—Audible clicks were heard when ¼ in. thick crystals were bent drastically at 450° to 500°C. No microstructural evidence of mechanical twinning was observed.[1]

4—Slip lines have been observed in tensile specimens deformed at 600°C, and are coincident with (111) planes, the close-packed planes of the diamond cubic structure.[1,2] The slip direction has not been established.

5—A germanium crystal has been compressed approximately 20 pct along a <110> axis at 700°C.[3]

The results reported subsequently were obtained in exploratory experiments intended to indicate some aspects of the behavior of germanium single crystals when tested in simple tension.

Specimen Preparation

A single crystal bar of *n*-type germanium was used. It was of purity corresponding to a resistance range of 2 to 20 ohm-cm. Tensile specimens were prepared by cutting small rectangular bars

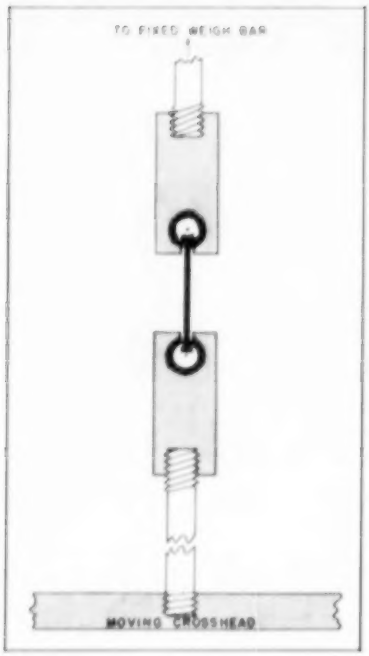

Fig. 1 — Illustration shows gripping arrangement for tensile testing germanium single crystals.

with a diamond impregnated wheel and then grinding to produce a nominal 1.1 gage length, with a 0.030x0.060 in. cross section having 0.060x0.060 in. shoulders at each end. The specimens were oriented so that the tension axis corresponded to a <111> crystallographic direction and the specimen faces were (110) planes. All specimens were cut with the same orientation from the same large crystal.

Testing Procedures

The gripping technique, shown in Fig. 1, permitted the specimen to be positioned so that it hung from its upper shoulders until the crosshead was moved. After positioning the specimen at room temperature, a tubular furnace was raised to surround the specimen. No protective atmosphere was used. Temperatures were measured with a Pt—Pt-Rh thermocouple fastened to the lower grip near the specimen.

An Instron tensile testing machine was used, utilizing its 20 lb and 50 lb scales. This machine imposes a controlled constant rate of crosshead motion and autographically records load vs time. In the present experiments, time is taken to be equivalent to elongation, since the problem of attaching an extensometer to germanium is particularly difficult.

Results

Tensile test results are presented in Figs. 2 and 3. The stress values are reported as nominal stress, i.e., axial load divided by the original cross sectional area, and strain values are reported as elongation divided by original gauge length.

Figs. 2 and 3 show the effect of temperature on a series of specimens tested at a strain rate of 0.005 min^{-1}. Note the transition from relatively brittle behavior showing 1 to 2 pct elongation at 550° to 600°C, to very plastic behavior showing 35 pct elongation at 670°C. A pronounced *yield point* was observed at 550° and 600°C, but was not evident at 625°C and above. A second presumably identical specimen, tested at 600°C, behaved entirely differently, showing no *yield point*, a higher flow curve, and much less ductility. The flow stress at 625°C is intermediate to that at 650° and 670°C.

Rate of straining is particularly important. At 650°C and a strain rate of 0.005 min^{-1}, plastic yielding occurred at a stress of 2000 psi and continued to about 7 pct elongation (crystal No. 5). In another test at the same temperature, not shown, but with a strain rate of 0.05 min^{-1}, the specimen broke at a stress of 4500 psi with no apparent plastic deformation.

In test No. 5 at 650°C the specimen was strained 4 pct at a rate of 0.005 min^{-1} and then the head motion was stopped; the stress relaxed 18 pct in 1.2 min. The load was reduced to 3200 psi and the deformation continued at 0.005 min^{-1} to 7.2 pct elongation. The relaxation period produced no apparent effect on the subsequent flow curve. At 7.5 pct elongation the rate was abruptly increased from 0.005 min^{-1} to 0.05 min^{-1}. The tenfold increase in strain rate produced an immediate 8 pct increase in flow stress. Plastic deformation continued for an additional 1 pct elongation at this relatively fast rate which had previously produced brittle fracture of an undeformed specimen at the same temperature.

All fractures of these tensile specimens were of the cleavage type along a plane approximately perpendicular to the tension axis. There was no apparent necking before fracture, even in specimen No. 6, which elongated 35 pct before fracture.

This particular specimen revealed an interesting substructure when mechanically polished and etched with 2 pct nital. In the micrograph of Fig. 4, the tension axis, originally [111], is vertical; the promi-

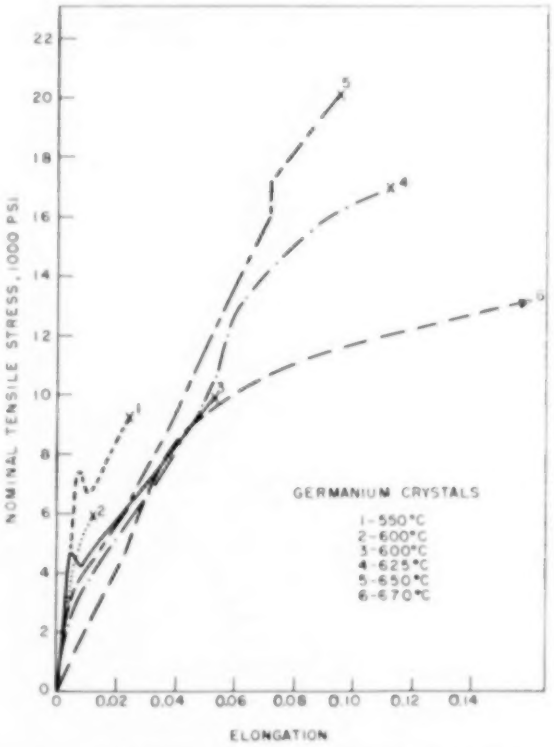

Fig. 2—Load-elongation curves for germanium single crystals at several temperatures are plotted.

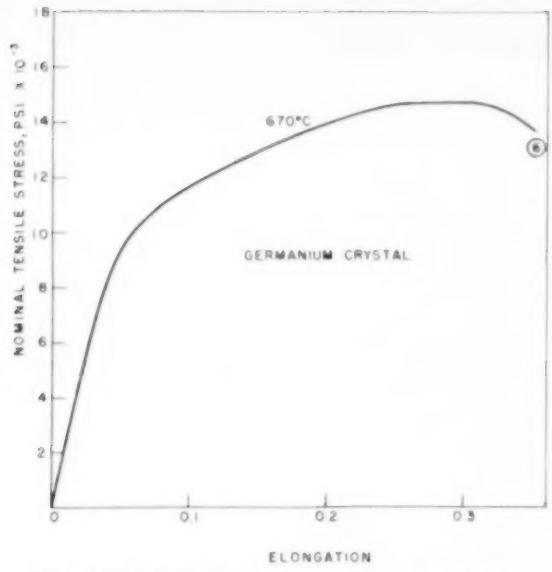

Fig. 3—Load-elongation curve for germanium single crystal extended 35 pct in tensile test at 670°C is plotted.

nent substructure lines define angles of 55° and 30° to the tension axis. The X-ray back reflection pattern from this sample showed considerable distortion and fragmentation and partial Debye rings.

Seitz[6] discussed Gallagher's creep test results in terms of dislocation theory. The incubation time for plastic flow was analyzed in terms of thermal fluctuations helping the applied stress to overcome the locking of dislocations by impurities, in the manner proposed by Cottrell.[7] Another consequence of impurity locking of dislocations is the yield point phenomenon, such as is frequently met in Fe-C alloys. The tests reported in Fig. 2 show germanium to have a yield point at 550° and 600°C, but virtually none at 625°C and above. The strong temperature dependence of the yield strength is also consistent with impurity locking of dislocations.

Conclusions

Tensile tests on germanium single crystals show the following:

Fig. 4 — Micrograph shows substructure developed in germanium crystal extended 35 pct at 670°C. X250. Area reduced approximately 25 pct for reproduction.

1—Germanium is very ductile at 670° and is very brittle below 550°C at a strain rate of 0.005 min^{-1}.

2—The flow stress of germanium is particularly sensitive to the rate of straining; an increase in strain rate raises the ductile to brittle transition temperature and increases the flow stress.

3—Germanium crystals have an upper yield point and a lower yield point at 550° and 600°C but not at 625°C and above.

Acknowledgments

C. J. Gallagher supplied the germanium crystals used in this work and contributed helpful discussion and criticism. E. A. Smith assisted in performing the tests.

Discussion of this paper, if any, will appear in JOURNAL OF METALS, November 1956, and in AIME Metals Branch *Transactions*, Vol. **206**, 1956.

References

[1] C. J. Gallagher: *Physical Review* (1952) **88**, p. 721.
[2] R. G. Treuting: *Trans.* AIME (1952) **194**, p. 1044; JOURNAL OF METALS (September 1952).
[3] L. Graf, H. Lecour, and K. Seiler: *Ztsch. für Metallkunde* (1953) **44**, p. 113.
[4] G. L. Pearson, W. T. Read, Jr., and F. J. Morin: *Physical Review* (1954) **93**, p. 666.
[5] J. H. Keeler: Private communication.
[6] F. Seitz: *Physical Review* (1952) **88**, p. 722.
[7] A. H. Cottrell: *Dislocations and Plastic Flow in Crystals*, (1953) p. 133. New York: Clarendon Press.

Technical Note

Hot-Rolled Textures of Titanium Alloys

by C. J. McHargue, J. R. Holland, and J. P. Hammond

IT has been reported that both beryllium[1] and zirconium[2] developed the same basic textures during rolling at temperatures up to 1475°F as at room temperature, differing only by an increase in the spread of basal planes toward the transverse direction as the temperature of deformation was increased. Iodide titanium[3] rolled at 1050°F has a texture similar to the cold-rolled texture, {0001}, 25° to 30° from the rolling plane toward the transverse direction, <1010>. Rolling iodide titanium at 1450°F produced a more random condition with the basal planes parallel to the rolling plane and no direction strongly aligned with the rolling direction.

C. J. McHARGUE, Junior Member AIME, is associated with Metallurgy Div., Oak Ridge National Laboratory, Oak Ridge, Tenn., J. R. HOLLAND, Junior Member AIME, and J. P. HAMMOND, Member AIME, are associated with Dept. of Mining and Metallurgical Engineering, University of Kentucky, Lexington, Ky.
TN 290E. Manuscript, May 25, 1955.

a—Ti-3.8 pct Al alloy was rolled at 1450°F.

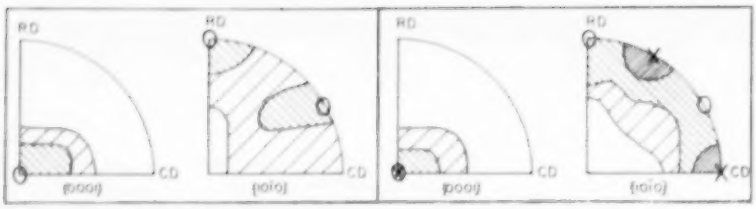

b—Ti-3.8 pct Al alloy was rolled at 1600°F.

Fig. 1—Rolling Ti-3.8 pct Al alloy at 1450° and 1600°F resulted in the textures given in *a* and *b*. The circled portions of the figures are {0001} <10$\bar{1}$0> and the crossed areas, {0001} <11$\bar{2}$0>.

The preparation of the alloys used for this study and the X-ray techniques have been described elsewhere.[5] All strips were reduced 90 pct in thickness in passes of approximately 10 pct and were heated before passes to 50°F above rolling temperatures.

The results on binary alloys containing 3.8 pct Al, 14.75 pct Zr, and 15.4 pct Ta are presented as Figs. 1 through 3 and are summarized in Table I.

In each instance, rolling at 1050°F (Table I) resulted in a texture similar to that developed by cold-rolling.[1] An increase in the spread of the basal plane in the transverse direction with increasing temperature of rolling was noted.

Rolling at 1450°F produced different textures in each of the three alloys studied. The alloy containing 3.8 pct Al developed a sharp {0001} <10$\bar{1}$0> texture similar to that found in sheet rolled at lower temperatures; see Fig. 1a. The pole figures for the Ti-14.75 pct Zr specimen showed an increase in the amount of material oriented parallel to the rolling plane, an increase in spread toward the transverse direction, and an alignment of both <10$\bar{1}$0> and <11$\bar{2}$0> with the rolling direction, Fig. 2. At 1450°F the Ti-15.4 pct Ta alloy was in the $\alpha + \beta$ region and the pole figures of the sheet rolled at this temperature show a marked increase in the degree of scatter of the basal plane toward the transverse direction. Both <10$\bar{1}$0> and <1120> are aligned with the rolling direction, Fig. 3.

It was necessary to roll the Ti-3.8 pct Al alloy at 1600°F in order to obtain significant differences in the texture. A sharp (0001) <1120> texture was developed by this treatment, Fig. 1b.

Since rolling at 1050°F gave basically the cold-rolled texture, it is likely that the picture relative to the deformation elements operating in these alloys at 1050°F varies little from that for room temperature deformation. Rolling at higher temperatures tended to align the <11$\bar{2}$0> with the rolling direction (Table I), as was the case for the higher temperature annealing textures.[6] This reorientation may be explained on the basis of high angle boundary migration occasioned by oriented nucleation and/or oriented growth.

Acknowledgments

This work was sponsored by the Aeronautical Research Laboratory (WCRRL), Wright Air Development Center under Contract No. AF 33(038)-19574. The authors are grateful for the aid received and permission to publish these results.

References

[1] A. Smigelskas and C. Barrett: *Trans.* AIME (1949) 185, p. 149; JOURNAL OF METALS (February 1949).
[2] R. McGeary and B. Lustman: *Trans.* AIME (1951) 191, p. 995; JOURNAL OF METALS (November 1951).
[3] C. McHargue and J. Hammond: *Trans.* AIME (1953) 197, p. 57; JOURNAL OF METALS (January 1953).
[4] C. McHargue, S. E. Adair, Jr., and J. Hammond: *Trans.* AIME (1953) 197, p. 1149; JOURNAL OF METALS (September 1953).
[5] C. J. McHargue and S. E. Adair, Jr.: *Second Summary Report* (January 1953) Contract No. AF 33 (038)-19574.

Table I. Comparison of Hot-Rolled Textures with the Cold-Rolled

Alloy	Cold-Rolled	Hot-Rolled, 1050°F	Hot-Rolled, 1450°F	Hot-Rolled, 1600°F
Ti-3.8 pct Al	{0001} <10$\bar{1}$0>	{0001} <10$\bar{1}$0>	{0001} <10$\bar{1}$0>	{0001} <11$\bar{2}$0>
Ti-14.75 pct Zr	{0001} 30°RP <10$\bar{1}$0>	{0001} 30°RP <10$\bar{1}$0>	{0001} 30°RP <10$\bar{1}$0> {0001} 30°RP <11$\bar{2}$0>	
Ti-15.4 pct Ta	{0001} 30°RP <10$\bar{1}$0>	{0001} 30°RP <10$\bar{1}$0>	{0001} in a narrow band along equator of pole figure <10$\bar{1}$0> and <1120>	

[a] RP denotes rolling plane.

Fig. 2—Textures resulted when Ti-14.75 pct Zr alloy was rolled at 1450°F. The circled portions of the figures are {0001} tilted 30° to the rolling plane <10$\bar{1}$0> and the crossed areas, {0001} tilted 30° to the rolling plane <1120>.

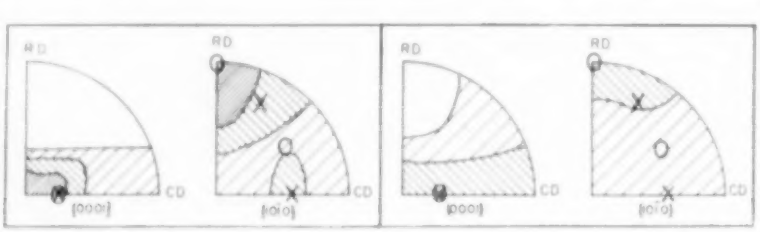

Fig. 3—Textures resulted when Ti-15.4 pct Ta alloy was rolled at 1450°F. Circled portions of the figures are {0001} tilted 30° to the rolling plane <10$\bar{1}$0> and crossed areas, {0001} tilted 30° to the rolling plane <1120>.

Mechanism of Plastic Flow in Titanium At Low and High Temperatures

An investigation was made of the mechanism of plastic flow in coarse grained specimens of both sponge and iodide titanium at low (−196°C) and high (500° and 800°C) temperatures. Deformation by slip occurs predominantly on a {1010} plane and in a $<11\bar{2}0>$ direction over this entire temperature range, and secondary slip on {1011} planes becomes more prevalent with increasing temperature. The crystallographic habit of the predominant twin type is temperature-dependent, and deformation by twinning increases as the temperature of testing is lowered. Kink bands were not observed at −196°C and rarely at the high temperatures.

by F. D. Rosi, F. C. Perkins, and L. L. Seigle

ALTHOUGH the deformational mechanisms in α-titanium at atmospheric temperature have been extensively investigated,[1-4] there is little information regarding the influence of testing temperature on these mechanisms. The only available data come from the recent work by McHargue and Hammond,[5] who extended single crystals of iodide titanium at a temperature of 815°C. No significant changes in the types of slip and twinning planes were observed, but increased activity on the type I, order 1 pyramidal slip planes and on the type II, order 2 twinning planes was reported. These planes contribute very little to the deformation process at room temperature.[1, 3]

Since there is interest in titanium as a material for use at both low and high temperatures, the present investigation was undertaken to examine the slip and twinning behavior in coarse grained specimens of titanium at −196°, 500°, and 800°C in order to determine the general effect of temperature on the mechanism of plastic deformation.

Experimental

Material Used and Specimen Preparation—Both sponge and iodide titanium were used in the present investigation; chemical analyses appear in Table I. These materials were arc-melted under argon into 25 g slugs, which were then cold-rolled approximately 90 pct to a sheet thickness of 0.05 in. Since the strain-anneal technique was used for obtaining coarse grains, the cold-rolled sheets were made into tensile specimens which were then annealed to produce a relatively coarse uniform grain structure prior to critical straining. The details of the strain-anneal treatment, size of grains, and the method for preparing the specimen surface for optical microscopy have been described in a previous report.[1]

In order to obtain a wider spread in crystal orientation for the present work, it was necessary to vary the rolling schedule to reduce the degree of preferred orientation in the annealed sheets prior to critical straining.

Methods for Tensile Testing—The apparatus for experiments at the temperature of liquid nitrogen (−196°C) consisted of two concentric stainless steel

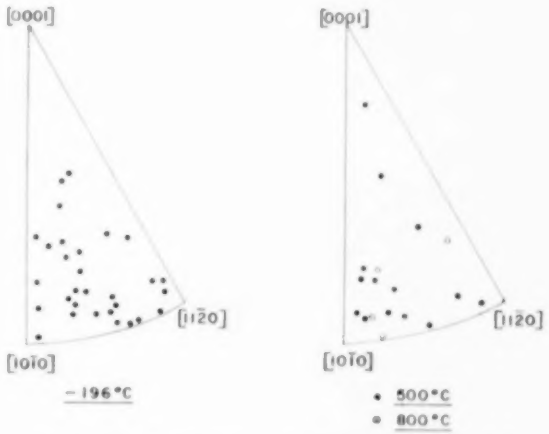

Fig. 1—Original orientations of course crystals studied in tension at the different temperatures indicated are shown in the two diagrams.

F. D. ROSI, Associate Member AIME, formerly associated with Sylvania Electric Products Inc., is associated with Research Laboratories, Radio Corp. of America, Princeton, N. J., F. C. PERKINS, Junior Member AIME, formerly associated with Sylvania Electric Products Inc., is associated with Chrysler Corp., Detroit, and L. L. SEIGLE, Member AIME, is associated with Sylvania Electric Products Inc., Bayside, N. Y.

Discussion of this paper, TP 3958E, may be sent, 2 copies, to AIME by Apr. 1, 1956. Manuscript, Sept. 29, 1954. Philadelphia Meeting, October 1955.

Table I. Chemical Analysis of Materials Prior to Arc-Melting

Titanium Material	Impurity Content, Pct								
	Fe	N	O	Cu	Al	Sn	Pb	Mn	Ti
DuPont sponge	0.10	0.009	0.05 to 0.08	—	—	—	—	—	99.77
New Jersey zinc iodide	0.0065	0.002	—	0.001	0.0065	0.002	0.0025	0.004	99.975

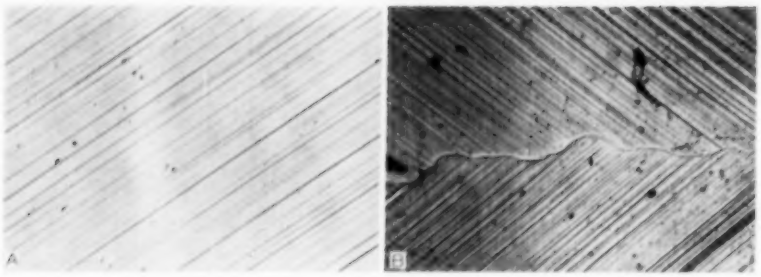

Fig. 2—Appearance of type I prismatic {1010} slip on a single system in coarse crystals at —196°C is illustrated in the two micrographs. *A*, X100. *B*, X50. Area reduced approximately 35 pct for reproduction.

Fig. 3—Appearance of {1010} duplex slip at —196°C is shown in the micrograph. X100. Area reduced approximately 35 pct for reproduction.

Fig. 4—Micrograph illustrates the nature of {1010} slip bands at an early stage of deformation (<1 pct) at —196°C. X100. Area reduced approximately 35 pct for reproduction.

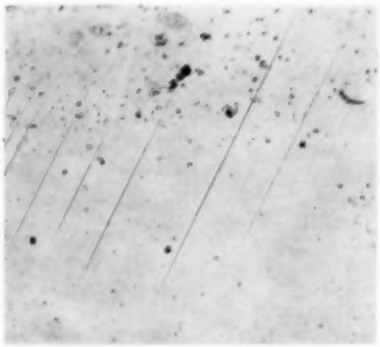

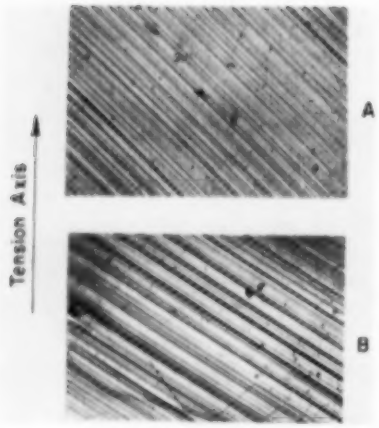

Fig. 5—Micrographs and diagram show the effect of crystal orientation on the development of type I prismatic slip bands at —196°C. χ_0 is the angle which the slip plane makes with the stress axis. $\chi_0 = 44°$ for micrograph *A* and $\chi_0 = 56°$ for micrograph *B*. X50. Area reduced approximately 30 pct for reproduction.

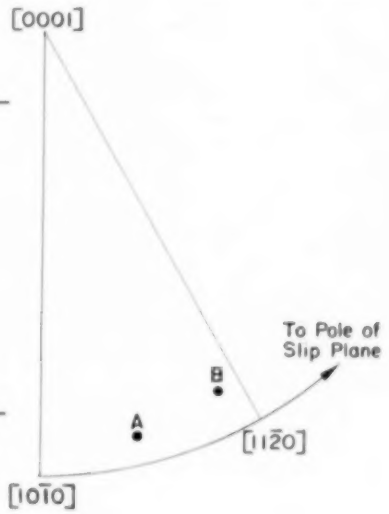

tubes, 2½ and 8 in. diam with a stainless steel plate containing the lower part of the grip assembly welded to the bottom of the inner tube. Santocel powder and a split cork ring at the bottom of the inner tube were used for thermal insulation.

The apparatus used for the elevated temperature experiments (500° and 800°C) was similar to that described previously with the addition of a brass bellows welded to the upper open end of the inner tube to serve as a flexible seal and permit extension of the specimen in purified argon. Heating was accomplished by means of insulated Nichrome windings around the inner tube, and Sil-O-Cel powder was used for thermal insulation. The specimen temperature was maintained within ±3°C by the use of a Micromax controller, and the temperature readings were obtained with a chromel-alumel thermocouple placed in contact with the specimen at the center of its gage length.

Tensile tests at both temperatures were made with a Baldwin-Southwark-Tate-Emery hydraulic machine at a predetermined cross-head speed of 0.009 in. per min. To determine the extension of the individual grains, whenever desirable, the distance between parallel fiducial marks was measured with a traveling microscope.

Determination of Slip and Twinning Planes—The method of identification of the slip and twinning planes was based on the use of a stereographic plot of a back-reflection Laue photograph describing the region where slip and twinning were observed. Great circles representing the normals to the slip and twinning traces on the surface of the specimen were located on this plot. In order to distinguish clearly between the slip and twin markings, the specimen, after deformation, was carefully repolished and etched to remove the slip bands.

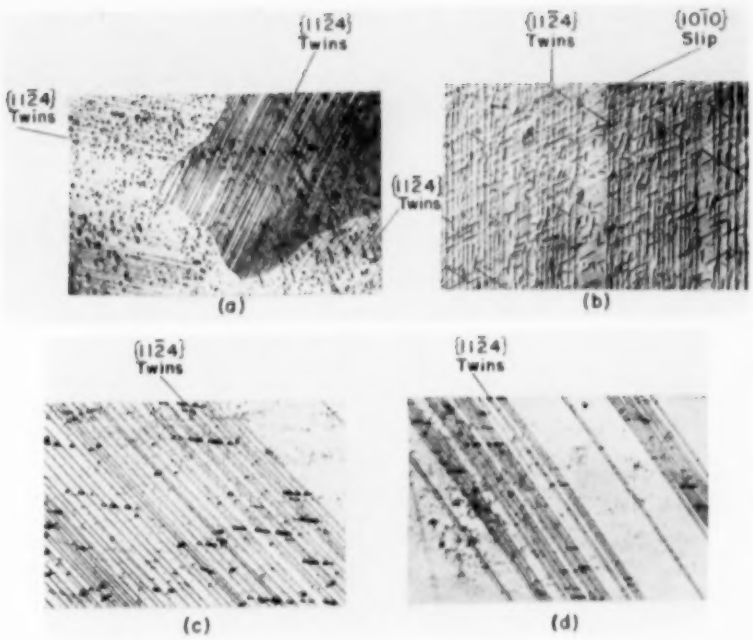

Fig. 6—Profuse twinning on {1124} planes at —196°C is shown in the four sections. *a* and *b* are as-deformed crystals, and *c* and *d* are repolished and etched crystals. *a*, X30; *b*, X250; *c*, X100; and *d*, X60. Area reduced approximately 35 pct for reproduction.

Fig. 7—Three part figure shows the occurrence of minor twin types at *a*—the grain boundaries, *b*—the specimen edge, and *c*—an included grain. *a*, X250; *b* and *c*, X100. Area reduced approximately 35 pct for reproduction.

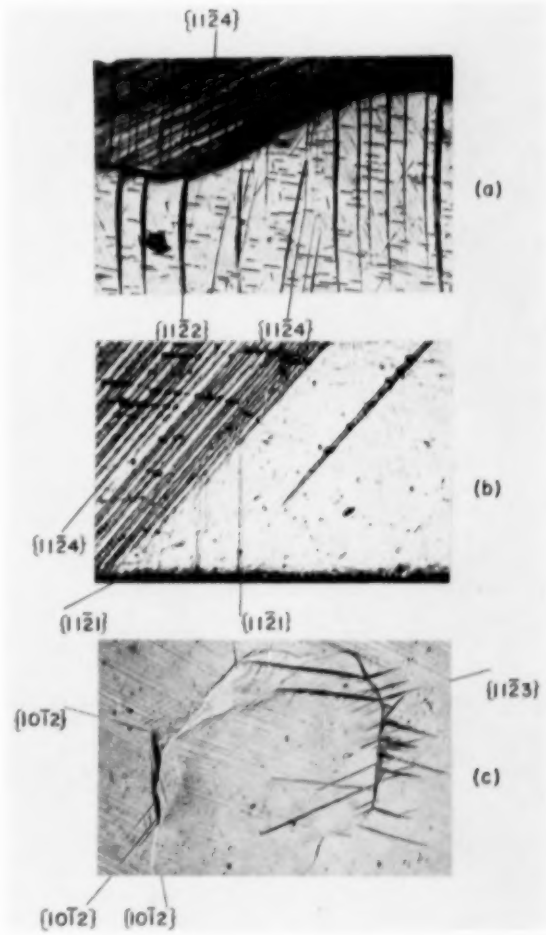

Table II. Slip and Twinning Elements in Titanium at Various Temperatures

Testing Temperature, °C	Slip Elements	Literature References	Twinning Planes	Literature References
—196	{1010} <1120>	Present study	1) {1124} 2) {1122} 3) {1121} 4) {1012} 5) {1123}	Present study
20	1) {1010} <1120> 2) {0001} <1120> 3) {1011} <1120>	1-3 2,3 1,3	1) {1121} 2) {1012} 3) {1122}	1-3 1-3 1,2
500	1) {1010} <1120> 2) {1011} <1120>* 3) {0001} <1120>*	Present study	{1012}	Present study
860	1) {1010} <1120> 2) {1011} <1120>*	5, present study	1) {1121} 2) {1122}	5

* The slip direction was assumed on this system at these testing temperatures.

In specimens where two or more poles on the stereographic plot could account for the observed slip or twin trace, the two-surface method of analysis[5] was used to distinguish the correct pole. All predominant slip and twinning planes observed in the present study were confirmed by this method of analysis, and the accuracy of these determinations fell within the accuracy of the employed X-ray technique.

Results

The original orientations of the crystals studied in tension are presented in Fig. 1. These orientations were determined by the back-reflection Laue X-ray technique. Since the slip and twinning behavior was

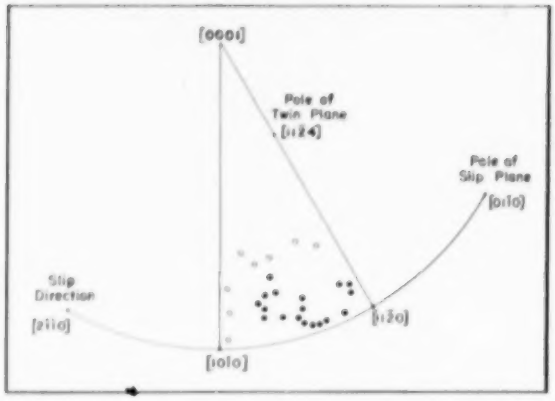

Fig. 8—Effect of crystal orientation on the occurrence of {1124} twins is shown in the diagram. Open circles represent little {11$\bar{2}$4} twinning while the filled circles represent profuse {1124} twinning.

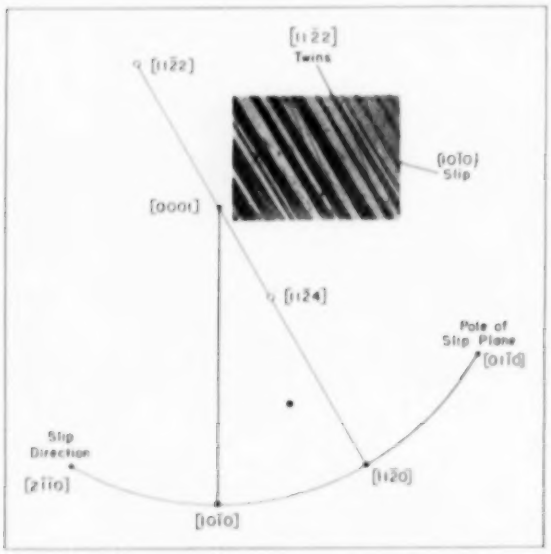

Fig. 9—Diagram and micrograph illustrate the orientation of a crystal in which extensive {1122} twinning had occurred. Micrograph, X50. Area reduced approximately 50 pct for reproduction.

found to be the same for both iodide and sponge titanium, no distinction will be made between these materials in presenting the experimental results.

Tests at −196°C—*Slip Behavior:* Deformation by slip was observed to occur solely on prismatic planes of the type {10$\bar{1}$0} in 30 crystals extended in liquid nitrogen despite several attempts to produce multiple slip by complex deformation. This is in contrast to the slip behavior of titanium at room temperature, where slip has been reported to occur not only on {10$\bar{1}$0} planes[1-4] but also on the (0001) plane[2] and {10$\bar{1}$1} planes.[1,6] However, the predominant slip plane is the same at both temperatures {10$\bar{1}$0}. The failure to observe first order pyramidal {10$\bar{1}$1} slip at −196°C suggests that slip is inhibited on these planes at low temperatures. On the other hand, the absence of basal slip could be attributed to an orientation effect, since the work of Anderson et al.[2] suggests that basal slip would not be likely for most of the crystal orientations shown in Fig. 1.

In a number of crystals, the effective slip direction for slip on the {10$\bar{1}$0} planes was found by X-ray analysis to coincide with a type I digonal axis of indices <11$\bar{2}$0>. This determination was made by following the movement of the specimen axis during extension.

It was possible to predict from the law of maximum shear-stress the choice of the {10$\bar{1}$0}<11$\bar{2}$0> slip system in all cases of simple extension. Accordingly, duplex slip was observed when two slip systems were geometrically equally favorable for glide. Typical examples of single and duplex slip on {10$\bar{1}$0}<11$\bar{2}$0> systems at −196°C are shown in Figs. 2 and 3. In both cases, the slip bands are well defined and very regularly spaced. At −196°C the slip bands appear finer, closer spaced, and more uniformly distributed along the crystal than at room temperature.

The appearance of {10$\bar{1}$0} slip bands in the very early stages of deformation is shown in Fig. 4 for a crystal whose original orientation was close to the stereographic boundary where duplex slip could be anticipated. It may be seen that the slip bands do not traverse the entire grain but appear as segments whose ends vanish in their path through the crystal. The appearance of this early stage slip is similar to that observed in high purity aluminum by Crussard,[5] Rosi and Mathewson,[7] and more recently Chen and Pond.[8] It was observed that as the strain increases deformation prefers to occur through the formation of new slip bands between the old. This results in a decrease in the average spacing between slip bands and, hence, an increase in slip band density with increasing strain. This low temperature slip behavior in titanium is similar to that in alumi-

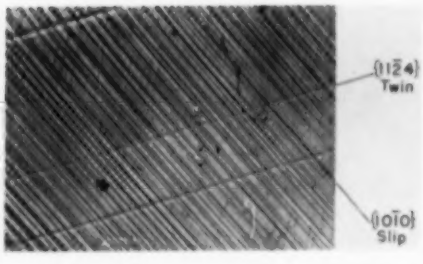

Fig. 10—Nature of {1124} twin markings in crystals of different orientation are shown left and right. Left shows markings obliquely inclined to prismatic slip bands; right, those approximately parallel to prismatic slip bands. X200. Area reduced approximately 45 pct for reproduction.

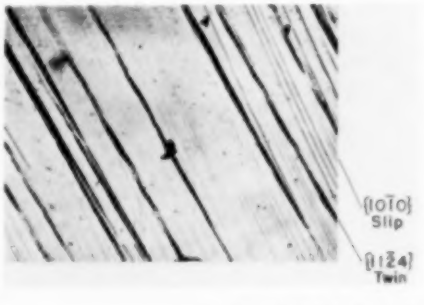

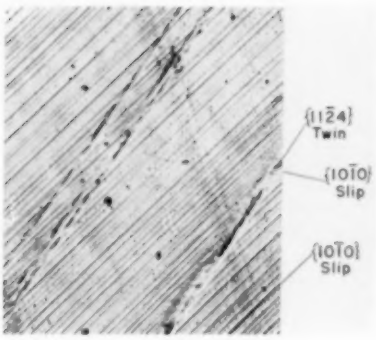

Fig. 11 — Appearance of secondary {1010} slip is shown in the immediate vicinity of {1124} twins. X200. Area reduced approximately 45 pct for reproduction.

Fig. 12—Micrograph illustrates the appearance of {1122} twin segments in the immediate vicinity of {1124} twins. X250. Area reduced approximately 40 pct for reproduction.

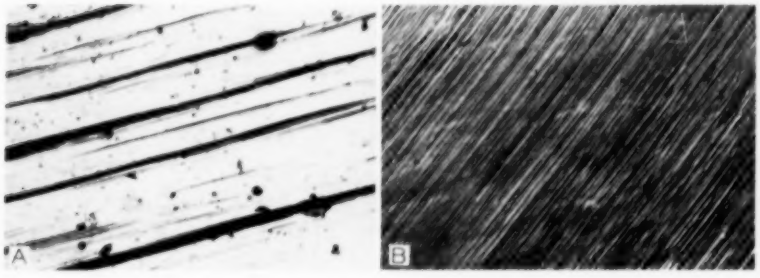

Fig. 13—Nature of slip band development in crystals extended at 500°C is illustrated. *A*—Micrograph shows moderate deformation. X75. *B*—Micrograph shows severe deformation. X100. Area reduced approximately 45 pct for reproduction.

num at atmospheric and subatmospheric temperatures.[6, 7, 8, 10]

It was recently pointed out[11] that the appearance of {10$\bar{1}$0} slip bands in titanium at room temperature is orientation-dependent, in that for a given shear the slip bands become coarser and more widely spaced as the angle χ_0, which the slip plane makes with the stress axis, increases. To study this effect at low temperatures, two crystals of selected orientation were deformed similar amounts and examined metallographically. These results are summarized in Fig. 5, which clearly shows only a mild tendency for slip bands to cluster with an increase in the value of the angle χ_0 at low temperatures.

Twin Behavior: Five twin types were observed in the specimens deformed in tension at —196°C. In order of frequency, these are: {11$\bar{2}$4}, {11$\bar{2}$2}, {11$\bar{2}$1}, {1012}, and {1123}.

The predominance of the {11$\bar{2}$4} type is clearly demonstrated in the micrographs of Fig. 6, where it is also apparent that twinning on these planes contributes significantly to the extent of deformation in these crystals. In general, the occurrence of the other twin types was confined to regions of complex stressing in the vicinity of grain boundaries, included grains, and specimen edges (see Fig. 7); and consequently, they contributed very little to the gross deformation. The short segments appearing in several of the crystals in Figs. 6 and 7 represent the Widmanstätten pattern of titanium hydride, which was removed in most specimens by heating in vacuum at 850°C for 24 hr.[12] The habit plane of this precipitate was found to coincide with a type I prismatic plane.

Extensive twinning on {11$\bar{2}$4} planes was observed in those extended crystals whose original orientations are indicated by the solid circles in the stereographic triangle of Fig. 8. Open circles represent crystals in which only minor amounts of {11$\bar{2}$4} twinning were observed. It appears that {11$\bar{2}$4} twinning becomes increasingly more difficult as the symmetry position for duplex slip is approached, or the central region of the stereographic triangle, where the resolved shear-stress factor for basal slip is a maximum, is approached.

The stereographic construction of Fig. 8 also shows the operative slip system and twinning plane for the indicated orientations. In all cases, twinning occurred on (11$\bar{2}$4) planes; and it is significant that, in crystals exhibiting extensive twinning (solid circles), these planes make an angle of 40° to 50° with the tension axis. Thus, it appears that the inception of twinning may be governed by a maximum shear-stress criterion, although the existence of a critical shear-stress for twinning has not been proven. Similar conclusions were reached regarding the selection of {11$\bar{2}$1} twins in the room temperature deformation of titanium.[11]

The occurrence and extent of participation of the minor {11$\bar{2}$2} and {11$\bar{2}$1} twin types also seemed to be orientation-dependent. An example of extensive twinning on {11$\bar{2}$2} planes (and to a much lesser extent on {11$\bar{2}$4} planes) is given in Fig. 9, which also shows a standard (0001) plot indicating the original orientation of the crystal as well as the operative twinning planes. Both the (11$\bar{2}$2) and (11$\bar{2}$4) planes lie on the same zone and make angles with the tension axis of 38° and 56°, respectively. It may further be noted that, in a crystal where twinning occurred solely on a {11$\bar{2}$1} plane, this plane made an angle of approximately 45° with the tension axis as compared with 20° for the *predicted* {11$\bar{2}$4} plane. These observations support the concept of a maximum shear-stress criterion for the selection of active twinning planes.

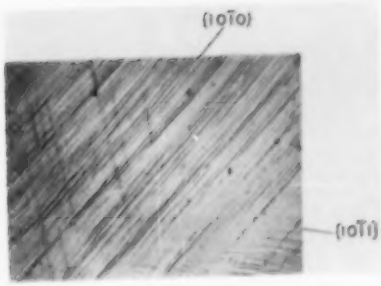

Fig. 14 — Micrograph illustrates the appearance of {10$\bar{1}$0} and {10$\bar{1}$1} slip bands in a crystal extended at 500°C. X50. Area reduced approximately 45 pct for reproduction.

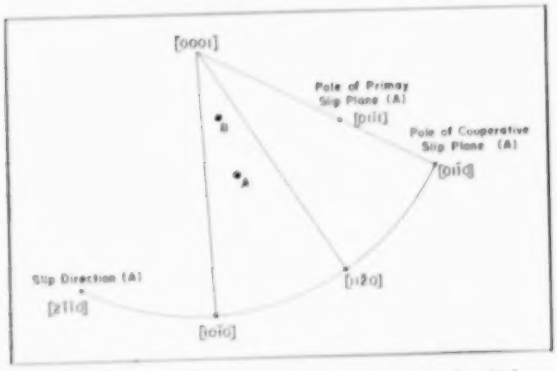

Fig. 15—Diagram shows the orientation of crystals in which {10$\bar{1}$1} slip and {10$\bar{1}$2} twinning had occurred.

In summary, the present results indicate that the same twins occur at −196°C and at room temperature but that 1—a greater proportion of the deformation occurs by twinning at low temperatures and 2—the preponderance of twinning shifts from the {11$\bar{2}$1} to the {11$\bar{2}$4} planes.

Appearance of Twin Types: Testing at −196°C had little effect on the characteristic appearance of the {11$\bar{2}$1} twin type; possibly the twins appear somewhat finer at the low temperatures than at room temperature.[1, 2] As shown in Fig. 9, twins of the {1122} type are thick and similar in appearance to the {10$\bar{1}$2} twins at room temperature.[1, 2] Both the predominant {11$\bar{2}$4} twins and the {11$\bar{2}$1} twins appear as narrow bands of constant thickness (Fig. 7) whose character seems to vary with orientation, as indicated in Fig. 10. Generally speaking, in crystals where the twin traces make a large angle with the prismatic slip bands (Fig. 10a), the twins themselves invariably appear as fine lines not unlike the slip bands; whereas when the twins run almost parallel to the slip bands (Fig. 10b), they appear as chains of roughly elliptical segments resembling {112} twinning in iron.

It is also interesting that slip on a secondary {10$\bar{1}$0} plane or twinning on a {1122} plane frequently occurred in the immediate vicinity of {11$\bar{2}$4} twins, as illustrated by Figs. 11 and 12. This localized secondary slip may be responsible for the segmented appearance of the {11$\bar{2}$4} twins.

Tests at 500° and 800°C—*Slip Behavior:* Extensive slip on a {10$\bar{1}$0} plane and along a <11$\bar{2}$0> direction occurred in all but two crystals extended at 500° and 800°C. Examples of slip at 500°C are shown in Fig. 13; and it may be seen that in one of the crystals there is a marked clustering of slip bands similar to that observed at room temperature but never at −196°C. Thus, with increasing deformation at high temperatures a tendency exists for {10$\bar{1}$0} slip bands to appear adjacent to those already formed. A like tendency has been reported for aluminum[9-11] and cadmium and zinc.[12] In a few crystals tested at 500°C, secondary slip on the {10$\bar{1}$1} pyramidal planes was observed. This slip plane was rarely encountered at room temperature (observed only in several crystals subjected to complex stressing).[1] Increased activity of {10$\bar{1}$1} slip at elevated temperatures is also encountered in magnesium, where above 225°C slip frequently occurs on the {10$\bar{1}$1} planes in addition to the basal plane.[13] The recent work of McHargue and Hammond[6] indicates that there is even more activity on these planes at still higher testing temperatures. Typical appearance of cooperating prismatic and pyramidal slip at 500°C is shown in the micrograph of Fig. 14.

In tests at 500°C, {10$\bar{1}$0} prismatic slip was not observed in two grains whose initial orientations are indicated in the stereographic plot of Fig. 15. In grain *A*, {10$\bar{1}$1} pyramidal slip was the predominant deformation mechanism, and a small amount of basal slip was also present in the vicinity of the grain boundary. The operative plane was that on which the resolved shear-stress was a maximum. This observation is particularly interesting in view of the recent work of Anderson, Jillson, and Dunbar,[7] who reported slip solely on the basal plane at room temperature in single crystals having orientations similar to grain *A*. Thus, it would appear that a tendency exists for pyramidal slip to replace basal slip at elevated temperatures. It is interesting that many of the pyramidal slip markings in grain *A* appeared wavy; close examination revealed that this could be attributed to cooperative slip on {10$\bar{1}$0}, which has the same slip direction as the operative {10$\bar{1}$1} plane; see Fig. 15. Deformation in grain *B* was almost entirely by twinning. However, some small slip markings were observed in the vicinity of the twin interfaces, which could best be attributed to {10$\bar{1}$1} slip.

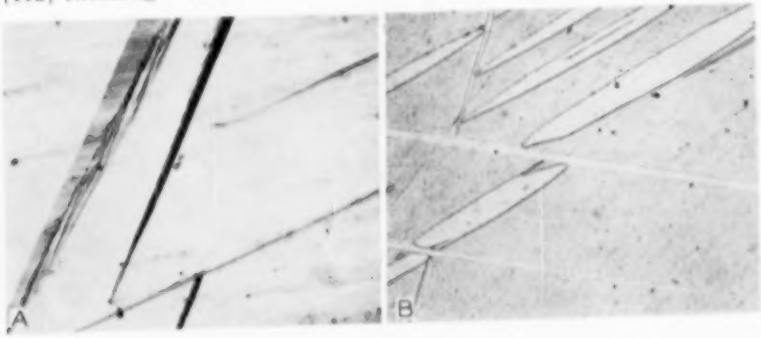

Fig. 16—Appearance of {10$\bar{1}$2} twins at 500°C is shown for crystals *A* and *B* whose original orientations are shown in the diagram, Fig. 15, as filled circles. X70. Area reduced approximately 45 pct for reproduction.

Twin Behavior: With the exception of the two grains whose orientations are shown in Fig. 15, twinning was not observed in the specimens extended at 500° and 800°C. This is not consistent with the results of McHargue and Hammond,[8] who reported many examples of {1121} and {1122} twinning in the extension of iodide single crystals at 815°C. The apparent discrepancy could not be attributed to an orientation effect, since several of the crystals exhibiting these twin types had orientations similar to those of the present work. Neither can it be attributed to the extent of deformation, since many of the grains in the present study were severely deformed, in a few cases to fracture. However, the presence of grain boundaries in the authors' specimens could conceivably be a contributing factor, since the work of several investigators[15, 20] indicates that twinning occurs more readily in single crystals than in coarse grained material.

In the two grains of Fig. 15, twinning occurred on planes of the {1012} type, as shown in Fig. 16. In crystal *B*, where both the prismatic and basal planes are poorly oriented for slip, twinning was the predominant mode of deformation. This behavior was also observed in a similarly oriented grain extended at room temperature.[8, 21] The shape of the {1012} twins is the same at room and elevated temperatures.

Appearance of Kink Bands: Observations of kink bands were made in crystals where extensive slip on a single $\{10\bar{1}0\}\langle 11\bar{2}0\rangle$ system had occurred. As reported for other metals,[16-21] these bands represent disoriented regions of the crystal which are bounded by parallel bend planes making an angle of approximately 90° with the active slip planes. The typical appearance of kink bands at 500°C is shown in the micrographs of Fig. 17. It is interesting to note the continuity of the fine kink band across the low energy grain boundary in the lower micrograph of Fig. 17.

X-ray analysis showed that the kink bands at 500°C have the same crystallographic geometry as those observed at room temperatures.[17] The bend planes coincided with a {1120} plane, whose normal was the active slip direction; hence, the rotation at the bend plane was about the [0001] direction, which represents the intersection of the {1120} bend plane with the [1010] slip plane.

Kinking appeared less frequently at 500°C than at room temperature, and no kink bands were detected in the liquid nitrogen tests. The recent work on kink bands in aluminum by Laloeuf and Crussard,[17] Honeycombe,[19] and Chen and Mathewson[20] suggests that, in crystals where complex slipping can be expected, kink bands are not necessary to the glide process. Since the multiple glide occurred in many of the crystals extended at the elevated temperature, it is possible to understand the decrease in kinking at 500°C from this viewpoint. On the other hand, failure to detect kinking at the subatmospheric temperature might not indicate less kinking but a refinement of the kink bands to the point where they are optically undetectable. This latter view is supported by the work of Honeycombe,[19] who employed X-ray micrography to detect the presence of optically unresolvable kink bands in aluminum deformed at low temperatures. Their absence could also be attributed to the increased participation of twinning at low temperatures.

Discussion of Results

The results of the present and existing determinations of slip and twinning elements in titanium at various temperatures are summarized in Table II. These elements are listed in order of their frequency of occurrence. It is apparent that the $\{10\bar{1}0\}\langle 11\bar{2}0\rangle$ slip mechanism occurs over the entire temperature range and that slip on the $\{10\bar{1}1\}\langle 11\bar{2}0\rangle$ and $(0001)\langle 11\bar{2}0\rangle$ systems increases with increasing temperature of testing. Moreover, the contribution of pyramidal slip at the higher temperatures increases at the expense of both basal and prismatic slip. Apparently the critical resolved shear-stress for pyramidal slip decreases more rapidly with increasing temperature than that for basal or prismatic slip.

The data in Table II also emphasize the fundamental importance of the slip direction. Although the choice of glide plane varies with temperature and orientation, the slip direction is always the same and is the direction of closest packing. Thus, irregularities in the surface markings resulting from $\{10\bar{1}1\}$ slip could be attributed to cooperative slip on $\{10\bar{1}0\}$ along the same digonal I axis. This general behavior has been observed in aluminum[22] and magnesium[14] at elevated temperatures and in several body-centered-cubic metals.[23-26]

With two exceptions,[14, 27] previous investigations[12, 13, 16, 28] have consistently shown that the contribution of twinning to the gross deformation process increases as the temperature of testing is lowered. This is also true for titanium, as shown in Table II. Not only is there an increase in the number of available twin types at −196°C, but there is also an increase in the amount of deformation by {1124} twinning at the expense of {1010} slip.* Evidently the critical stresses for slip increase more rapidly with decreasing temperature than those for twinning. Since the predominant twin type changes with temperature as well as with crystal orienta-

* Twinning on both the {1124} and {1123} planes were reported by Liu and Steinberg[6] at room temperature but under very different conditions of testing.

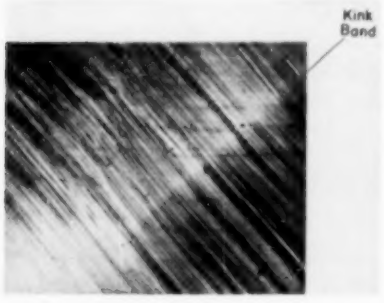

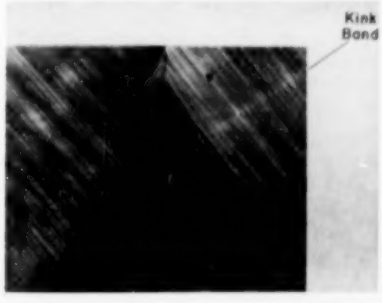

Fig. 17—Two micrographs illustrate the appearance of kink bands in crystals moderately extended at 500°C. X50. Area reduced approximately 45 pct for reproduction.

tion, it also appears that critical stresses for twinning vary differently for different twin types.

In disagreement with McHargue and Hammond,[6] who observed both twin types at 815°C, neither {1121} or {1122} twinning was found at elevated temperatures. Since crystals of similar purity, orientation, and amounts of deformation were used in both studies, this discrepancy cannot be attributed to any of these important variables. It is conceivable, however, that crystal size is an important factor. In the present study, multiple glide on secondary planes was frequently observed at elevated temperatures. Since this behavior was not reported by McHargue and Hammond, it might be attributed to the smaller grain size in the present work. Assuming that both secondary slip and twinning are competitive stress-relief mechanisms,[11] the occurrence of either one would tend to eliminate the necessity of the other. These considerations could also apply to the observed lack of kinking, which is also a stress-relief process, at both elevated and low temperatures.

Finally, it may be pointed out that, because of the large number of available slip and twinning planes, titanium of relatively high purity can be expected to exhibit appreciable ductility over the entire temperature range investigated. This view is supported by recent tests of vacuum-annealed material of both commercial and iodide purity.[25, 26]

Conclusions

An investigation was made of the mechanisms of plastic flow in coarse grained specimens of arc-melted sponge and iodide titanium extended at −196°, 500°, and 800°C. The results of this study may be summarized as follows:

1—No difference was observed in the slip and twinning behavior for the different purities.

2—At −196°C, slip occurred solely on a {10$\bar{1}$0} plane and in a <1120> direction, whereas twinning was observed on the {1121}, {1122}, {11$\bar{2}$3}, {11$\bar{2}$4}, and {10$\bar{1}$2} planes. The predominant twin type was the {11$\bar{2}$4}.

3—At the high temperatures, slip occurred extensively on a {10$\bar{1}$0}<1120> system and much less frequently on a {10$\bar{1}$1} plane. The activity on this secondary slip plane increased with an increase in the temperature of testing. Twinning was observed only on the {10$\bar{1}$2} planes.

4—Kink bands were not observed at −196°C and only rarely at the high temperatures.

5—The crystallographic habit of the predominant twin type is temperature-dependent, and deformation by twinning increases as the temperature of testing is lowered.

6—The data suggest that the temperature variation in the critical shear-stress for slip and twinning is different for different crystallographic families of planes.

Acknowledgment

This work was sponsored by the Aeronautical Research Laboratory, Wright Air Development Center, under Contract No. AF 33 (616) 422.

Discussion of this paper, if any, will appear in JOURNAL OF METALS, November 1956, and in AIME Metals Branch *Transactions*, Vol. **206**, 1956.

References

[1] F. D. Rost, C. A. Dube, and B. H. Alexander: Mechanism of Plastic Flow in Titanium—Determination of Slip and Twinning Elements. *Trans.* AIME (1953) **197**, p. 257; JOURNAL OF METALS (February 1953).

[2] E. A. Anderson, D. C. Jillson, and S. R. Dunbar: Deformation Mechanisms in Alpha Titanium. *Trans.* AIME (1953) **197**, p. 1191; JOURNAL OF METALS (September 1953).

[3] A. T. Churchman: Preparation of Single Crystals of Titanium and Their Mode of Deformation. *Nature* (1953) **171**, p. 706.

[4] T. S. Liu and M. A. Steinberg: Twinning Single Crystals of Titanium. *Trans.* AIME (1952) **194**, p. 1043; JOURNAL OF METALS (October 1952).

[5] C. J. McHargue and J. P. Hammond: Deformation Mechanisms in Titanium at Elevated Temperatures. *Acta Metallurgica* (1953) **1**, No. 6, p. 700.

[6] M. C. Crussard: Slip in High Purity Aluminum Crystals. *Revue de Metallurgie* (1945) **42**, p. 286.

[7] F. D. Rost and C. H. Mathewson: A Study of the Plastic Behavior of High Purity Aluminum Single Crystals at Various Temperatures. *Trans.* AIME (1950) **188**, p. 1159; JOURNAL OF METALS (September 1950).

[8] N. K. Chen and R. B. Pond: Dynamic Formation of Slip Bands in Aluminum. *Trans.* AIME (1952) **194**, p. 1085; JOURNAL OF METALS (October 1952).

[9] K. Yamaguchi: The Slip-Band Produced when crystals of Aluminum Are Stretched, I—Extension at Room Temperature. *Scientific Papers* Inst. of Physical Chemistry Research, Tokyo (1928) **8**, p. 289; II—Extension at High (and Low) Temperatures. *Scientific Papers* (1929) **9**, p. 277.

[10] A. F. Brown: Slip Bands and Hardening Processes in Aluminum. *Journal* Inst. of Metals (1951) **80**, p. 115.

[11] F. D. Rost: Mechanism of Plastic Flow in Titanium—Manifestations and Dynamics of Glide. *Trans.* AIME (1954) **200**, p. 58; JOURNAL OF METALS (January 1954).

[12] C. M. Craighead, G. A. Lenning, and R. I. Jaffee: Nature of the Line Markings in Titanium and Alpha Titanium Alloys. *Trans.* AIME (1952) **194**, p. 1317; JOURNAL OF METALS (December 1952).

[13] E. Schmid and W. Boas: *Kristallplastizitat.* (1935) Berlin. J. Springer.

[14] P. W. Bakarian and C. H. Mathewson: Slip and Twinning in Magnesium Crystals. *Trans.* AIME (1943) **152**, p. 226; METALS TECHNOLOGY (April 1943).

[15] E. B. Pfeil: *Carnegie Scholarship Memoirs* Iron and Steel Inst. (1926) **15**, p. 319; (1927) **16**, p. 153.

[16] R. W. Cahn: Plastic Deformation in Alpha Uranium. *Acta Metallurgica* (1953) **1**, p. 49.

[17] A. Laloeuf and C. Crussard: Relation Between the Deformation and Recrystallization of Monocrystals of Aluminum. *Revue de Metallurgie* (1951) **48**, p. 462.

[18] R. W. Cahn: Slip and Polygonization in Aluminum. *Journal* Inst. of Metals (1951) **19**, p. 129.

[19] R. W. K. Honeycombe: Inhomogeneities in the Plastic Deformation of Metal Crystal. *Journal* Inst. of Metals (1951) **80**, p. 45.

[20] N. K. Chen and C. H. Mathewson: Structural Studies of Plastic Deformation in Aluminum Single Crystals. *Trans.* AIME (1951) **191**, p. 653; JOURNAL OF METALS (August 1951).

[21] E. C. Burke and W. R. Hibbard, Jr.: Plastic Deformation of Magnesium Single Crystals. *Trans.* AIME (1952) **194**, p. 295; JOURNAL OF METALS (March 1952).

[22] W. Boas and E. Schmid: Dependence of Crystal Plasticity on Temperature. III—Aluminum. *Ztsch. für Physik* (1931) **71**, p. 703.

[23] G. I. Taylor and C. F. Elain: Distortion of Iron Crystals. *Proceedings* Royal Soc., London (1926) **112**, p. 337; and H. J. Gough: Alternating Torsion of Alpha-Iron. *Proceedings* Royal Soc., London (1928) **118**, p. 498.

[24] C. F. Elain: The Distortion of β-Brass and Iron Crystals. *Proceedings* Royal Soc., London (1936) **153A**, p. 273.

[25] L. C. Tsien and Y. S. Chow: The Glide of Single Crystals of Molybdenum. *Proceedings* Royal Soc., London (1937) **163A**, p. 19.

[26] E. N. da C. Andrade and L. C. Tsien: The Glide of Single Crystals of Sodium and Potassium. *Proceedings* Royal Soc., London (1937) **163A**, p. 1.

[27] N. N. Davidenkov, A. F. Kolesnikov, and K. N. Federov: *Journal of Experimental and Theoretical Physics* (1933) **3**, p. 350.

[28] C. S. Barrett and C. T. Haller: Twinning in Polycrystalline Magnesium. *Trans.* AIME (1947) **171**, p. 246; METALS TECHNOLOGY (December 1946).

[29] Plastic Flow and Recrystallization of Titanium. *Progress Report Nos. YE 54-530 and YE 54-541* to Aeronautical Research Laboratory, WADC, by Sylvania Electric Products Inc. (Sept. 1, 1952 to Mar. 1, 1953.) Contract No. AF 33 (616) 422.

[30] G. A. Lenning, C. M. Craighead, and R. I. Jaffee: The Effect of Hydrogen on the Mechanical Properties of Titanium. *First Summary Report* to Watertown Arsenal by Battelle Memorial Inst. (July 31, 1952) Contract No. DA-33-019-ORD-220.

Technical Note

Preferred Orientations in a Meta-Stable Body-Centered-Cubic Zr-Cb Alloy

by J. H. Keeler

AN alloy of zirconium containing 18 atomic pct Cb was found to be body-centered-cubic and readily deformable at room temperature. The behavior of this alloy provided an opportunity to determine if

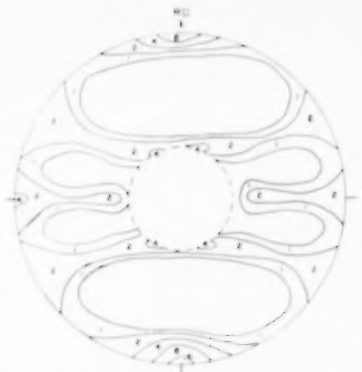

Fig. 1—(110) pole figure for 98.8 pct cold reduced Zr and 18 pct Cb sheet. The (110) poles are in the rolling direction and the (100) plane is tilted out of the rolling plane in a spread ±47° about the rolling direction.

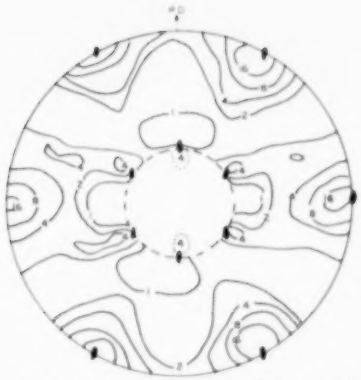

Fig. 2—(110) pole figure for 98.8 pct cold reduced Zr and 18 pct Cb sheet annealed for 1 hr at 1400°C. The (111) plane lies principally in the rolling plane with the <112> direction in the rolling direction, as shown by the symbols. Closed ellipse designates (111) [112].

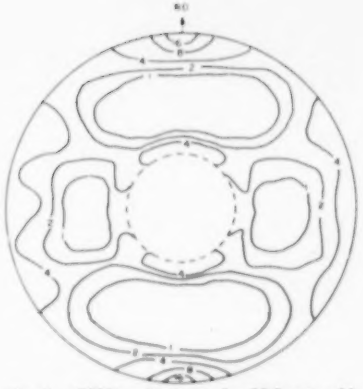

Fig. 3—(0002) pole figure for 98.8 pct cold reduced Zr and 18 pct Cb sheet transformed to the hexagonal-close-packed phase by a 25 hr anneal at 500°C. The similarity between this pole figure and that in Fig. 1 is evidence that the Burgers orientation relationship was valid for this transformation.

the deformation and annealing textures of body-centered-cubic zirconium alloys would be similar to the more familiar body-centered-cubic metals.

The alloy was prepared by arc melting in a water cooled copper crucible and under an argon atmosphere. The ingot which weighed 100 g was made from crystal bar zirconium and high purity columbium. The as-melted ingot was ground flat on top and bottom surfaces to a thickness of about 0.250 in., cold rolled to a thickness of 0.084 in., annealed, and was then cold rolled at room temperature to a thickness of 0.001 in. The final 0.009 in. of reduction was done between sheets of alloy steel. All annealing was carried out in evacuated tubes of Vycor or quartz containing zirconium foil as a getter.

The transmission pole figures were determined by the quantitative method of Decker, Asp, and Harker,[1] modified by Geisler,[2] using an X-ray spectrogoniometer with CuKα radiation. The apparatus and technique have recently been described in detail.[3]

The deformation texture shown in Fig. 1 is very similar to the deformation textures of other body-centered-cubic materials such as those reported for iron,[4] Fe-Si alloys,[5] vanadium,[6] molybdenum,[7] and tantalum.[8] Here, the (110) poles are in the rolling direction and the (100) plane is tilted out of the rolling plane in a spread ±47° about the rolling direction. Annealing the cold rolled alloy for 1 hr at 650°C, just above the $\alpha \rightarrow \beta$ transformation,[9] produced a texture similar to that in Fig. 1, but slightly sharpened.

Annealing at temperatures high in the β-stable region, at 900°, 1200°, and 1400°C for 1 hr, produced textures similar to that shown in Fig. 2 for the specimen annealed at 1400°C. The dotted areas are estimated from back-reflection examination of this specimen. In this texture, the (111) plane lies principally in the rolling plane with the <112> direction in the rolling direction. The 900° and 1200°C annealing treatments did not produce textures quite as sharply defined as the one shown in Fig. 2. These annealing textures are quite similar to those found for iron,[4] Fe-Si alloys,[5] vanadium,[6] and tantalum.[8]

This alloy could be transformed to the hexagonal-close-packed modification by a 25 hr anneal at 500°C. The (0002) pole figure for a specimen so transformed is shown in Fig. 3. The striking resemblance to the (110) pole figure for the body-centered-cubic modification shown in Fig. 1 is evidence that the Burgers orientation relationship between the two phases is operative. As would be anticipated, the (0002) basal planes of the hexagonal-close-packed phase are parallel to the (110) planes of the body-centered-cubic phase.

Summary

The deformation and annealing textures of a body-centered-cubic Zr-Cb alloy are similar to the textures of the more familiar body-centered-cubic metals.

The preferred orientation of the newly transformed hexagonal-close-packed phase is related to the parent body-centered-cubic phase by the Burgers orientation relationship.

Acknowledgments

The author wishes to thank L. J. Hartford, who assisted in the sample preparation, and Ann S. Cooper, who obtained the X-ray data. Valuable suggestions by A. H. Geisler contributed to the work. This work was carried out under Contract No. W-31-109-Eng-52 for the AEC.

References

[1] B. F. Decker, E. T. Asp, and D. Harker: *Journal of Applied Physics* (1948) **19**, p. 388.

[2] A. H. Geisler: *Modern Techniques in Physical Metallurgy*. (1953) p. 131. Cleveland. ASM.

[3] J. H. Keeler and A. H. Geisler: *Trans.* AIME (1955) **203**, p. 395; JOURNAL OF METALS (February 1955).

[4] G. Kurdjamow and G. Sachs: *Ztsch. für Physik* (1930) **62**, p. 592.

[5] C. S. Barrett, G. Ansel, and R. F. Mehl: *Trans.* AIME (1937) **125**, p. 516.

[6] C. J. McHargue and J. P. Hammond: *Trans.* AIME (1952) **194**, p. 745; JOURNAL OF METALS (July 1952).

[7] M. Semchyshen and G. A. Timmons: *Trans.* AIME (1952) **194**, p. 279; JOURNAL OF METALS (March 1952).

[8] J. W. Pugh: Private communication; to be published.

[9] B. A. Rogers and D. F. Atkins: *Trans.* AIME (1955) **203**, p. 1024; JOURNAL OF METALS (September 1955).

J. H. KEELER, Member AIME, is associated with Metallurgy & Ceramics Research Dept., Research Laboratory, General Electric Co., Schenectady.

TN 289E. Manuscript, Apr. 29, 1955.

Heterogeneous Nucleation Of the Martensite Transformation

Experiments on powders of an Fe-Ni alloy have shown that the martensite transformation appears to start on heterogeneous nucleation sites. The nature of these sites is hypothesized and a mechanism for burst phenomenon in Fe-Ni alloys is set forth qualitatively on the basis of these heterogeneous nucleation sites.

by R. E. Cech and D. Turnbull

FISHER, Hollomon, and Turnbull have developed a theory for the nucleation of martensite.[1, 2] They first tested the theory on Fe-C alloys and low alloy steels. The major factor influencing nucleation of martensite was considered to be statistical composition fluctuations occurring in small regions at high temperature and *frozen-in* on quenching. These local regions of varying size and composition serve as nucleation centers. They become supercritical, one by one, as temperature is progressively lowered, resulting in temperature-dependent or athermal transformation.

Fisher next applied nucleation theory to substitutional solid solution alloys.[3] Detailed predictions were made for Fe-Ni alloys because of the availability of free energy data on this system.[4] It was shown that composition fluctuations that were significant energy-wise did not occur, and nucleation frequencies could be calculated from average properties of the system. Nucleation was predicted to occur as time-dependent and having the functional relationship to give a *C* curve of nucleation frequency vs temperature. The analysis further predicted that the nucleation frequency was extremely sensitive to composition. Experimentally, it would be found that the transformation in some compositions is so slow that measurable amounts will not form in a reasonable length of time. With other compositions, only slightly different, the nucleation frequency becomes so great that the material becomes transformed while still distant in temperature from the maximum nucleation frequency. On quenching an alloy of such composition, the observed transformation kinetics would be similar to those found in Fe-C alloys.

Cech and Hollomon[5] repeated experiments of Kurdjumov[6] in which the kinetics of transformation were similar to those predicted by Fisher for Fe-Ni alloys. The alloy studied in this investigation contained 73.3 pct Fe, 23.0 pct Ni, and 3.7 pct Mn.

R. E. CECH, Junior Member AIME, and D. TURNBULL, Associate Member AIME, are Research Assistant, Physical Metals Section, and Head, Chemical Metals Section, respectively, Research Laboratory, General Electric Co., Schenectady.

Discussion of this paper, TP 3992E, may be sent, 2 copies, to AIME by Apr. 1, 1956. Manuscript, Oct. 25, 1954. Philadelphia Meeting, October 1955.

Fisher,[7] using an idealized model for the extent of transformation as a function of the number of martensite crystals per grain of parent phase, derived nucleation frequencies from the transformation curves of Cech and Hollomon. Complicating influences such as coupling effects between grains in the polycrystalline specimens were neglected. Nevertheless, excellent agreement was found between the theoretically and experimentally derived nucleation frequencies.

These experiments, however, could not provide a critical test of the theory. Experimental nucleation frequencies could vary widely from those calculated, depending upon the extent of deviation from *ideal* partitioning and the extent of coupling effects. Further, since the compositions of material theoretically analyzed and experimentally determined were different, the free energy changes involved in the experimental work could only be estimated. Also, the effect of heterogeneities on the transformation kinetics was not considered. For these reasons, it was decided that experiments designed to test the validity of the Fisher analysis must be conducted on binary Fe-Ni alloys, which were the ones considered theoretically by Fisher.

The martensite transformation in Fe-Ni alloys has been the subject of considerable study. Machlin and Cohen[8] have shown that transformation proceeds in a manner quite unlike that in any other ferrous alloy system. They found that single crystals would transform to a large extent in a single burst. In large grain polycrystalline specimens, frequently more than one grain and sometimes the whole specimen would transform at the same instant in this manner. Results on filings indicated that different particles would undergo the burst transformation at widely different temperatures. These results support the conclusion that the transformation behavior could not be described by a single nucleation frequency as would be the case if the nucleation were homogeneous.

It appeared that further work was necessary to define the factors responsible for burst-type transformation, so that the conditions could be altered to favor homogeneous nucleation of martensite if such could be accomplished. This report summarizes the results of some experiments conducted with powdered Fe-Ni alloys for this purpose and the re-

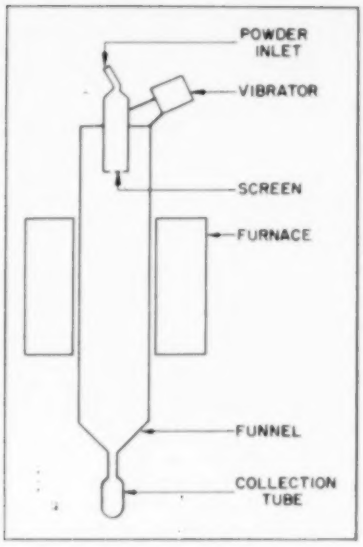

Fig. 1 — Diagram shows shot tower apparatus for treating powder used with vertical hydrogen furnace.

sults are discussed with respect to the mechanism of martensite formation.

Powder Preparation

Selection of Method—A number of methods used in preparing small particles were considered for this investigation. Filings cut from solid specimens were deemed unsuitable for a detailed study of the martensite transformation. The filings as cut are highly deformed and, even after being annealed in a separator matrix of inert material, are susceptible to accidental deformation because of their very anisotropic shape. Since the martensite transformation is extremely structure-sensitive, the kinetics would be altered by this deformation. Furthermore, the grain size would be, at best, only loosely specified by the particle size, since the maximum grain diameter of an annealed material tends to be that of the minimum dimension of the specimen.[9] This condition also means that the filings would, in general, be polycrystalline. Therefore, the coupling effects that occur in massive samples would be expected to occur, but to a lesser extent, in filings.

Another method of preparing powders by feeding the desired alloy into a *Metallizer* spray gun and collecting the sprayed powder in a bath of water or oil was attempted. Metallographic examination of these powders indicated excessive amounts of oxide inclusions and heavy scale on the surface. Therefore, this method of powder preparation was also considered unsuitable.

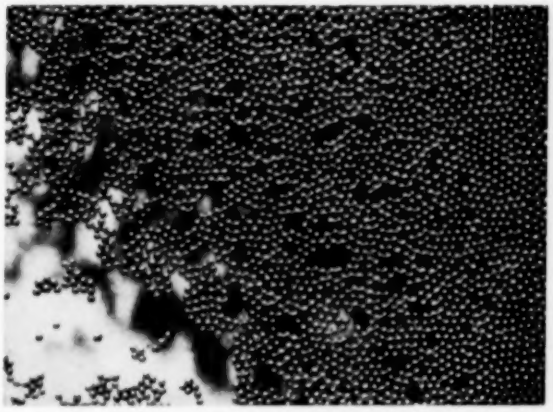

Fig. 2—Powder produced by dropping method consisted of 69.8 pct Fe and 30.2 pct Ni, 75 to 100 μ diam.

Oxide-Forming Procedure—The method adopted for preparing Fe-Ni alloy powders for this investigation utilized the component oxides Fe_2O_3 and NiO for the starting material. The impurity content of these oxides is listed in Table I. The oxides were weighed in proper proportions to form a 500 g mixture containing 30.2 wt pct Ni and 69.8 wt pct Fe, referring to metallic content. The oxides were then mixed wet in an Eppenbach colloid mill for 30 min, using a final shear plate clearance of 25μ. This mixing procedure has been found to be equivalent to 200 hr of wet ball milling.[10] The oxide particle size prior to mixing was approximately 8μ, each particle consisting of cauliflowerlike groups of 1μ particles. These groups were broken down in mixing to give a final particle size of about 1μ as determined by electron micrographs of mixed powders.[11] The mixed slurry was dried to a cake and fired in air at 1350°C for 8 hr, thereby permitting interdiffusion of oxides to form the spinel $(0.71\ Fe, 0.29\ Ni)_3O_4$. No trace of free ferric oxide could be detected by X-ray diffraction of the heat-treated material. Free nickel oxide is not detectable in this manner, owing to superposition of diffraction lines.

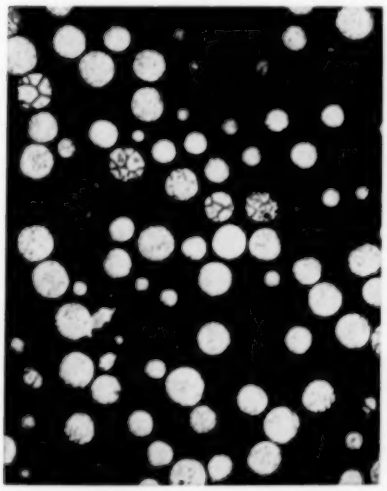

a—Micrograph shows martensitic fraction of specimen.

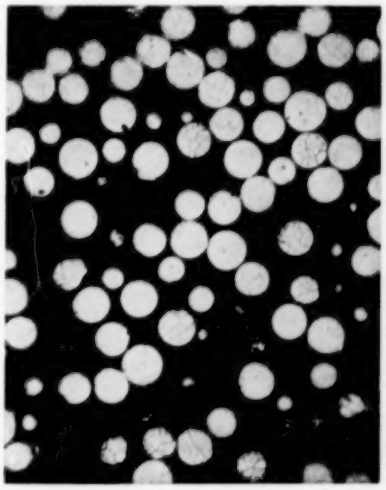

b—Micrograph shows untransformed fraction of specimen.

Fig. 3—<37μ particles after quenching to —196°C are shown in *a* and *b*. Samples were etched to delineate grain boundaries.

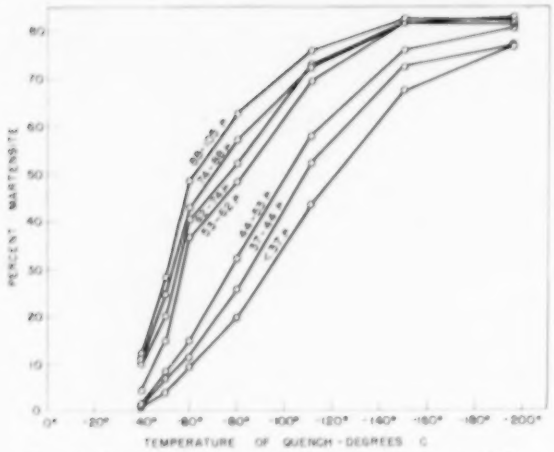

Fig. 4—Chart illustrates martensite transformation in 30.2 pct Ni and 69.8 pct Fe alloy powder.

In a recent determination of the Fe_2O_3-NiO system, Palmer[12] found the $(Fe,Ni)_2O_3$ region to extend from 23 to 50 mol pct NiO (14 to 35 wt pct Ni) at the diffusing temperature of 1350°C. Thus, upon homogenization, the oxides should be expected to form a single phase solid solution of uniform composition. Also, since the smallest particles used in the investigation were 25μ or more in diameter, they were composed of 10^4 or more component oxide particles. This number is sufficiently large to insure nearly average composition in the particles. The uniformity of composition was checked experimentally by two methods to be discussed later in the report.

Particle-Size Establishment and Reduction—The spinel was crushed to particles < 200μ diam in a diamond mortar and these further crushed to a size range of from 25 to 100μ in a dry ceramic ball mill. This powder was then separated into three fractions, each of a different particle size, and hydrogen-reduced at 630°C for 4 hr. After reduction, the particles contained only a small percentage of unreduced spinel as detected by X-ray diffraction examination.

Shotting—The powder was next treated in an apparatus best described as a shot tower. A vertical hydrogen furnace 30 in. in height, with a 4 in. tube diam, cold chambers at both top and bottom, and a powder-dispensing apparatus at the top, was used to melt the individual powder particles as they were dropped through the apparatus. Fig. 1 illustrates the major parts of this apparatus.

Reduced alloy powders were dispensed as a dust into the furnace at 1480°C. After melting and resolidifying while being dropped, the particles were collected in a hydrogen-filled vial and stored at room temperature until needed. Fig. 2 illustrates the appearance of the shotted powder. If the furnace temperature is sufficiently high, all the particles melt on passing through the furnace. Little agglomeration occurs if the size range shotted is kept fairly narrow. If a broad size range is shotted, a sweeping action occurs whereby the rapidly falling large particles pick up small ones in the molten region. This agglomeration markedly decreases the number of small particles. Aside from this, the sizes after shotting are the same as before, being displaced only by the amount necessary for coalescence from irregular to spherical particles.

Completeness of Oxide Removal—It was of interest to determine the ability of the shotting treatment to remove residual oxides in the particles. X-ray diffraction of powders revealed no trace of oxide. However, a more critical experiment was thought necessary. Spinel powder in a size range below 53μ was shotted at 1480°C in hydrogen without prior reduction. The resultant powder was found to be entirely free of oxide, indicating that complete reduction had occurred. It was deduced from this experiment that the prereduced powder would also be completely reduced. The prior reduction step was necessary to prevent loading the furnace atmosphere with water vapor, however.

Number of Grains Per Particle—The powder produced by the shotting procedure should for the most part be composed of single crystals. This supposition follows as a consequence of the kinetics of nucleation in the liquid to solid transformation. Assuming that most particles will be free of extraneous nuclei, they should, in general, supercool before nucleation of the solid phase. The first nucleus that forms will, on giving up the latent heat of fusion, raise the temperature of the particle, thus preventing further nucleation in the unsolidified portion of the particle. Solidification would then be expected to proceed from this nucleus throughout the entire particle. Fig. 3 shows a number of particles in cross section, etched to bring out grain boundaries. It is seen that about one-eighth of the particles contain boundaries intersecting the surface. If it is assumed that another one-eighth has grain boundaries that do not intersect the surface, three-fourths of the particles remain as single crystals.

Quenching Treatment

A measured quantity of loose powder was quenched by dropping into a rapidly stirred bath of Freon 11,

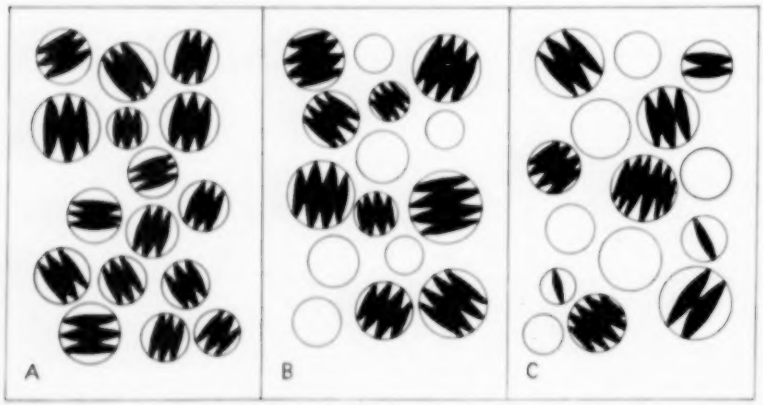

Fig. 5—Drawings are of possible arrangements for dispersal of martensite in powders. A—Uniform degree of transformation in all particles is illustrated. B—Uniform degree of transformation in some particles and no transformation in others are shown. C—Varying degrees of transformation in some particles with no transformation in others are illustrated.

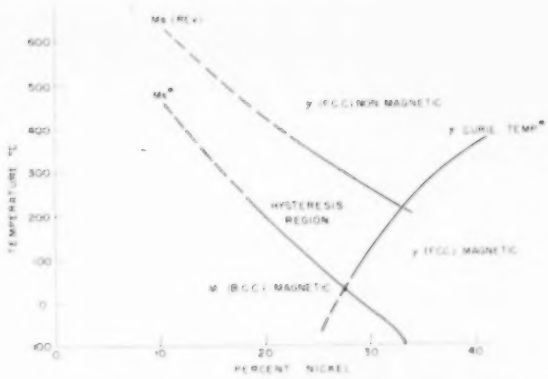

Fig. 6—Diagram charts martensite start, martensite reversal start, and Curie temperature of Fe-Ni alloys. See Hansen.[10]

Freon 12, or liquid nitrogen held to a stated temperature ±0.1°C. After 2 sec at temperature, the powder was withdrawn by a glass-sheathed magnet and quenched into absolute alcohol at room temperature. Since both γ and martensite (M) phases are magnetic below room temperature, complete removal of the powder from the bath was accomplished. The powder was then sized by screening into seven size groups ranging from $<37\mu$ to 88 to 105μ. The amount of martensite in each group was determined by integrated intensities of X-ray diffraction peaks from the phases present.

The (110)M and (111)γ peaks were measured on a General Electric XRD-3 X-ray diffraction spectrometer using cobalt radiation monochromated by the Ross-Kirkpatrick[13, 14] technique. Martensite percentages were determined from the calculated and measured energy ratios of the peaks using the method described by Averbach and Cohen.[15] The validity of the method was tested by making nine artificial mixtures of γ and M phase Fe-Ni alloy powders. Deviations of martensite percentage (measured and known) in the calibration specimens were random and indicated the probable error of a martensite determination to be 1.7 pct M (somewhat less at low martensite contents).

Results

The amount of martensite present after quenching specimens to −40.0°, −50.0°, −60.0°, −80.0°, −111.0°, −150.0°, and −196.0°C is shown in Fig. 4. It is seen that the percentage of martensite in a specimen is a function of particle size, those specimens composed of small particles having a lesser extent of transformation than specimens of larger size particles.

The curves in Fig. 4 do not present a complete picture of the kinetics of martensite formation in these powders, however. It is necessary to ascertain the distribution of martensite within the particles comprising each specimen.

Three possible martensite distribution configurations are illustrated in Fig. 5. If the configuration is as shown in Fig. 5b or 5c, a magnetic separation can be accomplished under proper conditions, thereby differentiating between these configurations and the one of Fig. 5a.

A diagram (Fig. 6) has been included for reference purposes, indicating the M_s, M_r (reverse), and Curie temperatures of Fe-Ni alloys. The austenite magnetic inversion occurs over a range of temperature. The Curie temperature curve reported in Fig. 6 was obtained by a linear extrapolation of the flat portion of a magnetic property curve to its intercept on the temperature axis. In practice, it is necessary to heat to 40° to 50°C above the defined Curie temperature to remove the last trace of ferromagnetism. The martensite Curie temperature is only slightly lower than that of pure iron. It can be seen from Fig. 6 that in the composition studied the austenite is paramagnetic below the temperature at which martensite reversal starts. Therefore, a temperature region exists in which transformed and untransformed particles may be magnetically separated.

The separation was accomplished by placing a specimen of one size range in a horizontal Pyrex *conducting glass* tube together with a thermometer, heating above the austenite Curie temperature, and drawing off the magnetic fraction of the specimen with a magnet held near the tube. The tube was heated by passage of an electric current controlled manually with a Variac and the specimen protected from oxidation by performing the operation under a hydrogen atmosphere. The magnetic separation involved a number of successive separations, with a weak alternating magnetic field used first, and then a strong magnetic field of 1600 gauss for final scavenging of the untransformed fraction. The ferromagnetic fraction of the specimen could not be as thoroughly cleaned of nonferromagnetic particles as the reverse. When the magnetic field was applied to lift the particles, they would entrap some non-

Table I. Stated Impurity Content of Oxides

	Fe_2O_3,* Pct	NiO,† Pct
SO_4	0.10	0.002
Substance not precipitated by NH_4OH	0.01	—
Cu	0.005	0.008
Zn	0.005	0.005
Insoluble in HCl (principally silica)	0.06	—
N (in compounds)	—	0.002
Cl	—	0.004
Pb	—	0.001
Co	—	0.005
Fe	—	0.004
Alkalies and earths	—	0.10

* Supplied by J. T. Baker Chemical Co., Lot No. 72250.
† Supplied by J. T. Baker Chemical Co., Lot No. 3495.

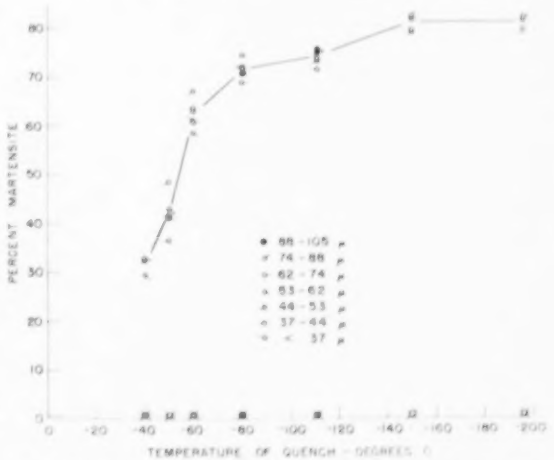

Fig. 7—Results of X-ray diffraction analyses show martensite contents of separated powders.

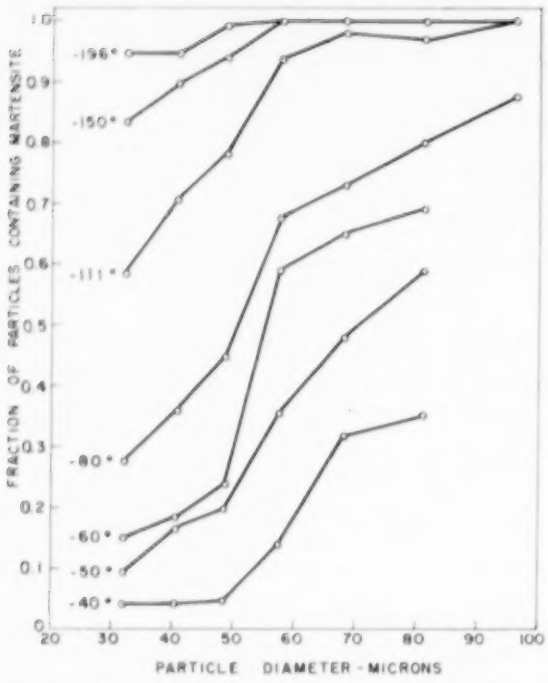

Fig. 8—Fraction of particles contains martensite as a function of particle size.

ferromagnetic particles. Repeated lifting and shaking of the powder was necessary to remove these trapped particles.

After separation of the specimens, the two fractions of each specimen were analyzed by X-ray diffraction to determine the amount of martensite present. The results are shown in Fig. 7. The nonmagnetic portion, when properly cleaned, contained no detectable trace of martensite. It is estimated that a minimum of 1 pct martensite is necessary for certain detection by the X-ray method used. The magnetic portion transforms to an extent that is determined only by the temperature of quench and is independent of particle size. The scatter of individual points, it is believed, results from the additive sum of errors in removing the last traces of untransformed particles in the magnetic separation, and in determining the amount of martensite.

A separate experiment was performed to test the ability of the strong permanent magnet to remove from the untransformed fraction those particles having only a small quantity of martensite. Two martensitic particles 105μ diam were melted into a solder droplet. This droplet was placed with copper powder in the separation tube, and a separation procedure identical to that used for the specimens was performed at room temperature. It was found that the 1600 gauss magnet easily removed the lead particle from the powder. From the calculated weight of the magnetic particles and the weight of the solder droplet, the amount of martensite was found to be 0.6 pct. From the result of this experiment, it is probably safe to assume that the nonmagnetic fraction of the specimens contained less than 0.6 pct martensite.

The possibility that composition variations were responsible for the marked differences in transformation behavior of the particles was tested in two ways. First, it was assumed that particles low in nickel content would be more likely to undergo a martensitic transformation at a given temperature than would those having a higher nickel content. Accordingly, a quantity of powder was quenched to a temperature such that roughly half of the particles underwent a martensitic transformation. Martensitic and untransformed particles were then separated and chemical analyses were performed on the separated fractions. Second, it was noted (Fig. 6) that austenitic particles low in nickel content would have a lower Curie temperature than those higher in nickel content. It is expected that if a slight difference of Curie temperature exists between particles, a magnetic separation conducted at a temperature where the particles were very slightly magnetic would result in preferential removal of the most strongly magnetic particles of the specimen. A separation of completely austenitic particles into two portions was made under the conditions described previously and these were chemically analyzed for nickel content.

Table II. Chemical Analysis of 30.2 Pct Ni, 69.8 Pct Fe (Nominal) Powder

	Wt Pct Ni ± 0.1 Pct
Particles separated by extent of transformation	
Untransformed	30.22
Transformed	30.24
Particles separated by assuming a Curie temperature difference	
Higher Curie temperature	30.15
Lower Curie temperature	30.23

The results of both sets of chemical analyses (Table II) indicate that no composition segregation occurred between particles. These chemical analyses also served to establish the true alloy content of the powders used in the investigation.

Since the powders were used as solidified from the melt the possibility of *coring* within each particle exists. To test this possibility a quantity of powder, 44 to 62μ diam, was dispersed in alumina powder and annealed for 48 hr at 1100°C *in vacuo*. Specimens of this powder quenched to −40°, −50°, −60°, and −80°C contained 7.4, 17.6, 31.5, and 49.9 pct martensite, respectively, after the subzero treatment. This compares favorably with martensite contents of unannealed powders after similar quenching treatments. The absence of a heat-treating effect in these powders supports a similar finding by Machlin and Cohen[5] on filings of an Fe-Ni alloy.

From the data shown in Figs. 4 and 7, it is apparent that *it is the relative number of particles undergoing transformation at a given temperature that varies with particle size.* From the values of the martensite percentages in specimens before and after separation, the relative fractions of the particles containing martensite have been calculated. These are plotted as a function of particle size in Fig. 8.

It would be preferable in these experiments to use direct weight measurements of separated fractions. In the present investigation, losses due to sticking of powder to containers used in the experiments made quantitative weight measurements quite difficult. Specimen fractions were weighed in a few cases and these are listed in Table III, together with the weight fractions calculated from martensite

percentages for comparison. Since the experimental errors in both methods of determination are additive, the scatter is not thought unreasonable.

To test the possibility that some martensite reversal may occur in the elevated temperature magnetic powder separation technique, the Curie temperature and M_s (reversal) temperature were determined in a more precise manner on an apparatus similar in design to one constructed by Buehl and Wulff.[17]

Austenitic powder in an evacuated tube was slowly heated in a nonhomogeneous magnetic field, and the force of magnetic attraction was measured. It was found that the Curie range was spread over a large temperature interval extending from below room temperature and leveling off at 200° to 220°C to a paramagnetic state. A small amount of transformation was then induced in the sample by a low temperature treatment and the magnetic attraction remeasured as a function of temperature. The first indication of martensite reversal occurred as a sharp change in galvanometer deflection at 306° to 308°C. Magnetic separations had been performed at temperatures ranging from 240° to 260°C—well within the hysteresis region. Therefore, it is felt that no martensite reversal occurred in the magnetic separations.

In an attempt to determine if the difference in transformation behavior was reflected in the metallographic structure, the transformed and untransformed fractions of a specimen quenched to −196°C were examined (Fig. 3). It is seen that, although grain boundaries are present in some particles, they are present in about equal numbers in both fractions. If these boundaries act to accelerate the transformation, they should all be present in the transformed fraction. It is concluded from this that grain boundaries exert a negligible influence on transformation in these powders.

Discussion

These results indicate that the first measurable quantity (>½ pct) of martensite forming in a particle occurs as a burst and that the burst temperature (M_s) of a given particle may vary from above −40° to below −196°C for the alloy studied.

Once transformation has begun in a particle, it proceeds in a small temperature interval to an extent that is a function only of temperature and is independent of particle size. In the temperature region considered, the amount of martensite in the transformed particles was so great that it is probable that cessation of transformation at a given temperature was due to strain set up by the martensite already present. Further cooling was then necessary to provide additional driving force to extend transformation into the strained region.

Table III. Fraction of Specimen Transformed, Temperature of Quench −80°C

Particle Size, μ	Fractional Weight	Calculated from Percentages
74 to 88	0.77	0.80
62 to 74	0.73	0.73
53 to 62	0.58	0.68
44 to 53	0.38	0.45

A striking feature of these results is that M_s is much less than the M_s temperature (−20°C approximately) of polycrystalline bulk Fe-Ni alloys of the same composition. About 1/20 of the <37 and 37 to 44μ diam particles remained untransformed after quenching to −196°C. Thus, the temperature of initial martensite formation in small particles may be as much as 176°C lower than in bulk specimens of the same composition.

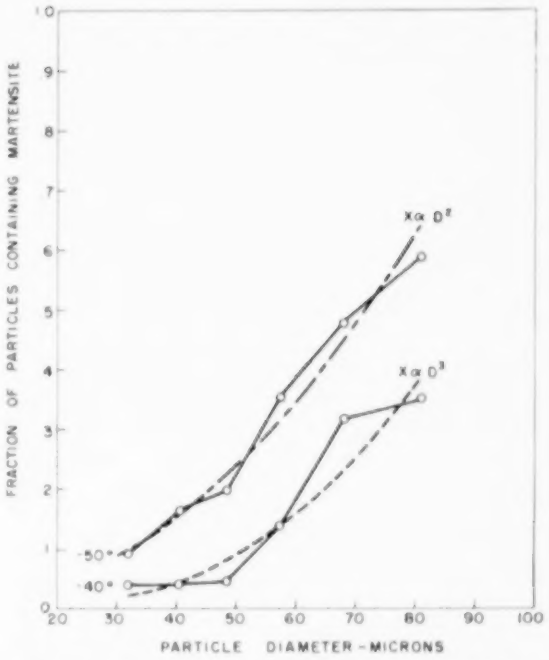

Fig. 9—Comparison of the data at two temperatures with $\chi \propto D^n$, the corresponding *best fit* relationship, is illustrated. For −50° (χ) n is superscript 2 and for −40° (χ) n is 3.

The data support the hypothesis that heterogeneities in a spectrum of potencies exist in the particles. Nucleation occurs at these sites and, once nucleated, martensite proceeds to form cataclysmically through the particle. The probability of finding a heterogeneity of a given potency in a particle increases with increasing particle size. It is not known, as yet, whether the heterogeneities reside on the surface or are distributed through the volume. The fraction (χ) of the particles containing martensite would vary as the diameters (D) squared if the sites reside on the surface or as the diameters cubed if they are dispersed throughout the alloy. At −40°, −50°, −60°, and −80°, χ (where χ does not exceed ~0.65) varies as D^2 or D^3, but the scatter is too great to permit a decision on which function ($\chi \propto D^2$ or $\chi \propto D^3$) best describes the data. The comparison of the data at two temperatures with the corresponding *best fit* relationship is illustrated in Fig. 9. The scatter could result from errors in martensite percentage determinations and from variations of the mean particle diameter in each size group.

The burst phenomenon in Fe-Ni alloys can best be reconciled with nonburst transformation in most other alloys if it is postulated that the martensite transformation as commonly found in nature is always nucleated preferentially at heterogeneities. If these heterogeneities consist solely of structure imperfections, the martensite transformation kinetics should not be markedly different in Fe-Ni alloys than in other ferrous alloys. However, if the most potent heterogeneities were extraneous particles—such as carbides or nitrides—which either nucleate

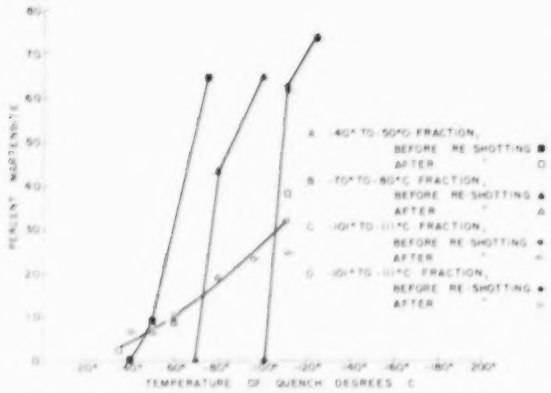

Fig. 10—Chart shows transformation in selected fractions before and after shotting.

martensite directly or indirectly through the strain associated with their presence, then martensite nucleation would be more difficult in Fe-Ni alloys which usually are freer of such inclusions. Thus, austenite would *supercool* below the usual M_s temperature. When nucleation does occur on a less potent site, the excess driving free energy would cause transformation to proceed immediately to a large extent.

To test the postulate of direct martensite nucleation by extraneous impurities, a critical experiment was performed. A quantity of powder was prepared by shotting with the furnace at a temperature of 1560°C, *80° higher than in the previous experiment.* From a portion of this powder, all particles undergoing initiation of transformation between −40° and −50°C were taken by alternately quenching and magnetically separating the particles. Similarly, from the other portions of the powder, the fractions transforming in the −70° to −80° and −101° to −111°C range were taken. To test for thermal history effects between the magnetic separation temperature and subzero quenching temperature, a fourth fraction (−101° to −111°C) was taken from the untransformed residues of the −40° to −50° and −70° to −80°C specimens. The extent of transformation of these fractions is plotted (closed points) in Fig. 10. It can be seen that particles transform to a large extent within a small temperature interval following initiation of transformation as was surmised from the previous experiment. Also, the good agreement between the two −101° to −111°C fractions indicates that no thermal history effect exists in the +250° to −80°C temperature interval.

The four specimens *A*, *B*, *C*, and *D* were then reshotted separately with the furnace at a temperature of 1540°C. The purpose of the reshotting treatment was to ascertain whether or not the particles would *remember* their transformation temperatures prior to reshotting. If insoluble particles were directly responsible for initiating the transformation as in the liquid to solid transformation, such a memory should be observed.

After reshotting, the specimens were screened for particles in the 44 to 62μ size range. The selected particles were then quenched to a number of subzero temperatures. The amounts of martensite present in the specimens after quenching are shown in Fig. 10 (open circles). It is apparent that the particles retain no memory of their transformation temperature prior to reshotting. *This result indicates that extraneous impurities do not nucleate martensite directly in these powders.* The transformation curve of reshotted powder does differ from that of the previous experiment, however, and in a way that may be significant. It can be seen by comparing with Fig. 4 that the extent of transformation in the 44 to 62μ reshotted powder is much less than that which formed in similar size powders in the previous experiment. To find the cause for this difference, all specimens were quenched to −111°C and put together. A magnetic separation was made, and the fraction of the particles containing martensite was determined by weight. The martensite content of the transformed fraction (65.3 pct) was similar to that of the previous experiment under similar conditions. However, the fraction of the particles containing martensite was markedly different for the reshotted powder—0.61 vs 0.85 estimated from the previous experiment, Fig. 8. On requenching the shotted powder to −196°C, it was found that 0.975 of the specimen was transformed. This compares to about 0.99 of the specimen in the previous experiment transformed.

These results give support to the hypothesis that extraneous particles nucleate martensite indirectly through the strain sites associated with their presence in the metal. With no variable other than the degree of superheating above the melting point changed, the average probable temperature of martensite nucleation was varied considerably. This effect could be accomplished if the superheating treatment acts to decompose or dissolve some impurities, thereby bringing about a different population of impurity-caused strain centers in the reshotted powder. It is probable that martensite is nucleated both at structural imperfections and at impurity strain centers. If nucleation occurred only on structural imperfections, no superheating effect should be observed; but if nucleation is entirely on impurity strain centers, the superheating effect should be more pronounced than that actually found.

Since the transformation is heterogeneously nucleated in a 30.2 pct Ni alloy and can be suppressed on rapid cooling to below the predicted temperature of rapid homogeneous nucleation, it follows that the driving free energy for transformation may be insufficient for homogeneous nucleation at a measurable rate with this alloy. A decrease of nickel content to increase the free energy change of transformation is therefore desirable. Also, since heterogeneous nucleation sites are found in all particles in the 25 to 100μ range, a further subdivision of particles to smaller size is required in order to localize these on a fraction of the particles. Further experiments in this direction are in progress.

It is interesting to note that the transformation kinetics of powdered Fe-Ni alloy, which appear to be due to singularities in the material, are very similar to the kinetics predicted by Fisher, Hollomon, and Turnbull for transformation in Fe-C alloys. In this latter case, transformation was initiated by singularities of another kind; namely, carbon-poor regions from statistical fluctuations of composition at elevated temperature, frozen-in on quenching and converted to ferrite prior to becoming supercritical for growth as martensite.

In certain qualitative respects, the authors' results are in excellent agreement with those of Machlin and Cohen. However, the authors have

found an effect of particle size on the transformation behavior nearly one order of magnitude larger than reported by Machlin and Cohen and differ with them in important respects on interpretation. In the following, Machlin and Cohen's most important experimental findings will be compared with the authors' and the divergencies in interpretation will be discussed.

The finding of Machlin and Cohen that the burst temperature M_s varies markedly among specimens is confirmed. However, they reported a maximum spread of 20° to 30°C in M_s, while the authors find that M_s in small particles may be at least 176°C lower than in bulk specimens of the same composition. The greater effect found in the present investigation is probably due to the smaller size of the particles and to the authors' method of preparation which was solidification of liquid droplets in hydrogen (Machlin and Cohen's particles were filings).

Machlin and Cohen did not relate the probability p of burst formation to particle diameter D. The authors have found that the dependence of p on D can be described by the relation $p \propto D^n$ where $2 \leq n \leq 3$.

Machlin and Cohen concluded that the nucleation of martensite in Fe-Ni alloys is catalyzed by structural heterogeneities (strained regions) and that the catalytic potency of these heterogeneities is somewhat variable. To explain the present results, the authors have to assume a much wider variability of catalytic potency than supposed by Machlin and Cohen and that homogeneous nucleation of martensite in the 30.2 pct Ni alloy is not perceptible at any temperature ≥ -196°C. Further, there is some evidence indicating that compositional, as well as structural, heterogeneities may play an important role in the nucleation of martensite.

The authors' results and those of Machlin and Cohen are entirely consistent with the general theory of martensite nucleation advanced by Fisher, Hollomon, and Turnbull. This theory was originally applied to the problem of nucleation of martensite in structurally perfect austenite crystals. Fisher and Turnbull[15] and Hollomon and Turnbull[16] have extended the application of the theory to the formal description of the probability of martensite nucleation in structurally imperfect crystals. The theory[16] predicts that the undercooling required for a perceptible frequency of martensite nucleation may be at least 100°C less in the vicinity of a dislocation than in a structurally perfect crystal element.

Machlin and Cohen preferred to describe their results in terms of their *reaction path* theory of martensite nucleation. This theory was criticized by Hollomon and Turnbull primarily because of its formal incompleteness and because, when taken literally, it seems to predict that the volume and free energy of the martensite nucleus is zero. For these reasons, the authors reject the Machlin and Cohen theory but with the recognition that they have made an important contribution to the understanding of the austenite-martensite kinetics by demonstrating the importance of heterogeneities in martensite nucleation.

It was shown by Machlin and Cohen that a small amount of martensite (< ½ pct) was formed in bulk specimens prior to the burst. In these experiments, no evidence of preburst martensite was found, but the authors could not detect less than ½ pct with their methods. However, the formation or nonformation of a small amount of preburst martensite is not considered significant to the current interpretation. If an Fe-Ni particle contains < ½ pct martensite at −196°C and transforms to 80 pct martensite upon the introduction of the proper nucleus, the interesting and significant question, in the authors' opinion, is why it is necessary to undercool so drastically in order to form the proper nucleus in the >99.5 pct austenitic portion of the specimen.

The explanation for burst transformation set forth by Machlin and Cohen utilized the preburst martensite as the source of strain embryo regions which nucleate martensite at a later time or lower temperature in a sudden cataclysmic fashion. The reason given for nonburst transformation in alloys other than Fe-Ni was that the cooperative effect (one martensite platelet relieving the strain of another) was less in systems having a {225} habit than those having a {259} habit (Fe-Ni alloy).

The authors' explanation of burst transformation in Fe-Ni alloys vs nonburst in most other alloys is that Fe-Ni alloys are comparatively free of extraneous heterogeneities that may be sources of internal strain and the austenite must be *supercooled* further below the equilibrium temperature before nucleation can occur on a less potent site. Cataclysmic formation of more martensite plates then occurs because of the excess free energy available at the temperature of nucleation. The observance of a liquid phase superheating effect on subsequent burst temperature supports the extraneous heterogeneity postulate.

Conclusions

The following conclusions may be drawn from the experimental findings of the present investigation.

1—The first measurable quantity of martensite (> ½ pct) forming in a particle occurs as a burst. The burst temperature in different particles of the same size and composition may vary widely. In some particles, martensite does not form even on quenching to a temperature as low as −196°C. These particles undergo a suppression of 176°C in the temperature of onset of transformation as compared to polycrystalline (bulk) alloy of the same composition.

2—The relative number of particles that undergo transformation to martensite on quenching to a given temperature is proportional to diameter squared or cubed.

3—Once transformation is initiated in a particle, it proceeds within a small temperature interval to an amount characteristic of all transformed particles of that temperature, independent of particle size.

4—Grain boundaries exert no accelerating effect on the initiation of martensite in the powders investigated.

5—The results of a critical experiment support a hypothesis that martensite is nucleated at strain sites caused by extraneous heterogeneities. Structure imperfections probably cause additional nucleation of martensite.

6—Burst phenomenon in Fe-Ni alloys can be reconciled with nonburst transformation in most other alloys by postulating that all ferrous alloys contain heterogeneous nucleation sites, but those in Fe-Ni alloys are fewer and less potent. With Fe-Ni alloys, the austenite must be supercooled to a temperature at which nucleation can occur on the relatively ineffective sites present. The excess free

energy then permits immediate transformation to a large extent in the grain having the nucleus and in neighboring grains.

Acknowledgments

We are pleased to acknowledge the assistance of Beulah Decker in helpful discussions on the X-ray method of phase determination and of D. S. Hallgren for assistance in the X-ray determinations. We thank L. T. Piekarski for many valuable suggestions concerning the material preparation and G. G. Palmer, General Electric Co. Electronics Park, for making available his unpublished results on the NiO-Fe_2O_3 equilibrium diagram.

Discussion of this paper, if any, will appear in JOURNAL OF METALS, November 1956, and in AIME Metals Branch *Transactions*, Vol. **206**, 1956.

References

[1] J. C. Fisher: Eutectoid Decomposition. *Thermodynamics in Physical Metallurgy* ASM (October 1949) p. 201.
[2] J. C. Fisher, J. H. Hollomon, and D. Turnbull: Kinetics of the Austenite-Martensite Transformation. *Trans.* AIME (1949) **185**, p. 691; JOURNAL OF METALS (October 1949).
[3] J. C. Fisher: Martensite Nucleation in Substitutional Iron Alloys. *Trans.* AIME (1953) **197**, p. 918; JOURNAL OF METALS (July 1953).
[4] F. W. Jones and W. I. Pumphrey: Free Energy and Metastable States in the Iron-Nickel and Iron-Manganese Systems. *Journal* Iron and Steel Inst. (1949) **163**, p. 121.
[5] R. E. Cech and J. H. Hollomon: Rate of Formation of Isothermal Martensite in Fe-Ni-Mn Alloy. *Trans.* AIME (1953) **197**, p. 685; JOURNAL OF METALS (May 1953).
[6] G. V. Kurdjumov and O. P. Maksimova: Work Required in the Formation of Martensite Nuclei. *Doklady Akademii Nauk SSSR* (1950) **73**, No. 1, p. 95.
[7] J. C. Fisher: Application of Nucleation Theory to Isothermal Martensite. *Acta Metallurgica* (1953) **1**, No. 1, p. 32.
[8] E. S. Machlin and M. Cohen: Burst Phenomenon in the Martensitic Transformation. *Trans.* AIME (1951) **191**, p. 746; JOURNAL OF METALS (September 1951).
[9] J. E. Burke: Some Factors Affecting the Rate of Grain Growth in Metals. *Trans.* AIME (1949) **180**, p. 73; METALS TECHNOLOGY (October 1948).
[10] V. C. Wilson and L. T. Piekarski: Studies on Maximum Permeability of Nickel-Zinc Spinels. Unpublished.
[11] L. T. Piekarski and E. F. Fullam: Unpublished research.
[12] G. G. Palmer: Phase Behavior in Nickel Ferrites. *Eighteenth Symposium on Ceramic Dielectrics* Rutgers University (March 1954).
[13] P. A. Ross: A New Method of Spectroscopy for Faint X Radiation. *Journal* Optical Soc. of America (1928) **16**, p. 433.
[14] P. Kirkpatrick: On the Theory and Use of Ross Filters. *Review of Scientific Instruments* (1939) **10**, p. 186.
[15] B. Averbach and M. Cohen: X-ray Determination of Retained Austenite by Integrated Intensities. *Trans.* AIME (1948) **176**, p. 401; METALS TECHNOLOGY (February 1948).
[16] M. Hansen: *Aufbau der Zweistofflegierungen.* (1936) p. 697. Berlin. J. Springer Co.
[17] R. Buehl and J. Wulff: A Simple Magnetic Apparatus for Phase Transformation Studies of Ferrous Alloys. *Review of Scientific Instruments* (1938) **9**, p. 224.
[18] J. C. Fisher and D. Turnbull: Influence of Stress on Martensite Nucleation. *Acta Metallurgica* (1953) **1**, p. 310.
[19] J. H. Hollomon and D. Turnbull: *Progress in Metal Physics.* (1953) **4**, pp. 333-388. London. Pergamon Press.

Thorium-Columbium and Thorium-Titanium Alloy Systems

On the basis of data obtained from microscopic examination, melting observations, cooling curves, X-ray analyses, and resistance measurements, phase diagrams have been proposed for the Th-Cb and Th-Ti alloy systems. Both are simple eutectic systems and have no terminal solid solubility or intermediate phases. The eutectic between thorium and columbium occurs at a composition of about 8 wt pct Cb and a temperature of 1435°C. The Th-Ti eutectic occurs at 1190°C at the composition 12 wt pct Ti. No change was observed in the transformation temperature of thorium in either system or in the titanium transformation.

by O. N. Carlson, J. M. Dickinson, H. E. Lunt, and H. A. Wilhelm

RECENT study of thorium and its alloys has been promoted because of the possibility of employing this metal in nuclear reactors. Their corrosion resistant properties, nuclear characteristics, and high melting points put columbium and titanium among the many metals being employed in the study of thorium alloys. Since a knowledge of the phase relationships would be important in the application of such an alloy, investigations were undertaken to propose phase diagrams for the Th-Cb and Th-Ti systems.

Experimental Procedures

Thorium metal sponge was specially prepared for use in this investigation. Carbon in a quantity less than 0.04 wt pct was the principal impurity. There was also less than 0.01 pct each of iron, calcium, zinc, aluminum, and nitrogen in the thorium.

Columbium, both as a powder and sheet metal, was obtained from the Fansteel Metallurgical Corp. The manufacturer's specifications indicated that the metal contains less than 1 wt pct total impurities. An analysis of the metal showed approximately 0.18 pct C in the powder and less than 0.05 pct C in the sheet. The titanium used was commercial sponge, reported to be 99.5 pct Ti. An analysis showed that this metal contained 0.2 pct Fe.

Preparation of Alloys—Since the metals used in this investigation are reactive and might become contaminated on melting in a refractory crucible, the alloys were prepared by arc melting. The titanium sponge was employed in the form of small lumps while the columbium additions were made either as pressed pellets of powder or as clippings from sheet. The alloying material and the thorium sponge were melted together under argon in conventional arc melting equipment employing a tungsten electrode and a water cooled copper crucible.

O. N. CARLSON, J. M. DICKINSON, H. E. LUNT, and H. A. WILHELM are associated with Ames Laboratory, AEC, Iowa State College, Ames, Iowa.

Discussion of this paper, TP 4022E, may be sent, 2 copies, to AIME by Apr. 1, 1956. Manuscript, Dec. 18, 1954. Philadelphia Meeting, October 1955.

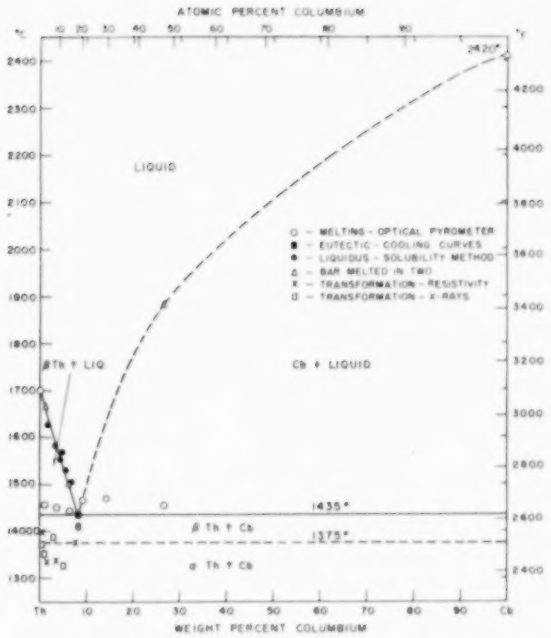

Fig. 1—Diagram has been proposed for the Th-Cb system and shows that thorium and columbium form a simple eutectic system with the eutectic in the high thorium region.

Each alloy was remelted three or four times and inverted after each melting to obtain complete mixing. The arc melted alloys were given a homogenization treatment at 1050°C for 100 hr in vacuo.

The desired compositions of the alloys could be obtained merely by weighing the materials for the charge accurately, since there was very little change in weight as a result of melting. In an alloy where the exact composition was of importance, a chemical analysis was also obtained on the alloy. In these cases the chemical analysis agreed with the intended composition within the limits of error of the analytical procedure.

Metallography—Since most of the alloys were quite soft, special precautions had to be taken in the grinding and polishing operations. The grinding operations were performed on silicon carbide papers lubricated with either kerosene or water. The alloys were polished first on a Microcloth-covered wheel using Linde A polishing compound. With Th-Cb alloys this was followed by an electrolytic polish in 3 normal HNO_3 containing 1 pct KF at a current density of 1 amp per sq cm. Th-Cb alloys were etched in this same electrolyte using a current density of about 100 ma per sq cm. Alloys containing more than 90 pct Cb were etched by immersion in a bath of concentrated HNO_3 containing 5 pct HF.

Two different etchants were used for the Th-Ti alloys. The thorium-rich alloys were etched by immersion in a solution of 10 pct HF in ethanol, whereas a mixture of equal volumes of HNO_3, H_3PO_4 and glycerol containing 5 pct HF was used with the titanium-rich specimens.

Determination of Melting Range—The solidus was determined for each of the alloy systems by observing the temperatures at which melting of the alloys began through a Pyrex window. An optical pyrometer was employed to make temperature readings in a small diameter hole drilled in the alloy specimen. The sample in bar form was clamped between two water cooled electrodes and then heated by its own electrical resistance and a high current. During the heating the temperature in the hole was continuously observed until melting was evident. This determination was carried out under a high vacuum. The temperature at which the liquid was first observed on heating was corrected for absorption by the window to give the solidus temperature for the alloy composition.

Early exploratory work indicated that both alloy systems had single eutectics. After locating roughly the temperature and composition of each of these eutectics, a solubility method was used to determine the liquidus curves for both systems. The high current apparatus used in the solidus determination was converted to a resistance-type tube furnace by installing a thin walled tantalum tube heater between the electrodes. An alloy of composition corresponding to the eutectic was placed in a thick walled crucible prepared from one of the pure constituents. This combination was then heated in the tantalum tube furnace to the desired temperature where it was held to react and come to equilibrium. After rapid cooling from this temperature, samples

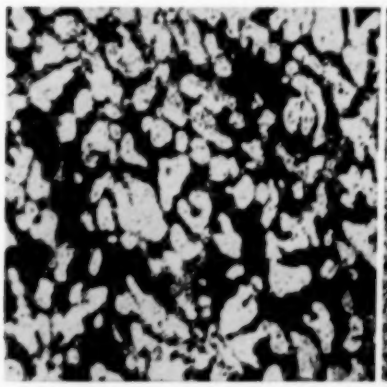

Fig. 2—Micrograph of 3.9 pct Cb alloy shows primary thorium (light) in eutectic matrix. Sample was etched electrolytically in HNO_3-KF bath. X250. Area reduced approximately 10 pct for reproduction.

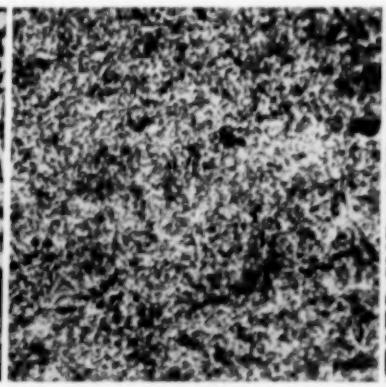

Fig. 3—Micrograph shows 8.0 pct Cb alloy annealed at 1100°C for 8 hr. Eutectic composition is partially spheroidized. Sample was electrolytically etched in HNO_3-KF bath. X500. Area reduced approximately 10 pct for reproduction.

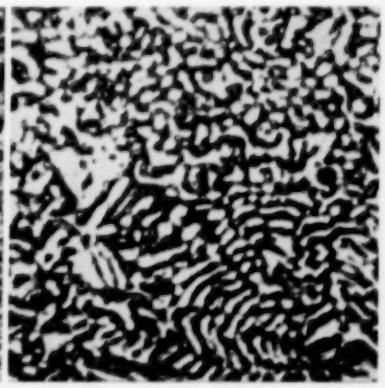

Fig. 4—Micrograph of 59.8 pct Cb alloy, as-arc melted, shows columbium dendrites (light) and eutectic (dark). Sample was electrolytically etched in HNO_3-KF bath. X250. Area reduced approximately 10 pct for reproduction.

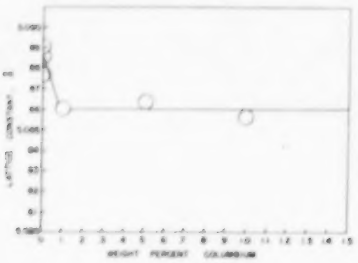

Fig. 5 — Diagram shows the effect of columbium additions on the lattice constant of thorium.

for chemical analysis were drilled from that portion which had been molten. The analysis gave the solubility of the crucible component in the liquid phase at the specified temperature. This corresponds to a point on the liquidus curve.

A number of alloys were also investigated by electrical resistivity measurements, X-ray diffraction techniques, and heating and cooling curves.

Experimental Results

The phase diagrams proposed for the Th-Cb and Th-Ti systems have been constructed on the basis of data from melting experiments, thermal analyses, X-ray diffraction patterns, and metallographic examinations. Both systems are of the simple eutectic type with little or no solid solubility and no intermediate phases.

Th-Cb System—As can be seen from the proposed diagram shown in Fig. 1, thorium and columbium form a simple eutectic system with the eutectic in the high thorium region. The composition of the eutectic was located by microscopic examination. A 3.9 pct Cb alloy shows typical structures of alloys containing primary thorium in a eutectic matrix as can be seen in Fig. 2. An 8.0 pct Cb alloy, shown at a higher magnification, Fig. 3, contains essentially all eutectic and is considered to be the eutectic composition. Fig. 4 is a micrograph of a 59.8 pct Cb alloy showing the typical structure of the alloys that contain primary dendrites of columbium in a eutectic matrix. Microscopic examinations of as-arc melted alloys containing 1.4, 5.8, 6.3, 7.7, 9.0, 9.4, 12.6, 25.5, 52.2, 72, 95, and 99 pct Cb are in agreement with these observations. In addition, the 5.8, 6.3, 9.4, 25.5, and 52.2 pct Cb alloys were examined microscopically after annealing at 1100°C for 300 hr followed by annealing treatments at 1285° to 1350°C for 2 hr. The only change observed in any of these alloys was a coarsening of the eutectic.

X-ray diffraction studies confirmed these observations and interpretations. A powder specimen of a 52.2 pct Cb alloy was prepared by taking filings from the alloy and annealing the filings for 113 hr at 600°C in an evacuated quartz capillary. Powder patterns were taken using a Debye-Scherrer powder camera. α thorium and columbium were identified as the two phases present in this alloy. On the basis of X-ray phase identification and microstructures, it is apparent that the alloy system is a eutectic-type system with no intermediate phases.

Values for the eutectic temperature were determined by thermocouple, optical pyrometer, and electrical resistivity measurements. Repeated heating and cooling curves on the 8 pct Cb alloy using a Pt—Pt-13 pct Rh thermocouple gave a small but reproducible thermal arrest at 1435±7°C. Melting temperatures obtained by the optical pyrometer method on this and other alloys are in good agreement with the value for that of the eutectic obtained by cooling curves, but have a tendency to be slightly higher. These data have been plotted in Fig. 1. Electrical resistivity measurements gave a value of about 1435°C for the eutectic temperature. After an evaluation of the data obtained by the different methods employed, a value of 1435°C has been designated as this eutectic temperature.

The thorium liquidus data were obtained primarily from solubility measurements at elevated temperatures as has been described in the preceding section. These data, when plotted as shown in Fig. 1, fall roughly on a straight line between the thorium melting point and the eutectic point. Several observations were made concerning the liquidus curves incidental to the solidus determinations by the optical pyrometer method. In three cases it was possible to get an approximate value of the temperature of the bar when it melted in two. These temperatures have been taken as an indication of the temperature at which melting is nearly complete, corresponding roughly to a point on the liquidus. As can be seen in Fig. 1, two of these values fall surprisingly close to the thorium liquidus obtained by the solubility method.

X-ray diffraction methods were employed to determine the extent of solid solubility between thorium and columbium at room temperature. No measurable change was observed in the lattice constant of columbium (a_o = 3.301Å) upon the addition of thorium, which is taken as evidence that a negligible amount of thorium is dissolved in columbium at lower temperatures. However, the X-ray data on columbium in α thorium could be interpreted as evidence for a very limited solubility. Fig. 5 is a curve representing a plot of observed lattice constants of thorium with increasing columbium content. There is a discontinuity in this curve occurring at a columbium concentration of about 0.1 pct. The

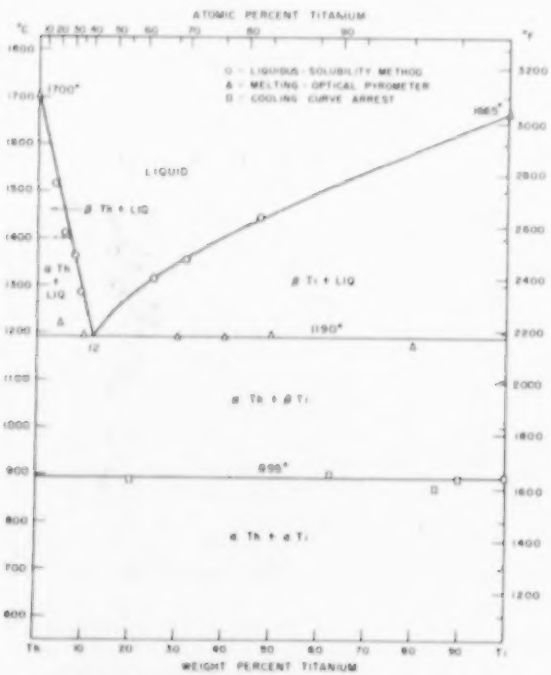

Fig. 6—Diagram which has been proposed for the Th-Ti system is shown.

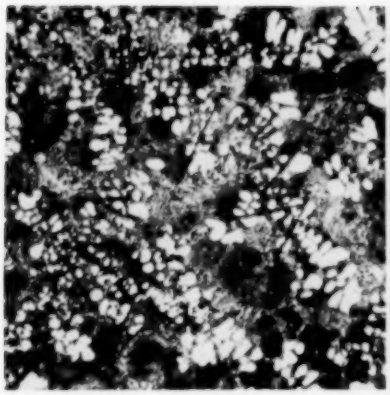

Fig. 7—Micrograph of 10 pct Ti alloy, as-arc melted, shows primary thorium (light) in fine eutectic matrix. Sample was etched with 10 pct HF in ethanol. X250. Area reduced approximately 10 pct for reproduction.

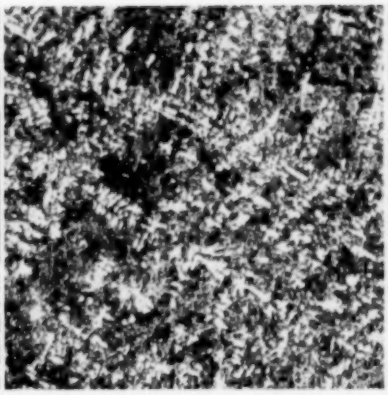

Fig. 8—Micrograph of 20 pct Ti alloy, as-arc melted, shows primary titanium (light) in eutectic matrix. Sample was etched with 10 pct HF in ethanol. X250. Area reduced approximately 10 pct for reproduction.

Fig. 9—Micrograph of 60 pct Ti alloy, as-arc melted, shows primary titanium in eutectic matrix. Sample was etched with HNO_3-H_3PO_4-HF in glycerol. X250. Area reduced approximately 10 pct for reproduction.

solubility limit of columbium in α thorium at lower temperatures is therefore not greater than 0.1 pct.

Chiotti[1] has reported an allotropic form of thorium that exists above 1400±25°C. This high temperature form is body-centered-cubic and has a lattice constant of about 4.12A at that temperature. The effects of impurities on the transformation are not fully known; however, carbon has been shown to raise this transformation temperature markedly. Since the actual temperature at which the transformation occurs in high purity thorium is not accurately known, it is very difficult to establish with any degree of certainty the effects of columbium on the transformation temperature. Electrical resistivity vs temperature curves were obtained on several thorium-rich alloys and, as can be seen from the points plotted in Fig. 1, the temperatures at which breaks were observed in the resistivity curve were badly scattered between 1335° and 1385°C. However, the resistivity breaks observed in Th-Cb alloys all occur at a somewhat lower temperature than that observed for thorium.

High temperature X-ray diffraction data on this transformation were obtained for several thorium-rich alloys using an X-ray camera designed by Chiotti.[2] This camera consists of a specimen holder and furnace which are used as auxiliary equipment with a Norelco high angle goniometer. The apparatus can be used for obtaining X-ray diffraction patterns at temperatures up to 1600°C in vacuo.

The data obtained with this equipment have been plotted in Fig. 1. There is a wide variation in the values observed for the transformation temperature but, as with the resistance measurements, the X-ray data indicate that the addition of columbium lowers the transformation temperature of thorium slightly. The transformation temperature is shown as 1375°C in the proposed diagram. That this lowering is actually due to the solubility of columbium in β thorium rather than to some secondary effect is questionable.

Th-Ti System—The diagram proposed for the Th-Ti system is shown in Fig. 6. The eutectic nature of the system was ascertained from the microscopic investigation of alloys at approximately 10 pct intervals across the system. Fig. 7 is a micrograph of a 10 pct Ti alloy and shows primary dendrites of thorium in a eutectic matrix. As can be seen in Fig. 8, a 20 pct Ti alloy contains primary titanium and eutectic as does a 60 pct Ti alloy, Fig. 9. Microscopic examination of alloys of other compositions across the system revealed structures that were consistent with these observations. In addition, an X-ray powder pattern of the 60 pct Ti alloy, which had been annealed at 1050°C for 100 hr, was used to identify the phases present as α thorium and α titanium. These data are considered as evidence that a single eutectic exists between thorium and titanium and that there are no intermediate phases in the system.

The composition of the eutectic has been located by metallographic methods. An 11.6 and a 12.7 pct Ti alloy appear to lie very close to the eutectic point. A small amount of primary thorium can be observed in the 11.6 pct alloy, see Fig. 10, whereas primary dendrites appearing in the microstructure of a 12.7 pct alloy have been interpreted as those of titanium. The eutectic composition has been placed at 12.0 pct Ti, between these two compositions.

The eutectic temperature of 1190°C was determined from optical pyrometer measurements of the melting temperatures of several alloys. These data have been plotted in Fig. 6.

Both the thorium liquidus and the titanium liquidus were determined experimentally by the

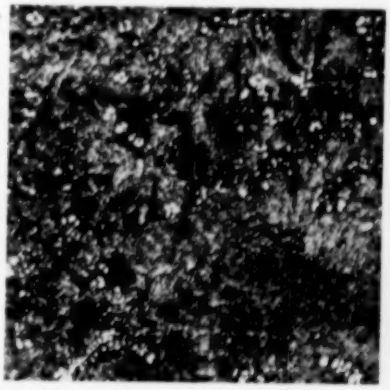

Fig. 10 — Micrograph of 11.6 pct Ti alloy, as-arc melted, shows small dendrites of primary thorium in eutectic matrix. Sample was etched with 10 pct HF in ethanol. X250. Area reduced approximately 10 pct for reproduction.

solubility method described in an earlier section of this paper. They were found to be smooth curves with no points of inflection. Chemical analyses were obtained on samples from the various liquidus determinations and appear as plotted points in Fig. 6. The melting point of the commercial sponge titanium was 1610°C as determined by the optical pyrometer method. The melting point of crystal bar titanium was also determined and found to be 1665°C. The latter value has been used in the construction of Fig. 6.

Table I. Lattice Constants of Th-Ti Alloys

Alloy Composition, Wt Pct	Lattice Constants in A*	
	a_0	c_0
Th	5.0874	—
Th-5 pct Ti	5.0834	—
Th-10 pct Ti	5.0839	—
Crystal bar Ti[5]	2.9504	4.6833
Commercial Ti	2.952	4.702
Ti-10 pct Th	3.952	4.696
Ti-20 pct Th	2.953	4.693

* The values listed are held to be reproducible to ±0.0005A for the thorium constants and ±0.001 for the titanium constants.

No investigation was made of the effect of titanium upon the temperature of the thorium transformation. However, there is no microscopic evidence for any appreciable solid solubility at the 1400°C transformation temperature, indicating that the transformation is relatively unaffected.

The titanium transformation in the alloys was studied by cooling curve methods employing a differential thermocouple. Commercial titanium was found to transform on cooling at 894°C, slightly higher than the 885°C value reported for crystal bar titanium.[5] As can be seen from the data plotted in Fig. 6, no significant change in this transformation temperature was observed in the Th-Ti alloys.

The extent of solid solubility was investigated by X-ray diffraction methods. Diffraction patterns were obtained on filings of annealed alloys using a Debye-Scherrer powder camera. Errors due to film shrinkage were corrected for by means of a film calibration device[6] and the parameters were calculated by the method of least squares. The results are summarized in Table I. The thorium lattice constants for the 5 and 10 pct Ti alloys, both of which are in the two phase region, are in good agreement with one another but differ from the value for pure thorium by a small but real amount. If the assumption is made that this change in lattice constant is attributable to titanium in solid solution and, further, that the solution approximately obeys Vegard's law,[7] then the extent of solid solubility corresponding to the observed decrease may be calculated. A calculation based on this assumption indicated a maximum solubility of 0.087 pct Ti. It was therefore concluded that the solubility of titanium is not greater than 0.1 pct in α thorium at room temperature. Microscopic evidence is in agreement with this.

It will be noted from Table I that there is considerable variation in the lattice constants, especially in the c_0 values for the unalloyed titanium metal. This variation is an indication of the presence of influential impurities in one or both titanium specimens. There is a small but measurable decrease in the c_0 value of the commercial titanium upon the addition of thorium. Since the a_0 value is unaffected by thorium additions and the change in c_0 is only 0.006A, the solubility of thorium in α titanium must be, at most, a very small amount.

Discussion of Results

No solid solution regions are shown in either of the proposed diagrams although X-ray evidence in both systems indicates the possibility of some very limited solid solubility. The small decrease in the thorium lattice constant by the addition of either columbium or titanium and the decrease in the c_0 value for titanium may both be the result of a scavenging action. Carbon dissolved in thorium metal increases the lattice constant of thorium quite appreciably. Should columbium or titanium precipitate the carbon normally dissolved in the thorium metal as an insoluble carbide, there would be a decrease in the thorium lattice. Similarly, oxygen dissolved in titanium expands the lattice. The addition of thorium might result in removal of the oxygen from solid solution in the titanium and thus decrease this lattice constant. The observed changes in lattice constants are sufficiently small to be accounted for by the possible scavenging action. Therefore, solid solubilities at room temperature are quite likely negligible as indicated in the diagrams.

The type of alloying observed for both systems might well have been predicted from an application of the Hume-Rothery rules of alloying.[7] The atomic radii of thorium and titanium differ by about 22 pct while thorium and columbium differ by 19 pct. Since extensive solid solubility does not occur between metals differing in size by greater than 15 pct, limited solid solubility, at most, would be expected. Also, the greater the difference in electronegativity between two metals, the greater the tendency to form compounds. Since there is no great difference between the electronegativities of thorium, titanium, and columbium the absence of intermediate phases is not too surprising.

Acknowledgment

The authors wish to thank the analytical group of the Ames Laboratory under the direction of C. V. Banks and especially B. LaMont for the chemical analyses.

Discussion of this paper, if any, will appear in JOURNAL OF METALS, November 1956, and in AIME Metals Branch *Transactions*, Vol. **206**, 1956.

References

[1] P. Chiotti: High Temperature Crystal Structure of Thorium. *Journal* Electrochemistry Soc. (1954) **101**, p. 567.

[2] P. Chiotti: Adaptation of a Geiger Counter X-ray Diffractometer for High Temperature Investigations. *Review of Scientific Instruments* (1954) **25**, p. 683.

[3] R. J. Van Thyne, H. D. Kessler, and M. Hansen: The Systems Titanium-Chromium and Titanium-Iron. *Trans.* ASM (1952) **44**, p. 974.

[4] M. H. Jellinek: Non-Uniform Shrinkage of X-ray Films. *Review of Scientific Instruments* (1949) **20**, p. 368.

[5] H. T. Clark, Jr.: The Lattice Parameters of High Purity Alpha Titanium and the Effects of Oxygen and Nitrogen on Them. *Trans.* AIME (1949) **185**, p. 588; JOURNAL OF METALS (September 1949).

[6] C. S. Barrett: *Structure of Metals.* (1943) p. 202. New York and London. McGraw-Hill Book Co. Inc.

[7] W. Hume-Rothery: *The Structures of Metals and Alloys.* (1936) London. Institute of Metals.

Comparison of Techniques in a Study Of Zinc Self-Diffusion

Self-diffusion in zinc has been used as an instrument for comparison of the absorption and sectioning techniques as a means of studying diffusion. Single crystal as well as polycrystal samples were used and the temperature range of diffusion extended from 200° to 415°C. For temperatures above 200°C, the data indicate that the results obtained from the absorption technique agree with those obtained from the sectioning technique. The effect on the values of the diffusion coefficient of electroplating vs evaporation as a means of applying the tracer was investigated and no significant difference observed. It was found that an excess or deficiency of tracer did not materially affect the results obtained from the sectioning technique, but invariably caused errors with the absorption technique.

by F. E. Jaumot, Jr. and R. L. Smith

NEARLY all self-diffusion experiments and many alloy diffusion experiments have employed radioisotopes as the instrument for following the diffusion. Of the various techniques in which radioisotopes are applicable, the two most widely used are the sectioning and absorption techniques. In the former, the diffusion coefficient is obtained from a curve of log concentration vs the square of the mean penetration depth. In the latter, the diffusion coefficient is calculated from a knowledge of the decrease in activity at the surface after diffusion. In spite of the importance of knowing the reliability of the diffusion data and the widespread use of these two techniques, they had not been directly compared experimentally on the same samples. Thus, such a comparison was worthwhile.

The specific system chosen for this comparison was the self-diffusion of zinc, since the metal was readily obtainable in high purity, single crystals were easily grown, and the anisotropic features of the diffusion added an additional factor of interest to the comparison. Self-diffusion in both single and polycrystals was investigated, since the possibility existed that grain boundaries and grain boundary diffusion might produce different effects for the different techniques. Also, the effects of electroplating vs evaporation as a means of applying the radioactive tracer, and the effects of applying an excess or deficiency of tracer material were studied.

The general experimental procedures and the mathematical analyses of both techniques have been described previously in some detail,[1-10] and only those points essential to an understanding of the present work will be discussed here.

The mathematical analysis of the sectioning data requires only a knowledge of the solution of Fick's equation.

$$C = \frac{C_o}{\sqrt{\pi Dt}} e^{-x^2/4Dt} \qquad [1]$$

where C_o is the initial concentration, C is the concentration at depth x, D is the diffusion coefficient, and t is the time. Thus, D is obtainable directly from the slope of ln C vs $(x)^2$.

F. E. JAUMOT, JR. and R. L. SMITH, Members AIME, are associated with Solid State Physics Div., Franklin Institute Laboratories for Research and Development, Philadelphia.

Discussion of this paper, TP 4138E, may be sent, 2 copies, to AIME by Apr. 1, 1956. Manuscript, Dec. 21, 1954.

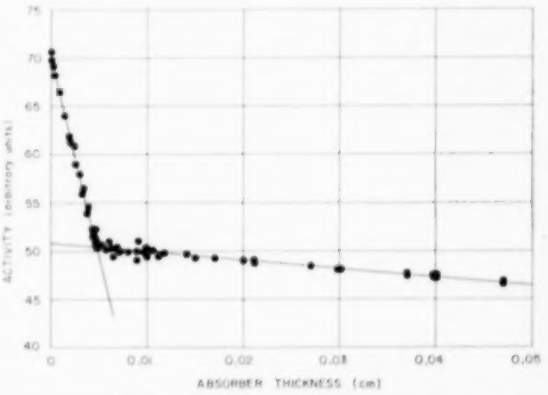

Fig. 1—Typical curve for absorption of the radiation from Zn^{65} by zinc is charted.

In the absorption technique, the fraction, F, of counts remaining after diffusion can be related[4-10] to the diffusion coefficient through

$$F = e^{z}\left[1 - \frac{2}{\sqrt{\pi}}\int_{o}^{\sqrt{z}} e^{-y^2}\,dy\right] \qquad [2]$$

where

$$z = \mu^2 Dt \qquad [3]$$

and μ is the absorption coefficient of the solvent metal for the radiation from the solute. Having obtained F from the experiment, the value of z can be read from a plot of F vs ln z, and D can then be calculated if μ is known. The necessity of knowing the absorption coefficient causes most of the criticism of the absorption technique. It is very difficult to measure μ accurately under the conditions existing in the diffusion experiment, but it is absolutely necessary, as will be indicated briefly later. Portions of this problem have been discussed in detail elsewhere.[10]

The difficulties involved in the measurement of the absorption coefficient arise from three principle factors: the physical characteristics of the absorber, the geometry, and complex radiation spectra. The first two are heavily dependent upon the third. If

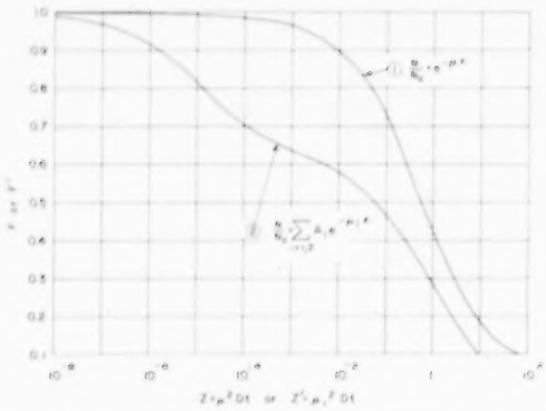

Fig. 2—Theoretical curves of fraction of counts remaining after diffusion as a function of the parameter $Z = \mu^2 Dt$ are plotted.

β-rays are the principle radiation being detected, electroplated or evaporated films[2] rather than thin foils must be used in the determination of the absorption coefficient. In the present experiment, thin foils and evaporated and electroplated films all gave similar results for the complex absorption coefficient, principally because the fraction of positrons in the complex spectra is very small.

The problem of complex radiation did, however, occur in the present experiment, since zinc emits auger electrons, conversion electrons, positrons, X-rays, and γ rays.[15] When complex radiation is present, as it often is in artificial isotopes, it cannot be assumed that the absorption can be expressed by the usual exponential relation, $e^{-\mu x}$. For example, Fig. 1 gives a typical curve for the absorption of Zn^{65} radiation in zinc, as determined with the diffusion geometry. The usual equation, Eq. 2, no longer applies, since it is based on a simple absorption. Thus, one must modify the curve of F vs ln z to take the complex absorption into account. That this modification can be severe is illustrated in Fig. 2, where the curves of F vs ln z are plotted for the case of simple absorption and for the experimentally determined absorption of the present experiment. Although the F vs ln z curve is quite different from that for simple absorption, the present case is much simpler than one would expect from the complexity of the radiation involved, primarily because the penetration distance in zinc of auger and conversion electrons is negligible, the number of positrons is very small, and the thin window counter used counted only about 1 pct of the γ rays ejected.

Table I. Values of D_0 and Q Obtained from the Curves of ln D vs $1/T$

	Sectioning				Absorption
	Miller and Banks	Liu and Drickamer	Shirn et al.	Present Work	Present Work
$Q_{\perp}$, kcal per mol	30.4	19.6	21.8	22.0±0.3	22.0±2.1
$Q_{\parallel}$ kcal per mol	31	25.9	24.3	24.9±0.9	23.5±1.7
$D_{0\perp}$ cm² per sec	0.05	0.021	0.13	0.076	0.068
$D_{0\parallel}$ cm² per sec	0.09	1.60	0.58	0.39	0.12
Q (poly) kcal per mol				22.7±1.2	23.5±2.2
D_0 (poly) cm² per sec				0.19	0.11

Geometry is the most serious of all difficulties in the usual diffusion experiment, particularly when β-rays are involved, since in that case it is possible to get values of the activity at the surface, N, which are greater with absorbers than without them.[16] To overcome the uncertainties due to geometry, it is absolutely essential that the absorption coefficient, usually complex, used in the expression for F be determined experimentally, using geometries which are as closely as possible identical to the diffusion geometry. Berkowitz[16] has shown that this procedure will generally result in an expression for the total activity at the surface

$$N/N_0 = \sum_{i=1}^{n} A_i e^{-\mu_i x} \qquad [4]$$

where N_0 is the initial activity, without absorbers, and A_i is a geometrical factor. It can be shown[16] that if $Z = \mu_1^2 Dt$,

$$F(Z) = \sum_{i=1}^{n} A_i G\left(\frac{\mu_i^2}{\mu_1^2} Z\right) \qquad [5]$$

where

$$G(Z) = e^{z}\left[1 - \frac{2}{\sqrt{\pi}} \int_0^{\sqrt{z}} e^{-y^2}\, dy\right] . \qquad [6]$$

Here, μ_1 is generally taken to be the larger of the μ's in Eq. 4, but this is not required. Curve 2 of Fig. 2 was obtained from Eq. 5, using the data in Fig. 1.

Experimental Techniques

The technique used for the sectioning method was a standard one and has been described previously (see, for example, ref. 1). The only new feature was the use of a high precision jeweler's lathe which allowed removal of sections 0.0005 cm thick; thus, many more sections were obtained. One marked advantage of thin sections is the reduction in the possibility of unknowingly sectioning at an angle to the original diffusion interface. It is easy to see with the unaided eye whether or not the tool is removing material across the entire sample. Using $\frac{5}{8}$ in. diam samples one finds a maximum possible angle of error of about 3×10^{-5} radians.

The details of the absorption technique have been described in previous work.[1-16]

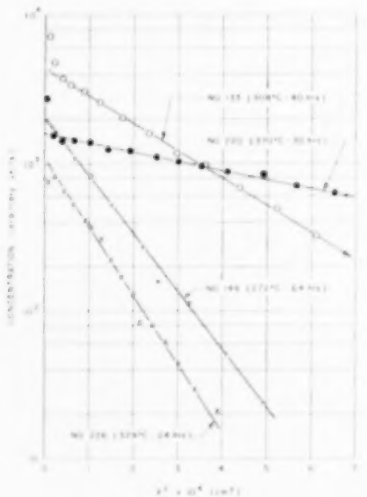

Fig. 3—Typical curves of concentration vs square of the penetration depth for diffusion in single crystals are plotted. In samples 133 and 149, diffusion was parallel to the c-axis; in samples 220 and 226, perpendicular to the c-axis.

Zinc used in the experiment was obtained from Belmont Smelting and Refining Co., and was 99.99+ pct pure. The single crystals were grown using a modified Bridgman method and the orientation of each sample determined by back-reflection Laue photographs. Samples with faces oriented parallel to the c-axis had a maximum deviation of 6° and those with faces perpendicular to the c-axis were oriented to within the accuracy of our measurements, about 1.5°. The polycrystal samples were prepared in three grain sizes: small, about 4 mm^2; medium, about 9 mm^2; and large, about 25 mm^2 by quenching, air cooling, and furnace cooling. A small amount of crystal growth occurred during the diffusion runs but there was no recrystallization. The other details of the preparation of the specimens, the method of electroplating and the plating solution were similar to those described by Shirn and co-workers.[1] Some samples were also coated with Zn^{65} by evaporation from a tungsten filament.

The specimens were placed in pairs, with active faces together, in evacuated Pyrex tubes for the diffusion anneals. Active faces need not be placed together for the sectioning technique, but for the absorption technique it is necessary to prevent evaporation from the faces of the sample. In fact, the absorption data is obtained by counting the samples in pairs so that any exchange in active material is compensated for. In a few cases, particularly at the higher temperatures, some evaporation did occur as evidenced by activity on the Pyrex capsules and, of course, these samples could not be used for absorption technique determinations. The specimens were annealed at temperatures ranging from 415° to 200°C for times ranging from 18 to 168 hr. A resistance furnace containing a large copper inertia block was used and the temperature controlled by a Celectray controller. The maximum temperature variation at the samples was about ±2°C.

After the diffusion anneal, and after the samples had been *counted* to obtain the necessary data for the absorption analysis, 30 to 100 mils were removed from the cylindrical surfaces of the samples to eliminate possible surface effects. Sections 0.5 to 1.5×10^{-4} cm thick were removed, carefully collected and weighed to determine their thickness more precisely, and their activity determined using standard techniques.[4]

Results

Diffusion runs were made at five temperatures from 200° to 415°C. At least six and as many as 18 samples with faces oriented parallel to the c-axis and six to 18 with faces oriented perpendicular to the c-axis were used at each temperature for the single crystal diffusion. For the polycrystal diffusion, 24 samples were used at each temperature.

Typical data for the logarithm of the concentration as a function of the square of the penetration depth for diffusion perpendicular and parallel to the c-axis are shown in Fig. 3. Fig. 4 shows similar curves for polycrystalline data, and indicates the number of sections it was possible to obtain. The arrows terminating the curves, in some cases, indicate that the curves extended to greater penetration depths. Curve 1S in Fig. 4 indicates that the first few points are abnormally low. This occurred only in a few cases and then only at the highest temperatures. Such behavior was not thoroughly investigated but it may be due to an evaporation effect.

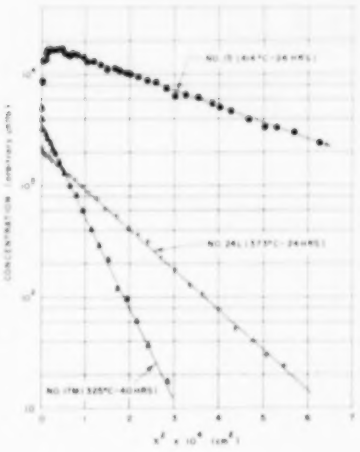

Fig. 4—Typical curves of concentration vs square of the penetration depth for diffusion in polycrystalline samples are plotted.

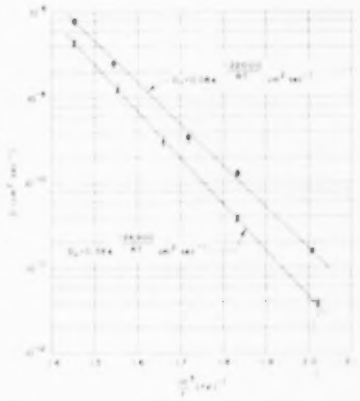

Fig. 5—Chart shows the dependence of D on $1/T$ for self-diffusion in single crystals of zinc, using the sectioning technique.

Values of the diffusion coefficient obtained from single crystal samples at the various temperatures are summarized in Figs. 5 and 6, where the logarithm of D is plotted against the reciprocal of the absolute temperature. Fig. 5 gives the data as obtained by the sectioning technique and Fig. 6 gives the results from the absorption technique. In all cases, the vertical lines give the spread in the data.

Fig. 7 gives the results for polycrystal diffusion obtained by the sectioning and absorption techniques.

All the data obey the usual exponential relation

$$D = D_o\, e^{-Q/RT} \qquad [7]$$

and the values of D_o and Q are summarized in Table I, for single and polycrystal diffusion.

Discussion

The errors involved in diffusion experiments are large and often difficult to estimate. These errors have been discussed in great detail. See, for example, refs. 1, 6, and 13. It is difficult to see how an error of less than 10 pct could be claimed for any given single value of D. At the same time, if a sufficient number of samples are used over an appreciable temperature range, and Eq. 7 is obeyed, it would seem reasonable that Q could be determined to within a few percent. On the other hand, the frequency factor, D_o, is very sensitive to variations in Q and an error of 50 pct is not considered unusual.

Table I includes the values of Q and D_o obtained by Shirn and co-workers,[1] Liu and Drickamer,[16] and by Miller and Banks.[2] All values for parallel diffu-

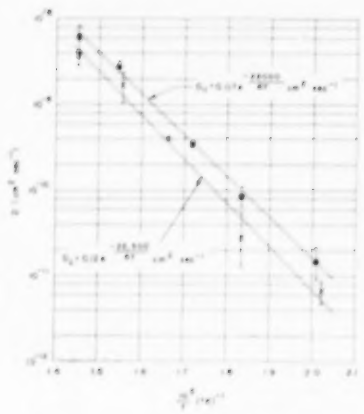

Fig. 6—Chart shows the dependence of D on $1/T$ for self-diffusion in single crystals of zinc, using the absorption technique.

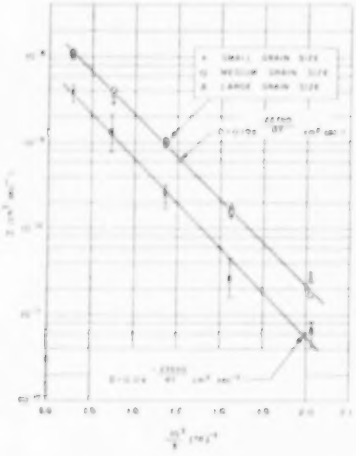

Fig. 7—Chart shows the dependence of D on $1/T$ for self-diffusion in polycrystalline samples of zinc. The upper curve represents the sectioning technique; the lower curve, the absorption technique.

sion are in reasonable agreement, but for perpendicular diffusion the present work is in good agreement only with Shirn, and in reasonable agreement with Liu and Drickamer. The discrepancy in Miller and Banks' results has been discussed previously[1] and will not be repeated here. Liu and Drickamer's results indicate a greater difference in the activation energies for parallel and perpendicular diffusion than found by Shirn or the authors (6.3 vs 2.5 and 2.9 kcal respectively). It would appear that their $Q_{\parallel}$ is somewhat low. When their data for $D_{\perp}$ vs $1/T$ are fitted by the method of least squares, the values $Q_{\perp} = 24.8$ kcal per mol and $D_{0\perp} = 0.66$ cm^2 per sec are found, which are in better agreement with Shirn and the present authors. Although the values obtained for Q and D_0 are in agreement with those of Shirn et al., the actual values of D are roughly a factor of two smaller. The most plausible explanation for this difference is a difference in the treatment of the surfaces. Birchenall and various coworkers have made a study of the effects of surface treatment. A publication which includes a discussion of this phenomenon (in connection with cobalt self-diffusion) is in preparation.[16]

If one considers only the values obtained by the sectioning method, the data indicate that the activation energy for polycrystal diffusion falls between the activation energies for parallel and perpendicular diffusion, as one might expect. Fig. 7, on the other hand, indicates that D is higher for every temperature for polycrystals than for either case of single crystals. Although the difference in values of D is within experimental error, the authors feel that it is a result of a real grain boundary effect.

It was mentioned that three grain sizes were used in the polycrystal diffusion. In Fig. 7, the different symbols represent the *mean* value of the diffusion coefficients for the different grain sizes. The spread in the data, which is not shown, is sufficiently large for each grain size to cover the average value for the other grain sizes. The average values alone indicate that for temperatures above 200°C there is no grain size effect. A similar result was obtained for the absorption technique, so that in Fig. 7 the mean values of D obtained from all grain sizes are plotted and the data spread indicated. It might be pointed out that the spread in the data from the sectioning technique was considerably less than that shown for the absorption method. At the same time, the overall spread in the polycrystal data is much larger than for single crystals. This is to be expected, entirely apart from a grain boundary effect, when there is anisotropy of diffusion.

Comparison of the Techniques

Figs. 5 and 6 and Table I indicate that the absorption technique gives quite good results for single crystal diffusion. Although it is believed that this is the first case of the two techniques having been compared using the same samples, there are data in the literature which allow other comparisons. These data are given in Table II. It is to be emphasized that, although these data were chosen because they represent some of the better diffusion work, they were obtained under different conditions at different temperatures and at different times. Except in the case of the data on gold and one determination for copper the agreement for the two techniques is reasonably good.

In a recent paper involving the diffusion of iron in wüstite and cobalt in cobaltous oxide these techniques were compared.[17] Although the results from the two techniques were comparable, in general, it was found that in the case of iron in wüstite below 850°C the absorption technique was inaccurate. However, Himmel et al.[18] obtained values for the diffusion of iron in wüstite below 850°C by the absorption technique which agree well with those obtained by Carter and Richardson[17] using the sectioning technique.

The results of other workers indicate that the conclusion, based on the present work, that the two techniques under consideration are capable of giving comparable results, may be quite generally valid.

Table II. A Comparison of Q and D_0 Values for Different Metals Obtained Using the Sectioning and Absorption Techniques

Metal	Technique	D_0 Cm^2 Sec^{-1}	Q Kcal per Mol^{-1}	Sample Type*	Temperature Range, °C	Reference
Au	Sectioning	9.8	62.9	P	800° to 1000°	3
	Absorption	2.1	50.3	P	800° to 1000°	4
Ag	Sectioning	0.724	45.5	S	650° to 950°	5†
	Sectioning	0.895	45.95	P	725° to 950°	6
	Absorption	0.895	45.95	S and P	500° to 900°	7
Cu	Sectioning	0.1	44.9	P	750° to 1000°	8‡
	Sectioning	0.1	45.1	S	800° to 1000°	9
	Sectioning	0.6	45.1	S	800° to 1000°	9
	Absorption	0.3	46.8	P	650° to 850°	10
	Absorption	11.0	57.2	P	750° to 950°	11

* P represents polycrystal, S, single crystal.
† These data actually represent the results of the combined data of all work on self-diffusion in silver.
‡ These data were obtained from the diffusion of gold in copper.

The authors believe that the extent to which this is true is directly proportional to the care exercised in the treatment of the absorption coefficient.

It is interesting that the data also show agreement between the values of D_o and Q, within experimental error, for polycrystal diffusion. There is no reason to assume that a grain boundary effect could lead to similar results for both techniques. That it does so to the extent indicated by the data is probably due to the smallness of the grain boundary effects at elevated temperatures which, if larger, would cause the curve ln C vs x^3 to deviate from a straight line, making a volume diffusion coefficient unobtainable. Also, the apparent agreement results partly because large errors are tolerated, particularly for the absorption technique.

Fig. 7 indicates that, although the values of D_o and Q obtained for diffusion in polycrystalline zinc by the two techniques agree within the possible error, the actual D values differ by a factor of three. This is in contrast to the single crystal data which yield very similar values of D for the two techniques. It is somewhat difficult to explain this polycrystal behavior; the lower values of D from the absorption technique mean that, experimentally, the surface activity observed was higher than the true value. This is subject to the assumption that the value of the complex absorption coefficient used was the correct one. The single crystal results indicate that it was. Therefore, the lower D values are most probably due to increased scattering (in the forward direction) of the radiation due to the grain boundaries.[2]

It is also interesting to note that the largest differences in the values of Q and D_o for the two techniques occur for diffusion perpendicular to the c-axis in single crystal samples. Also, the uncertainty in the values of Q and D_o as obtained from the sectioning technique are three times as great for perpendicular diffusion as for parallel. A similar effect was noted by Shirn,[1] and the present workers are inclined to agree that this may be a real effect.

The possible effects on the diffusion results of electroplating vs evaporation as a means of applying the tracer were also investigated. In no case was there any difference in the results. However, electroplating is preferred since the percentage of samples it is necessary to reject because of surface irregularities is lower and considerably less radioactive material is wasted.

The effects on the value of the diffusion coefficient of an initial excess or deficiency of tracer material were investigated and found to be negligible in the case of the sectioning technique, providing that sufficient diffusion had occurred. That is, only the first few points in the ln C vs x^2 curves are affected. However, the results from the absorption technique are strongly affected. An excess of tracer always gave a low value of D and a deficiency gave a high value, both by at least an order of magnitude in comparison with the *normal* absorption and sectioning data. What constitutes an excess or a deficiency of tracer material is not easily expressed in terms of thickness of the plated layer since specific activities of different batches of the same isotope may vary widely. However, it appears that for zinc (and previous results[12, 15] indicate that perhaps in general) the optimum activity, using a thin mica end window counter tube, is between 4,000 and 10,000 counts per min per sq cm of surface counted. Less than 1,000 is definitely a deficiency and more than 40,000 is excessive. In the present experiments our *deficiency* samples exhibited counts of between 300 and 2,000 per min per sq cm, and our *excess* samples, between 40,000 and 100,000.

Figs. 5 through 7 show that, in general, the spread in the data and consequently the probable error is greater for the absorption method. This is illustrated in detail in Fig. 8, where the maximum spread in the data for single crystal diffusion is compared for the two cases. It should be pointed out that some experiments making use of the absorption technique do not show large data spreads[12, 15] but, in fact, show deviations compatible with those from the sectioning technique. The maximum and minimum values of the activation energies given in the tables of Fig. 8 were obtained by drawing curves which had the maximum and minimum slopes but which could be included within the data spread of at least four of the five experimental points. The D_o's were then calculated using these values of Q. The *best* values were obtained by fitting the data by means of least squares.

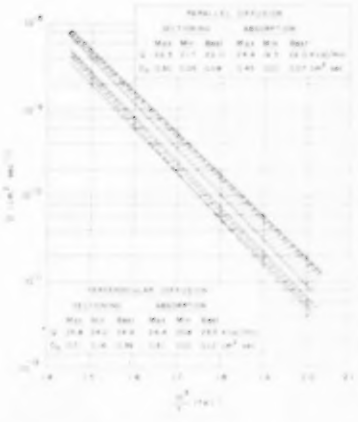

Fig. 8 — Maximum spread in the single crystal diffusion data is plotted. The solid lines bound the spread for the absorption technique; the dashed lines for the sectioning technique. The tables indicate the largest and smallest values of Q and D_o deducible from the data.

Conclusions

1—The absorption and sectioning techniques for determining self-diffusion coefficients in zinc yield comparable results, although there is a greater spread in data for the absorption method.

2—An excess or deficiency of tracer material is only seriously detrimental in the case of the absorption method.

3—There is apparently no appreciable difference in the amount of surface blocking whether the radioactive tracer is applied by electroplating or evaporating.

4—There is no significant grain size effect on diffusion in polycrystalline samples at temperatures above 200°C.

5—Self-diffusion parallel and perpendicular to the c-axis in zinc is probably best represented by the equations

$$D_{\parallel} = 0.08\, e^{-25{,}000/RT} \text{ cm}^2 \text{ per sec}$$
$$D_{\perp} = 0.39\, e^{-24{,}900/RT} \text{ cm}^2 \text{ per sec.}$$

Acknowledgments

The authors wish to express their appreciation to the U.S. AEC for their financial support of this work. The authors also wish to thank L. Arne for his aid in carrying out many of the experimental details, and F. C. Nix for his interest throughout the course of the work.

Discussion of this paper, if any, will appear in JOURNAL OF METALS, November 1956, and in AIME Metals Branch *Transactions*, Vol. **206**, 1956.

References

[1] G. A. Shirn, E. S. Wadja, and H. D. Huntingdon: *Acta Metallurgica* (1951) 1, p. 513.
[2] P. H. Miller and F. L. Banks: *Physical Review* (1942) 61, p. 648.
[3] A. M. Sagrubski: *Bulletin* Academy of Science, USSR (1937) p. 993. Physical Series.
[4] A. C. McKay: *Trans.* Faraday Soc. (1918) 34, p. 845.
[5] L. Slifkin, D. Lazarus, and T. Tomizuka: *Journal of Applied Physics* (1952) 23, p. 1032.
[6] W. A. Johnson: *Trans.* AIME (1941) 143, p. 107; METALS TECHNOLOGY (January 1941).
[7] R. E. Hoffman and D. Turnbull: *Journal of Applied Physics* (1951) 22, p. 634.
[8] A. D. Martin, R. D. Johnson, and F. Asaro: *Journal of Applied Physics* (1954) 25, p. 364.
[9] M. S. Maier and H. R. Nelson: *Trans.* AIME (1942) 147, p. 39; METALS TECHNOLOGY (January 1942).
[10] C. L. Raynor, L. Thomassen, and L. J. Rouse: *Trans.* ASM (1942) 30, p. 313.
[11] J. Steigman, W. Shockley, and F. C. Nix: *Physical Review* (1939) 23, p. 605. See for derivation of Eq. 2.
[12] A. E. Berkowitz, F. E. Jaumot, Jr., and F. C. Nix: *Physical Review* (1954) 95, p. 1185.
[13] F. C. Nix and F. E. Jaumot, Jr.: *Physical Review* (1951) 82, p. 72.
[14] A. E. Berkowitz: *Journal of Applied Physics* (1955) 26, p. 403.
[15] J. E. Perkins and S. K. Hagrees: *Physical Review* (1953) 92, p. 686.
[16] T. Liu and H. G. Drickamer: *Journal of Chemical Physics* (1954) 22, No. 2, p. 312.
[17] R. E. Carter and F. O. Richardson: *Trans.* AIME (1954) 200, p. 1244; JOURNAL OF METALS (November 1954).
[18] L. Himmel, R. F. Mehl, and C. E. Birchenall: *Trans.* AIME (1953) 197, p. 827; JOURNAL OF METALS (June 1953).
[19] C. E. Birchenall: Private communication.

Strain Rate Effects in Tungsten

The yield strength of annealed tungsten was found to have a strain rate exponent 12 times as great as that of low carbon steel. The effects of temperature and strain rate could be correlated through the Zener-Hollomon parameter with a heat of activation associated with yielding of 32,000 cal per g-atom. This heat of activation is independent of strain although both the temperature and strain rate dependence of the yield strength vary with strain.

by James H. Bechtold

MOST metals have mechanical properties that are relatively insensitive to strain rate, especially at temperatures below that at which creep is important. In iron[1] and molybdenum,[2] however, relatively large strain rate effects are observed in the temperature range where the rapid increase in yield strength occurs which leads to the ductile to brittle transition. In this temperature range Zener and Hollomon[4] have suggested that the effects of strain rate $\dot{\epsilon}$ and temperature T on the yield strength σ_y could be correlated through a single parameter, P, in the following manner

$$\sigma_y = f(P) = f(\dot{\epsilon}e^{Q/RT}) \qquad [1]$$

where Q is a heat of activation characteristic of the metal and associated with some unspecified relaxation process. They also observed that if the temperature is restricted to a relatively narrow range—below room temperature for steel—that the logarithm of the yield strength could be expressed as a linear function of the logarithm of P.

$$\sigma_y \sim P^r \sim [\dot{\epsilon}e^{Q/RT}]^r. \qquad [2]$$

From this relation the logarithm of stress should be a linear function of the logarithm of the strain rate at constant temperature:

$$\sigma_y(T = C) \sim \dot{\epsilon}^r \qquad [3]$$

where r will be referred to herein as the strain rate exponent. At a constant strain rate the logarithm of stress should be a linear function of $1/T$,

$$\sigma_y(\dot{\epsilon} = C) \sim e^{q/RT} \qquad [4]$$

where

$$q = Qr \qquad [5]$$

and is referred to herein as the temperature exponent. These equations have been found to relate the effects of temperature and strain rate on the yield strength of molybdenum in the temperature range wherein the ductile to brittle transition occurs, —75° to +150°C.[2]

Bechtold and Shewmon[3] have shown recently that the ductile to brittle transition in annealed tungsten occurs in the temperature range +150° to +350°C. In this temperature range the yield strength in-

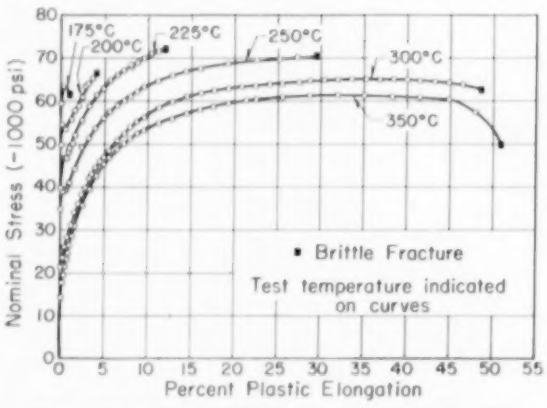

Fig. 1—Chart plots load elongation curves for tungsten. Constant strain rate is 2.8×10^{-4} sec^{-1}.

J. H. BECHTOLD, Associate Member AIME, is Research Engineer, Research Laboratories, Westinghouse Electric Corp., East Pittsburgh, Pa.

Discussion of this paper, TP 4064E, may be sent, 2 copies, to AIME by Apr. 1, 1956. Manuscript, Jan. 12, 1955. Philadelphia Meeting, October 1955.

creases rapidly with decreased test temperature and the logarithm of the yield strength is a linear function of 1/T. The temperature exponent, q, Eq. 4, was found to be approximately 5,400 cal per mol which is very large compared with the 100 to 200 cal per mol observed for steel by Zener and Hollomon, and 1,700 cal per mol observed by Bechtold[2] for molybdenum. The heat of activation of a relaxation process which might occur in an observable time at 150° to 350°C should be about 25,000 to 50,000 cal per mol. For a heat of activation of this magnitude the strain rate exponent, r, Eqs. 3 and 5, would have to be between 0.10 and 0.20. Zener and Hollomon give $r = 0.0125$ for steel. Consequently, in order to have reasonable activation energies associated with yielding, the strain rate exponent for yielding must be at least eight times as great in tungsten as in steel.

The effect of strain rate on the yield strength of tungsten should be a rather critical test of the general applicability of the Zener-Hollomon parameter to correlating the effects of temperature and strain rate on mechanical properties of metals at low temperatures. If the strain rate effects are of the magnitude predicted, i.e., if the heat of activation is a reasonable value, considerable confidence in the general utility of the relation is justified. Conversely, if large strain rate effects are not observed, the general applicability of the equation must be questioned and no significance can be attached to the activation energies so calculated.

Material and Test Procedure

The tungsten used for the present investigation was from the same lot of 0.300 in. diam swaged rod as that used by Bechtold and Shewmon[3] for determining the temperature dependence of the tensile properties of tungsten. In the previous investigation the specimens were annealed for ½ hr at 1950°C in hydrogen whereas in the present investigation the specimens were annealed for 1 hr at 2000°C under a vacuum of less than 1×10^{-4} mm Hg. The vacuum annealed specimens were not analyzed chemically after heat treatment; however, the behavior of the vacuum system during annealing indicated that a considerable volume of gas was removed from the tungsten, probably hydrogen, nitrogen and carbon monoxide. The ductility of the vacuum annealed tungsten also indicated that it was somewhat purer than the hydrogen annealed specimens as is discussed later. The microstructure of the vacuum annealed specimens was identical with that of the H_2 annealed specimens. The tensile specimens were ground to a uniform 0.200 in. diam over a 1¼ in. gage length, type *A* in ref. 3. The method of testing was also the same as that used previously.

Table I. Strain Hardening Characteristics of Tungsten

Test Temperature, °C	Strain Rate, Sec⁻¹	Strain Hardening Exponent n*	Stress at Unit Natural Strain, K,* † 1000 Psi	Rate of Strain Hardening at δ = 0.03,‡ 1000 Psi
175	2.8×10^{-4}	§	§	§
200	2.8×10^{-4}	0.20	135	450
225	2.8×10^{-4}	0.21	128	430
250	2.8×10^{-4}	0.25	128	440
275	2.8×10^{-4}	0.29	137	480
300	2.8×10^{-4}	0.34	139	480
350	2.8×10^{-4}	0.36	140	480
250	9.8×10^{-3}	§	§	§
250	5.7×10^{-3}	0.20	132	440
250	2.8×10^{-3}	0.22	132	450
250	9.8×10^{-4}	0.24	135	460
250	5.7×10^{-4}	0.25	136	460
250	2.8×10^{-4}	0.25	128	440
250	9.8×10^{-5}	0.285	133	460
250	4.2×10^{-5}	0.33	137	470
250	9.8×10^{-6}	0.36	148	500

* n and K as defined by flow equation $\sigma = K\delta^n$.
† Calculated from flow equation at $\delta = 0.10$.
‡ $d\sigma/d\delta = nK\delta^{(n-1)}$.
§ Too little plastic deformation for evaluation.

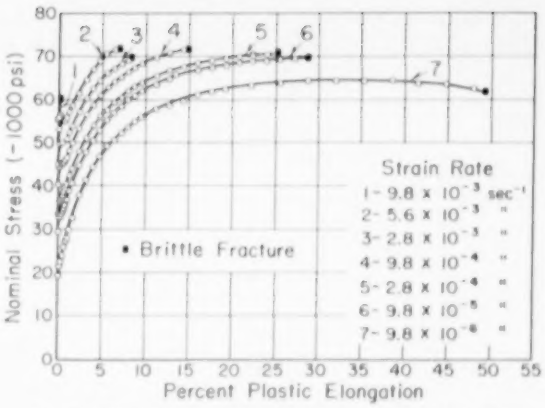
Nominal Stress (–1000 psi)
Percent Plastic Elongation
Strain Rate
1- 9.8 x 10⁻³ sec⁻¹
2- 5.6 x 10⁻³ "
3- 2.8 x 10⁻³ "
4- 9.8 x 10⁻⁴ "
5- 2.8 x 10⁻⁴ "
6- 9.8 x 10⁻⁵ "
7- 9.8 x 10⁻⁶ "
• Brittle Fracture

Fig. 2—Chart plots load elongation curves for tungsten. Constant temperature is 250°C.

Results

Stress-Strain Curves—Several typical nominal stress percent plastic elongation curves are shown in Figs. 1 and 2. A marked similarity in the effects of changes in temperature and strain rate on tensile properties is readily evident. The curves show a consistent increase in yield and flow stress with decreased test temperature or increased strain rate. Since the temperatures and strain rates examined covered a range in which both continuous and discontinuous yielding occur, the conventional yield criterion, such as the upper or lower yield point, or the stress at a given strain, could not be used consistently as measures of yield strength. For this reason the proportional limit is used to define the yield strength. Reduction in area at fracture is used as the criterion of ductility.

Marked upper and lower yield points are observed only at temperatures below 250°C with strain rates above 1×10^{-4} sec⁻¹. From previous observation of other body-centered-cubic metals, marked upper and lower yield points were expected at much higher temperatures. The reason none were observed above 250°C is believed to be that the cooling rate from the 2000°C recrystallization anneal was too fast for interstitial carbon and/or nitrogen atoms to segregate into the vicinity of edge dislocation and form a strong *Cottrell* type of condensed atmosphere. Slow cooling or an anneal at about 800°C would probably develop sharp yield points at higher temperatures.

True stresses and natural strains were calculated from the load-elongation data from the limit of the yield point elongation to the strain at the maximum load point, and are plotted on logarithmic coordinates for several test temperatures and strain rates in Figs. 3 and 4. The linearity indicates an exponential flow equation of the type

$$\sigma = K\delta^n \qquad [6]$$

where σ = true stress, δ = natural strain, K = a constant, the true stress at unit natural strain, and n = a constant, referred to as the strain hardening exponent. Strain hardening exponents were obtained

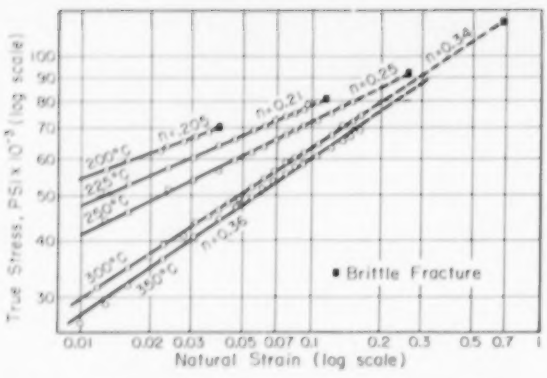

Fig. 3—Chart plots true stress-natural strain curves of annealed tungsten. Strain rate is 2.8×10^{-4} sec^{-1}.

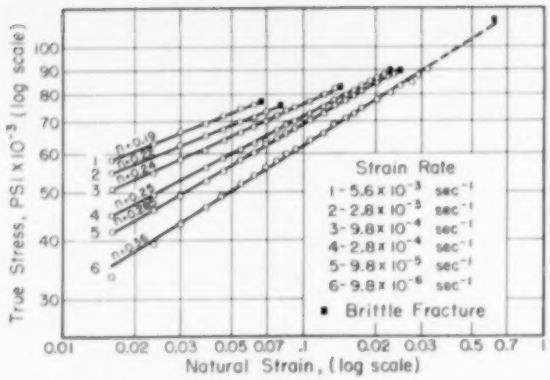
True Stress, PSI x 10⁻³ (log scale)
Natural Strain, (log scale)
Strain Rate
1 - 5.6 x 10⁻³ sec⁻¹
2 - 2.8 x 10⁻³ sec⁻¹
3 - 9.8 x 10⁻⁴ sec⁻¹
4 - 2.8 x 10⁻⁴ sec⁻¹
5 - 9.8 x 10⁻⁵ sec⁻¹
6 - 9.8 x 10⁻⁶ sec⁻¹
• Brittle Fracture

Fig. 4—Chart plots true stress-natural strain curves of annealed tungsten at 250°C.

by fitting the best straight lines to the experimental data over the strain range $\delta = 0.015$ to $\delta = 0.15$, or to fracture if fracture occurred prior to this strain, and are recorded in Table I. K values were calculated from the strain hardening exponents and the flow stresses at $\delta = 0.1$, and are also tabulated in Table I. The strain hardening exponents, n, decrease with decreased test temperature from a maximum of 0.36 at 350°C to 0.20 at 200°. Data not reported here indicate that n also decreases above 350°C. This behavior is consistent with observations on molybdenum[2] and iron.[4] The effect of strain rate on the strain hardening exponent is exactly the same, n decreasing from 0.36 at the slowest strain rates to 0.20 at the highest. The stress at unit strain, K, is relatively insensitive to temperature or strain rate.

Differentiating Eq. 6 gives the rate of work hardening

$$\frac{d\sigma}{d\delta} = nk\delta^{n-1} = n\frac{\sigma}{\delta}. \qquad [7]$$

Rates of work hardening were evaluated for several constant strains and are recorded for $\delta = 0.03$ in col. 5, Table I. The effect of temperature and strain rate on $d\sigma/d\delta$ depends on the strain level at which the comparison is made. At $\delta = 0.03$, $d\sigma/d\delta$ is relatively independent of either temperature or strain rate. However, when compared at a lower strain level, $d\sigma/d\delta$ is slightly larger at the lower temperatures or the higher strain rates. When compared at considerably higher strain levels, above $\delta \sim 0.10$, $d\sigma/d\delta$ is slightly smaller at lower temperatures or higher strain rates. At all temperatures and strain rates, $d\sigma/d\delta$ drops off rapidly with increased strain.

Table II. Temperature and Strain Rate Exponents and Activation Energy for Yielding of Tungsten

Strain Level	Temperature Exponent q, Cal per Mol	Strain Rate Exponent r	Activation Energy for Yielding, Cal per Mol
Yield Strength	4,860	0.15	32,000
$\delta = 0.01$	3,590	0.11	32,000
$\delta = 0.03$	2,170	0.073	30,000
$\delta = 0.05$	1,760	0.059	30,000
$\delta = 0.10$	1,330	0.042	32,000

Temperature Effects—The logarithm of the yield strength and of the 0.03 and 0.10 strain flow stresses determined at a constant strain rate of 2.8×10^{-4} sec^{-1} are plotted as a function of $1/T$ for the temperature interval 175° to 350°C in Fig. 5. The open points are data of Bechtold and Shewmon and the solid points are data from the present investigation. Both sets of data points fall quite well on the same straight lines and the slopes of the lines were determined by least squares using both sets of data. The temperature exponents, q, in Eq. 4 for the yield strength and for the several isostrain flow stresses are recorded in col. 2, Table II. This temperature exponent is observed to depend markedly on strain, varying from 4,900 cal for the yield strength to 1,300 cal for the 0.1 strain flow stress.

Although the yield strength of the present vacuum annealed tungsten is about the same as that of the hydrogen annealed tungsten of Bechtold and Shewmon, the ductility above 200°C of the former is considerably better as indicated by the reduction in area curves in Fig. 5. The better ductility of the vacuum annealed tungsten is probably due to a higher brittle fracture strength resulting from higher purity. Both samples, however, become completely brittle below 175°C. The fractures in all of the specimens, even the vacuum annealed ones tested at 350°C, had the bright, crystalline appearance typical of brittle fracture although at the higher temperatures fracture was preceded by considerable plastic strain.

Although the experimental data points in Fig. 5 fall quite well on straight lines, these straight lines cannot be extrapolated to predict yield strengths or isostrain flow stresses at temperatures much above 350°C. Data not shown here for tests above 350°C fall considerably above a straight line extrapolation of the curves. Yield strengths cannot be determined by the tensile test below 175°C, since fracture precedes yielding. Consequently, it is impossible to say if the linearity of log σ vs $1/T$ continues below this temperature. However, it is considered very unlikely that the yield strength would continue to increase as rapidly at lower temperatures as an extrapolation of the straight lines in Fig. 5 predicts.

Strain Rate Effects—The effect of strain rate was examined in detail at only one temperature, 250°C, which is in about the center of the ductile to brittle transition zone. The logarithms of the yield strength and of the 0.03 and 0.10 flow stresses are plotted as a function of the logarithm of the strain rate in Fig. 6. The experimental points are observed to fall quite well on straight lines in agreement with Eq. 3. The best straight lines were fitted to the data points by least squares and the slopes, i.e., the strain rate

exponents r are recorded in col. 3, Table II. The strain rate exponent of the yield strength is within the range predicted from the temperature dependence using the Zener-Hollomon equation. The strain rate exponents like the temperature exponents depend markedly on the strain level, varying from 0.15 for the yield strength to 0.042 for the 0.10 strain flow stress.

Although both the temperature and strain rate exponents depend markedly on strain, the heat of activation, $Q = q/r$, in the Zener-Hollomon parameter is independent of strain within the limits of experimental error and equal to 32,000 cal per mol as shown in col. 4, Table II. The pronounced strain dependence of the temperature and strain rate exponents and strain independence of the activation energy agree with observations on molybdenum.[3]

The effect of strain rate on ductility is almost as pronounced as it is on the yield strength as shown by the reduction in area curve in Fig. 6. Comparing the reduction in area curves in Fig. 5 with that in Fig. 6 reveals a very close similarity in the effects of increased strain rate and decreased temperature on ductility. The decrease in ductility is a direct result of the increase in yield strength which raises the ductile to brittle transition temperature. Fractures appeared bright and crystalline and occurred catastrophically even at the slowest strain rates.

The effect of strain rate on the tensile properties of tungsten is much greater than that observed for any of the more common metals such as iron, copper, or aluminum.[5] It is worth noting that the strain rate range covered in these tests does not greatly exceed the variation in strain rate that is often encountered and usually disregarded as unimportant in most commercial tensile testing of common metals. The importance of controlling the strain rate accurately when studying the mechanical properties of annealed tungsten is readily evident.

Discussion

The results of the tensile tests reported herein on annealed tungsten seem to confirm the general utility

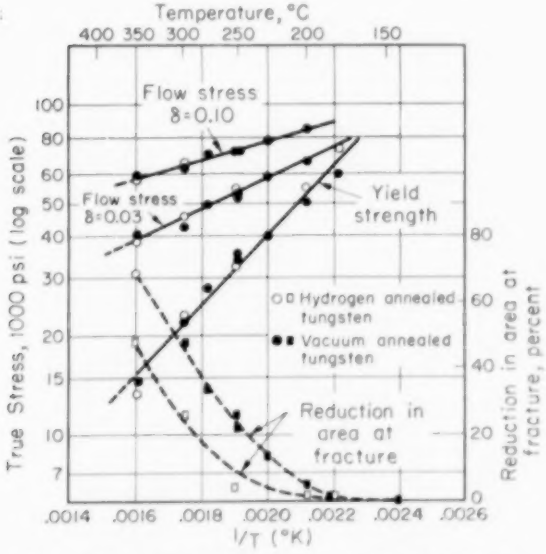

Fig. 5—Chart plots effect of temperature on the flow strength and ductility of annealed tungsten. Strain rate is 2.8×10^{-4} sec^{-1}.

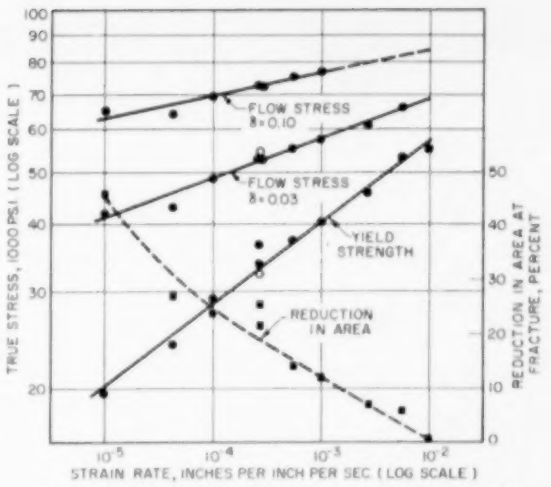

Fig. 6—Chart plots effect of strain rate on the flow strength and ductility of annealed tungsten at 250°C.

of the Zener-Hollomon parameter for correlating effects of temperature and strain rate on the yield strength and isostrain flow stresses of the body-centered-cubic metals in the temperature range of their ductile to brittle transition. The activation energies are of the magnitude which might be expected for some type of a relaxation process occurring in the respective temperature ranges. This activation energy is about 32,000 cal for tungsten over the temperature range +175° to 350°C, about 21,000 for molybdenum[3] over the temperature range −75° to +150°C, and 10,000 to 15,000 for steel[1] over the temperature range −195° to +25°C. These are equivalent temperature ranges for the respective metals in the sense that it is in these temperature ranges that the rapid increase in yield strength occurs[3] which brings about the ductile to brittle transition.

The heats of activation associated with yielding at low temperatures are much smaller than those reported by Dorn et al.,[6] also using the Zener-Hollomon relation, for correlating high temperature creep data. Dorn found a very good correlation of the heats of activation associated with high temperature creep and the heat of activation for self diffusion. The heats of activation for self diffusion are approximately 140,000,* 100,000* and 70,000* cal per mol for tungsten, molybdenum, and iron, respectively; much larger than the observed heats of activation associated with low temperature yielding. Obviously, yielding must be governed by different mechanisms in different temperature ranges. The extent of the temperature range over which yielding is governed by the mechanism associated with an activation energy of the magnitude observed here was not ascertained. Furthermore, the results reported here do not prove that there is a single activation energy even over the narrow temperature range examined since strain rate tests were made at only one temperature. However, results on iron[1] and molybdenum[3] would seem to indicate a single activation energy over this temperature range. It would be of particular interest to ascertain the temperature and strain rate dependence of yield and

* Estimated from melting point and activation energy for recrystallization.

flow stresses and the activation energy associated with yielding below 175°C. This cannot be done with the tensile test but it may be possible with compression tests, since it should be possible to reach much higher yield strength without brittle fracture.

The marked temperature and strain rate dependence of the yield strength of the body-centered-cubic metals at low temperatures is believed to arise from the anchoring of dislocations by interstitial solute atoms, such as carbon and nitrogen. There are at least three mechanisms by which these interstitial solute atoms can interact with dislocation.[7] The first is by interaction with precipitated carbide or nitride particles. The second arises from the possibility of relief of hydrostatic stress by the solute atoms segregating into the dilated portion of edge dislocations. The third arises from the possibility of relief of shear stresses around both screw and edge dislocations by the solute atoms taking up preferred interstitial sites around the dislocation. The latter mechanism is believed to be the one chiefly responsible for the pronounced temperature and strain rate effects in the body-centered-cubic metals.[8]

Summary and Conclusions

The mechanical properties of annealed tungsten are extremely sensitive to strain rate in the temperature range 175° to 350°C, wherein the ductile to brittle transition occurs. The strain rate exponent, r, in the equation $\sigma_y \sim \dot{\epsilon}^r$ is about 12 times as large as for steel.

† Subscript with σ in this equation represents *yielding*.

The effects of strain rate and temperature on the yield strength and isostrain flow stresses could be correlated by the Zener-Hollomon parameter. The activation energy associated with yielding is 32,000 cal per mol and, within the limits of experimental error, is independent of strain.

The marked strain rate and temperature dependence of the yield strength of tungsten and of other body-centered-cubic metals is believed to be due to the interaction of interstitial solute atoms with dislocation arising from the relief of internal stresses by the solute atoms assuming preferred interstitial sites in the vicinity of the dislocations.

Discussion of this paper, if any, will appear in JOURNAL OF METALS, November 1956, and in AIME Metals Branch *Transactions*, Vol. **206**, 1956.

References

[1] C. Zener and J. H. Hollomon: *Journal of Applied Physics* (1944) 15, pp. 22-32.

[2] J. H. Bechtold: *Trans.* AIME (1953) 197, pp. 1469-1475; JOURNAL OF METALS (November 1953).

[3] J. H. Bechtold and P. G. Shewmon: *Trans.* ASM (1954) 46, p. 397.

[4] R. L. Smith, G. Spangler, and R. M. Brick: *Trans.* ASM (1954) 46, p. 973.

[5] A. Nadai and M. J. Manjoine: *Journal of Applied Mechanics* (1941) 63, pp. 77-91.

[6] O. D. Sherby, R. L. Orr, and J. E. Dorn: *Trans.* AIME (1954) 200, p. 71; JOURNAL OF METALS (January 1954).

[7] F. R. N. Nabarro: *Report on Strength of Solids.* (1948) London, Physical Soc.

[8] J. H. Bechtold: Tensile Properties of Tantalum at Low Temperatures. *Acta Metallurgica* (1955) 3, p. 249.

Interaction of Precipitation and Creep In Mg-Al Alloys

Microstructural studies of a Mg-10.3 pct Al alloy showed that discontinuous precipitation during aging multiplies the grain boundary area available for easy deformation in elevated temperature creep. An increase of strain rate for a 6.2 pct Al alloy at 400°F, where precipitation and creep are concurrent, caused an increase in the volume percentage discontinuously precipitated at the completion of the process. The relatively poor elevated temperature creep resistance of heat treated alloys of the Mg-Al-Zn type was explained in these structural terms.

by C. S. Roberts

CREEP resistance of the heat treatable Mg-Al based alloys is poor compared to that of Mg-Ce based alloys. While the latter show a continuous precipitate,[1] Mg-Al alloys prefer a discontinuous precipitate at grain boundaries.[2, 3] It has been concluded that the excellent creep resistance of Mg-Ce alloys was primarily due to the continuous precipitation which especially localized at the grain boundaries.[1] The purpose of the present investigation was to obtain a parallel correlation, if such exists, between the poor creep resistance and the state of precipitation in Mg-Al alloys. Discontinuous precipitation produces about three times as many true grain boundaries as originally existed. This microstructure would be expected to have a marked influence in creep, where quantity of grain boundary area is important.

C. S. ROBERTS, Junior Member AIME, is associated with Metallurgical Laboratories, Dow Chemical Co., Midland, Mich.

Discussion of this paper, TP 4110E, may be sent, 2 copies, to AIME by Apr. 1, 1956. Manuscript, Nov. 29, 1954. Philadelphia Meeting, October 1955.

Experimental Procedure

The two experimental alloys contained 6.2 and 10.3 pct Al. They were made from electrolytic magnesium by alloying under flux and casting in 3 in. diam permanent molds. The ingots were extruded into 1¼ x ⅛ in. flat stock under the following conditions: billet preheat 700°F (2 hr), container and die temperature 700°F, speed 3 fpm, and area reduction ratio 45:1. The creep specimens were machined from blanks which had been solution heat treated 24 hr at 770°F and aged 16 hr at 400°F. Attempts were made to control the grain size as closely as possible for extruded stock. The grain size after solution heat treatment was about two thousandths of an inch for the 6.2 and five thousandths for the 10.3 pct Al alloy.

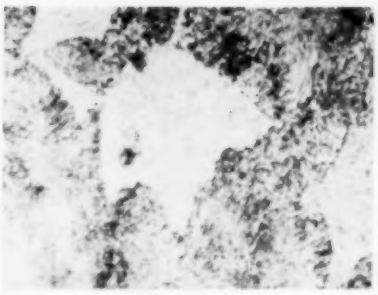

Fig. 1a—Micrograph shows 10.3 pct Al alloy after solution heat treatment and aging for 16 hr at 400°F. Sample was electropolished and etched in 10 pct HF. X1000. Area reduced approximately 45 pct for reproduction.

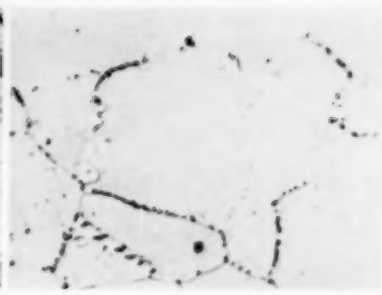

Fig. 1b—Micrograph shows 6.2 pct Al alloy after solution heat treatment and aging for 16 hr at 400°F. Sample was electropolished and etched in acetic glycol. X1000. Area reduced approximately 45 pct for reproduction.

The solution heat treatment temperature was selected to dissolve all the aluminum. The aging treatment was such that in the 10.3 pct Al alloy the volume of discontinuous precipitate had grown to the limit while in the 6.2 pct Al alloy more growth was possible during the creep test. The contrast between the microstructures is shown in Fig. 1. The 10.3 pct Al alloy is good for examining the influence of the final structure on the creep and the 6.2 pct Al alloy is suited for studying the influence of creep strain on concurrent precipitation.

The observations of microstructural changes were made on specimens which were electropolished and protected during testing by silicone oil. The procedure reported previously[4] was used with one modification. Difficulties in electropolishing the aged alloy resulted from adherence of the precipitate as a fine gray powder on the specimen surface. This obstacle was circumvented by electropolishing in the solution heat treated condition followed by aging in a silicone oil bath. In order to avoid complicating the deformation structure with complete precipitate detail, these specimens were tested in the unetched condition.

Except for a few tests on the 10.3 pct Al alloy at constant load, the creep testing was performed under constant stress conditions with the aid of a simple noncollinear loading beam.[5]

Influence of Discontinuous Precipitate on Creep

Microstructures of the 10.3 pct Al alloy after creep at 200° and 300°F showed evidence of the orientation relation developed by Smith.[3] At these testing temperatures, slip is the principal deformation mechanism. Whenever slip lines were seen in all four regions involved at a grain boundary (the two original grains and the two recrystallized volumes), their direction was consistent with the predicted relation. Fig. 2 shows such evidence. The slip line evidence is sufficient to show that, in general, an orientation difference exists from region to region in an originally single grain.

Although this report is not intended to deal with individual strain-time relationships, it is well to include a brief description of the characteristic creep curves obtained from the 10.3 pct Al alloy in the range 200° to 600°F. Primary creep decreased in magnitude with increasing temperature. Secondary creep is of finite length at all temperatures. The tertiary stage begins at lower strain levels as temperature increases and always at less than 4 pct. Necking of the specimen does not occur until tertiary creep is well advanced.

The structure shown in Fig. 2 is characteristic of deformation at the low end of the temperature range studied. As in electrolytic magnesium,[4] basal slip is profuse and finely spaced. The formation of low angle boundaries by kinking is present but there is no evidence of deformation twinning.

When the 10.3 pct Al alloy is tested at a high temperature and low stress, 600°F and 600 psi, deformation is highly localized at both the original and the precipitation-produced boundaries, Fig. 3. Inspection at X1000 failed to reveal slip lines. Subgrain formation by kinking is very rare. Fig. 3 shows a smooth series of relief steps similar to those found in electrolytic magnesium.[4] Apparently a cyclic process of boundary sliding and migration can operate in aged Mg-Al alloys at multitudes of new interfaces which result from the discontinuous precipitation process.

When approximately the same amount of strain occurred at 600°F and a higher stress, 1000 psi, subgrain formation by kinking entered as an observable deformation process. A specimen strained to the same extent at 2000 psi shows slip in the microstructure, Fig. 4. The newly formed boundaries are primary deformation sites at 600°F.

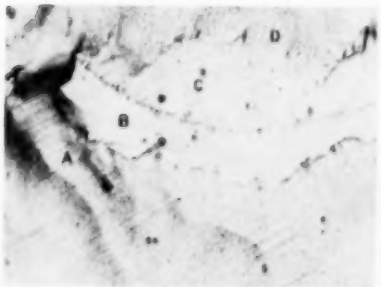

Fig. 2—Micrograph of 10.3 pct Al alloy after 5 pct creep at 300°F and 17,000 psi was taken with oblique illumination. Stress axis is vertical. X500. Area reduced approximately 45 pct for reproduction.

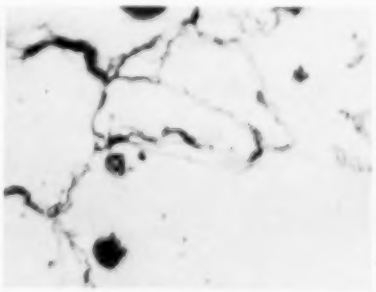

Fig. 3—Micrograph shows 10.3 pct Al alloy specimen after 4.5 pct creep at 600°F and 600 psi. Stress axis is vertical. X1000. Area reduced approximately 45 pct for reproduction.

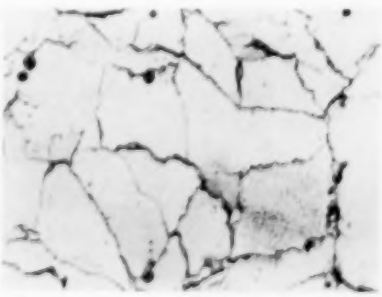

Fig. 4—Micrograph shows 10.3 pct Al alloy after 5 pct creep at 600°F and 2000 psi. Stress axis is vertical. X500. Area reduced approximately 45 pct for reproduction.

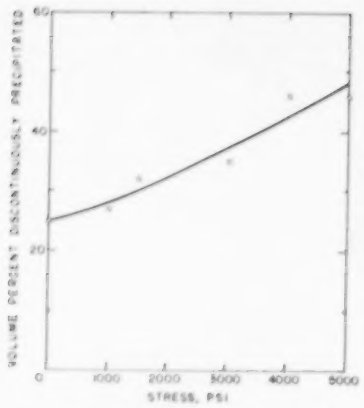

Fig. 5—Chart illustrates influence of stress (strain rate) on concurrent precipitation in 6.2 pct Al alloy at 400°F.

The creep curves from the 6.2 pct Al alloy generally show the same form and temperature dependence as those from the 10.3 pct Al alloy. A relatively larger primary stage accompanied the occurrence of a small amount of mechanical twinning at lower temperatures and higher strain rates. A preferred orientation study showed that the maximum basal plane pole density exceeded 20° inclination to the extrusion surface normal.

The influence of the testing stress on discontinuous precipitation at 400°F when strain rates are low is shown in Fig. 5. The data were obtained from specimens which were tested beyond the end of the race between the processes and generally well into the period of coalescence of overaged precipitate. As the stress is increased, the volume percentage which has discontinuously precipitated increases. This volume was quantitatively determined with the aid of a Hurlbut counter from electropolished surfaces which were approximately halfway in depth between the original surface and the center of the specimen. The scatter of the data is reasonable in view of the human judgment required in such a quantitative metallographic study. The zero stress point was obtained from a specimen aged to completion at 400°F.

Many examples of the acceleration of precipitation in general as a result of plastic deformation have been reported.[5, 7] Here is evidence that one type of precipitation is favored over another by the occurrence of plastic deformation. This is explained on the basis of build-up of elastic strain energy at the boundaries, favoring discontinuous precipitation. The unique appearance of concurrent discontinuous precipitate growth and deformation at the boundaries as they move is presented in Fig. 6.

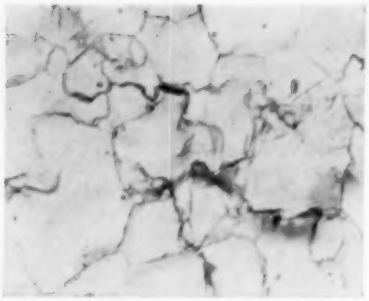

Fig. 6—Micrograph shows 6.2 pct Al alloy after 6 pct creep at 400°F and 500 psi. Stress axis is vertical. X500. Area reduced approximately 45 pct for reproduction.

Conclusions

1—The comparatively poor elevated temperature creep resistance of Mg-Al based alloys results from the ease of deformation at grain boundaries and the multiplication of these boundaries by discontinuous precipitation.

2—When the test temperature is such that precipitation is concurrent with creep, increasing stress or strain rate favors the discontinuous precipitate at the expense of the continuous type in Mg-Al alloys.

Acknowledgment

This research was performed under Contract No. AF 33(038)-16655 with the Metallurgy Research Branch, Aeronautical Research Laboratory, Directorate of Research, Wright-Patterson Air Force Base, Ohio.

Discussion of this paper, if any, will appear in JOURNAL OF METALS, November 1956, and in AIME Metals Branch *Transactions*, Vol. **206**, 1956.

References

[1] C. S. Roberts: Creep Behavior of Magnesium-Cerium Alloys. *Trans.* AIME (1954) **200**, p. 634; JOURNAL OF METALS (May 1954).

[2] A. H. Geisler: Precipitation from Solid Solutions of Metals. *Phase Transformations in Solids.* (1951) pp. 432-442. New York. John Wiley and Sons Inc.

[3] C. S. Smith: Microstructure. *Trans.* ASM (1953) **45**, pp. 564-568.

[4] C. S. Roberts: Creep Behavior of Extruded Electrolytic Magnesium. *Trans.* AIME (1953) **197**, p. 1121; JOURNAL OF METALS (September 1953).

[5] R. L. Fullman, R. P. Carreker, Jr., and J. C. Fisher: Simple Devices for Approximating Constant Stress During Tensile Creep Tests. *Trans.* AIME (1953) **197**, p. 657; JOURNAL OF METALS (May 1953).

[6] B. L. Averbach: The Effect of Plastic Deformation on Solid Reactions. Part I—Diffusion Reactions. *Cold Working of Metals.* (1949) p. 277. Cleveland. ASM.

[7] A. H. Sully and H. K. Hardy: Some Metallographic Observations of the Creep of Aluminum-Copper Alloys. *Journal* Institute of Metals (1953-1954) **82**, p. 264.

Technical Note

Occurrence of CsCl-Type Ordered Structures in Certain Binary Systems Of Transition Elements

by Paul A. Beck, J. B. Darby, Jr., and O. P. Arora

LAVES and Wallbaum[1] reported that the phases occurring at the compositions TiFe, TiRu, and TiOs, which are stable over a wide range of temperatures and are separated from neighboring phases by wide two phase fields, have a CsCl-type ordered structure. For TiRu and TiOs, this was recently confirmed by C. B. Jordan.[2] Recent results of Greenfield and Beck[3] show that solid solutions with ruthenium of the body-centered-cubic elements vanadium and tantalum (and presumably also of columbium) in group Va of the periodic table undergo CsCl-type ordering. Although detailed phase diagrams for these systems are not yet available, it would appear that these ordered structures are separated from the neighboring body-centered-cubic solid solutions by relatively narrow two phase fields.

P. A. BECK, Member AIME, J. B. DARBY, JR., and O. P. ARORA, Junior Member AIME, are Research Professor, Graduate Student, and Research Assistant, respectively, College of Engineering, University of Illinois, Urbana, Ill.

TN 311E. Manuscript, Aug. 8, 1955.

Correspondingly, the CsCl-type ordered structure in these systems appears to be less stable than that

Table I. Portion of the Periodic Table

	Groups				
	IVa	Va	VIa	VIIa	VIIIa
1st long period	Ti	V	Cr	Mn	Fe
2nd long period	Zr	Cb	Mo	Tc	Ru
3rd long period	Hf	Ta	W	Re	Os

in the titanium systems mentioned previously. It is interesting to note that, on passing over to the transition elements in the next group of the periodic table, VIa (see Table I), the body-centered-cubic solid solutions of these elements with the iron group elements apparently do not undergo ordering at all. Thus, Greenfield and Beck[2] did not note ordering in the alloys of ruthenium with chromium or tungsten, Raub[4] did not observe ordering in the Mo-Os system and, in a recent investigation directed specifically at this point, Tagaya, Nenno, and Nishiyama[5] found no CsCl-type ordering in the body-centered-cubic solid solutions of chromium and iron near the equiatomic ratio.

Taken as a whole, the foregoing results certainly suggest a correlation between the occurrence of the CsCl-type ordered structures with the location of the components in the periodic table. Such a correlation would indicate a definite increase in the relative bond strength between unlike atoms, as compared with that for like atoms when in binary alloys of iron group elements the other component is changed from a chromium group element, to a vanadium group element, to titanium. It appears reasonable to assume that the increasing attraction between unlike atoms might be the result of an increasing ionic component in the bond between them. If this explanation is correct, an increasing extent of electron transfer would be expected between unlike atoms in cubic alloys of iron group elements with elements of the VIa, Va, and IVa groups. This hypothesis might be tested by determining the variations of the atomic moment of one element when it is associated with various partners in alloys with similar structure, for instance, of iron in the cubic alloys FeCr, FeV, and FeTi, by means of the neutron diffraction method developed by Shull and Wilkinson.[6] If the number of 3*d* electrons associated with iron varies systematically with the alloy partner, so should the atomic moment of iron in these alloys.

In some of the binary systems of transition elements mentioned, the occurrence of a CsCl-type ordered structure may be suppressed due to the relatively greater stability of some other phase. For instance, the favorable ratio of atomic radii in the Zr-Fe system may result in the formation of a very stable Laves phase, instead of a CsCl-type ordered structure. However, in other systems the occurrence of such an ordered structure may be suspected even though not as yet experimentally found. One such system is Fe-V, where extensive body-centered-cubic solid solutions are known to form but no CsCl-type ordered structure has been reported. In view of the very slight difference in the atomic scattering factor for X-rays of most wave lengths between the two component atoms, the presence of superlattice lines for such alloys could be detected only if the wave length of the X-rays used is properly chosen.[7, 8] In the case of Fe-V alloys, the CrKα radiation is almost ideally suited, since it gives nearly maximum difference between the scattering factors for iron and vanadium without causing fluorescence with either atom.

Alloys of iron with 45, 50, and 55 atomic pct V were prepared by induction melting. Previous work by Darby and Beck[9] showed that in this binary system the σ phase is stable only below 1200°C, in contrast to previous indications.[10] Specimens of the alloys were homogenized for three days at various temperatures between 1200° and 1300°C in evacuated quartz tubes and quenched in cold water. Microscopic examination in this condition showed essentially a single phase. (A small amount of a second phase was observed and tentatively interpreted as VN.) Filings from the homogenized specimens were reannealed for a few minutes at the homogenizing temperatures in evacuated quartz tubes and quenched in brine. X-ray diffraction patterns were taken from these filings in a 20 cm diam asymmetrical focusing camera with CrK radiation. The X-ray pattern showed, in addition to the body-centered-cubic lines corresponding to CrKα and CrKβ radiations, also the CrKα reflection from (100).* The interpretation of this diffraction line as a superlattice line was confirmed by using FeK radiation, which made the line disappear, as expected. However, a line corresponding quite well to the $\sin^2\theta$ value for (111) Kα, was also present with iron radiation and, therefore, had to be attributed, at least partly, to an impurity phase. Correspondingly, the presence of a superimposed (111) Kα superlattice line could not be ascertained. Also, in the pattern taken with CrK radiation, no line was found at the Bragg angle corresponding to (210); the intensity may have been too low for detection. Because of the lack of positive identification of superlattice lines, other than the (100), the present experiments were not as decisive in establishing the occurrence of CsCl-type ordering in FeV as might have been hoped. A more definite decision could be achieved by using neutron diffraction, since the scattering factor of iron and vanadium for thermal neutrons differs much more than for CrKα X-radiation, and thus the superlattice lines should be relatively more intense.

* In addition, the X-ray pattern showed weakly the most intense diffraction lines of the σ phase. Presumably, quenching of the powder enclosed in an evacuated quartz tube was not fast enough to suppress the formation of σ completely. A few lines arising apparently from an impurity phase were also detected.

Acknowledgments

This work was supported by the Office of Ordnance Research, U. S. Army, Contract No. DA-11-022-ORD-1175. J. B. Darby was recipient of a Union Carbide and Carbon Corp. Fellowship.

References

[1] F. Laves and H. J. Wallbaum: Zur Kristallchemie von Titan-Legierungen. *Naturwissenschaften* (1939) **27**, p. 674.

[2] C. B. Jordan: Crystal Structure of TiRu and TiOs. *Trans.* AIME (1955) **203**, p. 832; JOURNAL OF METALS (July 1955).

[3] P. Greenfield and P. A. Beck: Intermediate Phases in Binary Systems of Certain Transition Elements. *Trans.* AIME (1956) **206**, p. 265; JOURNAL OF METALS (February 1956).

[4] E. Raub: Die Legierungen der Platinmetalle mit Molybdän. *Ztsch. für Metallkunde* (1954) **45**, p. 23.

[5] M. Tagaya, S. Nenno, and S. Nishiyama: On the Fe-Cr Superlattice. *Memoirs* Inst. of Scientific and Industrial Research, Japan (1952) **9**, p. 76.

[6] C. G. Shull and M. K. Wilkinson: Neutron Diffraction Studies of the Magnetic Structure of Alloys of Transition Elements. *Physical Review* (1955) **97**, p. 304.

[7] A. J. Bradley and J. W. Rodgers: The Crystal Structure of the Heusler Alloys. *Proceedings* Royal Soc., London (1934) **144A**, p. 340.

[8] F. W. Jones and C. Sykes: The Superlattice in Beta Brass. *Proceedings* Royal Soc., London (1937) **161A**, p. 440.

[9] J. B. Darby, Jr. and P. A. Beck: Intermediate Phases in the Cr-Mo-Co System at 1300°C. *Trans.* AIME (1955) **203**, p. 765; JOURNAL OF METALS (June 1955).

[10] *Metals Handbook* (1948) p. 1219. Cleveland. ASM.

Effects of Oxygen, Nitrogen, and Carbon on The Ductility of Cast Molybdenum

High purity molybdenum ingots containing controlled amounts of a single impurity element (oxygen, nitrogen, or carbon) were prepared. These ingots were tested for ductility by bending test specimens at various temperatures. The relationship between the plastic behavior of the ingots and their chemical composition has been determined.

by L. E. Olds and G. W. P. Rengstorff

MANY proposed applications for molybdenum require ductility at or near room temperature. At the present time, it is possible to obtain wrought molybdenum with considerable ductility only if special fabrication techniques are used to control the grain structure. Starting with arc-cast or powder metallurgy ingots, the usual methods for obtaining ductility rely on fabrication procedures that result in fibered microstructures in the finished product. Recently, it has been found that the ductility of either powder metallurgy or arc-cast molybdenum can be improved by uniform recrystallization of the metal to a very fine equiaxed grain structure.[1]

The need for a fibered or a fine grained structure may limit the practical usefulness of molybdenum. For example, welding, which may be used in fabricating the metal, generally produces coarse grained structures that lead to brittleness. This applies, certainly, to currently available commercial molybdenum.

Although commercial molybdenum is brittle when the grains are coarse, it has been shown experimentally that fine grained structures are not always essential for ductility. For instance, as-cast molybdenum with a coarse columnar grain structure is ductile if it is sufficiently pure.[2] Because high purity cast molybdenum has good ductility even when coarse grained, it is probable that the brittleness in coarse grained commercial molybdenum is caused by the impurity content of the metal.

Although the general effects of impurities on the cold ductility of molybdenum have been known in a qualitative manner for some time, no quantitative evaluation of these effects has been available. The present investigation was made in order to determine more accurately the effects of oxygen, nitrogen, and carbon on the cold ductility of cast molybdenum.

Oxygen has long been known to be detrimental to ductility, although the minimum amount which will embrittle molybdenum has been open to speculation. Parke and Ham[3] showed that ingots with oxygen contents above 0.003 pct could not be forged. Maringer and Schwope[4] have described the embrittlement of molybdenum wire by oxygen. A discussion on the effects of heat treatment on the distribution of oxygen in molybdenum has been given by Perry, Spacil, and Wulff.[5]

Although nitrogen would also be expected to have harmful effects on ductility, no extensive work has been done previously to determine whether this is so. However, Tury and Krausz[6] found that wires presumably with less than 0.007 pct N were brittle.

Carbon is added to commercial cast molybdenum for deoxidation. Parke and Ham[3] have shown that molybdenum containing as much as 0.06 pct C could be forged if the oxygen was kept below 0.003 pct. Also, Bruckart and others[7] found that the room temperature ductility of sintered molybdenum improved with carbon contents up to 0.84 pct. However, Rengstorff and Fischer[8] found that residual carbide particles in cast molybdenum apparently had an unfavorable effect on room temperature ductility.

L. E. OLDS and G. W. P. RENGSTORFF, Member AIME, are associated with Battelle Memorial Institute, Columbus, Ohio.

Discussion of this paper, TP 4068E, may be sent, 2 copies, to AIME by Apr. 1, 1956. Manuscript, Dec. 30, 1954. Philadelphia Meeting, October 1955.

Table I. Analyses of Cast Molybdenum Containing Intentional Impurities

Ingot	Ppm O	Ppm H	Ppm N	Wt Pct C	Wt Pct S
High Purity					
Control	1.9	0.2	0.9*	0.002	0.0005
Sensitivity of analyses	±0.5	±0.06		±0.001	±0.0005
Oxygen Series					
Oxy 1	1	0.1	5†		
Oxy 2	2	0.5	4†		
Oxy 3	6	0.2	7†		
Sensitivity of analyses	±1	±0.1			
Nitrogen Series					
N1	3	0.3	8*	0.004	0.001
N2	2	0.3	14*	0.003	0.0008
N3	3	0.3	37*	0.002	0.0017
N4	15	0.6	330‡	0.004	0.0032
Sensitivity of analyses	±2	±0.3		±0.001	±0.0005
Carbon Series					
C1	4	0.3	<4†	0.003	
C2	2	0.4	3	0.006	
C3	<2	0.2	<3	0.008	
C4	4	0.2	3	0.010	
C5	2	0.2	3	0.020	
C6	2	0.2	<3	0.024	
Sensitivity of analyses	±2	±0.3		±0.001	

Spectrographic Analyses of High Purity Control Ingot, Wt Pct

Fe	0.005	Ti	<0.001 not detected
Mg	0.002	Bi	<0.0005 not detected
Si	0.002	Cr	<0.0005 not detected
Cu	0.0005	Mn	<0.0005 not detected
Al	<0.001 not detected	Ni	<0.0005 not detected
Pb	<0.001 not detected		

* Diffusion extraction method. Sensitivity = ±0.8 ppm.
† Vacuum fusion method. Sensitivity = ±4 ppm.
‡ Kjeldahl method. Sensitivity = ±10 ppm.

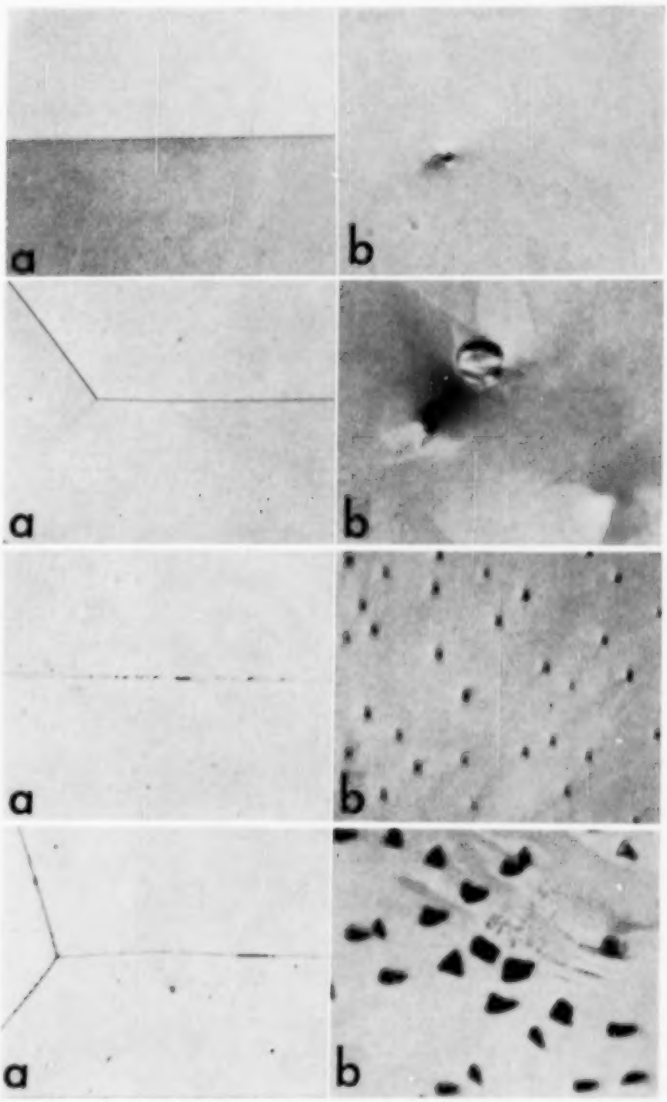

Fig. 1—Micrograph is of high purity cast molybdenum. X2000. a—Polished section, etched in warm $(NH_4)_2HPO_4$:H_2O_2, is shown. b—Grain surface of unetched sample is shown.

Fig. 2—Micrograph is of cast molybdenum containing 0.0001 pct O_2. a—Polished section of sample was etched in Murakami's etchant. X500. b—Grain surface was unetched. X2000.

Fig. 3—Micrograph is of cast molybdenum containing 0.0002 pct O_2. a—Polished section of sample was etched in Murakami's etchant. X500. b—Grain surface was unetched. X2000.

Fig. 4—Micrograph is of cast molybdenum containing 0.0006 pct O_2. a—Polished section of sample was etched in Murakami's etchant. X500. b—Grain surface was unetched. X2000.

In order to determine the effects of specific impurities, it was necessary to prepare ingots as pure as possible except for the impurity under study. Arc-melting in high vacuum has been found to reduce both the metallic and nonmetallic impurity contents in molybdenum to extremely low values, especially if the ingots are remelted one or more times by the same procedure. This method was used to prepare molybdenum low in undesired impurities for this investigation. The initial melting stock was commercial sinter bar. Melting was carried out at pressures of less than 0.2μ Hg.

Ingots containing oxygen or nitrogen were first purified by arc-melting sintered molybdenum twice in a vacuum by the procedure described by Rengstorff and Fischer.[3] Oxygen or nitrogen was then added by final remelting under low pressures of the desired gas, using electrode tips machined from purified molybdenum ingots. The ingots in the oxygen series were melted in commercial oxygen flowing at pressures of 0.6, 1, and 3μ Hg. The ingots in the nitrogen series were melted under static pressures of 10, 100, 1,000, and 60,000μ Hg in high purity lamp grade nitrogen.

Carbon was added to the initial charge in the form of a master alloy made by vacuum melting purified molybdenum with high grade spectrographic graphite. The carbon-containing ingots were purified by melting three times in vacuum, twice by the usual method, and the third time with purified electrode tips. Nominal carbon contents were <0.005, 0.005, 0.010, 0.015, 0.020, and 0.025 pct.

A control ingot to which no impurity elements were intentionally added was purified by melting three times in a manner similar to the other ingots. The purity of this ingot was about 99.99 pct.

Analyses of Ingots

The analyses of the ingots are listed in Table I. Techniques used to obtain these values were:

Oxygen and Hydrogen—The oxygen and hydrogen contents of all ingots were determined by a special vacuum fusion process described by Mallett and Griffith.[4]

Nitrogen—The vacuum fusion technique was found to give values for nitrogen in molybdenum which were generally lower than those obtained by the Kjeldahl method. An investigation was made

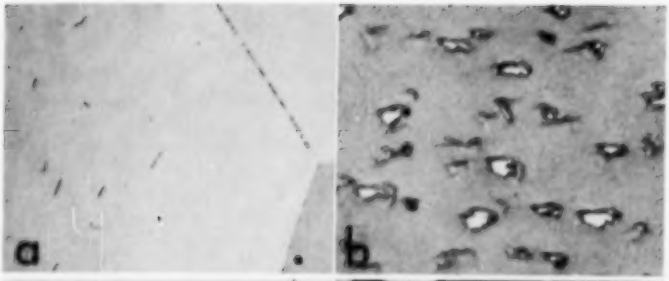

Fig. 5—Micrograph is of cast molybdenum containing 0.0008 pct N_2, etched in warm $(NH_4)_2HPO_4$:H_2O_2. a—Polished section of sample is shown. X500. b—Grain surface of sample is shown. X2000.

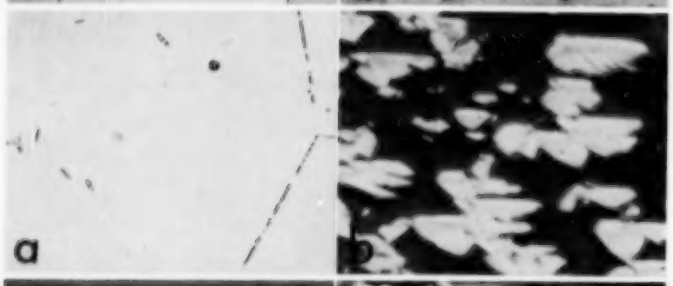

Fig. 6—Micrograph is of cast molybdenum containing 0.0037 pct N_2, etched in warm $(NH_4)_2HPO_4$:H_2O_2. a—Polished section of sample is shown. X500. b—Grain surface of specimen is shown. X2000.

Fig. 7—Micrograph is of cast molybdenum containing 0.033 pct N_2, etched in warm $(NH_4)_2HPO_4$:H_2O_2. a—Sample is of polished section. X500. b—Grain surface of specimen is shown. X2000.

to determine which method was giving the correct value. This led to a modification of the vacuum fusion method of analyzing for nitrogen. It was found that in the usual vacuum fusion procedure, in which the sample is dissolved in a carbon-saturated molten iron bath, not all of the nitrogen in the samples was released. By eliminating the iron bath, and merely heating the samples in a high vacuum, nitrogen values were obtained that agreed well with those obtained by the Kjeldahl method. This modified analytical process is referred to as the diffusion extraction method of analyzing for nitrogen.

Table II. Temperature Ranges and Methods for Molybdenum Ductility Tests

Temperature Range, °C	Method of Heating or Cooling Specimens
Above 200	Resistance wound furnace, argon atmosphere
50 to 200	Immersion heated silicone oil
−75 to 50	Dry ice in alcohol
−90 to −75	Liquid nitrogen in hexane

Diffusion extraction is a means for accurately determining nitrogen contents in ranges near and below the lower limit of the Kjeldahl method. The sensitivity of diffusion extraction analyses is about ±0.8 ppm in contrast to a sensitivity of ±10 ppm for the Kjeldahl method.

Carbon—The carbon analyses were made by a high precision combustion method. CO_2 liberated by combustion was absorbed in a $Ba(OH)_2$ solution, and the resulting changes in electrical conductivity of the hydroxide were accurately measured.

To check these analyses, several ingots were analyzed for carbon by vacuum fusion techniques. The results obtained by both methods were in good agreement.

Sulphur—Some of the ingots were analyzed for sulphur by a sensitive photometric method described by Luke.[9]

Metallics—Spectrographic analyses were made to determine the metallic impurity content of the high purity ingot. All samples were dissolved in acid, evaporated to dryness, and arced with graphite electrodes. Impurities in the resulting oxide were compared with standards. These standards were

Table III. Bend Test Data for High Purity Cast Molybdenum (Control Ingot) and for High Purity Cast Molybdenum Containing Additions of Oxygen

Temperature, °C	Bend Angle, Degrees			
	Control Ingot	Ingot No. Oxy 1, 0.0001 Pct O_2	Ingot No. Oxy 2, 0.0002 Pct O_2	Ingot No. Oxy 3, 0.0006 Pct O_2
260				10,11,12,13
240				16
220		4	3,15,16	1,9
200		90	0,0,4	0,2
180		0,90,90,90	0,0,0	0,0,0,0,2
140		90	2	
120			1,2	
100		0	0	
90			3	
80		85	0	
20	30	4		
0		4		
−20	23			
−30		20		
−40	4,15,15			
−60	3			
−70	0,4,7	0		
−75	4	2		
−80	0,3,4			
−85	0,3			

Fig. 8—Micrograph is of cast molybdenum containing 0.003 pct C, etched in warm $(NH_4)_2HPO_4$:H_2O_2. a—Polished section of sample is shown. X2000. b—Grain surface of specimen is shown. X2000.

Fig. 9—Micrograph is of cast molybdenum containing 0.010 pct C, etched in warm $(NH_4)_2HPO_4$:H_2O_2. a—Polished section of sample is shown. X1000. b—Grain surface of specimen is shown. X2000.

Fig. 10—Micrograph is of cast molybdenum containing 0.024 pct C, etched in warm $(NH_4)_2HPO_4$:H_2O_2. a—Polished section of specimen is shown. X1000. b—Grain surface of specimen is shown. X2000.

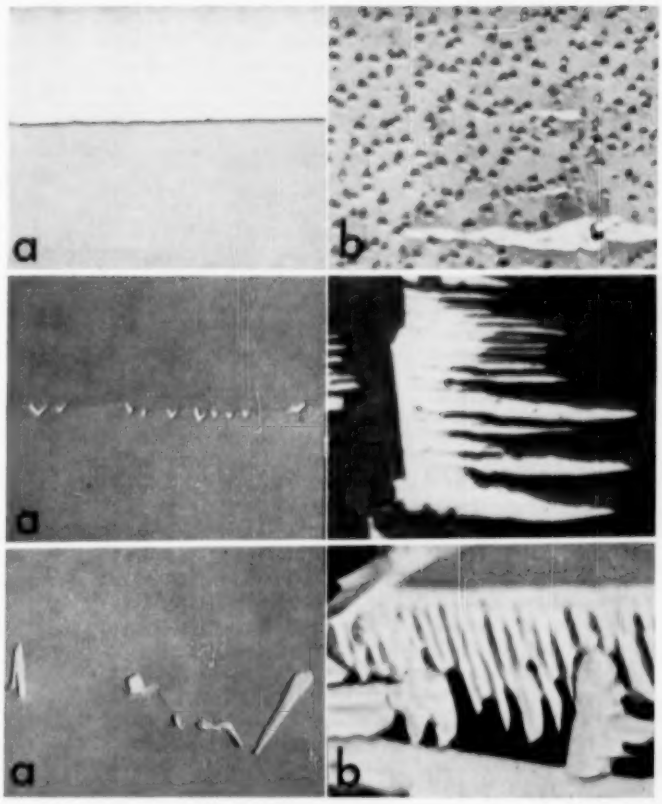

made by treating high purity molybdenum in the same manner as the final samples except that controlled amounts of impurities were added to the acid solution before it was dried.

Table IV. Bend Test Data for High Purity Cast Molybdenum Containing Additions of Nitrogen

Temperature, °C	Bend Angle, Degrees			
	Ingot N1, 0.0008 Pct N_2	Ingot N2, 0.0014 Pct N_2	Ingot N3, 0.0037 Pct N_2	Ingot N4, 0.033 Pct N_2
220				0,0,0,0
200				0,0,4,6
160				0,5
100				0
80			27	
60			0,0,6	0
40		0,1,6	0,3,4,4	
30			0,0,1	
20	0,10	0,6,19	0,0,0,1	0,0
0	0,0,8,10	0,1,13,17		
−20	1,2,6,11	6		
−40	0,0,0,2,2,2	2,4		
−60	0,1	0,0,0,2,2		
−70		0		

Microstructure

Fractography has been found to be a useful tool for identifying small amounts of precipitated phases when they occur at grain boundaries of cast molybdenum.[10] In this technique, a metal specimen is fractured and the exposed grain surfaces are examined under the microscope. All of the ingots were examined in this manner to assist in the identification of the precipitated phases found in the ingots. Samples cut from the ingots were also polished and examined by conventional metallographic techniques. Typical micrographs and fractographs of some of the ingots are shown in Figs. 1 through 10.

The grain boundaries in the high purity control ingot were clean and free from precipitated phases, as shown in Fig. 1. Only microporosity was observed on the grain surfaces in this ingot.

The addition of oxygen to cast molybdenum resulted in an increase in the amount of microporosity and in the precipitation of an oxide phase at grain boundaries. Figs. 2 through 4 show the manner in which the oxide phase increased in amount as the oxygen content of the ingots was increased from 0.0001 to 0.0006 pct. At approximately 0.0002 pct O, the grain surfaces were speckled with very fine particles of the precipitated phase, Fig. 3b. A further increase in oxygen content caused these fine particles to form into visible platelets, Fig. 4b. The precipitated phase observed in this series of ingots was of a reddish-brown color, probably MoO_2.

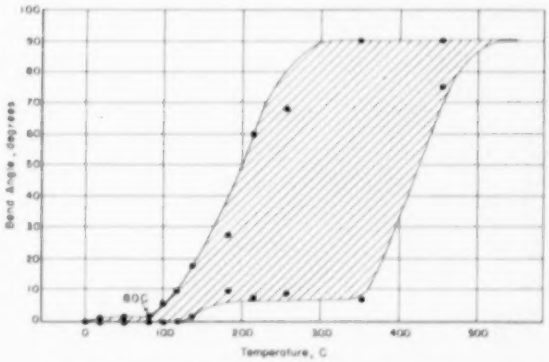

Fig. 11—Chart plots scatter in bend test data for commercial cast molybdenum.

Table V. Bend Test Data for High Purity Cast Molybdenum Containing Additions of Carbon

Temperature, °C	Bend Angle, Degrees					
	Ingot C1, 0.003 Pct C	Ingot C2, 0.006 Pct C	Ingot C3, 0.008 Pct C	Ingot C4, 0.010 Pct C	Ingot C5, 0.020 Pct C	Ingot C6, 0.024 Pct C
60	90				0,0,13,15	0,5
50					3,6,7,13	0,0
40	7			2,3,20	0,0,0,0,0	0,0,0,2,2,2
30						0,0
20	0,2,12	41	24	0,10	0,0	0
10	0	15	6,7	0,0		
0	4		0,6,25	0,0		
−10		5,9	0,0,0,0			
−15	3	0,0,14	0			
−20		0,0,0				
−30	0,3,7	0,1				
−40	0,0,1					

Micrographs and fractographs of the ingots which were melted in nitrogen are shown in Figs. 5 through 7. The phase which was observed in these ingots first occurred as platelets both at the grain boundaries and within the grains. As the nitrogen content was increased, the platelets grew in size and assumed a feathery structure, as may be seen in the fractograph of Fig. 7b. Because this phase resembled Mo_2C in some respects, attempts were made to establish positive identification. Preliminary examinations were made on freshly fractured grain surfaces of ingot N4, using electron diffraction and X-ray spectrometer techniques. However, only diffraction lines characteristic of molybdenum could be obtained. A number of grain surfaces were then lightly scraped to concentrate the intergranular phase for powder diffraction methods. The strongest lines in the diffraction pattern were those of molybdenum metal, but there were additional faint lines which could be attributed to the intergranular phase. This same family of lines resulted from several different scrapings. Although the lines representing the intergranular phase were too faint for precise measurements, the *d*-values that were obtained agreed well with similar values reported by Hagg for Mo_2N.[11] There were differences between the *d*-values obtained from the faint lines and the standard lines for MoO_2 and Mo_2C. On the basis of these results, the intergranular phase in the ingots of the nitrogen series was tentatively identified as Mo_2N.

Micrographs and fractographs of the ingots containing carbon are shown in Figs. 8 through 10. The grain surfaces in the cast molybdenum ingot containing 0.003 pct C (ingot C1) were covered with fine particles of another phase. As the carbon content increased, these particles grew larger and assumed the feathery shape typical of Mo_2C.[10] The carbide particles at grain boundaries were quite angular in shape, as may be seen in Figs. 9 and 10. Carbide particles within the grains were not so angular as those at the grain boundaries.

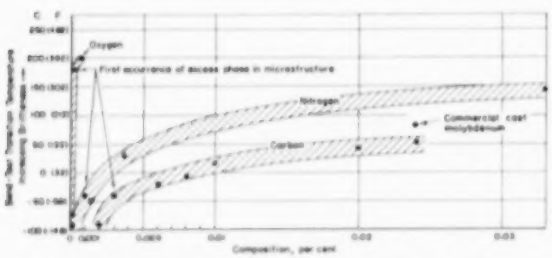

Fig. 12—Chart plots effect of oxygen, nitrogen, and carbon upon bend test transition temperature of cast molybdenum; and transverse grain orientation is illustrated. The strain rate is 0.038 in. per in. per sec; transition temperatures are based upon a 4° bend angle.

Ductility Tests

Molybdenum, like other body-centered-cubic metals, changes from ductile to brittle behavior as the testing temperature is lowered.[12] One measure of ductility is the temperature at which the transition from ductile to brittle behavior occurs. A specimen with a low transition temperature is considered to be more ductile than one with a high transition temperature. The effects of impurities on the ductility of cast molybdenum were evaluated by determining the manner in which the impurities affected the transition temperature of molybdenum.

A bend test was selected as a means for measuring the transition temperatures. Small specimens were supported as a simple beam and a load was applied to a ⅛ in. diam rod laid transversely across the center of the specimen. The specimens were 0.150 in. thick by 0.250 in. wide, and the length between supports was 0.625 in. They were tested in the unnotched condition with ground surfaces.

The various testing temperatures were obtained as shown in Table II.

Fischer and Jackson have shown that cast molybdenum is highly directional in properties.[13] Therefore, all specimens were cut from the ingots so that the columnar grains of the original ingot were transverse to the long axes of the specimen.

The rate of loading was 1 in. per min. At this speed, the initial rate of tensile strain in the outer fibers of the specimen was computed to be 0.038 in. per in. per sec. This is a faster rate of strain than is customary for most tensile or bend tests.

At the beginning of the experimental work, the transition was arbitrarily assumed to occur at the highest temperature at which all ductility vanished. It was later possible, however, to provide a better criterion for the evaluation of the transition temperatures. This was done by testing a large number of specimens of commercial carbon deoxidized cast molybdenum over a range of temperatures from complete ductility to complete brittleness. The results of these tests are shown in Fig. 11. In this graph, the extreme values of ten tests are plotted for each temperature. Thus, the curves represent the approximate limit of scatter in the test results.

For the regions of low ductility in Fig. 11, the most closely defined section is that at which the bend angle never exceeded four degrees. Therefore, the bend test transition temperature of all ingots in the present study was defined as the highest temperature at which a four degree bend angle would not be exceeded, regardless of the number of tests which might be performed at that temperature. The

number of specimens available from the ingots containing the impurity elements was insufficient to make possible the accurate location of this transition temperature. Therefore, the transition temperature chosen in the tests must be considered only as approximate. In most cases, the accuracy is believed to be about ±10°C.

On the basis of the data given in Tables III through V, approximate transition temperatures were assigned to the ingots, as listed in Table VI.

Discussion of Effects of Impurities in Cast Molybdenum

A comparison of the effects of oxygen, nitrogen, and carbon on the bend test transition temperature of cast molybdenum is given in Fig. 12. Minute amounts of oxygen severely embrittle cast molybdenum. Embrittlement is associated with oxygen contents in the range of 0.0001 to 0.0006 pct. An increase in the oxygen content from 0.0001 to 0.0002 pct was enough to raise the transition temperature from −60° to +200°C. It must be remembered, however, that these analyses for oxygen are at the extreme lower limit of the vacuum fusion method. The abrupt rise in transition temperature (drop in ductility) may not occur exactly between 0.0001 and 0.0002 pct O, but it does occur as close to that range as present analytical methods can detect.

Although nitrogen is not nearly so harmful as oxygen to the ductility of cast molybdenum, it is more harmful than carbon. The greatest increase in embrittlement occurred when nitrogen increased in amount below the solubility limit. The presence of an indigenous phase was first observed at a nitrogen content of about 0.001 pct. Beyond this approximate limit of solubility, the rate of embrittlement decreased. As little as 0.004 pct N caused the complete loss of ductility in molybdenum at room temperature.

Table VI. Transition Temperatures* of High Purity Cast Molybdenum Containing a Single Impurity Element

Ingot	Transition Temperature, °C
High purity control ingot	−80
Oxygen Series	
Oxy 1, 0.0001 pct O_2	−60
Oxy 2, 0.0002 pct O_2	200
Oxy 3, 0.0006 pct O_2	200
Nitrogen Series	
N1, 0.0008 pct N_2	−40
N2, 0.0014 pct N_2	−40
N3, 0.0037 pct N_2	40
N4, 0.033 pct N_2	140
Carbon Series	
C1, 0.003 pct C	−40
C2, 0.006 pct C	−30
C3, 0.008 pct C	−10
C4, 0.010 pct C	0
C5, 0.020 pct C	40
C6, 0.024 pct C	50

* Transition temperatures are based on 4° bend angle criterion.

It is interesting to compare the ductility of ingot N4 with the curve for the oxygen series, since this ingot had a relatively high oxygen content, 0.0015 pct O_2. On the basis of Fig. 12, this amount of oxygen would ordinarily be expected to give an ingot with a transition temperature above 200°C. Since the high nitrogen ingot had a transition temperature of only 140°C, it appears that nitrogen may partially offset the embrittling effect of oxygen.

Of the three impurity elements, carbon was the least harmful to ductility. Room temperature ductility of carbon-containing ingots did not vanish until the carbon content was approximately 0.014 pct. As in the case of nitrogen, the greatest increase in embrittlement was observed for carbon contents below the limit of solid solubility. For the ingots of the carbon series, a second phase was observed at a carbon content of 0.003 pct. Beyond this approximate solubility limit, the rate of embrittlement decreased with increasing carbon content.

The transition temperature for the commercial carbon deoxidized cast molybdenum ingot used to evaluate the bend test was 20°C above the carbon curve in Fig. 12. Although the agreement between the ductility of commercial carbon deoxidized molybdenum and the ductility of the ingots in the carbon series is not as close as could be desired, it does indicate that carbon is one major cause of the room temperature brittleness in commercial vacuum melted, carbon deoxidized cast molybdenum.

Conclusions

The following conclusions are drawn:

1—The cold ductility of cast molybdenum is severely harmed by minute amounts of oxygen. The oxygen content for room temperature brittleness is about 1 to 2 ppm (0.0001 to 0.0002 pct).

2—Nitrogen is detrimental to the cold ductility of cast molybdenum, but not nearly to the same extent as oxygen. Room temperature brittleness occurs at nitrogen contents of approximately 30 ppm (0.003 pct).

3—Carbon is harmful to the cold ductility of cast molybdenum, but it is not as harmful as either oxygen or nitrogen. Room temperature ductility vanished at carbon contents of about 140 ppm (0.014 pct).

4—The embrittling effects of oxygen and nitrogen are not additive. There was some indication that nitrogen may even offset some of the brittleness induced by oxygen.

Acknowledgments

The support of this work by the ONR is gratefully acknowledged. The generous assistance given by H. B. Goodwin, C. H. Lorig, R. B. Fischer, H. W. Lownie, Jr., C. B. Griffith, F. L. Wilkinson, and other staff members of Battelle Memorial Institute is appreciated by the authors.

Discussion of this paper, if any, will appear in JOURNAL OF METALS, November 1956, and in AIME Metals Branch *Transactions*, Vol. **206**, 1956.

References

[1] J. H. Bechtold: Recrystallization Applied to Control of the Mechanical Properties of Molybdenum. *Trans.* ASM (1954) **46**, pp. 1449-1469.

[2] G. W. P. Rengstorff and R. B. Fischer: Cast Molybdenum of High Purity. *Trans.* AIME (1952) **194**, pp. 157-160; JOURNAL OF METALS (February 1952).

[3] R. M. Parke and J. L. Ham: The Melting of Molybdenum in the Vacuum Arc. *Trans.* AIME (1947) **171**, p. 416; METALS TECHNOLOGY (September 1946).

[4] R. E. Maringer and A. D. Schwope: On the Effect of Oxygen in Molybdenum. *Trans.* AIME (1954) **200**, p. 365; JOURNAL OF METALS (March 1954).

[5] T. G. Perry, H. S. Spacil, and J. Wulff: Effective Heat Treatment of Molybdenum. *Metal Progress* (1954) **65**, pp. 75-77.

[6] P. Tury and S. Krausz: Effect of Molecular Nitrogen on Molybdenum at High Temperatures. *Nature* (1936) **138**, p. 331; (1937) **139**, pp. 30-31.

[7] W. L. Bruckart, M. H. LaChance, C. M. Craighead, and R. I. Jaffee: Properties of Some Hydrogen-Sintered Binary Molybdenum Alloys. *Trans.* ASM (1953) **45**, pp. 280-313.

[8] M. W. Mallett and C. B. Griffith: Vacuum-Fusion Analysis of Molybdenum. *Trans.* ASM (1954) **46**, pp. 375-388.

[9] C. L. Luke: Photometric Determination of Sulfur in Metals and Alloys. *Analytical Chemistry* (1949) **21**, pp. 1369-1373.

[10] C. A. Zapffe, F. K. Landgraf, Jr., and C. O. Worden, Jr.: Fractographic Study of Cast Molybdenum. *Trans.* AIME (1949) **180**, p. 616; METALS TECHNOLOGY (August 1948).

[11] G. Hagg: X-Ray Investigations of Molybdenum and Tungsten Nitrides. *Ztsch. fur Physikaltsche Chemie* (1930) **B7**, pp. 339-362.

[12] J. H. Bechtold: Effects of Temperature on the Flow and Fracture Characteristics of Molybdenum. *Trans.* AIME (1953) **197**, pp. 1469-1475; JOURNAL OF METALS (November 1953).

[13] R. B. Fischer and J. H. Jackson: The Ductility of Cast Molybdenum. *Trans.* AIME (1950) **188**, pp. 1149-1154; JOURNAL OF METALS (September 1950).

Creep of Copper at Intermediate Temperatures

Activation energies for creep of copper at intermediate temperatures, where crystal recovery was negligible, were determined by the simple technique of rapidly alternating the test temperature between T_1 and T_2 ($T_2 = T_1$ + about 10°K) throughout a constant stress creep test. The activation energy for creep ΔH was found to be 37,000± 3,000 cal per mol, independent of stress and strain. The same creep laws as have been previously established for high temperature creep were found to be valid for creep at intermediate temperatures. But the ΔH was found to be lower than that for self-diffusion in the intermediate temperature range whereas it is known to be equal to that for self-diffusion at high temperatures.

by T. E. Tietz and J. E. Dorn

IT is now well established that creep at high temperatures can be correlated by the functional relationship[1-4]

$$\epsilon = f(\theta) \qquad \sigma = \text{constant} \qquad [1]$$

where ϵ is the total plastic strain, f is the function that depends on the stress, $\theta = \int_0^t e^{-\frac{\Delta H}{RT}}\,dt$, t is the duration of test, e is the base of natural logarithms, ΔH is the activation energy for creep, R is the gas constant, T is the absolute temperature, and σ is the stress. Thus, identical values of θ are achieved during creep under a given stress at two alternate temperatures at the same total strain. At the same strain therefore

$$t_1 e^{-\frac{\Delta H}{RT_1}} = t_2 e^{-\frac{\Delta H}{RT_2}} \qquad [2]$$

where subscripts refer to the two alternate temperature conditions of test. Consequently, the activation energy for high temperature creep is readily obtained with the aid of Eq. 2. Activation energies so obtained have been observed to be insensitive to the creep strain at which they are evaluated, the applied stress, grain size, minor alloying additions,[1-4] cold worked state,[5] and the presence of thermally stable dispersions of intermetallic compounds in an α solid solution matrix.[6] Furthermore, the activation energy for high temperature creep is very nearly equal to that for self-diffusion in all cases where adequate data are available for comparison.[5, 7]

The apparent identity of the activation energies for high temperature creep and self-diffusion strongly suggest that high temperature creep arises from a dislocation climb process. This hypothesis is further strengthened by the fact that the energy of activation for high temperature creep is insensitive to the applied stress,[1,8] and by the observations that the correlation suggested by Eq. 1 cannot be extended to temperatures below those for rapid crystal recovery.[1]

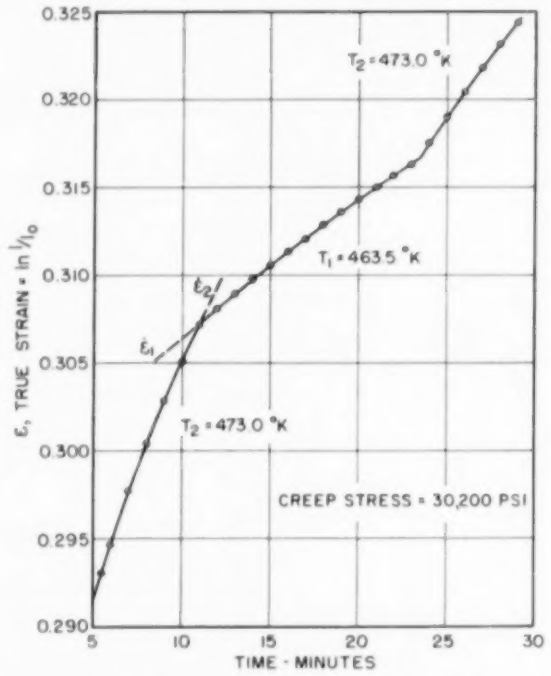

Fig. 1—Creep curve shows two temperature changes.

When using the activation energy for self-diffusion, Eq. 1 fails to give the required correlations between creep curves at various intermediate temperatures.[1] This suggests that the dislocation climb mechanism for creep might be superseded by some alternate mechanism in the intermediate range of temperatures. This investigation was initiated in a preliminary attempt to ascertain the type of creep law that might be valid in the intermediate range of temperatures. Special consideration, however, was given to the determination of the activation energy for creep in this range because the Becker-Orowan[5, 9] and the Mott-Nabarro[10] theories for transient creep suggest that the activation energy should increase

T. E. TEITZ, Member AIME, formerly Graduate Student, University of California, is Associate Physical Metallurgist, Stanford Research Institute, Stanford, Calif., and J. E. DORN, Member AIME, is Professor of Physical Metallurgy, University of California, Berkeley, Calif.

Discussion of this paper, TP 4052E, may be sent, 2 copies, to AIME by Apr. 1, 1956. Manuscript, Oct. 11, 1954. Philadelphia Meeting, October 1955.

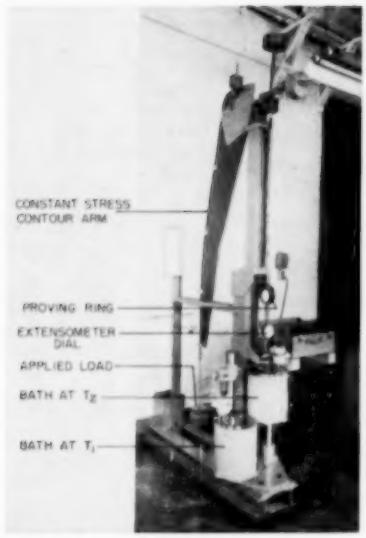

Fig. 2—Creep testing machine employs a special Andrade-type[15] contoured lever arm designed to maintain a constant stress on the specimen.

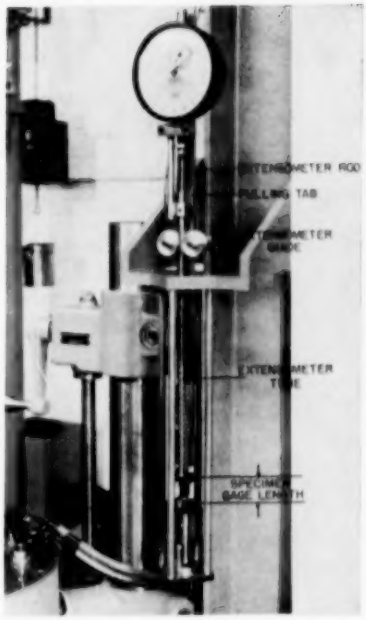

Fig. 3—Creep specimen and extensometer are shown in test position. Creep strains are measured by a concentric rod and tube-type extensometer.

with strain and the Kauzmann-Seitz[11, 12] types of thermal activation theories suggest further that the activation energy should decrease with increasing values of the applied stress. Thus, a knowledge of the effect of strain or stress on the activation energy for creep might provide definitive information on several possible mechanisms for creep.

Experimental Technique

The creep rate continually changes during isothermal-constant stress creep tests. Since all of the externally controllable variables are maintained constant, the change in the creep rate must be ascribed to structural changes that attend the process of creep. For example, it has been shown that the success of Eq. 1 for high temperature creep is attributable in part to the fact that identical structures are produced at the same values of θ for creep at a given stress, independent of the test temperature.[2] Special precautions must therefore be taken in any evaluation of the activation energy for creep, so that the value obtained is a true activation energy that is free from possible errors arising from neglect of structural differences.

A simple and direct technique for determining the activation energy for creep was used in the present investigation. As shown by the typical example given in Fig. 1, this technique consisted of alternating the temperature between T_1 and T_2 throughout a constant stress creep test. Since no abrupt changes in strain occurred and no spurious transients were detected in the creep rates, the structure was presumed to be the same the instant before and the instant following the rapid change in temperature. Consequently, for each point of temperature change, a true activation energy for creep at the given stress could be obtained from the well known relationship

$$\dot{\epsilon}_1 e^{\frac{\Delta H}{RT_1}} = \dot{\epsilon}_2 e^{\frac{\Delta H}{RT_2}} \qquad [3]$$

where $\dot{\epsilon}$ is the creep rate and the subscripts refer to the conditions just preceding and immediately following an abrupt change in temperature. This technique involves only the assumption that creep occurs by means of some thermal activation process; it is valid for any creep mechanisms that depend on thermal activation. Only one specimen is used in evaluating the activation energy and therefore the effects of sampling scatter on the calculated activation energy are eliminated; the accuracy of the activation energy so obtained depends exclusively on the accuracy with which the strain rates and temperatures can be determined.

A technique similar to that described here has been applied by Kuhlmann and Masing[13] and Lucas

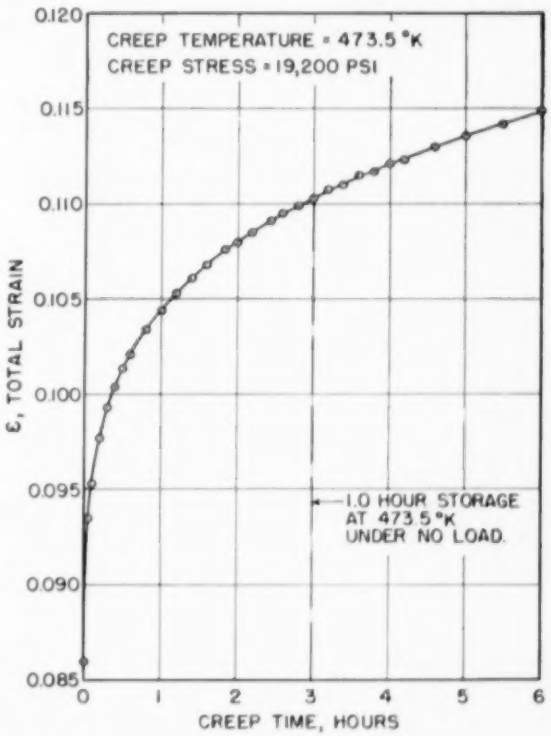

Fig. 4—Interrupted creep test shows effect of storage at creep temperature under no load for OFHC copper.

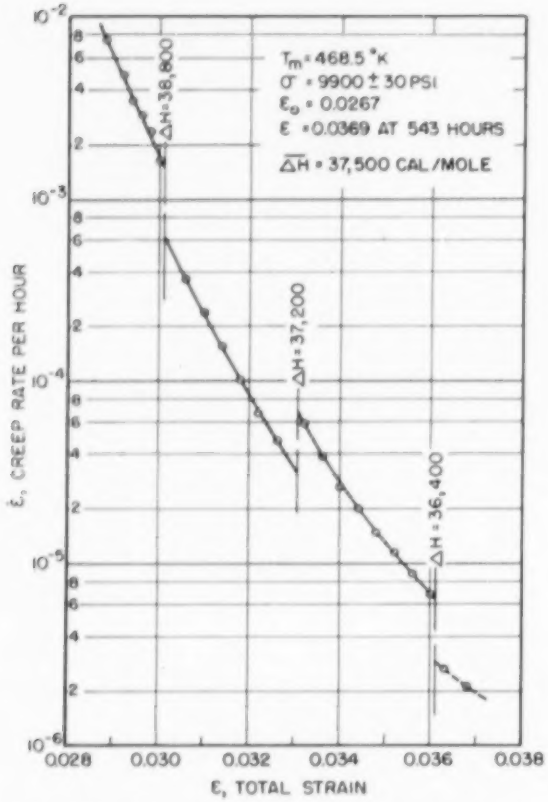
T_m = 468.5 °K
σ = 9900 ± 30 PSI
ε_o = 0.0267
ε = 0.0369 AT 543 HOURS
$\overline{\Delta H}$ = 37,500 CAL/MOLE
ΔH = 38,800
ΔH = 37,200
ΔH = 36,400
$\dot{\varepsilon}$, CREEP RATE PER HOUR
ε, TOTAL STRAIN

Fig. 5—Graph illustrates creep rate vs strain curves for use in the evaluation of ΔH for OFHC copper.

and Masing[4] to investigations on the creep of hard drawn springs of aluminum and copper.

Test Equipment

The experimental equipment that was used in this investigation is identified in Fig. 2. The load was applied to the specimen by means of a special Andrade-type[5] contoured lever arm that was designed so as to maintain a constant stress on the specimen throughout a creep test. As the specimen elongated, its cross-sectional area decreased and the lever arm correspondingly decreased to maintain the stress constant. Small deviations in strain between the gage section and the total reduced section, however, led to minor variations in the true stress on the specimen. In order to ascertain the variations in stress, a proving ring was placed in series with the specimen. The maximum variation in stress did not exceed about 1.2 pct throughout any one test and was usually much less.

Special silicone oil temperature baths were employed in order to obtain necessary accuracy in the test temperatures. A thermocouple on the specimen showed that the steady state temperature did not vary more than ±0.1°C throughout any one temperature cycle. Upon change in temperature, the time required for the specimen to come to within 0.2°C of the new test temperature was usually between 1 and 2 min and in all cases was less than 4 min. The creep strain rates were evaluated only after the steady state temperature was reached and, as shown in the context, they were extrapolated through the transient temperature range to the instantaneous value following the instant the temperature was changed.

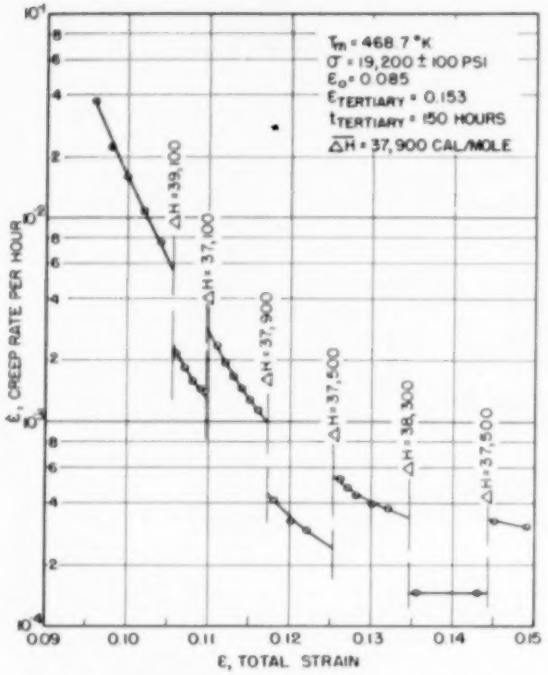

Fig. 6—Graph illustrates creep rate vs strain curves for use in the evaluation of ΔH for OFHC copper.

As shown in Fig. 3, the creep strains were measured by means of a concentric rod and tube-type extensometer which actuated a 0.0001 in. dial gage.

Test Material

Several simple requirements were demanded of the metal to be used in this investigation:

1—The metal should not exhibit rapid crystal recovery at the highest usable temperatures (about 470°K), of the silicone oil baths.

2—It should be relatively pure in order to provide reasonable freedom from possible auxiliary solid solution effects.

3—The metal should exhibit accurately determinable creep rates in the range from about 300° to 475°K over a reasonably broad range of stresses and strains.

A few preliminary investigations demonstrated that OFHC copper exhibited the required specifications. Tensile creep specimens of OFHC copper were machined from 0.125 in. thick sheet material with their axes parallel to the rolling direction. Each specimen was 0.250 in. wide and had a reduced section of 1.500 in., the central 1.000 in. of which constituted the gage section. After machining, the specimens were annealed in a helium atmosphere for 1½ hr at 748°K and then furnace cooled. The resulting average grain diameter was 0.02 mm.

A check on the recovery of the OFHC copper is illustrated in Fig. 4. A specimen was allowed to creep to about 11 pct total strain during which time the creep rate decreased several orders of magnitude due to the structural changes induced by the creep deformation. At this point, the stress was removed in order to permit recovery at the test temperature of 473.5°K. Following a period of 1 hr the stress of 19,200 psi was reapplied. The fact that the creep curve continued as if the test had not been interrupted for annealing suggests that recovery under

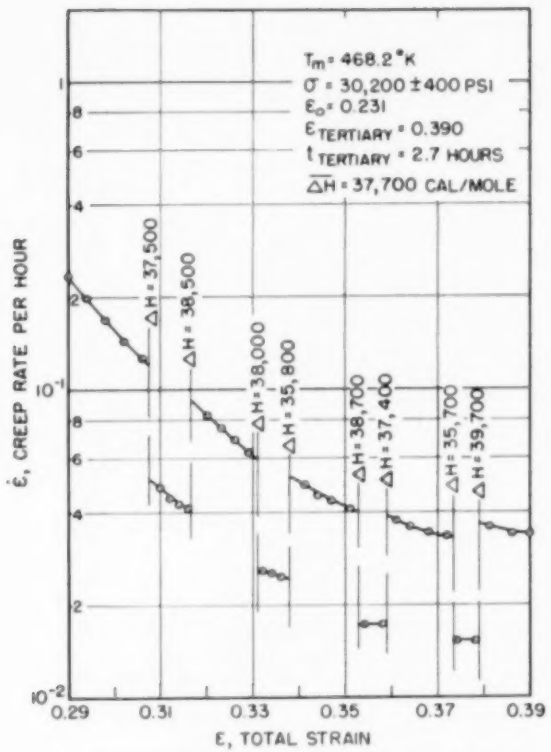

Fig. 7—Graph illustrates creep rate vs strain curves for use in the evaluation of ΔH for OFHC copper.

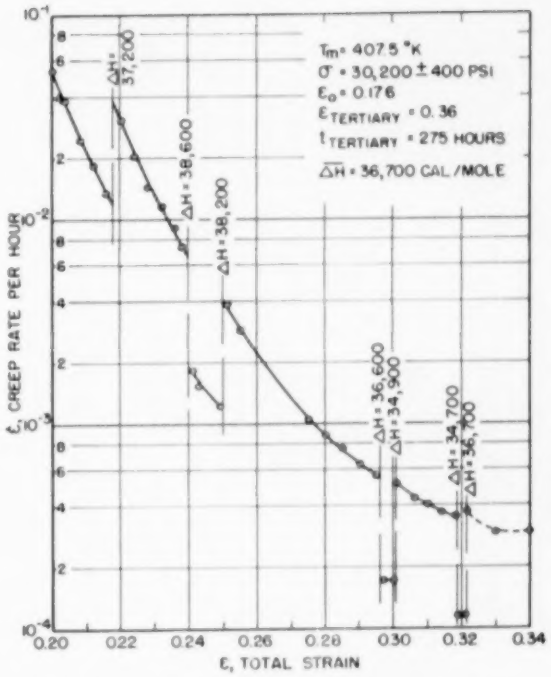

Fig. 8—Graph illustrates creep rate vs strain curves for use in the evaluation of ΔH for OFHC copper.

zero stress of the structural changes induced by the preceding creep was indeed negligible.

Experimental Results

Creep rates were determined by graphical differentiation of the original creep curves such as that illustrated in Fig. 1. Such derived creep rate vs total plastic strain curves are given in Figs. 5 to 11. T_s is the mean temperature, ϵ_o the initial strain on loading, and $\overline{\Delta H}$ the average activation energy of the test. The instantaneous activation energy for each change in temperature was determined from the two test temperatures and the extrapolated strain rates at the instant the temperature was changed in accord with Eq. 3.

Discussion

A detailed summary of all activation energies that were determined is recorded in Fig. 12. These data reveal that the activation energy for creep of OFHC copper over the range of intermediate temperatures from 348° to 469°K is about 37,000±3,000 cal per mol, independent of the total strain from $\epsilon \cong 0.03$ to 0.38, and independent of the applied stress from $\sigma \cong$ 9,900 to 38,300 psi. Obviously neither the Becker-Orowan and Mott-Nabarro nor the Kauzmann-Seitz types of creep theories apply to creep in the intermediate range of temperatures. The insensitivity of the activation energy to stress or strain is somewhat reminiscent of high temperature creep. However, the activation energy for high temperature creep is expected to be that for self-diffusion, namely about 48,000 cal per mol for copper.[5] The value obtained here, 37,000 cal per mol, suggests that a somewhat different mechanism for creep applies over the intermediate range of temperatures.

Additional insight into the details of creep at intermediate temperatures can be gained by further analysis of the data reported here. The decreasing creep rates obtained during the course of isothermal creep at constant stress are ascribable to changes in structure. Since the ΔH of the present investigation is insensitive to the strain, it is insensitive to the structural changes attending creep. Consequently,

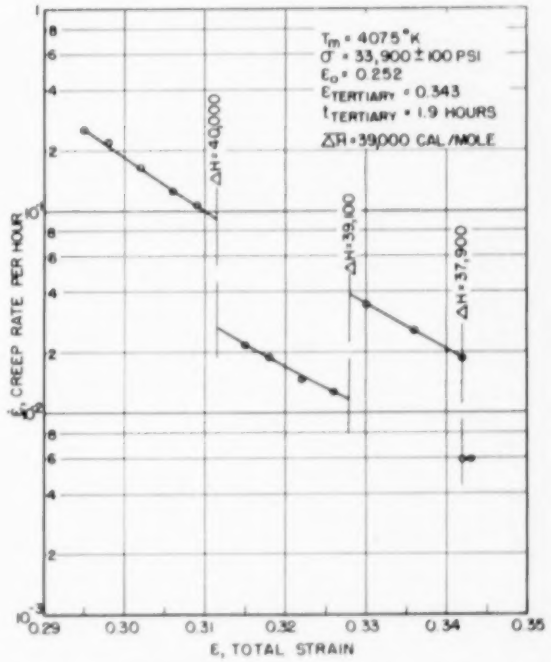

Fig. 9—Graph illustrates creep rate vs strain curves for use in the evaluation of ΔH for OFHC copper.

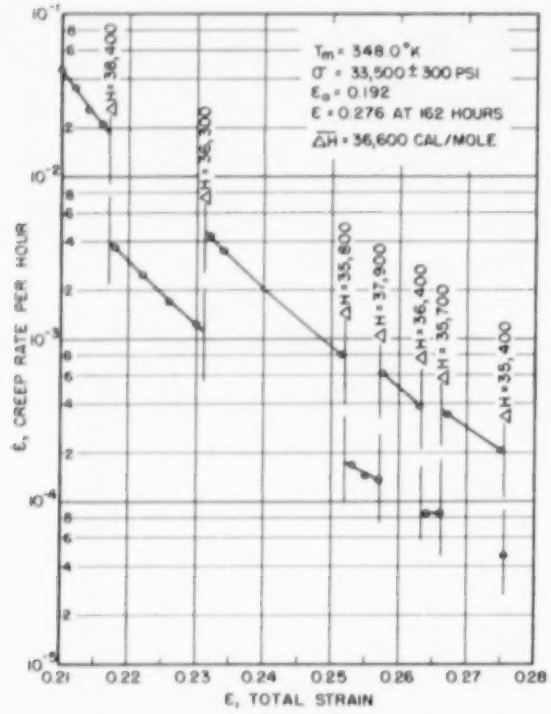

Fig. 10—Graph illustrates creep rate vs strain curves for use in the evaluation of ΔH for OFHC copper.

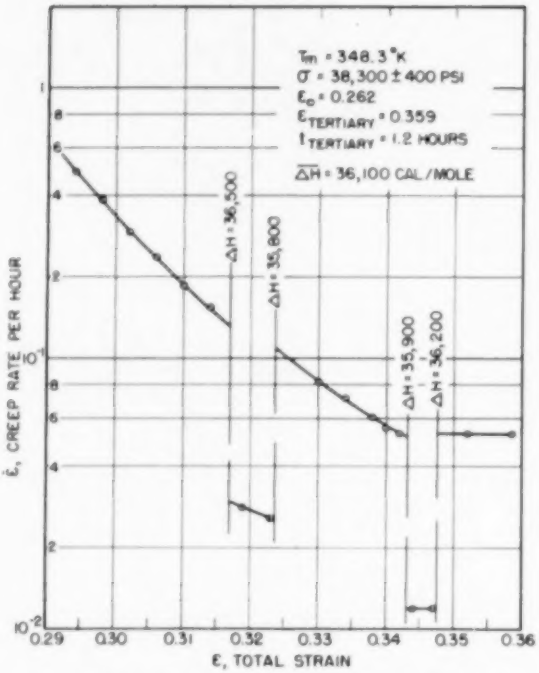

Fig. 11—Graph illustrates creep rate vs strain curves for use in the evaluation of ΔH for OFHC copper.

in the intermediate as well as the high temperature range of creep

$$\dot{\epsilon}e^{\frac{\Delta H}{RT}} = f \text{ (structure)} \qquad \sigma = \text{constant.} \quad [4]$$

Previous investigations have shown that the structure obtained for high temperature creep at a given stress depends only on the total strain, ϵ, or on θ, independent of the test temperature. The question naturally arises as to whether this law is also valid over the intermediate temperature range or whether the structure depends on other types of relationships.

In Fig. 13, $\dot{\epsilon}e^{\frac{\Delta H}{RT}}$ for a stress of 30,200 psi is plotted as a function of the total strain, ϵ, for each of two mean temperatures of 407.5° and 468.2°K. Similarly in Fig. 14, $\dot{\epsilon}e^{\frac{\Delta H}{RT}}$ is plotted for almost identical stresses of about 33,700 psi as a function of the total strain, ϵ, for each of the two mean temperatures of 348.0° and 407.5°K. Both sets of data reveal that

$$\dot{\epsilon}e^{\frac{\Delta H}{RT}} = F(\epsilon) \qquad \sigma = \text{constant.} \quad [5]$$

Consequently, the structure obtained during creep of an annealed specimen at a given stress in the intermediate range of temperatures depends on the strain and is independent of the test temperature in harmony with the corresponding high temperature creep law.

Inasmuch as recovery of the structural changes induced by creep of annealed copper was found to be negligible in the intermediate range of temperatures under investigation here, and inasmuch as the temperature differences were reasonably modest, the foregoing conclusion might have been antici-

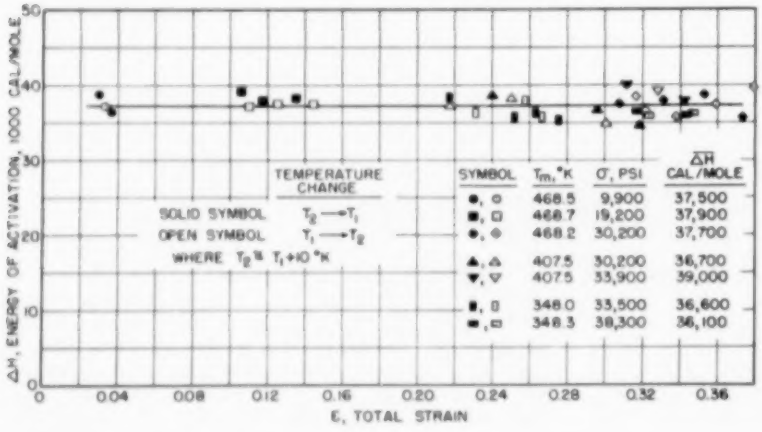
TEMPERATURE CHANGE
SOLID SYMBOL $T_2 \rightarrow T_1$
OPEN SYMBOL $T_1 \rightarrow T_2$
WHERE $T_2 \cong T_1 + 10$ °K
SYMBOL | T_m, °K | σ, PSI | $\overline{\Delta H}$ CAL/MOLE
●, ○ | 468.5 | 9,900 | 37,500
■, □ | 468.7 | 19,200 | 37,900
◆, ◇ | 468.2 | 30,200 | 37,700
▲, △ | 407.5 | 30,200 | 36,700
▼, ▽ | 407.5 | 33,900 | 39,000
●, □ | 348.0 | 33,500 | 36,600
■, □ | 348.3 | 38,300 | 36,100
ΔH, ENERGY OF ACTIVATION, 1000 CAL/MOLE
ε, TOTAL STRAIN

Fig. 12—Chart records detailed summary of energy of activation as a function of strain.

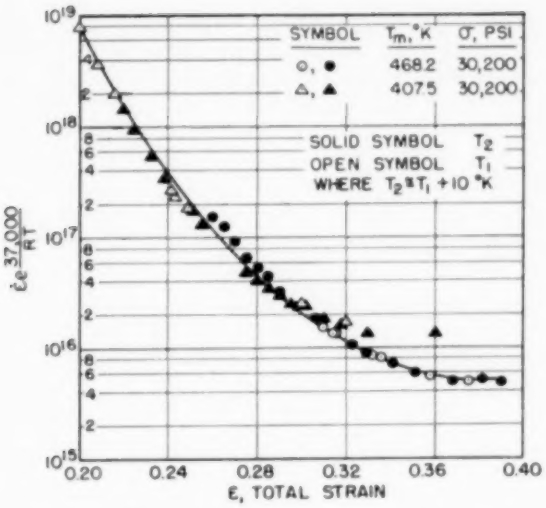

Fig. 13—$\dot{\epsilon}\, e^{\frac{\Delta H}{RT}}$ for a stress of 30,200 psi is plotted as a function of ϵ.

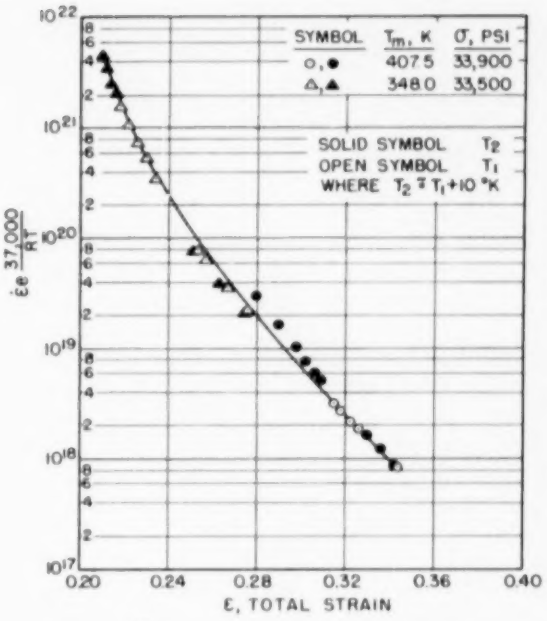

Fig. 14—$\dot{\epsilon}\, e^{\frac{\Delta H}{RT}}$ is plotted for stresses of about 33,700 psi as a function of the total strain, ϵ.

pated. On the other hand, the absence of recovery and the differences in the initial strain for creep at two alternate temperatures might suggest that the structure developed during creep at a given stress in the intermediate range of temperatures might not be a unique function of θ. However, as shown by the data given in Figs. 15 and 16, this conclusion appears to be incorrect, and

$$\dot{\epsilon} e^{\frac{\Delta H}{RT}} = \frac{d\epsilon}{d\theta} = \Psi(\theta) \qquad \sigma = \text{constant} \quad [6]$$

for both high and intermediate temperature creep. This is illustrated more forcefully by integrating Eq. 6 with respect to θ which gives the well established Eq. 1 for high temperature creep. Thus, both high and intermediate temperature creep obey the same laws as demanded by Eqs. 1, 5, and 6. The difference between creep in these two ranges arises from the fact that the activation energy for high temperature creep is that for self-diffusion whereas that for creep at intermediate temperatures is significantly less than that for self-diffusion. It is this difference rather than a failure of the laws of high temperature creep that was responsible for the poor correlations obtained by means of Eq. 1 in the intermediate range of temperatures when the ΔH for self-diffusion was applied.

Whereas theoretical support can be given for the coincidence of the activation energy for high temperature creep and that of self-diffusion, the authors have not yet been able to justify the activation

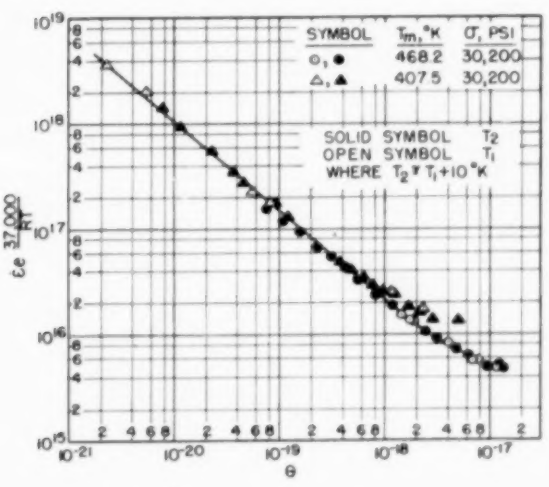

Fig. 15—$\dot{\epsilon}\, e^{\frac{\Delta H}{RT}}$ as a function of θ is illustrated.

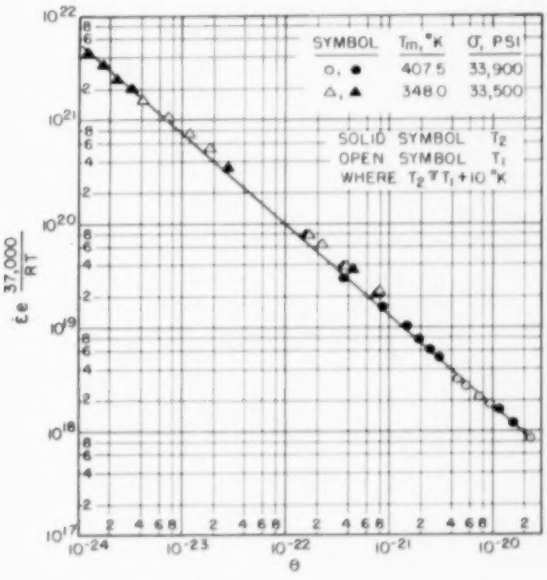

Fig. 16—$\dot{\epsilon}\, e^{\frac{\Delta H}{RT}}$ as a function of θ is illustrated.

energy of 37,000 cal per mol for the creep of copper in the intermediate temperature range. A simple dislocation climb model for high temperature creep suggests that as edge dislocations that are impeded by barriers climb out of their slip planes, the back stress that they induce on their Frank-Read sources decreases and new dislocations are released. Consequently, the creep rate should be proportional to the rate of dislocation climb which is dependent on the product of the number of vacancies present per unit volume, n_v, and the probability of an atom-vacancy exchange. Therefore

$$\dot{\epsilon} \propto n_v e^{-\frac{E_e}{kT}}$$

where E_e is the activation energy for an atom-vacancy exchange. Seitz[12] has suggested that the number of vacancies produced during creep is proportional to the creep strain. But at high temperatures, such vacancies should diffuse rapidly to various types of sinks so that approximately the equilibrium number of vacancies might be present.

Under these conditions

$$n_v \propto e^{-\frac{E_v}{kT}}$$

where E_v is the energy necessary to produce a vacancy. Consequently, the activation energy for high temperature creep would be $(E_v + E_e)$ which is that for self-diffusion. The similarity of the high and intermediate temperature laws for creep suggests that creep at intermediate temperatures might also arise from a dislocation climb process. At such intermediate temperatures, however, the number of vacancies per unit volume might well exceed the equilibrium number. Thus, the activation energy for creep at intermediate temperatures might approximate E_e. However, according to Brinkman et al.,[17] the activation energy for atom-vacancy exchange as determined by recovery of the electrical resistivity of cold worked copper is about 28,000 cal per mol which is appreciably less than the value of 37,000 cal per mol obtained for creep at intermediate temperatures. Furthermore, some dislocation climb and partial recovery should have occurred during the interrupted creep test previously described if a dislocation climb model were valid in the intermediate temperature range. Additional investigations will be required in order to elucidate the mechanism of creep at intermediate temperatures.

Conclusions

1—The activation energy for creep of copper over the intermediate range of temperatures from 348° to 469°K was found to be 37,000 ± 3,000 cal per mol, independent of the applied stress and the creep strain.

2—Neither the Becker-Orowan, Mott-Nabarro, nor the Kauzmann-Seitz types of creep mechanisms agree with the experimental results on creep at intermediate temperatures.

3—Creep at intermediate temperatures obeys the same general laws as creep at high temperatures, namely

$$\dot{\epsilon} e^{\frac{\Delta H}{RT}} = F(\epsilon) = \Psi(\theta) \qquad \sigma = \text{constant.} \quad [6]$$

But the activation energy for creep at intermediate temperatures differs from that for high temperature creep in that it is less than that for self-diffusion.

Acknowledgments

The authors gratefully acknowledge their appreciation to Oleg Sherby for his assistance in facilitating this study and to L. Crawford and M. Pryor for their aid in the construction of the equipment. They also wish to express their appreciation to G. Pelatowski for the preparation of the figures in this report.

Discussion of this paper, if any, will appear in JOURNAL OF METALS, November 1956, and in AIME Metals Branch *Transactions*, Vol. **206**, 1956.

References

[1] O. D. Sherby and J. E. Dorn: Creep Correlations in Alpha Solid Solutions of Aluminum. *Trans.* AIME (1952) **194**, pp. 959-964; JOURNAL OF METALS (September 1952).

[2] O. D. Sherby and J. E. Dorn: Some Observations on Correlations between the Creep Behavior and the Resulting Structures in Alpha Solid Solutions. *Trans.* AIME (1953) **197**, pp. 324-330; JOURNAL OF METALS (February 1953).

[3] O. D. Sherby, R. L. Orr, and J. E. Dorn: Creep Correlations of Metals at Elevated Temperatures. *Trans.* AIME (1954) **200**, pp. 71-80; JOURNAL OF METALS (January 1954).

[4] B. Fazan, O. D. Sherby, and J. E. Dorn: Some Observations on Grain Boundary Shearing During Creep. *Trans.* AIME (1954) **200**, pp. 919-922; JOURNAL OF METALS (August 1954).

[5] R. E. Frenkel, O. D. Sherby, and J. E. Dorn: Effect of Cold Work on the High Temperature Creep Properties of Dilute Aluminum Alloys. *Trans.* ASM (1955) **47**, pp. 632-649.

[6] W. H. Giedt, O. D. Sherby, and J. E. Dorn: The Effect of Dispersions on the Creep Properties of Aluminum-Copper Alloys. *Trans.* ASME (1955) **77**, pp. 57-63.

[7] J. E. Dorn: Some Fundamental Experiments on High Temperature Creep. *Journal of Mechanics and Physics of Solids* (1954) **3**, pp. 85-116.

[8] R. Becker: Über die Plastizitat amorpher und kristalliner fester Korper. *Physikalische Ztsch.* (1925) **26**, pp. 919-925.

[9] E. Orowan: Crystal Plasticity, I, II, III. *Ztsch. für Physik* (1934) **89**, pp. 605-659.

[10] N. F. Mott and F. R. N. Nabarro: Dislocation Theory and Transient Creep. *Report of a Conference on Strength of Solids*, Physical Soc., London (1948) pp. 1-19.

[11] W. Kauzmann: Flow of Solid Metals from the Standpoint of the Chemical-rate Theory. *Trans.* AIME (1941) **143**, pp. 57-83; METALS TECHNOLOGY (June 1941).

[12] F. Seitz and T. A. Read: Theory of the Plastic Properties of Solids, IV. *Journal of Applied Physics* (1941) **12**, pp. 538-554.

[13] D. Kuhlmann and G. Masing: Untersuchungen zur plastischen Deformation an Kupferdraht. *Ztsch. für Metallkunde* (1948) **39**, pp. 361-375.

[14] G. Lucas and G. Masing: Kriechen von Aluminiumdraht-Spiralen. *Ztsch. für Metallkunde* (1952) **43**, pp. 341-349.

[15] E. N. da C. Andrade and B. Chalmers: The Resistivity of Polycrystalline Wires in Relation to Plastic Deformation, and the Mechanism of Plastic Flow. *Proceedings* Royal Soc. (1932) **138A**, pp. 348-374.

[16] F. Seitz: On the Generation of Vacancies by Moving Dislocations. *Advances in Physics* (1952) **1**, pp. 43-89.

[17] J. A. Brinkman, C. E. Dixon, and C. J. Meechan: Interstitial and Vacancy Migration in Cu_3Au and Copper. *Acta Metallurgica* (1954) **2**, pp. 38-48.

[18] H. Laks, C. D. Wiseman, O. D. Sherby, and J. E. Dorn: Effect of Stress on Creep at High Temperatures. *Inst. of Engineering Research Report* University of California (1954) Series No. 22, Issue No. 37.

Technical Note

Allotropic Transformations in Titanium, Zirconium, and Uranium Alloys

by Austin E. Dwight

A. E. DWIGHT, Member AIME, is Metallurgical Engineer, Argonne National Laboratory, Lemont, Ill.

TN 287E. Manuscript, May 23, 1955.

IT has been shown by Oelsen and Wever[1] that the effect of a solute element on the allotropic transformation in iron is dependent upon the quantity

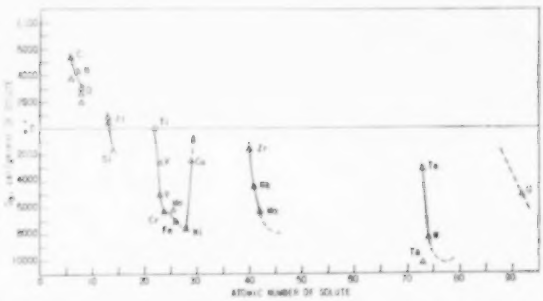

Fig. 1—Heat of reaction is shown vs atomic number of solute (solvent, titanium) for α-β transformation in titanium. Symbols represent: triangle, calculated data; circle, the solvent; and dashed line, extrapolated data.

Q_s in the equation $\ln \frac{x_\alpha}{x_\gamma} = \frac{-Q_s}{RT}$. In this equation x_α and x_γ refer to the atomic percent of solute x which can be held in solution at equilibrium in the α and γ phases, respectively, at temperature T (°K). Q_s is a thermodynamic index quantity, with units in cal per gram-mol of solute. It was further shown that Q_s varies in a periodic manner with the atomic number of the solute when iron is the solvent. In the present investigation, the equation was found to hold true for allotropic transformations in alloys in which titanium, zirconium, and uranium are the solvents.

From the published data on titanium-base alloys, a Q_s value has been calculated, using the modified equation $\log \frac{x_\alpha}{x_\beta} = \frac{Q_s}{4.57\,T}$. Where possible, T was specified as 1073° or 1273°K. The computed Q_s value for each solute element is plotted against the atomic number of the solute in Fig. 1. Although Q_s values for only 17 elements could be calculated, these are sufficiently scattered throughout the periodic table to locate curves for each period. The recognized α stabilizing elements, i.e., carbon, nitrogen, oxygen, and aluminum, have negative Q_s values; the β stabilizers have positive Q_s values.

The allotropic transformation in zirconium is so similar to that in titanium that a periodic variation in Q_s values would also be expected. The larger atomic radius of zirconium requires a slight shift of the zero line. Fig. 2 illustrates the Q_s values calculated for 11 solute elements in zirconium. Due to the shift in the zero line, tin is added to the list of α stabilizing elements.

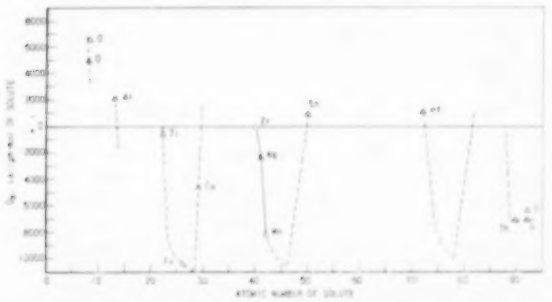

Fig. 2—Heat of reaction is shown vs atomic number of solute (solvent, zirconium) for α-β transformation in zirconium. Symbols represent: triangle, calculated data; circle, solvent; and dashed line, extrapolated data.

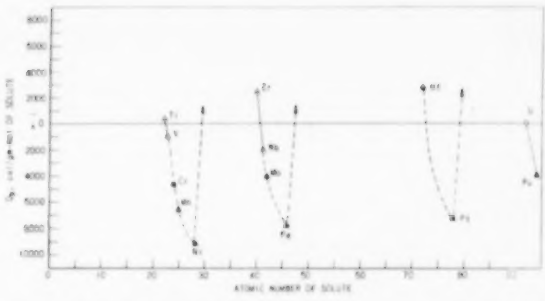

Fig. 3—Heat of reaction is shown vs atomic number of solute (solvent, uranium) for α-β transformation in uranium. Symbols represent: open triangle, calculated data; circle, solvent; dashed line, extrapolated data; and filled triangle, estimated data.

The existence of two allotropic transformations in uranium makes the application of the Q_s vs atomic number relation more complicated. The situation is quite different from that of iron, which also has two transformations, in that the three allotropes of uranium all have different crystal structures. There can be no equivalent of the γ loop found in iron-base diagrams. An analysis of available phase diagrams of uranium-base alloys shows only a few suitable for calculating Q_s values due to lower solubility in uranium and uncertainty as to phase boundary lines. Q_s values are shown in Figs. 3 and 4 for the α-β and β-γ transformations, respectively. Only titanium, zirconium, and probably hafnium are α stabilizers; other solutes are β stabilizers. All reported solutes except silicon are γ stabilizers.

Several practical applications of the Q_s vs atomic number relation are suggested. When conflicting phase diagrams have been published for a binary system having an allotropic transformation, comparison of the computed Q_s values with the periodic curves in Figs. 1 through 4 permits an estimate as to which version of the diagram is most nearly correct.

Secondly, when experimental data are lacking, a Q_s value obtained by extrapolation or interpolation of the curves gives an approximation. The effect of palladium on the allotropic transformation in titanium has not been reported, but by extrapolation, palladium should have a Q_s value of +8000 and should be a strong β stabilizer in titanium.

[1] W. Oelsen and F. Wever: *Archiv. für Eisenhuttenwesen* (1948) 19, p. 97.
[2] A. E. Dwight: *Report ANL-5091* Argonne National Laboratory (September 1953).

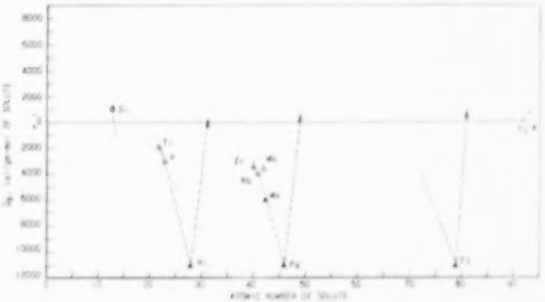

Fig. 4—Heat of reaction is shown vs atomic number of solute (solvent, uranium) of solute for β-γ transformation in uranium. Symbols represent: open triangle, calculated data; circle, solvent; dashed line, extrapolated data; and filled triangle, estimated data.

Self-Diffusion in Single and Polycrystals Of Zinc at Low Temperatures

Self-diffusion in zinc at temperatures below 200°C has been studied using both single crystal and polycrystal samples. Anomalous results were obtained for single crystal samples, the data indicating that in some cases grain boundary diffusion predominated. These anomalous results are presumed to be due to low angle lineage boundaries in the single crystals. When volume diffusion occurred in either single or polycrystal samples, the values for the diffusion coefficient were as much as several orders of magnitude larger than would be expected from high temperature data.

by F. E. Jaumot, Jr. and R. L. Smith

CONSIDERABLE work has been done on self-diffusion at temperatures in the neighborhood of two thirds of the melting temperature (in °K) and higher, but very little has been done at lower temperatures. This is particularly true of self-diffusion in single crystals. This paper reports work on self-diffusion in zinc at temperatures below 200°C where both polycrystalline and single crystal samples have been used. The measurements were made using both the sectioning and absorption techniques.

The experiments on diffusion at low temperatures were initiated primarily for three reasons: to obtain data from single crystal diffusion covering a wide range of temperatures, to obtain values of the activation energy for grain boundary diffusion, and to obtain, if possible, a lower limit to the temperatures at which the absorption technique may be used.

It is possible to determine whether volume or grain boundary diffusion predominates at low temperatures by analyzing the manner in which the concentration of the diffusing atoms varies with the depth of penetration. The analysis is possible only for the sectioning technique. For volume diffusion and for the boundary conditions of the present experiment, the curve of the logarithm of the concentration, C, vs the square of the penetration depth, x, is a straight line with the slope proportional to $-1/D$. If grain boundary diffusion predominates, Fisher[1] has shown that a curve of ln C vs the first power of the penetration depth should be a straight line. This linear dependence of concentration on depth has been observed experimentally by several investigators. (See, for example, refs. 3 and 4.)

Following Fisher's analysis, the grain boundary diffusion coefficient can be written as

$$D = \frac{2}{\delta} \cdot \sqrt{\frac{D_v}{\pi t}} \cdot \left[\frac{d\ (\ln C)}{dx}\right]^{-\frac{6}{5}}$$

where δ is the grain boundary width, D_v is the volume diffusion coefficient at the temperature involved, t is the time of diffusion, C is the concentration of diffusing material, and x is the depth of penetration.

A more general analysis employing the same model as Fisher's but with fewer assumptions has been given by Whipple.[2] In contrast to Fisher's analysis the more general analysis of Whipple does not always yield a straight line relation between ln C and x. Recently Turnbull and Hoffman[3] have discussed both analyses and have applied the Fisher-Whipple model to a more refined dislocation model of the grain boundary. They have also discussed the possibility of a large effect of grain boundary direction on diffusion.

In the case of the absorption technique, for which results are also given, one simply gets a value for the diffusion coefficient with no indication of the predominating mechanism.

Experimental Techniques

Single crystals of 99.99+ pct Zn were grown using a modified Bridgman method. Polycrystal samples were prepared in three grain sizes (small, about 4 mm²; medium, about 9 mm²; and large, about 25 mm²) by quenching, air cooling, and furnace cooling. The grains of the polycrystalline samples tended to be columnar, with some preferred texture such that the c-axis was inclined at about 20° to 25° from the normal to the diffusion face, particularly in the medium and large grain size samples.

The samples were cut from the rod, polished, and heavily etched, and faces cut accurately parallel using a jeweler's lathe. They were again etched to remove the lathe smear and annealed for 3 hr at 250° to 300°C. After annealing, they were etched, examined, and the orientation determined by Laue back reflection photographs. They were then electroplated with Zn^{65}. The plated surfaces were examined for uniformity; nonuniform coatings were removed by etching and the samples replated without additional preparation.

For the diffusion anneals, the samples were placed in pairs, with active faces together, in evacuated Pyrex tubes. Constant temperature baths were used, and the variation in temperature did not exceed ±1°C. Diffusion runs were made at 100°,

F. E. JAUMOT, JR. and R. L. SMITH, Members AIME, are associated with Solid State Physics Div., Franklin Institute Laboratories for Research and Development, Philadelphia.

Discussion of this paper, TP 4111E, may be sent, 2 copies, to AIME by Apr. 1, 1956. Manuscript, Jan. 18, 1955. Philadelphia Meeting, October 1955.

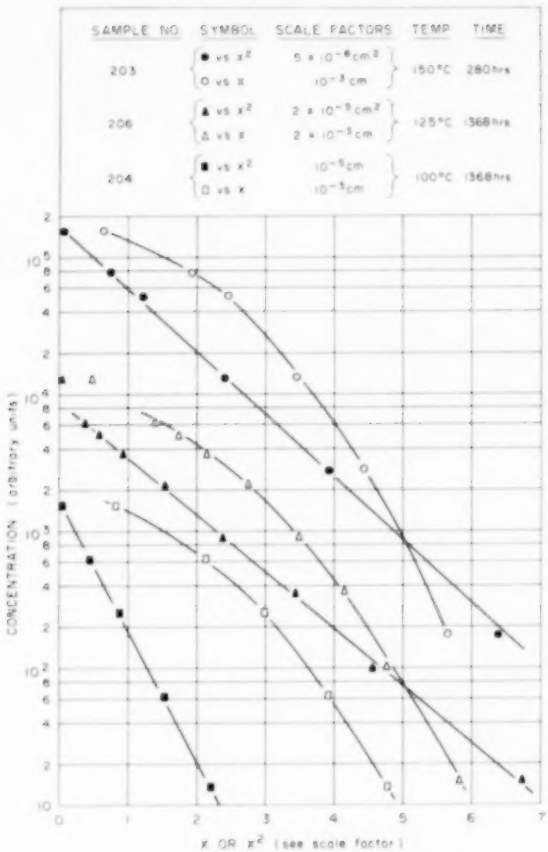

Fig. 1—Chart shows curves illustrating a linear dependence of ln C on x^2 for diffusion at various temperatures in zinc single crystals.

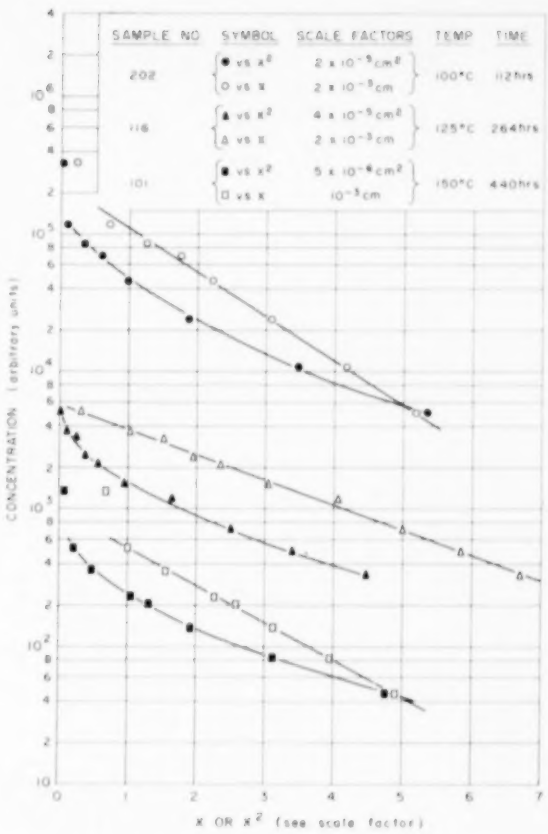

Fig. 2—Chart shows curves illustrating a linear dependence of ln C on x for diffusion in zinc single crystals.

125°, 150°, and 200°C for the single crystals, and 100°, 125°, 170°, and 200°C for the polycrystalline samples. Diffusion times ranged from 4 days to 3 months at each temperature. No dependence of the results on time was observed. At least eight and generally 12 single crystal samples of each orientation (parallel and perpendicular to the c-axis) and eight polycrystal samples of each of the three grain sizes were used at each temperature.

After diffusion and after the samples had been *counted* to obtain the necessary data for the absorption technique analysis, 30 to 100 mils were removed from the cylindrical surfaces of the samples to eliminate possible surface effects. Sections 0.5 to 1.5×10^{-4} cm thick were removed using a high precision jeweler's lathe,[5] carefully collected and weighed to determine their thickness more precisely, and their activity determined using standard techniques.

No change in the polycrystalline samples was observed after the diffusion run, although some grain growth occurred during the prediffusion anneal. The single crystals were not examined during the course of sectioning, but after the sectioning operation was completed they were etched and examined for recrystallization; none was observed.

Results

Laue back reflection X-ray photographs of the single crystals exhibited sharp spots indicating good single crystals. However, the curves of ln C vs x^2 for an appreciable number of samples did not turn out to be straight lines, indicating imperfect crystals. When this plot *was* a straight line, it gave values of D as much as several orders of magnitude larger than expected from high temperature data.[6] Most of the single crystal samples which did not yield a straight line for ln C vs x^2 gave excellent straight lines when ln C was plotted against x. Figs. 1 and 2 give curves of each type for diffusion at approximately 150°, 125°, and 100°C. All data for diffusion at 200°C produced linear curves of ln C vs x^2. In addition to the types of curves shown in Figs. 1 and 2, some samples gave curves in which ln C is linear in x^2 for small penetration depths and linear in x for large penetration depths. Finally, a few samples gave values of ln C which did not yield a linear plot against either x or x^2.

The results for polycrystal diffusion are illustrated in Figs. 3 and 4. Nearly perfect curves of both types were obtained at every temperature. The majority of the samples, however, gave either a linear dependence of ln C on x or a dependence of the *mixed* type shown in Fig. 5.

Fig. 6 gives the results obtained from single crystal samples using the absorption technique as well as those results calculated from the curves of ln C vs x^2 obtained from the sectioning technique. Fig. 7 gives similar results for diffusion in polycrystals. In all cases the same samples were used for both techniques. The designations S, M, and L in all

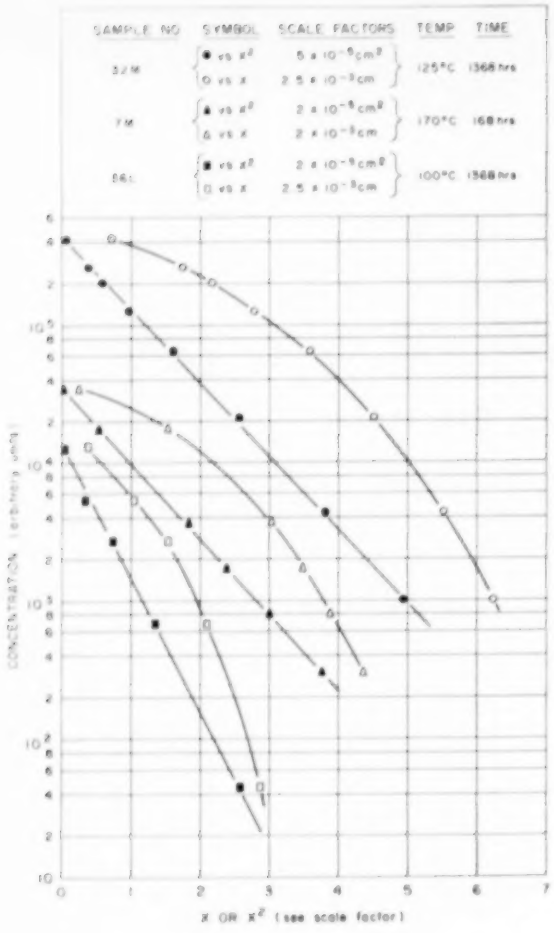

Fig. 3—Chart shows curves illustrating a linear dependence of ln C on x^2 for diffusion at various temperatures in polycrystalline zinc.

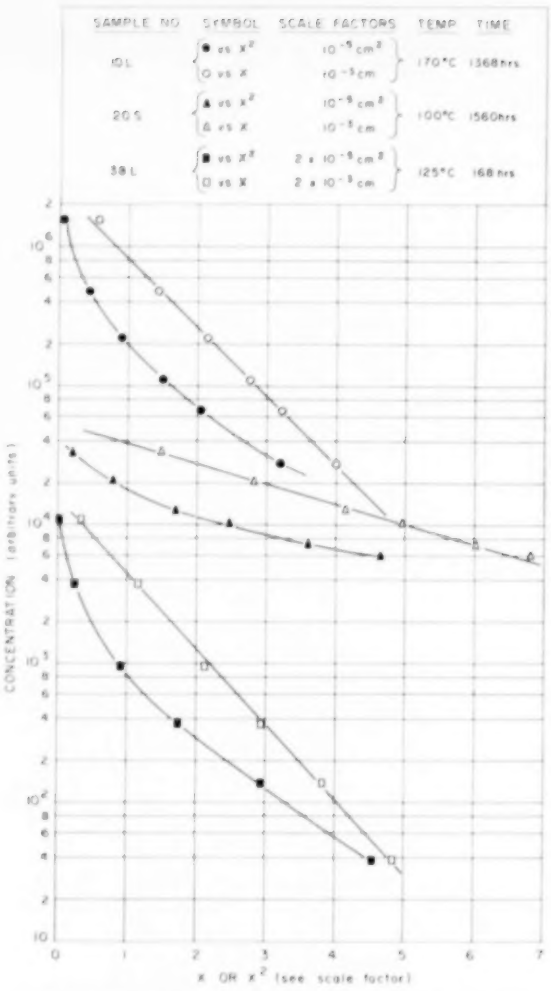

Fig. 4—Chart shows curves illustrating a linear dependence of ln C on x for diffusion in polycrystalline zinc.

figures refer to the small, medium and large grain size samples mentioned above.

Fig. 8 gives the results obtained using a grain boundary analysis on the single and polycrystal samples which yielded linear plots of ln C vs x. The data spread at each temperature is given by the vertical lines in Figs. 6, 7, and 8, unless fewer than four good determinations of D were possible, in which cases the individual values of D are plotted. A data spread is not shown for small grain size samples in Fig. 8 since it was within the size of the standard symbol used.

Discussion of Results

Since the data are such that the values of Q are uncertain by as much as 25 pct, little significance can be attached to the values of D_o.

The analysis of the data obtained using the absorption technique explicitly assumes a true volume diffusion, with ln C linear in x^2. Since the concentration depth data strongly suggest that diffusion is also taking place by means of some kind of short circuit paths, we can safely conclude that the absorption technique is not valid for the zinc samples used below about 200°C. The absorption data are included in Figs. 6 and 7 as a matter of interest. The explanation for the fact that the results from the two techniques are not too different, and for the small spread in the absorption technique data, probably is that the latter technique is quite insensitive to small changes in penetration depths, particularly after a critical depth has been reached.[6]

The polycrystal diffusion indicates a grain size effect at low temperatures for the values of D obtained from samples for which ln C was linear in x^2. When the grain boundary analysis applied there seemed to be no difference in the values obtained from the large and the medium grain sizes, but the values obtained from the small grain size samples were definitely higher (see Fig. 8). The activation energies are all about the same in the case of grain boundary diffusion, requiring D_o to be higher for small grain size samples.

The unlikelihood of a fundamental difference in diffusion behavior at low temperatures led to the possibility that sample irregularities were the cause of the anomalous results for single crystal samples. It has long been known that metal single crystals (particularly zinc) often exhibit a substructure formed of a network of lineage boundaries. These boundaries in zinc are generally very straight and are always nearly parallel to the direction of

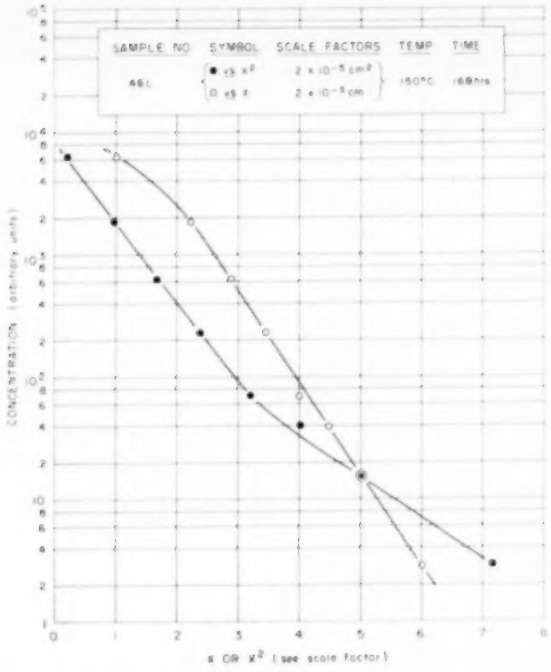

Fig. 5—Chart shows typical *mixed* concentration-depth curve for diffusion in zinc. This curve was obtained from a polycrystalline sample, but similar curves were also obtained from single crystal samples.

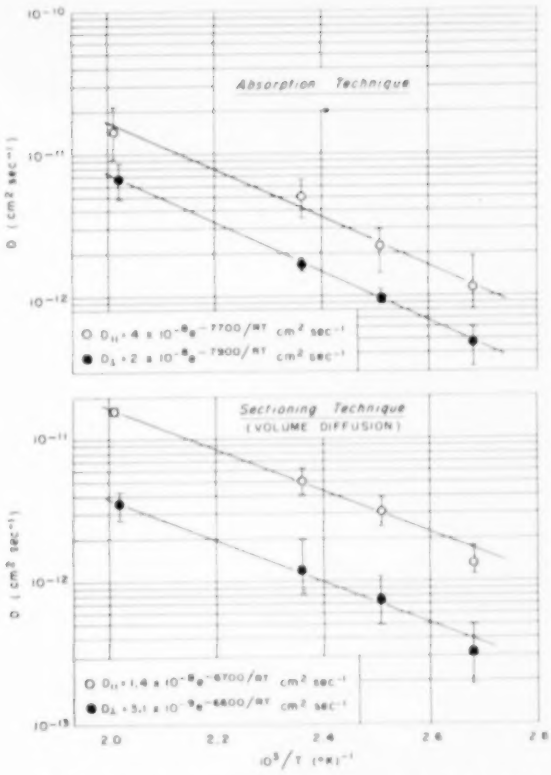

Fig. 6—Charts give summary of *D* values obtained for zinc single crystals from the absorption and the sectioning techniques for those samples which gave linear curves of ln *C* vs x^2.

growth. Steijn[7] has studied these boundaries and concludes that they are composed of Taylor-Orowan edge dislocations, each dislocation yielding an etch pit. The distance between etch pits indicates that the subcrystals differ in angular orientation by only about 15 to 30 sec. Thus, it is easy to see why the Laue photographs gave sharp spots indicating good single crystals.

In both polycrystal and single crystal samples the values of *D* obtained from the Fisher analysis lead to a higher activation energy than do the values of *D* obtained from a volume diffusion analysis. It is possible that the grain boundary analysis used does not apply, but it is more reasonable to assign the cause of this anomaly to the fact that some of the much faster diffusion along grain and lineage boundaries is included in the diffusion analyzed as volume diffusion. It is not entirely clear why the data should analyze as volume diffusion if a significant part of the diffusion is due to boundaries. It may be that many of the boundaries are discontinuous, so that rapid diffusion occurs along the boundaries initially but is blocked at their terminations, and thereafter the boundary is a new source for volume diffusion. Unfortunately, there is no good metallographic evidence for discontinuous boundaries of very small lengths.

The first actual experimental results involving dislocation boundaries were probably those of Hendrikson and Machlin[8] which, while obtained from a rather special experimental arrangement, indicate that the dislocation pipe diffusivity is at least as large and probably larger than that for large angle grain boundaries. Turnbull and Hoffman[9] have given very plausible theoretical arguments indicating that *preferential diffusion in certain directions (parallel to dislocation pipes) of low angle boundaries cannot always be ignored*. They emphasize that the diffusion coefficient in a low angle boundary is expected to be highly anisotropic, having a maximum value in a direction parallel to the dislocation pipes and a minimum ($D_p = D_\perp$) for diffusion in the direction normal to the pipes. In the present work diffusion was, in all specimens, nearly normal to the dislocation pipes, so that one is forced to conclude that such an array provides a short circuit path for diffusion which is comparable in efficiency to an array of pipes parallel to the diffusion direction. It is important to note that the lineage boundaries in the samples used for the present study are generally much longer than normal grain boundaries. Therefore, although the misorientation is small, the total flux through these boundaries could be large.

A serious difficulty arises from the fact that large grains in polycrystal samples also show lineage boundaries. These boundaries are more widely spaced in the polycrystal grain than in the *single* crystal but it is difficult to assume that they play no role in the diffusion. It is probable that their effect averages smoothly into the effect of the normal grain boundaries.

The experimental work of Hendrikson and Machlin is very significant in that it provides strong qualitative support for the work of Turnbull and Hoffman. At the same time, the present results obtained from a more complex situation seem to indicate that the issue is not as clear-cut as the foregoing work suggests. First of all, one has anomal-

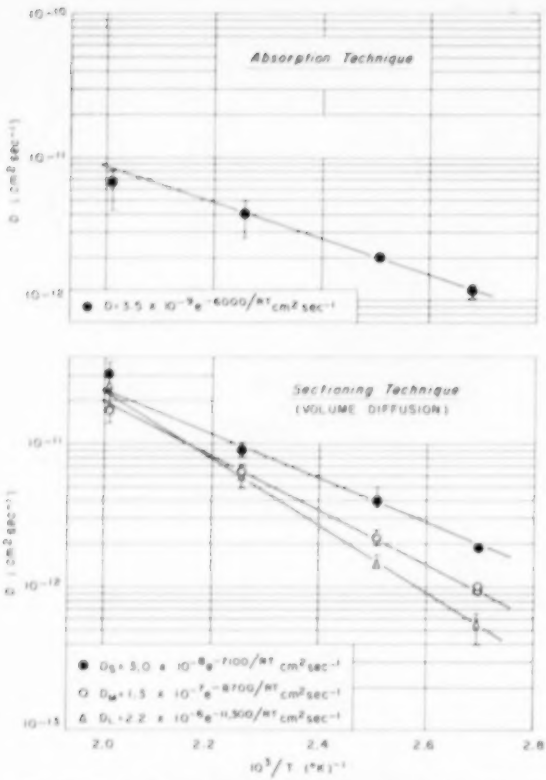

Fig. 7—Charts give summary of D values obtained for polycrystalline zinc from the absorption and the sectioning techniques for those samples which gave linear curves of ln C vs x^2.

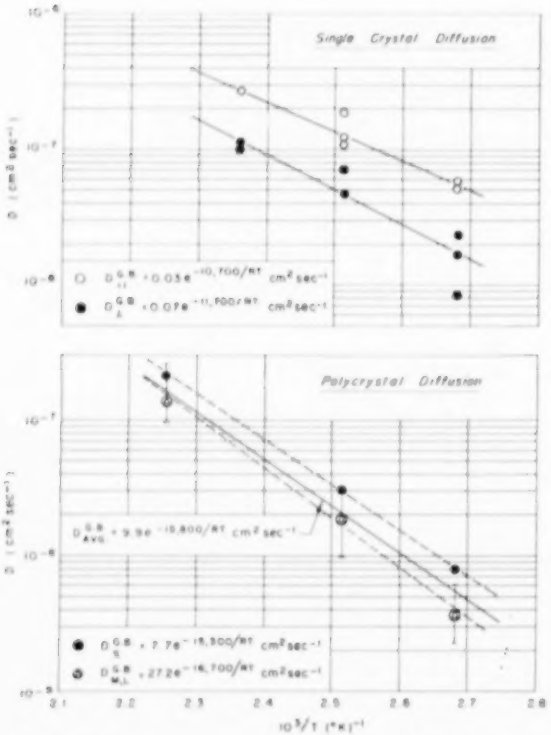

Fig. 8—Chart gives summary of D values obtained from linear curves of ln C vs x through the sectioning technique.

ously high diffusion coefficients for samples which exhibited penetration curves linear in x^2.* These high values of D undoubtedly arise as a result of the lineage boundaries. Also, the *single crystal* samples which exhibited penetration curves linear in x contained lineage boundaries in which the dislocation pipes were oriented, in the main, normal to the direction of diffusion. This *grain boundary* diffusion is certainly due to these lineage boundaries but the theory of Turnbull and Hoffman suggests that with the diffusion geometry used, D_g should be of the order of D_v, not several orders of magnitude larger. Perhaps most unexplainable of all, some polycrystalline samples exhibited *volume diffusion* at very low temperatures. Since this latter result occurred in only a few samples, if it were the only unusual result, it might be explained in terms of a high degree of grain boundary diffusion anisotropy; but this would appear to be stretching the point, in view of the single crystal data.

* The present experiment does not represent the first time that high values of D were deduced from ln C vs x^2 curves obtained from *single crystals* for *low* temperature diffusion. A diffusion coefficient 60 pct *higher than expected on the basis of high temperature diffusion* was observed at low temperatures (380.4°C) by the group at the University of Illinois[9] in the course of some extremely careful work on diffusion of antimony in silver.[10] Their experimental arrangement was such that they feel the maximum error could not exceed 10 pct. These determinations yielded a linear plot of the logarithm of concentration as a function of x^2. Hoffman and Turnbull[11] obtained an anomalously high self-diffusion coefficient for silver at 500°C, using the absorption technique.

Table I. Number* of Single Crystal Samples Which Yielded Curves of Log Concentration Linear in x^2, x, or Neither

Diffusion Temperature	Diffusion Parallel to c-axis			Diffusion Perpendicular to c-axis		
	ln C vs x^2	ln C vs x	Neither†	ln C vs x^2	ln C vs x	Neither†
200°C	8	0	0	11	0	1
170°C	—	—	—	—	—	—
150°C	6	1	1	9	2	2
125°C	6	3	1	6	2	1
100°C	11	2	0	10	3	1

* When values of D could be obtained from both portions of a mixed curve (see Fig. 5), they are included as two samples in Tables I and II.
† The curve of ln C was not linear in either x or x^2 over any appreciable penetration depth.

Table II. Number* of Polycrystal Samples Which Yielded Curves of Log Concentration Linear in x^2, x, or Neither

Diffusion Temperature	Small Grain Size			Medium Grain Size			Large Grain Size		
	ln C vs x^2	ln C vs x	Neither†	ln C vs x^2	ln C vs x	Neither†	ln C vs x^2	ln C vs x	Neither†
200°C	8	1	0	8	0	0	8	0	0
170°C	3	8	1	3	7	1	4	7	0
150°C	—	—	—	—	—	—	—	—	—
125°C	2	6	1	2	7	0	3	6	1
100°C	1	7	0	2	6	0	2	7	0

* When values of D could be obtained from both portions of a mixed curve (see Fig. 5), they are included as two samples in Tables I and II.
† The curve of ln C was not linear in either x or x^2 over any appreciable penetration depth.

The authors are inclined to believe that this is not the first experimental work in which varied results were obtained. When relatively few samples are used there is a strong tendency to throw out anomalous results obtained from only one or a few samples. In the present experiment the expected result

was only a most probable result. That is, the majority of the single crystal samples analyzed as if the diffusion were volume diffusion (ln C linear in x^n) while the majority of the polycrystal samples exhibited grain boundary diffusion (ln C linear in x) for temperatures below 170°C. The numbers of samples from which each type of D was obtained are given in Tables I and II.

The unexpected and anomalous results may suggest an uncontrolled experimental parameter. If one exists, it is most probably a question of impurities. The samples were prepared of relatively high purity zinc and, in addition, the lineage boundaries in the single crystals were examined by microradiography to ascertain whether or not the boundaries were composed of lead impurity inclusions. An amount of lead on the boundaries equivalent to 0.01 pct impurity should have been detected but none was observed. Additional purification of the zinc is being carried out and this question will be considered along with the directional characteristics of the boundaries in a continuation of the work.

Acknowledgments

The authors would like to express their gratitude to the U. S. AEC for its financial support of this work. The authors are indebted to Louis Arne for his aid in carrying out the experimental work and to L. Slifkin of the University of Minnesota for helpful suggestions and discussions.

Discussion of this paper, if any, will appear in JOURNAL OF METALS, November 1956, and in AIME Metals Branch *Transactions*, Vol. **206**, 1956.

References

[1] J. C. Fisher: *Journal of Applied Physics* (1951) **22**, p. 74.
[2] R. T. P. Whipple: *AERE Report T/R 1026* (1952).
[3] D. Turnbull and R. E. Hoffman: *Acta Metallurgica* (1954) **2**, p. 419.
[4] E. S. Wajda: *Acta Metallurgica* (1954) **2**, p. 184.
[5] F. E. Jaumot, Jr. and R. L. Smith: *Trans.* AIME (1956) **206**, p. 137; JOURNAL OF METALS (February 1956).
[6] R. E. Hoffman: *Atom Movements*. (1951) Cleveland. ASM.
[7] R. P. Steijn: *Trans.* AIME (1955) **203**, p. 406; JOURNAL OF METALS (February 1955).
[8] A. A. Hendrickson and E. S. Machlin: *Trans.* AIME (1954) **200**, p. 1035; JOURNAL OF METALS (September 1954).
[9] E. Sonder, L. Slifkin, and C. Tomizuka: Private communications.
[10] E. Sonder, L. Slifkin, and C. Tomizuka: *Physical Review* (1954) **93**, p. 970.
[11] R. E. Hoffman and D. Turnbull: *Journal of Applied Physics* (1951) **22**, p. 634.

Technical Note

Mechanism of Grain Boundary Sliding

by H. C. Chang and Nicholas J. Grant

EMPHASIS on the importance of grain boundary sliding as a mode of deformation at elevated temperatures has been presented elsewhere.[1] The extent to which boundary sliding occurs under certain creep conditions has been determined for high purity aluminum[2, 3] and aluminum alloys.[4] In general, boundary deformation extends quite far into the adjoining grains, resulting in a rather wide band of deformation along the grain boundaries. This has led some investigators to doubt that grain boundary sliding consists of shearing along the boundary surface; it has been contended instead that boundary sliding is a result of concentrated slip in the neighborhood of the deformed grain boundaries.[5, 6]

The purpose of this note is to present evidence that grain boundary sliding takes place by a bulk shear process.

In high purity polycrystalline aluminum, wherever and whenever there is grain boundary sliding, boundary migration and concentrated deformation along both sides of the deformed boundary are associated with it. Therefore, it has been rather difficult to obtain unambiguous evidence of boundary sliding. On the other hand, it would be expected in certain alloys of aluminum, when tested under particular conditions, that the severity of the interfering effects of boundary migration and concentrated deformation along the deformed boundary might be reduced. Current research in this laboratory[7] shows that a 20 pct Zn-Al solid solution alloy fractures in an intercrystalline manner during creep at 500°F with a small total elongation of not more than about 14 pct, and that it does so with extremely limited grain boundary migration. Accordingly, this alloy was chosen for the present study.

H. C. CHANG, Associate Member AIME, and N. J. GRANT, Member AIME, are Staff Member, Division of Industrial Cooperation, and Associate Professor, Dept. of Metallurgy, respectively, Massachusetts Institute of Technology, Cambridge, Mass.

TN 299E. Manuscript, July 7, 1955.

The experimental procedure was similar to that used in previous work and has been presented elsewhere.[4] Two parallel flat surfaces were milled from a round specimen. The gage portion of the specimen was 1 in. x .09 in. x .17 in. The specimens, which were annealed at 1030°F for 24 hr, showed two to four grains across the width of the test bar. The specimens were subjected to creep at 500°F at stresses of 2000 to 5000 psi. The rupture times were from 10 sec to 3 hr.

Appreciable boundary sliding occurred in all the tests. A typical example of boundary sliding is shown in Fig. 1. (The tension axis is vertical in the micrographs.) Sliding has taken place along the boundary between grains A and B unaccompanied by important boundary migration. The sharpness of the offset at the triple point can be clearly seen in grain C. As a result of sliding along the boundary between grains A and B, a new boundary surface between grains A and C was created. The offset at the triple point is about 0.07 mm. This boundary sliding is accompanied by the formation of rather sharp kinking bands and, of course, slip on several slip systems in grain C. This type of deformation has been referred to as fold formation[1] in previous work with high purity aluminum.

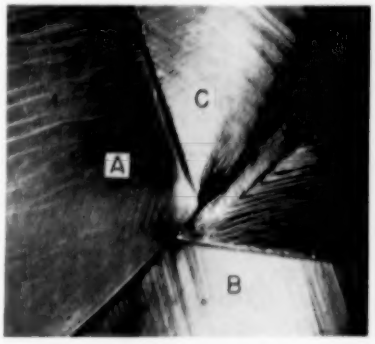

Fig. 1 — Boundary sliding is shown along boundary between grains *A* and *B* resulting in fold formation in grain *C*. Note the sharp offset at the triple point. X100. Area reduced approximately 35 pct for reproduction.

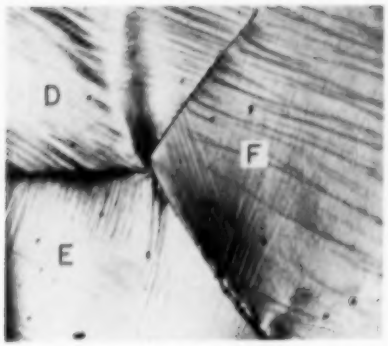

Fig. 2a—New grain boundary surface (between grains *D* and *F*) was created as a result of sliding along boundary between grains *E* and *F*. X75. Area reduced approximately 35 pct for reproduction.

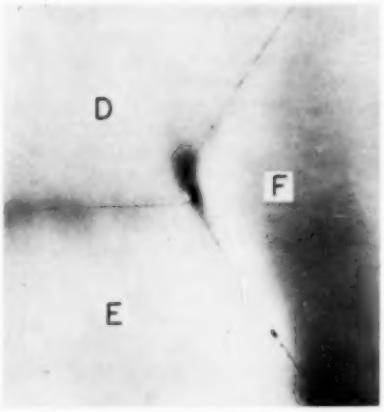

Fig. 2b—Same region as in Fig. 2a is shown, after polishing and etching. The sharp offset at the triple point is clearly seen. X150. Area reduced approximately 35 pct for reproduction.

In longer time tests, at slower strain rates, recovery takes place, if the temperature is high enough, and the offset at the triple point is rejoined by migration of the grain boundary.[1]

Another example of boundary sliding with a sharp offset at the triple point is shown in Fig. 2a. Fig. 2b shows the same region after electropolishing away a layer 0.2 mm thick. The shift of the boundary between grains *D* and *E* is clearly evident. The new boundary surface created between grains *D* and *F* has the same etching characteristics and the same width as the other grain boundaries. It is interesting to note that the corner of grain *F*, now bounded only by grain *D*, became slightly rounded, probably by a small amount of boundary migration to achieve lower surface energy. While there was some small evidence of boundary migration for this alloy tested at 500°F, in general the grain boundaries remained fixed during the short period of test, as can be seen from the micrographs.

In order to demonstrate that the new boundary surfaces created as a result of boundary sliding between grains *A* and *C* in Fig. 1 and between grains *D* and *F* in Fig. 2 are not cracks, the specimens were annealed at 900°F for 1 hr, repolished and etched. No evidence of cracks was noted in the places where the slide boundary surfaces existed before reannealing.

It is important to point out that in many hundreds of observations made to date, grain boundary sliding is always accompanied by fold formation in the grain on which the new boundary surface is created. This is the means whereby the grain can accommodate boundary sliding. The flexibility of fold formation has been demonstrated by Chang and Grant[1, 3] and Mullendore and Grant,[9] who observed that folds are regions of kinking, of single and double slip, and deformation bands. The observed length and area of the folds depend on the geometry and orientation of the grains and boundaries, the grain size, and the stress and temperature, but are always a measure of the extent of boundary sliding.

The observations presented in this note clearly demonstrate that there is bulk movement of two grains along a mutual boundary. Of course the boundary itself is not assumed to be uniquely plane, but is irregular. It is likely that one grain of the two involved in the sliding process is oriented more suitably for slip to occur in it. This observation is supported by repeated evidence of the greater amount of deformation in one grain as compared to the other in the sliding couple.

If displacement along the grain boundary were presumed to be due to a soft zone (dimensions of unknown magnitude but wide enough to accommodate slip of the usual spacing and for several

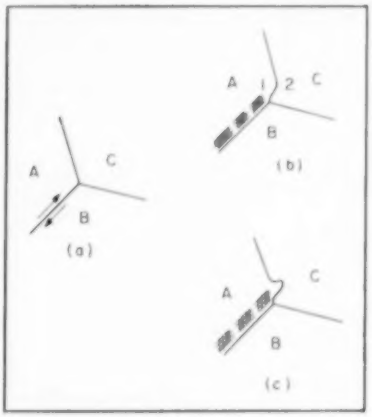

Fig. 3—Displacement of grain *A* along a softened band is shown by the shaded area. a—Drawing shows appearance of triple point before deformation. b—Displacement without rotation is illustrated, giving probable appearance of this region if it is assumed that the boundary between grains *A* and *C* can be stretched as a result of further deformation in the softened zone. c—Drawing shows displacement, assuming that the upper end of the boundary between grains *A* and *C* is fixed, with the probable appearance of this area after deformation.

bands), it is expected that boundary surfaces of the type suggested in Fig. 3 would probably result instead of the sharp surfaces experimentally observed and shown in Figs. 1 and 2. Considering the magnitude of the movement measured in Fig. 1 (0.07 mm), any discontinuous boundary surface should have been easily recognized. In fact, the movements followed and noted in Figs. 1 and 2 fail to disclose such discontinuities as are presumed in Fig. 3. It is not suggested that the boundary between grains *A* and *C*, Fig. 1, and between grains *D* and *F*, Fig. 2, moved parallel to the original boundaries, but the movement was a bulk one.

Acknowledgments

We wish to express our thanks to A. R. Chaudhuri for his helpful discussion, to G. Gemmell for providing data on the Al-Zn alloy, and to the Office of Naval Research, under whose support this work was done.

References

[1] H. C. Chang and N. J. Grant: *Trans.* AIME (1952) **194**, p. 619; JOURNAL OF METALS (June 1952).
[2] D. McLean: *Journal* Institute of Metals (1952) **81**, p. 293.
[3] H. C. Chang and N. J. Grant: *Trans.* AIME (1953) **197**, p. 1175; JOURNAL OF METALS (September 1953).
[4] D. McLean and M. H. Farmer: *Journal* Institute of Metals (1954-1955) **83**, p. 1558.
[5] NACA Conference on Creep, Battelle Memorial Inst. (June 1953).
[6] F. N. Rhines: *Symposium on Creep and Fracture at High Temperatures.* National Physical Laboratory, London (1954) Paper No. 4.
[7] G. Gemmell: Private communication.
[8] H. C. Chang and N. J. Grant: *Journal* Institute of Metals (1953-1954) **82**, p. 1517.
[9] A. W. Mullendore and N. J. Grant: *Trans.* AIME (1954) **200**, p. 973; JOURNAL OF METALS (September 1954).

Search for Oxidation-Resistant Alloys of Molybdenum

In an effort to find an oxidation-resistant alloy of molybdenum, binary and ternary alloys containing aluminum, chromium, cobalt, iron, nickel, silicon, titanium, tungsten, vanadium, and zirconium were screened. Fourteen other alloying additions were also tested. Many of the alloys were more oxidation-resistant than molybdenum, but none were entirely satisfactory.

by G. W. P. Rengstorff

MOLYBDENUM oxidizes extremely rapidly above 1450°F in air. At 1800°F, a loss of metal at the rate of 0.1 in. in 4 hr is typical. The high speed of this oxidation may be judged by comparison with the oxidation rate of 0.1 in. per year (0.00005 in. in 4 hr), sometimes taken as the maximum permissible oxidation rate at 1800°F for a satisfactory Fe-Cr-Ni alloy.

Great strides have been made in the development of coatings and cladding to protect molybdenum from oxidizing atmospheres. These developments in surface protection will undoubtedly make it possible to take advantage of the excellent hot strength of molybdenum and its alloys in many new applications. Still, even the best coating can protect molybdenum only as long as the surface layer is unbroken.

Research was undertaken to determine whether an alloy of molybdenum could be found which would resist oxidation. Such an alloy would not deteriorate suddenly when the protective surface layer was destroyed in a small area. In seeking an alloy of molybdenum to resist oxidation, the physical properties of molybdenum could not be sacrificed entirely.

The development of an alloy with the desired resistance to oxidation was not achieved. The information obtained on the effect of a large number of elements on the oxidation of molybdenum is, however, of value in the development of coatings. Indeed, many of the alloys tested for oxidation resistance were already known to have poor mechanical properties but were tested to aid in the development of coatings.

Oxidation of Molybdenum

The rapid oxidation of molybdenum is usually attributed to the volatility of MoO_3. Gulbransen and Wysong[1] have shown that molybdenum oxidizes very slowly up to 850°F, the temperature at which the oxide film begins to evaporate.

Melting as well as evaporation of molybdenum oxides promotes the oxidation of molybdenum. MoO_3 melts at 1465°F. MoO_2, the oxide which is believed to form at the metal-oxide interface, combines with MoO_3 to form a eutectic having a melting point of 1432°F.[2] The liquid oxide, even if nonvolatile, could cause poor resistance to oxidation by allowing easy transport of molybdenum and oxygen ions through the oxide. Actually, a sudden increase in the rate of oxidation of molybdenum at 1460°F has been observed[1] to coincide with the appearance of a liquid phase.

The formation of a volatile oxide is not unique with molybdenum. The problem is also encountered with vanadium, tungsten, and some of the Pt-Pd group of metals. Vanadium not only forms the volatile V_2O_5 but, like molybdenum, forms a liquid oxide coating. Few attempts have been made, however, to prevent the rapid oxidation of these metals by alloying.

Oxidation of Molybdenum Alloys

At the beginning of this work, very little was known of the oxidation resistance of molybdenum alloys. It was known that molybdenum disilicide (with 37 pct Si) has extremely good oxidation resistance,[3] but this compound is so brittle that it has few uses. It is an effective protective coating for molybdenum when allowance can be made for its brittleness. Chromium was known to retard the oxidation of molybdenum,[4] but at least 50 pct Cr was necessary to have an appreciable effect. Other, unpublished, reports show that a few other alloys have been given preliminary tests, but the results have not been promising.[5]

Choice of Alloys to be Investigated

An alloying element might be expected to protect molybdenum in either of two ways: Its oxide might combine with molybdenum oxide to form a stable, nonvolatile complex oxide (a molybdate); or the oxide of the alloying element might form in preference to molybdenum oxide, developing an impervious layer which would prevent the formation of a volatile molybdenum oxide.

The knowledge available about the formation of molybdates was meager. Therefore, the initial study was made on alloys of molybdenum with elements having especially stable oxides. On this basis, binary and ternary alloys containing the following six elements were investigated: aluminum, chromium, titanium, zirconium, silicon, and vanadium.

Nickel was also added as an alloying element. Although it does not form a more stable oxide than molybdenum, it does impart some oxidation resistance to copper and iron. Its inclusion in the study was fortunate because its alloys proved to be the most promising of those first tested. Apparently nickel formed a stable molybdate.

Because nickel was effective in reducing the oxidation rate of molybdenum, the elements iron, cobalt, and tungsten were added to the list.

The ten alloying elements mentioned form ten binary and 45 ternary alloying systems with molybdenum. A series of alloys was tested in each of these systems.

In addition, at least one test was made on the effect of each of the following alloying elements:

G. W. P. RENGSTORFF, Member AIME, is Assistant Chief, Process Metallurgy Div., Battelle Memorial Institute, Columbus, Ohio.

Discussion of this paper, TP 4030E, may be sent, 2 copies, to AIME by Apr. 1, 1956. Manuscript, Dec. 2, 1954. Philadelphia Meeting, October 1955.

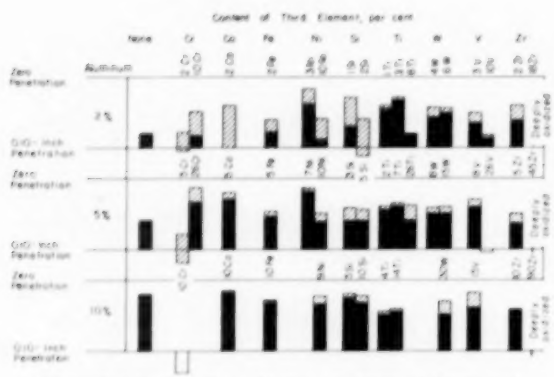

Fig. 1—Graph shows the oxidation resistance of binary and ternary molybdenum alloys containing aluminum.

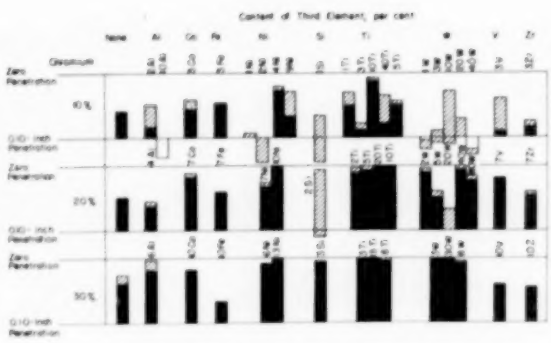

Fig. 2—Graph shows the oxidation resistance of binary and ternary molybdenum alloys containing chromium.

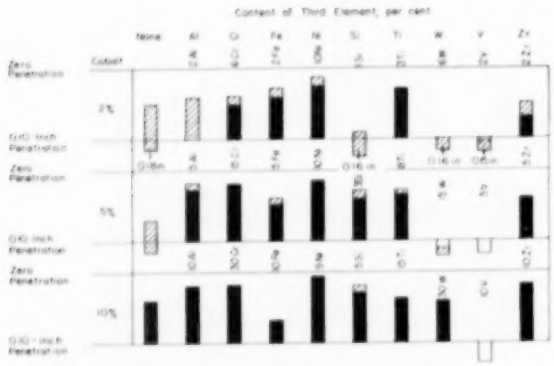

Fig. 3—Graph shows the oxidation resistance of binary and ternary molybdenum alloys containing cobalt.

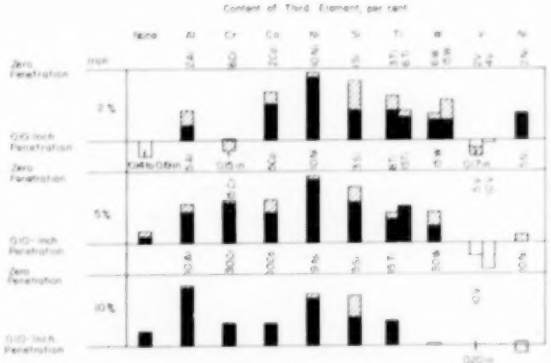

Fig. 4—Graph shows the oxidation resistance of binary and ternary molybdenum alloys containing iron.

boron, B-Fe, platinum, copper, lead, thorium, beryllium, tin, antimony, manganese, lithium, magnesium, zinc, silver, and bismuth.

Preparation of Gradient-Composition Ingots

To investigate the large number of composition ranges desired and yet avoid making an extremely large number of ingots, a method was developed for preparing *gradient-composition* ingots. Thus, a wide range of compositions could be investigated in a single ingot. In these gradient-composition ingots, the bottom was usually molybdenum and the concentration of the alloying addition was gradually increased toward the top of the ingot. The top of the ingot usually contained between 15 and 40 pct of the alloying element, but sometimes contained 100 pct.

In most of the ternary composition ingots, the ratio of the two alloying elements was kept constant. However, many of the nickel-containing alloys had 10 pct Ni on the bottom. In these alloys, the Ni-Mo ratio was kept constant, and the concentration of the third element was gradually increased toward the top.

The gradient-composition ingots were made by arc melting in an inert atmosphere. Gradients in composition are possible with arc melting because only a thin layer of metal is molten at a time. The ingots vary in composition as the charge materials are varied.

Each gradient-composition ingot was cut lengthwise through the middle, one half being used for the oxidation test and the other for hardness surveys and rechecking.

In order to form an initial protective oxide film on the alloys, each specimen was preoxidized in a gastight stainless steel tube for 6 hr at 2000°F in hydrogen previously saturated with water vapor at 75°F. A similar treatment, the Price-Thomas treatment, has been used successfully to form a protective aluminum oxide film on Cu-Al alloys.[7]

The actual oxidation tests consisted of heating the ingots, with a control sample of molybdenum, on insulating brick in a nickel-lined steel tube for 4 hr at 1800°F. Air was blown through the pipe at a controlled rate.

The oxidation resistance of each alloy was evaluated by measuring the thickness along the length of the half ingots before testing and after oxidizing and cleaning by grit blasting. The difference in thickness is a measure of the amount of oxidation under the conditions of the test. Essentially all of the oxidation occurred on the exposed side of the specimens; the sides in contact with the insulating brick were protected.

Validity of Screening Tests

The oxidation rates were, of course, the results of rough screening tests. The alloy contents were generally qualitative estimates. This was especially true in the gradient-composition ingots where the alloying elements sometimes vaporized rapidly or severely attacked the electrode tips to cause the general alloying level to deviate from the intended

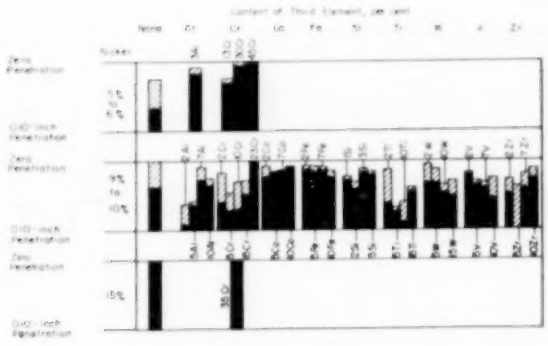

Fig. 5—Graph shows the oxidation resistance of binary and ternary molybdenum alloys containing nickel.

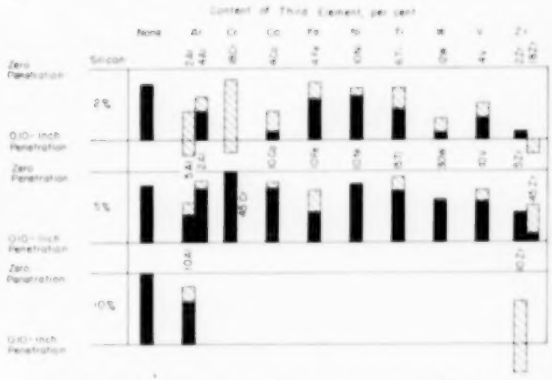

Fig. 6—Graph shows the oxidation resistance of binary and ternary molybdenum alloys containing silicon.

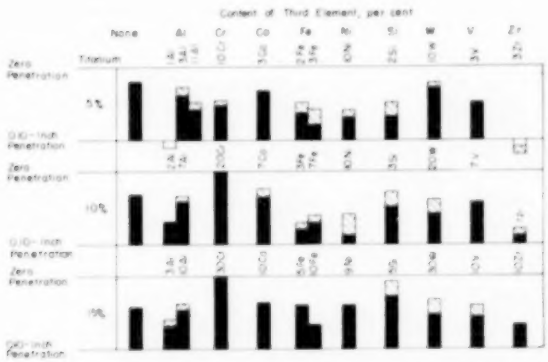

Fig. 7—Graph shows the oxidation resistance of binary and ternary molybdenum alloys containing titanium.

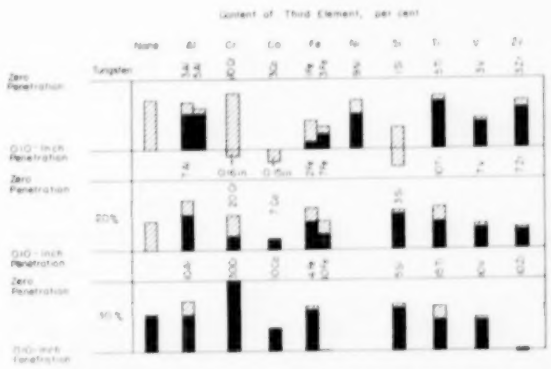

Fig. 8—Graph shows the oxidation resistance of binary and ternary molybdenum alloys containing tungsten.

composition. Also, large local fluctuations in composition can be expected from layering during arc melting.

Nevertheless, these tests were successful in determining the qualitative effect of the various alloying elements. They showed which alloying systems were worthy of further study. The desired oxidation-resistant alloy should oxidize only about 1/5000 as fast as molybdenum, so that conditions which would change the oxidation rate, even by a factor of ten or more, would hardly be significant.

The oxidation resistance of many alloys is completely destroyed by the presence of molybdenum oxide. However, this phenomenon, known as catastrophic oxidation, generally occurs in a static atmosphere. Since most of the tests described herein were made in flowing air, it is believed that the alloys tested were not greatly affected by catastrophic oxidation. In fact, a sample of Vitallium tested along with several samples of molybdenum and molybdenum alloys was oxidized severely only in corners protected from the flowing air. Nevertheless, the presence of gaseous and liquid oxides of molybdenum should be kept in mind when evaluating the results given in this paper.

Results of Screening Tests on Gradient-Composition Ingots

The bar graphs in Figs. 1 through 10 show the effect of each of ten alloying elements on the oxidation rate of molybdenum. They also show the effects of third elements on each of the binary alloys.*

* In these figures, *zero penetration* means oxidation-resistant. The value *0.10 in. penetration* is approximately the oxidation of unalloyed molybdenum. Oxidation resistance is given in inches penetrated by oxidation in flowing air during 4 hr at 1800°F.

In each of the graphs, 0.10 in. penetration was taken as the base line. This was the average rate of oxidation of unalloyed molybdenum under the conditions of the test (4 hr in flowing air at 1800°F). In the graphs, the height of the black bars is a measure of the oxidation resistance. Hence the more oxidation-resistant the alloy, the higher is its black bar. Alloys with bars rising completely up to the zero penetration line were, on the basis of the qualitative measurements obtained in these tests, entirely oxidation-resistant. The crosshatched areas represent the local variations in oxidation rate.

Other Alloys

In addition to the 55 alloy systems studied extensively, a number of other systems were tested for oxidation-resistance. Gradient-composition ingots could be prepared to test the oxidation resistance of some of these alloys. This procedure was impossible with other alloys because of excessive losses by vaporization.

The results of oxidation tests on molybdenum containing copper, lead, antimony, zinc, manganese, lithium, magnesium, and calcium are summarized in Table I.

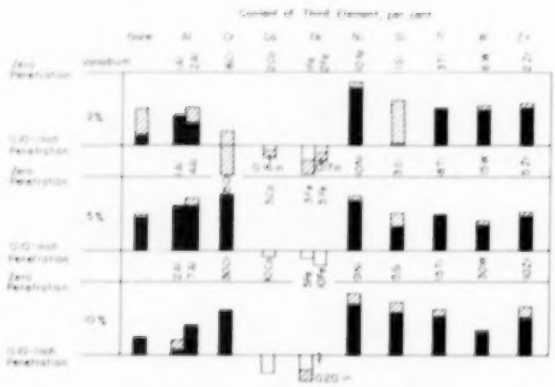

Fig. 9—Graph shows the oxidation resistance of binary and ternary molybdenum alloys containing vanadium.

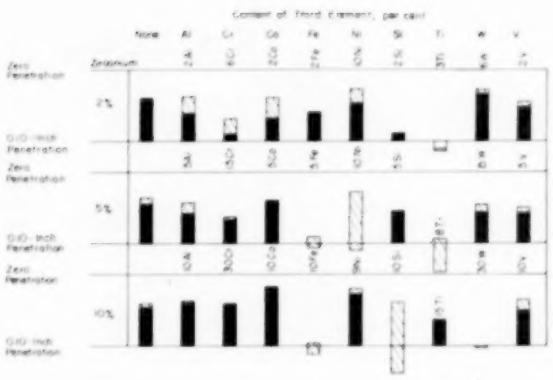

Fig. 10—Graph shows the oxidation resistance of binary molybdenum alloys containing zirconium.

The tests of copper, lead, tin, and antimony additions were made on bars pressed from metal powders containing 7 pct of the alloying element. These bars, together with a little powder of the alloying element to reduce composition changes due to vaporization, were sintered at 2100°F for one week in Vycor capsules. They were oxidized for up to 4 hr in a small muffle furnace under free circulation of air.

A zinc-containing alloy was prepared in the manner just described, except that, since it was too volatile for sintering, it was tested in the as-pressed condition.

For the manganese-containing alloys, bars pressed from metal powders containing originally 12 pct Mn were presintered at 2190°F at 2μ of mercury pressure. They were then sintered by self-resistance in hydrogen until clouds of vapor formed at about 2730°F; the current was then turned off immediately.

Lithium, magnesium, and calcium, because of their volatility, were added to the molybdenum powder by the impregnation method. Unmixed molybdenum powder was lightly compacted (9 tons per sq in.) and presintered at 2190°F. The resulting compact was placed in a steel pipe with enough of the alloying element to immerse the compact when the alloying element was molten. The pipe was welded shut and the mixture heated at 2000°F for one week. Resulting samples were tested for oxidation resistance in the manner described for the copper, lead, tin, and antimony alloys.

Table I shows that of all these alloy additions only the calcium alloy that had not been preoxidized resisted oxidation.

Alloys containing boron or boron and iron were prepared and tested as gradient-composition ingots. These alloying additions did not significantly improve the oxidation resistance of molybdenum.

The oxidation resistance of gradient-composition ingots containing up to 30 pct Pt was also tested. Platinum improved the oxidation resistance only slightly.

Attempts were made to prepare gradient-composition ingots with silver and bismuth. Their vaporization losses, however, were so great that satisfactory ingots could not be prepared nor could their composition be controlled. Oxidation tests on the resulting alloys did not show any beneficial effect from either element.

Small granules of arc melted 5 pct Be and 5 pct Th alloys were oxidized in the muffle furnace. Both alloys oxidized rapidly.

Tests on More Oxidation-Resistant Alloys

The screening tests showed that a few alloys had enough oxidation resistance to be worthy of further investigation. Alloys whose compositions are shown in Table II were prepared for further study.

All of these alloys except the Mo-Ca alloy were prepared by arc melting. This alloy was the remainder of the bar made by the impregnation process used for lithium, calcium, and magnesium.

Table I. Oxidation at 1800°F of Alloys of Molybdenum with Copper, Lead, Tin, Antimony, Zinc, Manganese, Lithium, Magnesium, and Calcium

Alloying Element	Estimated Composition, Pct	Pretreatment	Time of Test, Hr	Initial Weight of Sample, G*	Sample Lost by Oxidation, Pct
Copper	9.0	Preoxidized	2	4.8	96
		Not preoxidized	2	4.6	85
Lead	5.4	Preoxidized	2	4.4	91
		Not preoxidized	2	5.2	92
Tin	4.5	Preoxidized	2	4.9	86
		Not preoxidized	2	4.7	83
Antimony	5.9	Preoxidized	2	4.4	84
		Not preoxidized	2	4.8	75
Zinc	7.0	Not preoxidized	2	6.1	80
Manganese	~4.5	Not preoxidized	2	5.6	63
Lithium	Unknown	Preoxidized	2	4.5	100
		Not preoxidized	4	5.1	84
Magnesium	Unknown	Preoxidized	3	6.3	89
		Not preoxidized	4	6.3	76
Calcium	8.7 (analyzed)	Preoxidized	3	6.9	88
		Not preoxidized	4	6.8	None

* All samples were approximately ¼ in. thick.

Table II. Oxidation Tests on More Oxidation-Resistant Alloys

Alloy System	Intended Composition, Pct	Actual Composition, Pct
Mo-Ni	15 Ni	15.1 Ni
Mo-Ni-Co	85 Mo	82.1 Mo*
	13 Ni	15.6 Ni
	2 Co	2.3 Co
Mo-W-Cr	45 Mo	48.1 Mo*
	10 W	6.1 W
	45 Cr	45.8 Cr
Cr-Mo-W	90 Cr	92.0 Cr
	5 Mo	2.8 Mo*
	5 W	5.2 W
Mo-Cr-Ti	65 Mo	69.1 Mo*
	30 Cr	25.8 Cr
	5 Ti	5.1 Ti
Mo-Ca		8.7 Ca

* Percentages given here are by difference.

The oxidation tests on the Mo-Ca alloy were made in the same manner and in the same furnace as the 4 hr screening test on the sample which had not been preoxidized, except that the time was lengthened to 125 hr and another check was made at 4 hr. The results are shown in Fig. 11. One test was made at 2000°F instead of 1800°F, but this alloy could not withstand the higher temperature.

This Mo-Ca alloy oxidized at less than 1/100 the rate of unalloyed molybdenum. Such a reduction in oxidation rate is significant, but the rate is still much too rapid to justify considering the alloy as oxidation-resistant.

The increase in oxidation resistance of molybdenum imparted by calcium is probably due to the formation of calcium molybdate. This well-known molybdate is reported as having a melting point of 2450°F, well above the melting point of molybdenum oxides.[8]

The Mo-Ni alloy was prepared by a consumable-electrode arc melting process. The ingot was cut into pie-shaped specimens, ¼ in. thick, with an abrasive wheel. These specimens, which weighed about 14 g each, were oxidized for varying times up to 125 hr under the same conditions as the Mo-Ca alloy. Temperatures of these oxidation tests were 1600°, 1800°, and 2000°F. The results are given in Fig. 11.

The oxidation rate of this alloy at 1800° and 2000°F was about the same as that of the Mo-Ca alloy. It was much better than unalloyed molybdenum but still not good enough to be considered oxidation-resistant.

The oxidation resistance of the Mo-Ni alloy at 1600°F was much lower than at the higher temperatures of 1800° and 2000°F. The oxidation resistance at 2000°F was slightly better than at 1800°F. This increase in oxidation resistance with an increase in temperature is contrary to the behavior of most metals. Molybdenum itself, however, shows this same anomaly. Jones, Spretnak, and Speiser[9] attributed this to a change in the oxide. The oxide is liquid at all temperatures above about 1450°F, but it contains more oxygen at 1600°F than at 1800° or 2000°F. Also, more liquid is formed at the lower temperature. These factors combine to make the oxide more corrosive at 1600°F, and the resulting oxidation rate higher. The situation in the Mo-Ni alloy is different from that in unalloyed molybdenum because, in the alloy, the oxide is a solid at the oxidizing temperature. Therefore, the explanation must be different. The change in oxidation resistance probably results from a change in the stability or composition of the oxide of the alloy.

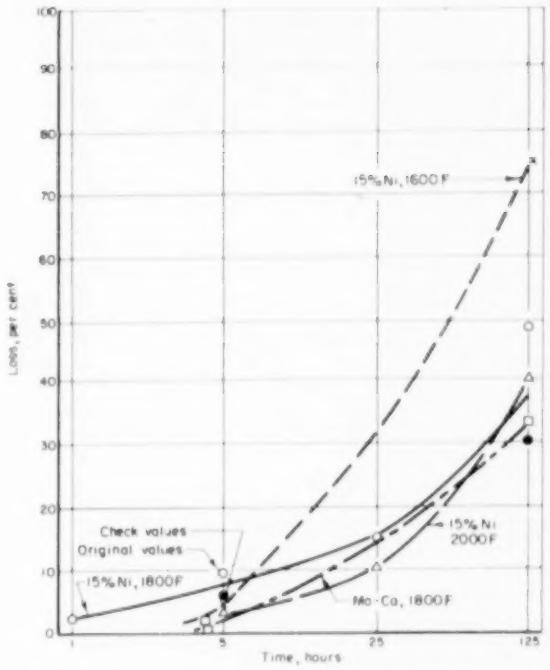

Fig. 11—Oxidation resistance of 15 pct Ni-85 pct Mo alloy as a function of time at 1600°, 1800°, and 2000°F and of an Mo-Ca alloy at 1800°F is charted.

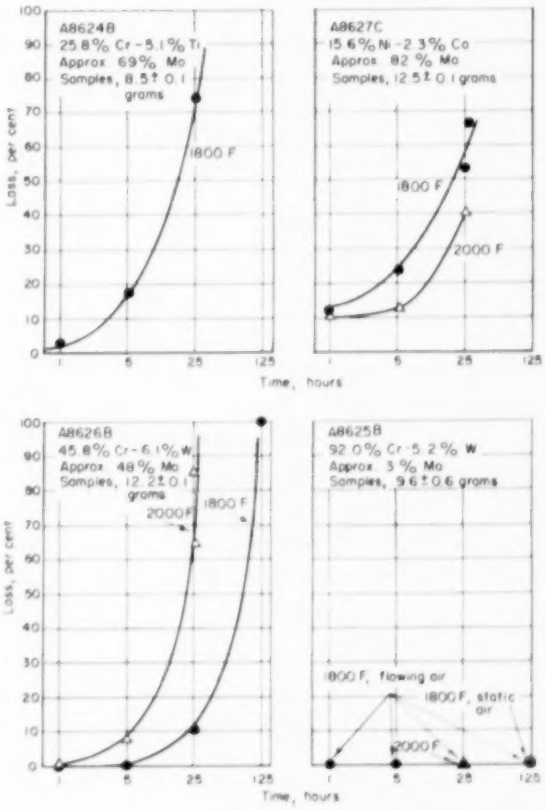

Fig. 12—Charts show the oxidation rate of various molybdenum alloys containing chromium, titanium, nickel, cobalt, and tungsten at 1800° and 2000°F.

The reduction in the oxidation rate of molybdenum by nickel is undoubtedly due to the formation of nickel molybdate. Brasunas and Grant[10] reported the existence of such a molybdate which appeared to decompose or melt at 2425°F. Spretnak, Speiser, and others at Ohio State University have been studying the properties of this molybdate. They have been particularly interested in stabilizing it to prevent a transformation which occurs at low temperatures. All of the Mo-Ni alloys reported here showed evidence of this transformation. It appeared as violent disruptions in the oxide after the samples had cooled well below a red heat.

The Mo-Ni-Co alloy was prepared by arc melting in argon with an inert electrode tip. This alloy was similar in composition to the Mo-Ni alloy, except that it contained 2 pct Co as well as 15 pct Ni. Specimens ¼ in. sq and 1 to 1⅜ in. long were machined from the ingots for arc melting studies. Samples were oxidized in flowing air at 1800° and 2000°F for periods up to 25 hr. They were weighed before and after testing to determine the amount of oxidation. The results, plotted in Fig. 12, show that the addition of a small amount of cobalt was detrimental to this alloy; the oxidation resistance was poorer than that of the 15 pct Ni alloy.

The Mo-Cr-Ti and the Mo-Cr-W alloys were made and tested in the same manner as the Mo-Ni-Co alloy. The results plotted in Fig. 12 show that these alloys are also far more resistant to oxidation than unalloyed molybdenum. Still, the oxidation rate is too high for them to be used where good resistance to oxidation is important.

A chromium-base alloy containing about 5 pct W and 3 pct Mo was made and tested in the same manner as the Mo-Ni-Co alloy. Results given in Fig. 12 show that this alloy is truly oxidation-resistant at 1800° and 2000°F in flowing air. The fact that this alloy also resisted oxidation in static air at 1800°F is evidence that it is not susceptible to catastrophic oxidation.

Conclusions

Results of oxidation tests of the many binary and ternary alloys reported here show that it is unlikely that any molybdenum-base alloy can be developed to combine high oxidation resistance at 1800° to 2000°F with the good physical properties of unalloyed molybdenum. It required at least 15 pct Ni or 25 pct Cr to reduce the oxidation rate of molybdenum by a factor of 100. This does not begin to approach the required oxidation rate if molybdenum alloys are to be seriously considered for high temperature applications in air. Furthermore, the high alloy contents destroy the desirable physical properties of molybdenum. It thus appears that molybdenum must be clad or coated or otherwise protected if it is to resist oxidation. Of course, it is still possible that an alloy of molybdenum containing enough alloying element to make it resistant to oxidation will also have desirable physical properties. It is more likely that such an alloy or intermetallic compound will be useful as a coating for molybdenum.

The oxidation rate of molybdenum is greatly reduced by calcium. A molybdenum compact impregnated with 8.7 pct Ca oxidized at about the same rate as an alloy containing 15 pct Ni. The physical properties of the compact were poor, however, and the reduction in oxidation rate is not enough to justify considering such an alloy suitable for coatings. It would seem, however, that lime or calcium molybdate might be usefully employed to prevent excessive losses of molybdenum by oxidation when it is heated to high temperatures in air for fabrication.

The fact that nickel forms a protective molybdate is worthy of further study, particularly in connection with cladding and coatings for molybdenum.

The use of gradient-composition ingots produced by arc melting greatly facilitated the study of a large number of alloy systems.

Acknowledgment

The support of this work by the Office of Naval Research is gratefully acknowledged. The author appreciates the generous assistance given by H. B. Goodwin, C. T. Greenidge, H. W. Lownie, Jr., W. G. Sachs, other staff members of Battelle Memorial Institute, and R. M. Parke, who was formerly a staff member.

Discussion of this paper, if any, will appear in JOURNAL OF METALS, November 1956, and in AIME Metals Branch *Transactions*, Vol. **206**, 1956.

References

[1] E. A. Gulbransen and S. S. Wysong: Thin Oxide Films on Molybdenum. *Trans.* AIME (1948) 175, pp. 628-647; METALS TECHNOLOGY (September 1947).

[2] G. W. Rathenau and J. W. Meijering: Rapid Oxidation of Metals and Alloys in the Presence of MoO_3. *Metallurgia* (1950) 42, pp. 167-172.

[3] B. Lustman: Oxidation of Molybdenum in Air at 1100 to 1600F. *Metal Progress* (1950) 57, pp. 629-630.

[4] E. A. Beidler, C. F. Powell, I. E. Campbell, and L. F. Yntema: The Formation of Molydenum Disilicide Coatings on Molybdenum. *Journal* Electrochemical Soc. (1951) 98, pp. 21-25.

[5] H. D. Kessler and M. Hansen: A Study of Arc-Melted Molybdenum-Rich Chromium-Molybdenum Alloys. *Trans.* ASM (1950) 42, pp. 1008-1032.

[6] Arc-Cast Molybdenum-Base Alloys. *First Annual Report* to ONR by Climax Molybdenum Co., Contract N8onr 78700, Task Order N89nr 78701 (Apr. 1, 1950).

[7] L. E. Price and G. J. Thomas: Oxidation Resistance in Copper Alloys. *Journal* Institute of Metals (1938) 63, p. 21.

[8] R. J. Meyer: Molybdän System No. 53. *Gmelin's Handbuch der Anorganischen Chemie* (1935) Berlin. Verlag Chemie.

[9] E. S. Jones, J. N. Spretnak, and R. Speiser: A Study of the Oxidation Characteristics of Molybdenum at Elevated Temperature. *First Technical Report* ONR Project NR 034 404, Contract No. N6onr-22528, Ohio State University Research Foundation (Oct. 1, 1951).

[10] A. deS. Brasunas and N. J. Grant: Accelerated Oxidation of Metals at High Temperatures. *Trans.* ASM (1952) 44, pp. 1117-1149.

Technical Note

Crystallographic Angles for Bismuth and Antimony

by Edward I. Salkovitz

E. I. SALKOVITZ is associated with U. S. Naval Research Laboratory, Washington.

TN 277E. Manuscript, Mar. 24, 1955.

RECENTLY a set of crystallographic angles for bismuth was calculated and a standard (111) projection was constructed. Since these calculations

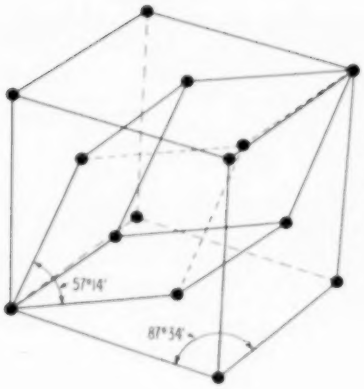

Fig. 1 — Face-centered rhombohedron with axial angle of 87°34' and simple rhombohedron with axial angle of 57°14'.

Fig. 2—Standard (111) stereographic projection for bismuth and antimony.

were made, attention has been called to the work of Yamamoto and Watanabe.[1] The table appearing in their paper was constructed primarily for the light-figure method of determining orientation, and angles between certain planes which are useful in the Laue method were not listed.

At first glance, it may appear that some confusion exists in the literature relative to notation. Thus the axial angle of bismuth is sometimes reported to be 57°14' and sometimes 87°34'. This discrepancy is resolved if the crystallography of bismuth is considered. Bismuth belongs to the rhombohedral system and consists of two interpenetrating face-centered-rhombohedral lattices. If a face-centered rhombohedron is used to characterize the structure (Fig. 1), the lattice parameter $a = 6.546$A and the axial angle (the angle between edges of the rhombohedron) is 87°34'. Such a unit cell may be compared with a cubic cell of the same lattice parameter but which has been elongated in the [111] direction. This face-centered-rhombohedral lattice, however, is not a primitive one. The primitive cell may be obtained by taking as a set of rhombohedral axes the halves of the face diagonals of the foregoing rhombohedron. This new set of axes now gives an axial angle of 57°14' and a lattice parameter $a = 4.736$A. Formulas for transforming the indices from one structure to the other are given by Wyckoff.[2] It is also possible to refer the cell to hexagonal axes, in which case the c/a ratio for bismuth is 2.609; for a face-centered-cubic lattice, c/a is 2.449.

For many purposes, it is more convenient to use the large face-centered rhombohedron as the unit cell and this is the representation used here. With this representation, the angle between the normals of any two planes has been calculated to the nearest minute using formulas given by Niggli.[3] These angles are compiled in Table I and the standard (111) projection is shown in Fig. 2. It should be noted that, when Miller indices (as contrasted to Bravais-Miller indices) are used with rhombohedral crystals, the indices of poles in the upper hemisphere of the stereographic projection are different from those in the lower. In Fig. 2 the set of indices to the right of a given pole refer to the upper hemisphere and the left set to the lower hemisphere.

Table I. Angles Between the Normals to $(h_1k_1l_1)$ and $(h_2k_2l_2)$

$h_1k_1l_1$	$h_2k_2l_2$		$h_1k_1l_1$	$h_2k_2l_2$	
111	211	20°37'	$10\bar{1}$	415	10°53'
	311	31°3'		$52\bar{7}$	16°6'
	411	36°58'		$11\bar{2}$	30°0'
	100	56°23'		$25\bar{7}$	43°54'
	511	71°38'		$14\bar{5}$	49°7'
	411	75°7'		011	60°0'
	$31\bar{1}$	80°34'			
	$21\bar{1}$	90°0'			
	321	23°29'			
	210	41°0'			
	$52\bar{1}$	52°30'			
	$41\bar{2}$	69°1'			
	$10\bar{1}$	90°0'			
	$20\bar{1}$	75°54'			
	$51\bar{4}$	90°0'			
	212	79°34'			
	$52\bar{7}$	90°0'			

Table II. Angles Between (100), (111), and (110) Poles

	Bismuth	Cubic Lattice
(100)/(110)	46°10'	45°
(110)/(111)	36°58'	35°16'
(111)/(100)	56°23'	54°44'

Because the axial angle for bismuth is almost 90°, it is possible to obtain a crude orientation rather quickly by referring to a cubic net. Indeed, Laue patterns of bismuth frequently show a pole of nearly fourfold symmetry (100), a pole of threefold symmetry (111), and a pole of twofold symmetry (110). Table II shows the angles between these poles for bismuth as well as for cubic crystals.

Table I and the stereographic net may also be used for antimony because its axial angle is 87°24' as compared to 87°34'.

[1] M. Yamamoto and J. Watanabe: *Journal Japan Inst. of Metals* (1951) **B15**, p. 514.
[2] R. W. G. Wyckoff: *Amer. Journal of Science* (1920) **4**, pp. 50, 317.
[3] P. Niggli: *Handbuch der Experimental Physik*. (1928) **7**, Pt. I, p. 151. Leipzig. Akad. Verlag., M.B.H.

Tensile Deformation of Molybdenum as a Function of Temperature and Strain Rate

True stress-true strain data are given for nominally pure molybdenum (99.95 pct) over the temperature range −196° to 1540°C (0.027 to 0.63 T/T_m). Strain rate sensitivity was determined by rate change tests and stress relaxation tests. Inhomogeneous yielding and strain aging effects were observed. The yield stress and tensile strength depend markedly on temperature below 400°C and are insensitive to temperature in the range 400° to 800°C. The ductile to brittle transition range is +25° to −25°C. Strain rate sensitivity and stress relaxation effects are very large near room temperature.

by R. P. Carreker, Jr. and R. W. Guard

THIS report presents data which were obtained as a part of a continuing program designed to document the deformation behavior of nominally pure metals over a wide temperature range.[1-4] This research program is rooted in the conviction that sufficient tensile and creep data of appropriate quality and detail does not exist to provide precise phenomenological descriptions of the deformation behavior of pure metals as a function of temperature, strain rate, and grain size. Such knowledge is needed to provide a firm base for alloy design and an experimental framework to which theories of deformation must conform. These data also complement a parallel exploratory program investigating the properties of refractory metals, including molybdenum, and their alloys.

Several important reviews and research reports dealing with the tensile properties of molybdenum as a function of temperature have appeared.[5-10] To a great extent the work to be reported in the present paper parallels that of Bechtold[6, 7] and of Pugh.[5] The authors' results are in general agreement with those of Bechtold and Pugh. The principle differences between the present experiments and those published previously are as follows:

1—Wire specimens prepared from arc cast molybdenum were used in the present experiments, bar specimens were used by others. Pugh[5] used arc cast material while Bechtold's most extensive results[6] were obtained on powder metallurgy specimens.

2—Several different grain sizes were tested in the present experiments.

3—The testing range was extended to cover from −196°C to 1570°C (0.027 to 0.63 T/T_m).

4—The combination of wire specimens, high speed autographic recording, and a stiff testing machine permitted more detailed study of initial yielding.

The principle contribution of the present paper is the demonstration of the relatively consistent mechanical properties of nominally pure arc cast molybdenum specimens of differing metallurgical history. Bechtold and Scott[8] have shown that arc cast and powder metallurgy molybdenum samples have comparable tensile properties in the range −75° to 200°C when processed to have the same recrystallized grain size.

R. P. CARREKER, JR. and R. W. GUARD, Junior Members AIME, are Research Associates, Research Laboratory, General Electric Co., Schenectady.

Discussion of this paper, TP 4000E, may be sent, 2 copies, to AIME by Apr. 1, 1956. Manuscript, Dec. 7, 1954. Philadelphia Meeting, October 1955.

Material

The molybdenum used in this investigation was supplied by the Climax Molybdenum Co. Its metallurgical history is outlined in Table I; the final products were 0.030 in. diam wire specimens annealed at 1100° and 1375°C and 0.060 in. diam wire

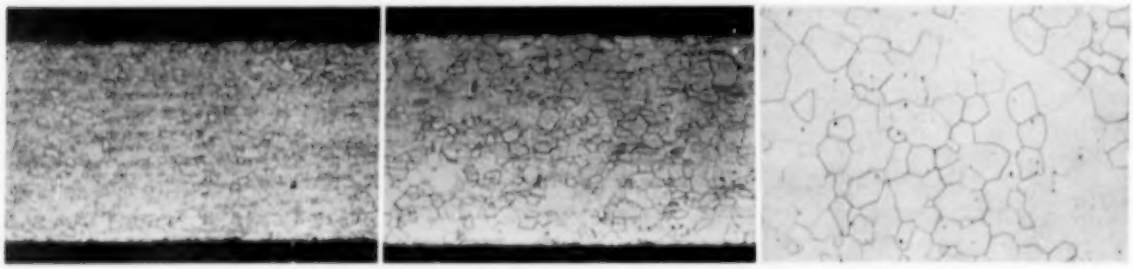

Fig. 1—Representative micrographs show annealed molybdenum after treatment.

a—Specimen was treated for 2 hr at 1100°C, 0.18 mm grain diam.

b—Specimen was treated for 2 hr at 1375°C, 0.34 mm grain diam.

c—Specimen was treated for 1 hr at 1600°C, 0.06 mm grain diam.

Table I. Material History

Supplier: Climax Molybdenum Co.; Heat No.: 413; Date: April 1949

Melting Practice: Arc-cast, carbon deoxidation, vacuum $<50\mu$, ingot 5 in. diam

Fabrication Practice: 1—*At Climax Molybdenum Co.*—Turn, forge to $2\frac{1}{2}$ in. octagon at 1275°C, turn to 2 in. diam, hot roll to 17x32 in. diam from 1175°C, machine straighten above 600°C.
2—*At General Electric Co.*—Hot swage to $\frac{5}{8}$ in. diam, at 1300°C. Progressively drop temperature to about 700°C as reduction proceeds. Cold swage to finish with 50 pct cold reduction at 0.030 in. diam and 0.060 in. diam

Annealing Practice: *Pure Dry Hydrogen Atmosphere*
1—2 hr at 1100°C, 0.030 in. diam, grain size 0.018 mm
2—2 hr at 1375°C, 0.030 in. diam, grain size 0.034 mm
3—1 hr at 1600°C, 0.060 in. diam, grain size 0.06 mm

Composition: *Nominal, Cited by Climax Molybdenum Co.*
<0.003 pct O
0.04 pct C

Fig. 2—Diagram gives schematic cross section of vacuum capsule for tensile testing in a wound furnace.

Fig. 3—Diagram gives schematic cross section of vacuum chamber for tensile testing above 1000°C.

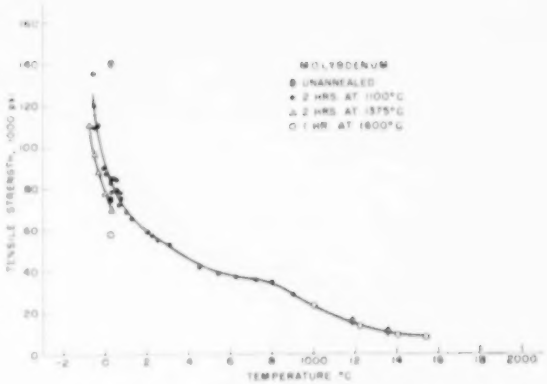

Fig. 4—Chart plots tensile strength of molybdenum as a function of temperature.

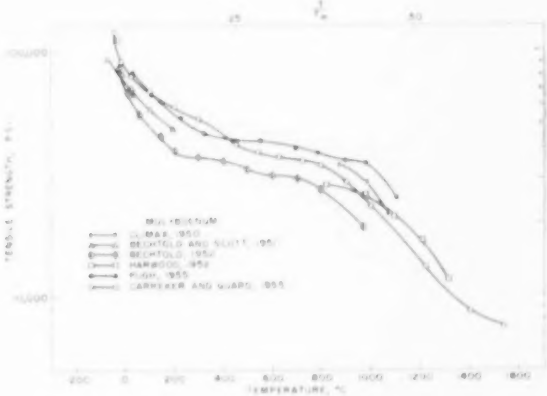

Fig. 5—Chart plots all available data on the tensile strength of arc cast molybdenum as a function of temperature.

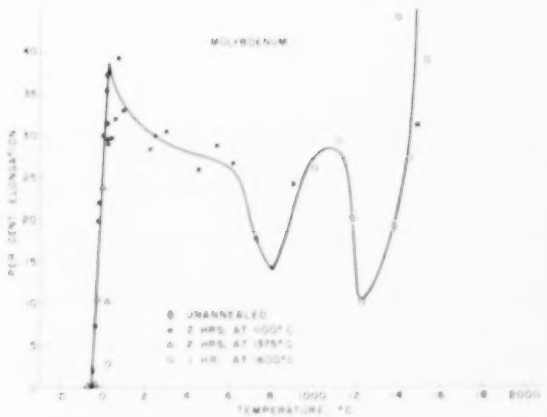

Fig. 6—Chart plots percentage of elongation of molybdenum as a function of temperature.

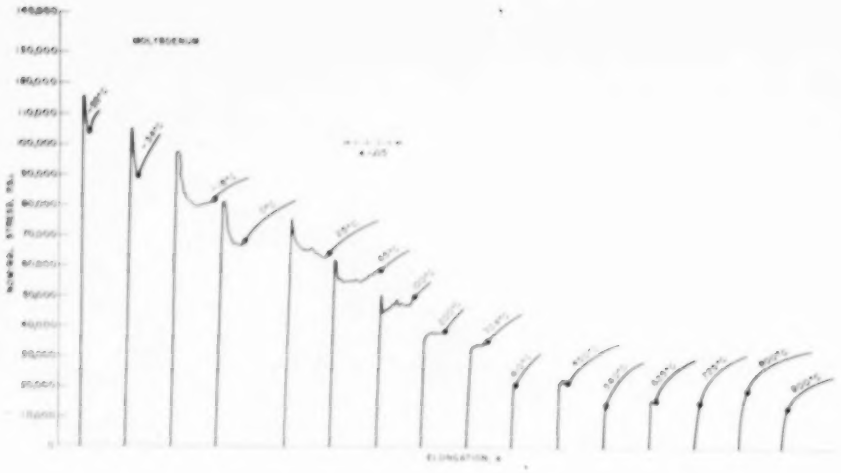

Fig. 7—Chart plots autographic records of initial yielding of molybdenum at selected temperatures.

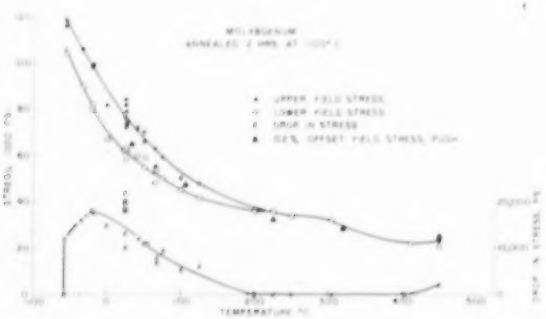

Fig. 8—Chart plots discontinuous yielding stresses as a function of temperature.

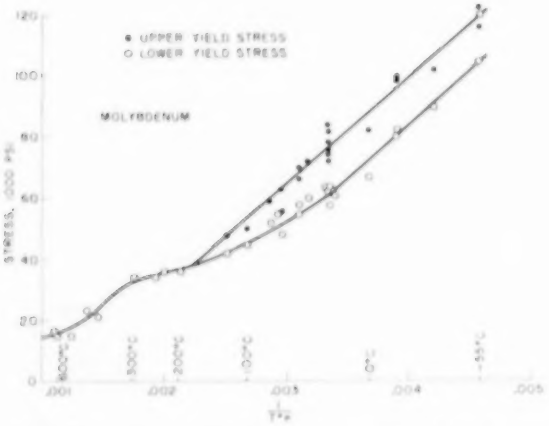

Fig. 9—Chart plots yield stress as a function of 1/T °K.

specimens annealed at 1600°C, having average grain diameters 0.018, 0.034, and 0.06 mm, respectively. In all cases the grain structure was substantially equiaxed. Representative micrographs are shown in Fig. 1. There may be some question about the 1100°C anneal producing complete recrystallization. It will be noted, however, that the properties of material so treated are in good agreement with the results of Pugh[5] and Bechtold[2] whose annealing temperatures and resulting grain sizes were 1400°C, 0.045 mm and 1150°C, 0.033 mm, respectively.

Testing Procedure

Many of the details of the tensile testing procedure have been described previously.[3] In this work, wire specimens were gripped between grooved plates and tested in tension at various temperatures, using an Instron testing machine. This electronically controlled machine records load vs time and imposes a constant rate of head motion, permitting time to be a measure of strain.

All tensile test specimens annealed at 1100° and 1375°C (0.030 in. diam) had 5.0 or 7.0 in. gage lengths. All specimens annealed at 1600°C (0.060 in. diam) were plunge-ground to 0.040 in. diam to produce a 2.0 in. gage length.

Specimen temperatures were obtained using various baths, including liquid nitrogen (−195°C), acetone and dry ice (−78°C), freon (−55° to 0°C), ice and water (0°C), and silicone oil, (25° to 300°C), and a nichrome-wound furnace for temperatures from 300° to 1000°C.

To prevent oxidation, all tests from 400° to 1000°C were conducted in a vacuum capsule at pressures below five μ. The vacuum capsule, Fig. 2, has not been described previously. The lower pulling rod passed through on *O* ring seal to the moving lower crosshead. The upper pulling rod was attached to the load cell and was brought into the vacuum capsule through a double bellows. The double bellows permitted movement of the vacuum chamber relative to the load cell without affecting the load measurement.

Tests above 1000°C were conducted in a tantalum resistance furnace, Fig. 3, which consisted of a ¾ in. diam x 13 in. long x 0.010 in. thick tantalum tube in a glass vacuum chamber. Molybdenum radiation shields were placed around the tantalum tube and the heating current was introduced through heavy copper connectors at the ends. During a test, the entire chamber was evacuated to 5 to 10 μ pressure. The vacuum chamber and lower pulling rod were rigidly attached to the moving (lower) crosshead. The upper pulling rod was brought out of the vacuum chamber through a double bellows and was attached to the load cell. The top of the vacuum chamber was attached to the machine frame.

All tests above 1000° were performed on specimens annealed at 1600°C. To insure that specimens

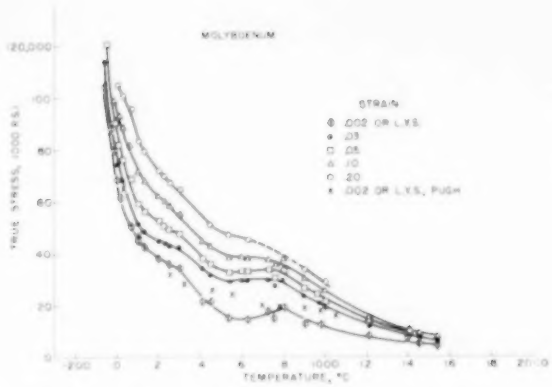

Fig. 10—Chart plots true flow stress at selected strains as a function of temperature.

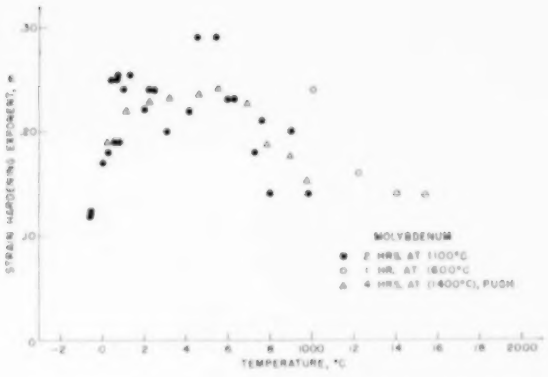

Fig. 12—Data points plot strain hardening, as measured by m of $\sigma = K\epsilon^m$, as a function of temperature.

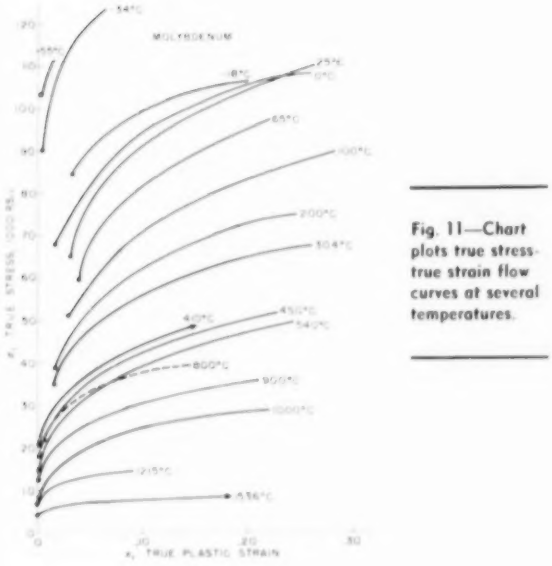

Fig. 11—Chart plots true stress-true strain flow curves at several temperatures.

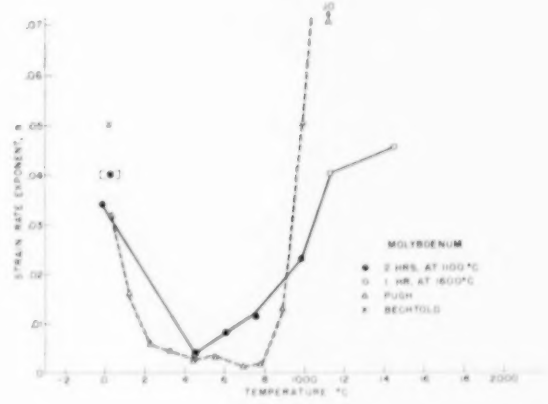

Fig. 13—Chart plots strain rate sensitivity, as measured by n of $\sigma = K\dot{\epsilon}^n$, as a function of temperature.

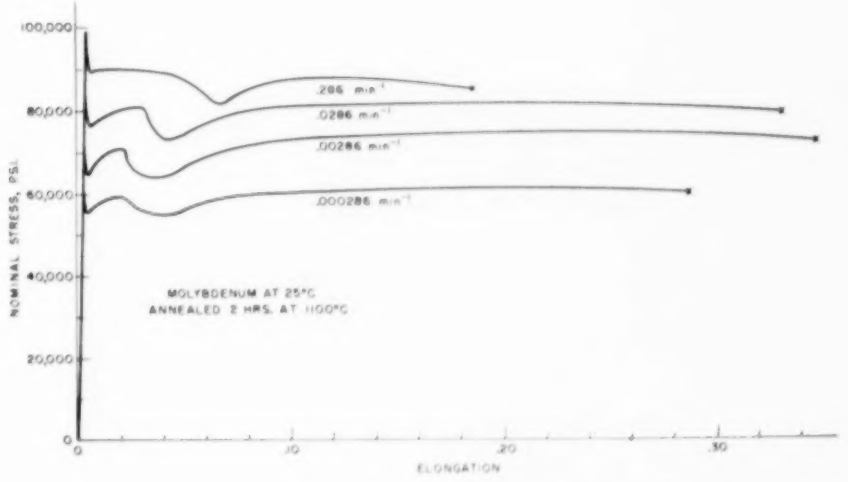

Fig. 14—Chart plots load-elongation flow curves for molybdenum as a function of strain rate.

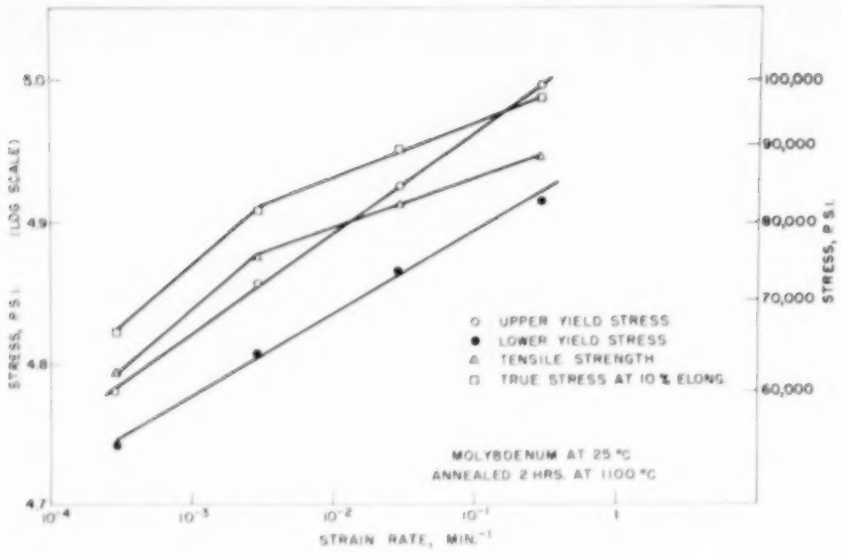

Fig. 15—Chart plots effect of strain rate on strength characteristics of molybdenum at room temperature.

could be gripped successfully and that the gage section was at a uniform temperature, the reduced 2.0 in. gage section was placed in the center of the 6.0 in. hot zone in the furnace and the 0.060 in. diam ends were gripped between grooved plates located outside the furnace. Temperatures were measured by a free-standing Pt—Pt-Rh thermocouple located near the center of the gage section. The maximum test temperature (1540°C) was limited by the mechanical strength of the thermocouple rather than by furnace performance.

Test temperatures below 1000°C, attained by use of baths or the wound furnace, were reproduced, maintained constant, and held uniform over the gage length within 2°C. The estimated accuracy of the temperatures above 1000°C is ±5°C.

A standard strain rate of 0.04 min^{-1} was used for specimens annealed at 1100° and 1375°C and a rate of 0.10 min^{-1} was used for the 1600°C annealed specimens. Some tests were conducted in which the strain rate was changed (0.04 to 0.004 to 0.04 min^{-1}) at a nominal strain of 0.1 in order to determine rate sensitivity. In addition to the tensile tests, some stress relaxation tests were performed at 25°C.

Analyzing Data

All test data were reduced to true stress σ and true (or natural) plastic strain ϵ, assuming constant volume during plastic deformation, so that elongation measurements define instantaneous areas. The constant volume assumption precludes analysis beyond the necking strain, but for wire specimens the uniform strain is virtually total elongation. σ and ϵ are defined by the familiar relations $\sigma = S(1 + e)$ and $\epsilon = \ln(1 + e)$ where S and e are the conventional stress and elongation, respectively.

Effect of Temperature

Fig. 4 shows the tensile strength of molybdenum as a function of temperature for each annealing treatment. Note the marked increase in tensile strength at lower temperatures. Note also the deviations from a monotonic decrease in strength with increasing temperature that occur near 300° and 800°C. These regions of increased strength are similar to like effects commonly observed in body-centered-cubic iron containing interstitial impurities.[11,12] Pure copper, on the other hand, does not exhibit such effects.[7] Fig. 5 compares the authors' tensile strength results with comparable data from the literature.

Fig. 6 shows the percentage of elongation as a function of temperature. The elongation measurements show minima at 800° and 1225°C and a ductile to brittle transition in the range +25° to −25°C. The quantity and reproducibility of these data are not sufficient to define such complex behavior precisely, but the trends are well established.

Discontinuous Yielding

It has been previously observed by several authors[1,8,9,10,13] that molybdenum exhibits discontinuous yielding similar to that observed in iron containing carbon. Fig. 7 shows the authors' observations of the pronounced effect of temperature on the initial yielding behavior of molybdenum. At −78°C and below, the material is completely brittle. At −55°C a specimen yielded discontinuously with a sharp drop in load and broke after about 1 pct plastic strain. Some evidence of discontinuous yielding persists up to 625°, but the drop in load is virtually absent above 200°C. See Figs. 7 and 8. These observations are in qualitative agreement with those of Tury and Krauz[10,14] on molybdenum containing nitrogen. Note, also, the qualitative agreement with Pugh's data[5] on yield strength.

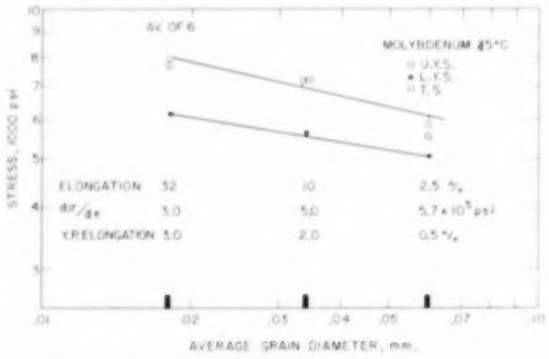

Fig. 16—Chart plots effect of grain size on the room temperature properties of molybdenum.

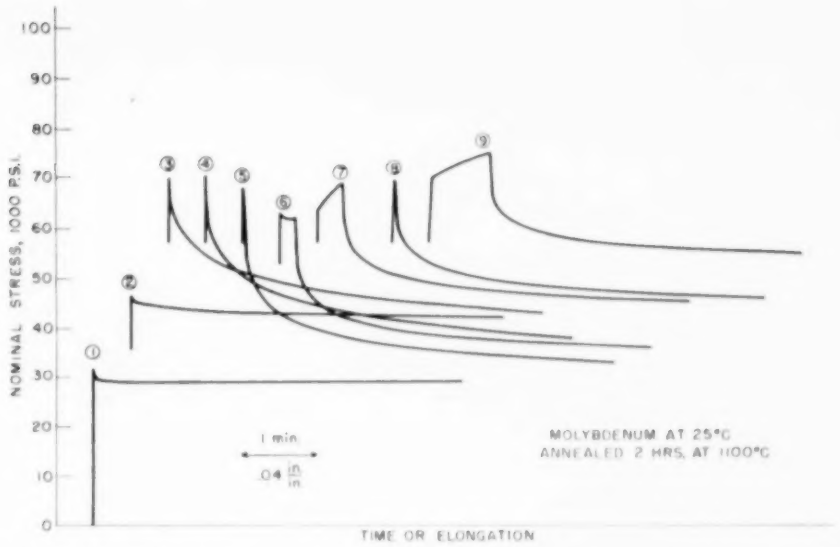

Fig. 17—Chart plots stress relaxation of molybdenum at room temperature.

In recent years, Cottrell[11,12] has proposed a theory of yielding which attributes discontinuous yielding in body-centered-cubic metals to the pinning of dislocations by impurities, interstitial atoms being particularly effective. Using Cottrell's concepts, Fisher[13] has predicted the temperature dependence of the yield strength to be $\sigma \cdot T =$ (constant). Fig. 9 shows that molybdenum obeys Fisher's rule from −55° to +125°C.

The deviations from monotonic decrease in strength with increasing temperature, Figs. 4 and 10, have also been related to the influence of impurity atoms on dislocations. The effect is another manifestation of strain aging, as discussed by Cottrell.[11]

Flow Stress

Fig. 10 shows the temperature dependence of the true flow stress at selected strains. The effect of strain aging is evident at 300° and 800°C. The data above 1000°C were obtained on specimens annealed at 1600° rather than the 1100° anneal given the other specimens. However, the 1600°C specimens gave flow stresses that are reasonable extrapolations of the lower temperature data.

The homogeneous portion of the plastic deformation of molybdenum is shown in Fig. 11, where true stress-true plastic strain curves are plotted for various temperatures. The dots at the beginnings of these curves coincide with the dots in Fig. 7, indicating the apparent division of inhomogeneous and homogeneous strain. The homogeneous deformation conforms to the equation $\sigma = K\epsilon^m$, the data defining quite good straight lines when plotted as log σ vs log ϵ. However, the slopes (the strain hardening exponents, m) are a complex function of temperature, as Fig. 12 shows. Such complex behavior is believed to be due to the same interstitial impurities which cause discontinuous yielding and strain aging. The data of Pugh[5] are included for comparison.

Effect of Strain Rate

Some data were obtained on the effect of strain rate on the flow stress at various temperatures. Rate changes tests were used, in which the strain rate was changed suddenly at a nominal strain of 0.1 from 0.04 min^{-1} to 0.004 min^{-1} and again from 0.004 min^{-1} to 0.04 min^{-1} on specimens annealed at 1100°C. The 1600°C annealed specimens were tested at 0.10 to 1.0 to 0.10 min^{-1} rates. Assuming the usual form of rate dependence, in which $\sigma = K\epsilon^n$, values of the strain rate exponent were calculated from the expression $n = \dfrac{\Delta \log \sigma}{\Delta \log \epsilon}$ and plotted in Fig. 13. The data of Pugh[5] and Bechtold[4] are included for comparison. The increase in strain rate sensitivity observed above 400°C is normal in pure metals, but the abnormally large value of n at −18°C is surprising. The bracketed point represents confirmation obtained at $\epsilon = 0.1$ using a different lot of specimens in a series of four tests at room temperature, 25°C, in which each specimen was tested at a different rate, the rates covering a range of 10^2. Fig. 14 is a tracing of the autographic record of these four tests; the rate effect is large. The inhomogeneous portions of the flow curves in Fig. 14 are qualitatively different from the comparable curves of Fig. 7. We cannot account for this difference. Fig. 15 shows the effect of strain rate at room temperature on the upper yield stress, the lower yield stress, the tensile strength and the true flow stress at 10 pct elongation. The highest strain rate, 0.286 min^{-1}, was sufficient to cause a significant decrease in the ductility, 15 pct elongation as compared to approximately 30 pct elongation with a strain rate of 0.0286 min^{-1} and less.

Effect of Grain Size

The temperatures of testing used on the three different specimen lots overlap at room temperature and so indicate the effect of grain size on flow characteristic at that temperature. Fig. 16 compares specimens of 0.018, 0.034 and 0.06 mm average grain diam on the basis of upper yield stress, lower yield stress, ultimate tensile strength, total percentage of elongation, yield point elongation and initial strain hardening ($d\sigma/d\epsilon$ after completion of inhomogeneous yielding). The effect of grain size upon these parameters is consistent with experience on iron containing interstitial impurities.

Stress Relaxation

The extremely high rate sensitivity noted at room temperature suggested an examination of the behavior of molybdenum in stress relaxation tests.

The procedure adopted consisted of loading the specimen at the rate of 0.04 min^{-1} to various stresses, then stopping the crosshead and recording stress as a function of time. After 5 min the stress was removed and changed to a different value and the process repeated. Fig. 17 shows the results obtained; the relaxation effects are large. Stress relaxation of such magnitude can have important practical consequences and is worthy of additional study.

Summary

Constant strain rate tensile tests have been performed on polycrystalline wires of nominally pure (99.95 pct) Mo over a temperature range extending from −196° to 1540°C (0.027 to 0.63 T/T_m). Tests were performed on three groups of specimens, annealed at 1100°, 1350°, and 1600°C to produce average grain diameters of 0.018, 0.034, and 0.06 mm. The data are presented as true stress-true strain plots, as well as plots of yield strength, tensile strength, and percentage of elongation as a function of temperature. These data were analyzed to determine the effect of temperature on the flow characteristics of molybdenum.

Rate change tests were used to determine the effect of strain rate on the flow stress as a function of temperature. Stress relaxation tests were conducted at room temperature.

It is concluded that:

1—Molybdenum shows discontinuous yielding in the temperature range −55° to 400°C and complex changes in yield strength, tensile strength, strain hardening and ductility with temperature. These complexities are believed to be related to the presence of interstitial impurities.

2—The yield strength, tensile strength and true flow stress at arbitrary strains are strongly dependent on temperature below 400°C, extrapolating to large values at low temperatures.

3—The lot of molybdenum investigated undergoes a transition from ductile to brittle behavior at 0°±25°C when annealed at 1100°C to produce a grain size of 0.018 mm average diam.

4—The strain rate sensitivity (defined as Δ log stress divided by Δ log strain rate) is a complex function of temperature. The strain rate exponent is unusually large near room temperature and passes through a minimum at approximately 400°C.

5—Stress relaxation occurs to a marked degree over short periods of time at room temperature.

6—The results of this investigation of the properties of molybdenum wires are in general agreement with the results Pugh[5] and Bechtold[6] obtained on bar specimens. Thus, nominally pure molybdenum specimens of differing metallurgical history show only minor differences in tensile properties when processed to comparable annealed conditions.

Acknowledgments

The help of E. A. Smith in performing the tensile tests is gratefully acknowledged. R. F. Berning and J. D. Lubahn participated in the design of the high temperature testing equipment. The results reported in this paper were obtained in the course of research for the Aeronautical Research Laboratory, Wright Air Development Center, under Contract No. AF 33 (616)-2120.

Discussion of this paper, if any, will appear in JOURNAL OF METALS, November 1956, and in AIME Metals Branch *Transactions*, Vol. **206**, 1956.

References

[1] R. P. Carreker, Jr: Plastic Flow of Platinum Wire. *Journal of Applied Physics* (1950) **21**, p. 1289.

[2] R. P. Carreker, Jr. and W. R. Hibbard, Jr.: Tensile Deformation of High Purity Copper as a Function of Temperature, Strain Rate and Grain Size. *Acta Metallurgica* (1953) **1**, p. 654.

[3] R. P. Carreker, Jr.: Tensile Deformation of Silver as a Function of Temperature, Strain Rate and Grain Size. To be published.

[4] R. W. Guard and W. R. Hibbard, Jr.: Tensile Creep of High-Purity Aluminum. *Trans.* AIME (1956) **206**, p. 195; JOURNAL OF METALS (February 1956).

[5] J. W. Pugh: The Tensile Properties of Molybdenum at Elevated Temperatures. *Trans.* ASM (1955) **47**, p. 984.

[6] Climax Molybdenum Co.: Tensile Properties of Arc-Cast Molybdenum. *Metal Progress* (1950) **B58**, p. 200.

[7] R. M. Parke: Molybdenum, A New High-Temperature Metal. *Metal Progress* (1951) **60**, pp. 81-95.

[8] J. H. Bechtold and H. Scott: Mechanical Properties of Arc-Cast and Powder Metallurgy Molybdenum. *Journal* Electrochemical Soc. (1951) **98**, pp. 495-503; *Metal Progress* (1952) **61**, pp. 82-88.

[9] J. H. Bechtold: Effects of Temperature on the Flow and Fracture Characteristics of Molybdenum. *Scientific Paper No. 1707* Westinghouse Research Laboratories (Nov. 17, 1952).

[10] S. Harwood: *Product Engineering* (1952) **23**, p. 121.

[11] A. H. Cottrell and B. A. Bilby: Dislocation Theory of Yielding and Strain Aging of Iron. *Proceedings* Physical Soc., London (1949) **62A**, pp. 49-62.

[12] A. H. Cottrell: Effect of Solute Atoms on the Behavior of Dislocations. *Report on the Conference on Strength of Solids* Physical Soc., London (1948) pp. 30-38.

[13] P. Tury and S. Krauz: Effect of Molecular Nitrogen on Molybdenum at High Temperatures. *Nature* (1936) **138**, p. 331.

[14] P. Tury and S. Krauz: Distortion and Yield Point of Molybdenum. *Nature* (1937) **139**, pp. 30-31.

[15] J. C. Fisher: Private communication.

Technical Note

Transformation of the TiO Phase

by Chih-Chung Wang and Nicholas J. Grant

TiO phase of the Ti-O system has the structure of NaCl and has a wide range of solid solubility.[1]

C. C. WANG, Associate Member AIME, formerly Research Assistant, Dept. of Metallurgy, Massachusetts Institute of Technology, is now Senior Engineer, Sylvania Electric Products Inc., Ipswich, Mass., and N. J. GRANT, Member AIME, is Associate Professor, Dept. of Metallurgy, Massachusetts Institute of Technology, Cambridge, Mass.

TN 301E. Manuscript, July 7, 1955.

In the course of studying the Ti-Cr-O ternary system, binary alloys were made of iodide titanium and high purity TiO_2. It was found from X-ray studies of the binary alloys that a transformation of the TiO appears to take place at a temperature near 925°C. Evidence of this phase change is best seen in Fig. 1.

Fig. 1A shows the X-ray spectrometer pattern ($CuK\alpha$ radiation) of an alloy of 25 wt pct O corresponding to the stoichiometric composition of TiO.

Table I. Powder Diffraction Data After 900°C For 70 Hr

d, A	Observed Intensity*	d, A	Observed Intensity*
5.589	VW	1.689	Ft
5.153	Ft	1.658	Ft
4.716	Ft	1.635	Ft
4.447	VW	1.619	Ft
4.128	VVW	1.603	Ft
3.750	VW	1.514	Ft
3.317	VW	1.482	VW
3.111	Ft	1.471	M
3.049	VVW	1.461	M
2.941	VW	1.279	VVW
2.784	VW	1.250	W
2.438	VVW	1.214	VVW
2.407	M	1.205	MW
2.384	M	1.194	MW
2.288	Ft	1.048	W
2.220	VVW	1.035	M
2.095	S		
2.067	S		
1.751	Ft		
1.703	Ft		

* *S* indicates strong; *M*, medium; *MW*, medium weak; *W*, weak; *VW*, very weak; *VVW*, very very weak; *Ft*, faint.

This alloy had been annealed at 1200°C for 13 hr and quenched. Its X-ray pattern, similar to a face-centered-cubic pattern, corresponds to the NaCl structure which is composed of two interpenetrating face-centered-cubic lattices of the two types of atoms. Fig. 1B shows the X-ray spectrometer pattern of this alloy annealed at 900°C for 70 hr and quenched. The existence of a new phase is indicated.

This transformation can be reversed. The alloy changes back to the NaCl structure if annealed at a temperature of 950°C or higher. As can be seen from the diffraction data read from a film taken with a Debye-Scherrer powder camera (114.6 mm) in Table I, this new phase has quite a complicated structure of possible low symmetry. It was not possible to solve its structure with these powder data. There is one significant fact, however. The prominent lines of the lower temperature phase seem to be coincident with, or are split from, the lines of the high temperature TiO phase. It has been reported previously that the diffraction pattern of the TiO phase broke down to two distinct body-centered-cubic structures when the alloy was annealed at 870°C for 48 hr.[2] This may have resulted from the coincidence of the prominent lines of the two phases.

The existence of this new phase was based only upon the X-ray diffraction data. No apparent change has been found from metallographic observations and hardness and density measurements. Densities of TiO before and after the noted transformations are about 4.93 g per cc.

Acknowledgment

The authors wish to express thanks to the Office of Naval Research, under whose Contract No. N5-ori-07881 this work was performed.

References

1 E. S. Bumps, H. D. Kessler, and M. Hansen: The Titanium-Oxygen System. *Trans.* ASM (1953) 45, p. 1008.
2 A. E. Jenkins: Discussion of ref. 1. *Trans.* ASM (1953) 45, p. 1025.

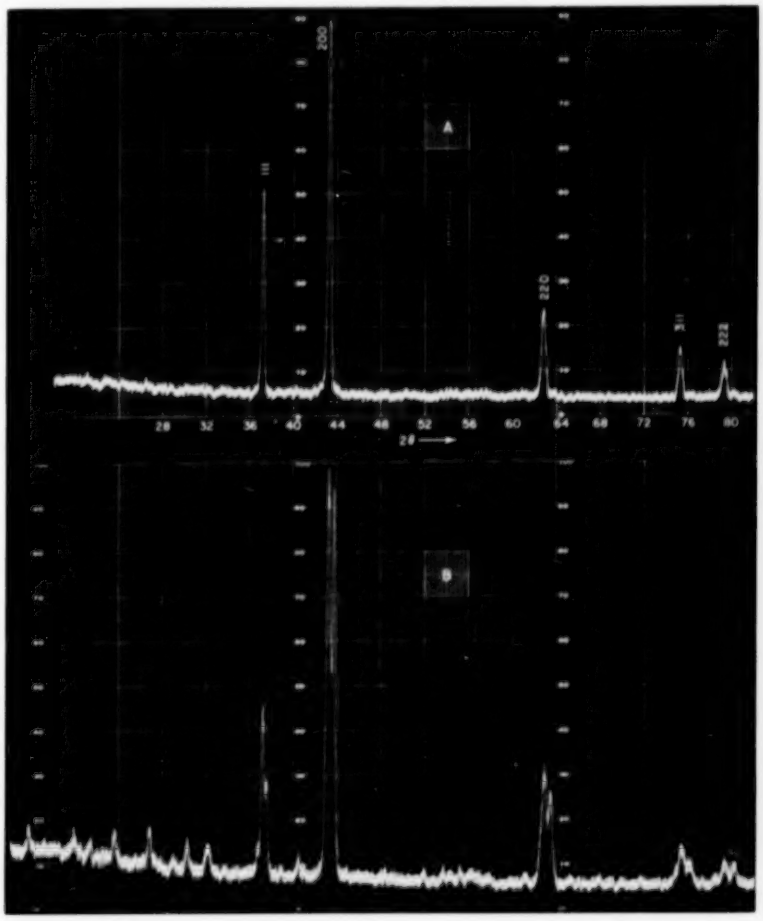

Fig. 1—Two-part chart shows the X-ray spectrometer pattern (CuKα radiation) for TiO (25 wt pct O). Section *A* shows the pattern for the TiO specimen annealed at 1200°C for 13 hr and quenched. Section *B* shows the pattern for the specimen after quenching and annealing at 900°C for 70 hr and quenching.

Internal Friction in Zirconium

Internal friction characteristics and temperature dependence of the torsion modulus for iodide zirconium containing 2.4 pct Hf were investigated, using a low frequency pendulum technique. The internal friction curve consists of a background which increases as the temperature increases, a maximum at 860°C apparently due to the allotropic transformation, a maximum due to grain boundary relaxation with an associated heat of activation of 58,000 cal per mol, and an anomaly below 350°C which may be associated with a precipitation phenomenon. Oxygen in small amounts reduces the grain boundary maximum substantially. The variation of the torsion modulus at 20°C was found to be 3450 Kg per mm² for the zirconium used in the present work.

by W. J. Bratina and W. C. Winegard

IT is well known that small amounts of certain solutes materially affect the ductility of zirconium. Lely and Hamburger,[1] as early as 1914, found that high purity zirconium exhibited a remarkable ductility, while Fast[2] has shown that oxygen and nitrogen can cause substantial embrittlement. Treco[4] has recently demonstrated that the ductility decreases sharply with the oxygen content, and that 2 atomic pct O_2 embrittles zirconium to such an extent that cold working is impossible.

The marked decrease in ductility is difficult to understand in view of the fact that Domagala and McPherson[3] report the solid solubility of oxygen in zirconium to be 29 atomic pct at 500°C. Another metal which behaves much the same as zirconium in this respect is titanium. Pratt et al.[5] investigated the internal friction characteristics of titanium and the effect of oxygen on the internal friction values. It is evident that internal friction measurements are of value for studying grain boundary segregation, as shown by Pratt et al.[5] for oxygen in titanium, by Pearson[6] for oxygen in copper, and by Maringer and Schwope[7] for oxygen in molybdenum.

With this in view, the internal friction characteristics of zirconium and the qualitative effect of oxygen on the grain boundary relaxation phenomenon were investigated.

Materials and Experimental Procedure

The zirconium used in the present work was supplied by the Foote Mineral Co. in the form of wire 0.05 in. diam. The analysis supplied by the manufacturer indicates the amount of hafnium as 2.4 pct, less than 0.01 pct O_2, less than 0.01 pct N_2, less than 0.02 pct H_2, and less than 0.001 pct C. Additional spectrographic analysis indicates the other main impurities as follows: 0.01 pct Fe, 0.05 pct Si, 0.008 pct Cu, <0.005 pct W, <0.001 pct Al, <0.05 pct Mg, <0.001 pct Ni, <0.02 pct Ca, and <0.01 pct Ti.

Microscopic examination of the material in the *as received* condition revealed very fine grains with numerous twins.

W. J. BRATINA, formerly associated with Dept. of Metallurgical Engineering, University of Toronto, Toronto, is now associated with the Ontario Research Foundation, Toronto, and W. C. WINEGARD is associated with Dept. of Metallurgical Engineering, University of Toronto.

Discussion of this paper, TP 4082E, may be sent, 2 copies, to AIME by Apr. 1, 1956. Manuscript, Feb. 18, 1955. Philadelphia Meeting, October 1955.

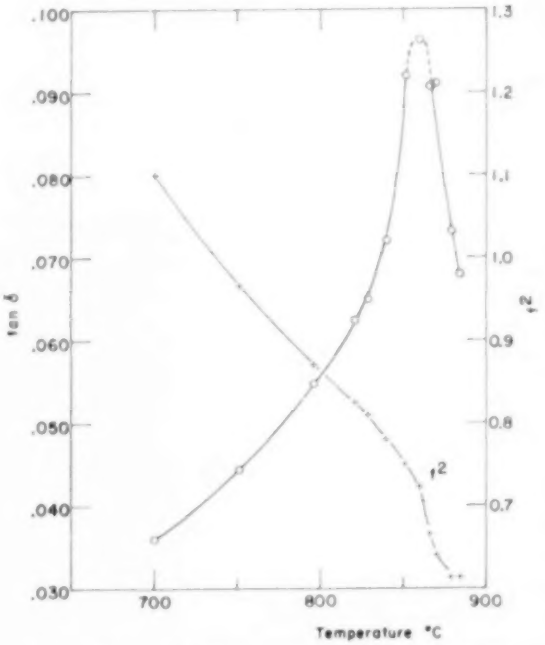

Fig. 1—The internal friction maximum and the deviation of the torsion modulus (represented as f^2) due to the α-β transformation in zirconium are charted.

Specimens were annealed either *in situ* in the internal friction apparatus or in evacuated silica tubes in an auxiliary furnace. When the specimens were annealed in the auxiliary furnace, they were wrapped in identical zirconium wire to prevent contamination by the container. Metallographic sections were taken in all cases. Some were taken from the specimens used for internal friction measurements after completion of the experiments, while others were taken from control specimens at intermediate stages of the experiments.

Internal friction values were obtained by measuring the free decay of a low frequency torsion pendulum (1 cycle per sec), the suspension of which was

the zirconium wire specimen. The apparatus was essentially the same as that used by Pratt et al.[5] The length of the wire between the grips was 30 cm and the maximum pendulum deflection produced a maximum torsional strain of less than 10^{-4} cm per cm at the surface of the specimen. The internal friction measurements were made during the controlled cooling of the specimen and the temperature fluctuations along the length of the specimen were about 1°C.

The internal friction defined by tan δ = logarithmic decrement/π was determined as a function of temperature.

Experimental Results and Discussion

The relaxation spectrum of zirconium appears to consist of four components, a general background which increases with increasing temperature, a maximum at approximately 860°C, a maximum between 500° and 700°C, and an anomaly below 350°C.

It was anticipated that the zirconium would become contaminated during the experiments at high temperatures; thus, each effect was investigated separately using different specimens.

Maximum Attributed to the α-β Transformation—The specimen was cleaned and then inserted in the furnace in the *as received* condition. The temperature was raised quickly (30 min) to 900°C and held for 15 min to establish a uniform temperature along the specimen. Internal friction measurements were taken, the results of which are shown in Fig. 1. The internal friction curve exhibits a very pronounced maximum, which corresponds to a sharp decrease in the torsion modulus line. The exact temperature of this maximum is difficult to determine, but it is approximately 860°C. In Fig. 1, the value for torsion modulus is represented by f^2 where f is the frequency of vibration in cycles per sec. Since the torsion modulus at any temperature, G_t, is proportional to f^2, then f^2 represents the variation of the torsion modulus with temperature. From the temperature of the maximum and the extremely high internal friction values, it is suggested that this maximum in the relaxation spectrum is associated with the α-β transformation which occurs at a temperature of 862°C for high purity zirconium. In the authors' case the allotropic transformation extends over a range of temperature due to both the 1.6 atomic pct O, present because of contamination and the 2.4 pct Hf in the zirconium.

Maximum Due to the Grain Boundary Relaxation Phenomenon—*Zirconium:* The variation of internal friction values from 350° to 650°C for two specimens with different grain sizes is shown in Fig. 2. From the graph, it may be seen that a deviation from the general background curve appears at approximately 425°C for the fine grained specimen, *a*. This deviation extends over a range of approximately 200°C and the value of internal friction is high. This maximum can be attributed to the relaxation across grain boundaries since it disappears when large grained specimens, *b*, are used and the amount of grain boundary area is reduced. To prevent grain growth and oxygen contamination, the temperature used in these experiments was only high enough to investigate the low temperature portion of the maximum.

A sharp decrease in the value of the ratio of torsion moduli G_t/G_∞ where G_∞ was found to be 3450 ± 50 Kg per mm^2, is for the fine grained specimen, *a*, also shown in Fig. 2. The extrapolated

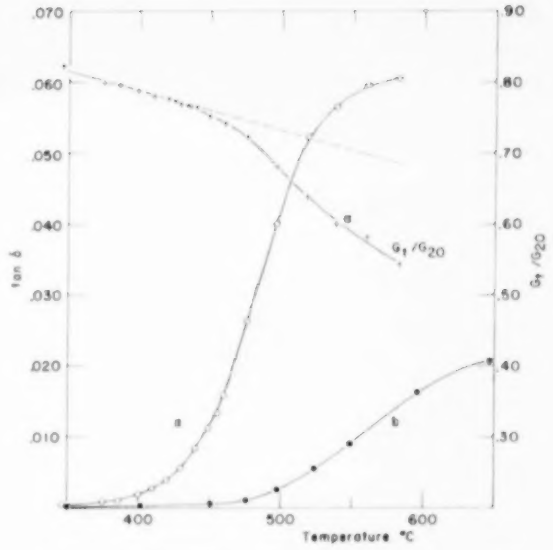

Fig. 2—Grain boundary relaxation effects in α zirconium for *a*, a specimen with an average grain diameter of 0.02 mm, and *b*, a specimen with extremely large grains, are plotted.

straight line corresponds to the torsion modulus of a single crystal specimen.

Although no exact mechanism has been proposed for the grain boundary relaxation phenomenon, the heat of activation, H, for the overall grain boundary relaxation may be calculated from the equation

$$\ln (f_a/f_b) = (H/R)\,\Delta(1/T)$$

where $\Delta(1/T)$ is the shift necessary to superimpose curves of tan δ vs $(1/T)$ for two different frequencies of vibration f_a and f_b.

Fig. 3 shows a plot of tan δ vs 1000/(T°K) for *a* equal to a frequency of 1.35 cycles per sec, and for *b* equal to a frequency of 0.64 cycles per sec at 20°C. The heat of activation is extremely sensitive to the value $\Delta(1/T)$; thus, all precautions were taken to avoid grain growth and contamination, since both affect the relative position of the curves. It was not necessary to heat the specimens above 520°C because only the low temperature side of the grain boundary maximum is important for determining

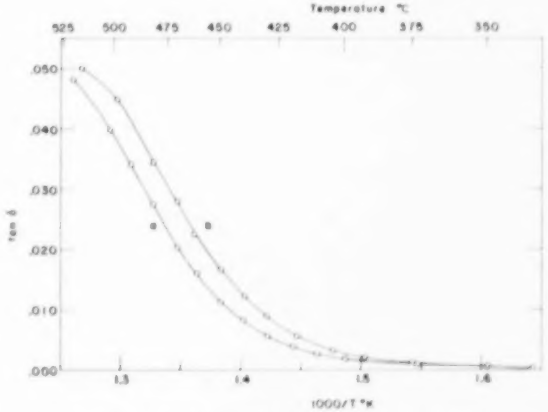

Fig. 3—Variation of internal friction due to grain boundary relaxation is plotted vs 1000/T for two frequencies of vibration of about *a*, 1.35; and *b*, 0.64 cycles per sec at 20°C.

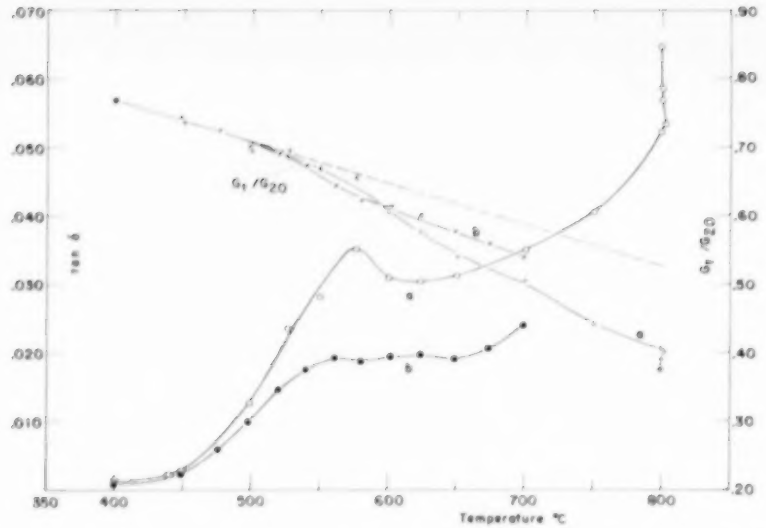

Fig. 4—Effect of oxygen on the grain boundary relaxation maximum is charted. The average grain diameter is 0.055 mm, and the total amount of oxygen is 0.62 atomic pct.

the heat of activation for the grain boundary relaxation. The average value of the heat of activation for the grain boundary relaxation in zirconium was found to be 58,000 cal per mol.

Effect of Oxygen on the Grain Boundary Relaxation Phenomenon: Oxygen was introduced into the zirconium by allowing the specimens to *contaminate* in the vacuum apparatus. This method was chosen to prevent the excessive grain growth which would have occurred if the normal high temperature annealing methods had been used. The disadvantage of such *oxidation* is that the exact composition of the material cannot be determined. In these qualitative experiments, the total increase in weight was considered to be equal to the amount of oxygen absorbed during the experiments.

The effect of the addition of oxygen on the grain boundary relaxation maximum is readily seen from Fig. 4. The curve marked *a* was obtained by annealing *in situ* for 1 hr at 800°C and then measuring the internal friction values. The average grain size of these specimens was 0.055 mm. The specimens were then reheated to 700°C and the measurements taken for curve *b*. The total amount of oxygen found after the completion of both experiments was 0.62 atomic pct. The only difference between the specimen from curve *a* to curve *b* was the small amount of oxygen that it must have picked up during experiment *b*, but the grain boundary relaxation maximum has been drastically reduced. There was no change in grain size between the two sets of experiments, and the effect seems much too large to be explained only by the small increase in solute content, unless it is assumed that the solute is segregated preferentially at the grain boundary region during the *b* experiments. The results seem to suggest that the solute began to segregate to the grain boundary regions during the cooling from 800°C, and that the second temperature increase to 700°C did not allow sufficient time or the temperature was not high enough to even out the distribution of oxygen between the grains and the grain boundary region. In fact, the reheating may have brought about more segregation. This is in general agreement with the work of Thomas and Chalmers[8] on grain boundary segregation. The variation of torsion modulus follows the variation in the internal friction curve, as shown in Fig. 4.

The Anomaly Below 350°C—Preliminary experiments show that the internal friction values are abnormally high below 350°C and that they are highest from 200° to 300°C. The value at any temperature, however, is not constant but decays with time, as shown in Fig. 5. Neither the grain size nor the oxygen content appears to affect this maximum, but annealing and slow cooling in vacuum seem to suppress it, while heating and quenching seem to enhance the anomaly.

An effect of this type may be caused by several factors. It is worthwhile to consider the effect in relation to the precipitation of zirconium hydride. It has been reported[9, 10] that at approximately 310°C hydrogen in solution begins to precipitate as zirconium hydride. It seems possible that the internal friction technique registers a disturbance in the material caused by the precipitation process. As the precipitation process approaches completion, the internal friction values would be expected to decrease, as shown in Fig. 5.

Summary

The internal friction characteristics and the temperature dependence of the torsion modulus for iodide zirconium (containing 2.4 pct Hf) have been investigated. Two distinct maxima in the relaxation spectrum have been observed as well as an anomaly at lower temperatures.

A very large maximum at approximately 860°C has been attributed to the α-β allotropic transformation and is accompanied by a sharp decrease in the torsion modulus. The second maximum between

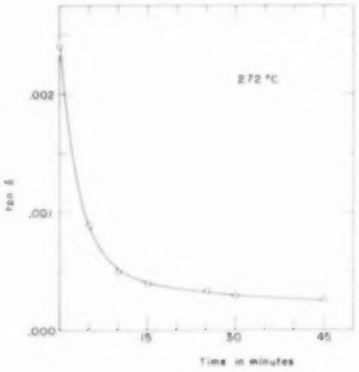

Fig. 5—Variation of internal friction values with time at 272°C is plotted.

500° and 700°C was found to be due to the relaxation across grain boundaries in polycrystalline specimens. This maximum is changed by changing the grain size and is not found in specimens with very large grains. The heat of activation for the grain boundary relaxation process was determined as 58,000 cal per mol. This same relaxation is responsible for a marked decrease in the torsion modulus values. The actual value for the torsion modulus at 20°C is 3450 Kg per mm².

Oxygen has a large effect on the grain boundary relaxation, even when present in amounts of approximately 0.6 atomic pct. This is explained by assuming significant preferential segregation of the solute at grain boundary regions.

An anomaly occurs below 350°C, which may be attributed to the process of precipitation of hydrogen as zirconium hydride.

Acknowledgments

The authors wish to thank L. M. Pidgeon, Head of the Dept. of Metallurgical Engineering, University of Toronto, for his encouragement and for the provision of laboratory facilities. The spectrographic analysis was supplied by Dominion Magnesium Ltd., and the metallography was done by Mrs. P. Karabinsky of the Ontario Research Foundation. The financial support of Defence Research Board of Canada, Grant 183, and the National Research Council of Canada is gratefully acknowledged. The authors are indebted to their colleagues at the Dept. of Metallurgical Engineering, University of Toronto, and in particular C. E. Elbaum for helpful discussion.

Discussion of this paper, if any, will appear in JOURNAL OF METALS, November 1956, and in AIME Metals Branch *Transactions*, Vol. **206**, 1956.

References

[1] D. Lely and L. Hamburger: *Ztsch. für Anorg. Allgem. Chemie* (1914) 87, p. 209.
[2] J. D. Fast: *Metallwirtschaft* (1938) 17, p. 459.
[3] R. M. Treco: *Trans.* AIME (1953) 197, p. 344; JOURNAL OF METALS (February 1953).
[4] R. F. Domagala and D. J. McPherson: *Trans.* AIME (1954) 200, p. 238; JOURNAL OF METALS (February 1954).
[5] J. N. Pratt, W. J. Bratina, and B. Chalmers: *Acta Metallurgica* (1954) 2, p. 203.
[6] S. Pearson: *Royal Aircraft Establishment Report No. Met.* 67 (1951).
[7] R. E. Maringer and A. D. Schwope: *Trans.* AIME (1954) 200, p. 365; JOURNAL OF METALS (March 1954).
[8] W. R. Thomas and B. Chalmers: *Acta Metallurgica* (1955) 3, p. 17.
[9] C. M. Schwartz and M. W. Mallett: *Trans.* ASM (1954) 46, p. 649.
[10] W. L. Mudge: *Symposium on Zirconium and Zirconium Alloys*, (1953) p. 146. Cleveland. ASM.

Experimental Observations Concerning the Collapse of Dislocation Loops During Annealing

The c-axis indentations in zinc crystals were shown to undergo 100 pct strain recovery on heating. The mode of deformation and the details of the polygonization and collapse of indentations were found to be consistent with a number of predictions of dislocation theory.

by Jack Washburn

IT has been observed that indentations of the type made by Jillson[1] in zinc crystals can, under certain conditions, be made to shrink in size and even completely disappear on heating the crystal, Fig. 1. The details of the process are interesting in that they afford a simple experimental illustration of several predictions of dislocation theory.

The indentations were made as shown in Fig. 2 by dropping a 0.2 g indenter with a hemispherical point on a cleavage face of a zinc crystal. Such indentations can be made through relatively great thicknesses in the c-axis direction. The material close to the struck surface, where mechanical twinning and complex distortion occurred, was removed by cleavage. The remaining crystal, which was about 1 cm thick, contained a dent that was accurately round and almost the same size on both top and bottom surfaces. The indentation had the form of a flat cone of half angle approximately 89°, having a rounded apex and a rounded intersection with the undeformed part of the crystal.

The mode of deformation was primarily slip on the three equivalent systems in the basal plane. Six types of dislocation loop (plus and minus in each of the three directions) as shown in Fig. 3 are required by the geometry of the indentation. The maximum shear strain in the radial direction amounted to approximately 2.5 pct. Slip was distributed in the usual, microscopically nonuniform, manner among the possible parallel slip planes. When an indentation was made close to a (2110) surface, three separate sets of interpenetrating slip bands appeared as shown schematically in Fig. 3. A small biaxial tension strain in the plane of (0001) is also a geometrical necessity for the formation of an indentation. If the sides of the dent are tilted 1° with respect to the undeformed surrounding crystal, and the surround-

J. WASHBURN, Member AIME, is Assistant Professor of Metallurgy, University of California, Berkeley, Calif.

Discussion of this paper, TP 4112E, may be sent, 2 copies, to AIME by Apr. 1, 1956. Manuscript, Feb. 28, 1955. Philadelphia Meeting, October 1955.

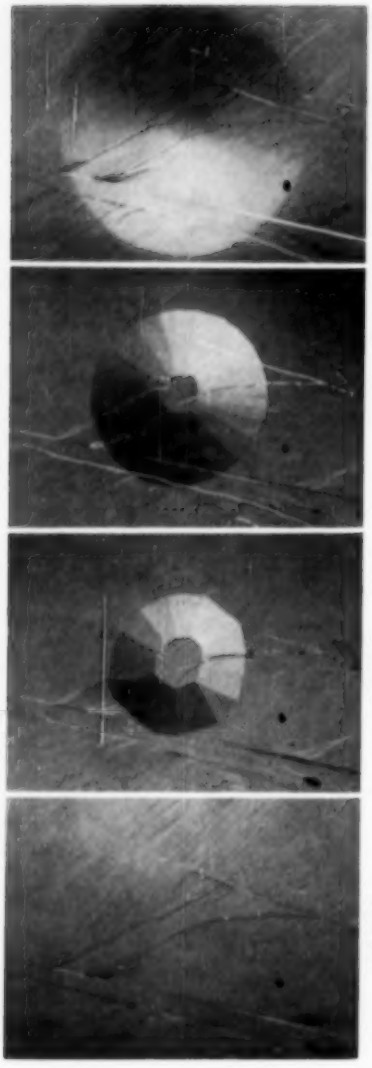

a—Crystal is shown directly after impact at room temperature.

b—Crystal has been heated to 300°C and immediately cooled to room temperature.

c—Crystal has been heated to 350°C and immediately cooled to room temperature.

d—Crystal has been heated to 400°C and immediately cooled to room temperature.

Fig. 1—Micrographs illustrate complete strain recovery of a conically distorted volume of crystal during annealing. X50. Area reduced approximately 35 pct for reproduction.

ing material is considered to be rigid, the extension required is 0.015 pct. This strain may not have been entirely elastic, particularly after heating to above 300°C. However, examination of cleavage surfaces in the vicinity of indentations revealed no evidence of deformation markings which could be interpreted as indications of nonbasal slip. Whether or not some nonbasal slip occurred, it appeared likely that residual stresses were present in the vicinity of an indentation, in a way that would tend to promote flattening.

Heating the crystal to successively higher temperatures resulted in the structural changes shown in Fig. 1. Sharp radial and circumferential boundaries formed as soon as the temperature was raised high enough to expect edge dislocation climb. The outer circumference shrunk inward and a flat area formed at the center which grew in diameter. The noncrystallographic directions assumed by most of the first formed boundaries required that they have a complex dislocation structure; they must have contained dislocations of more than one Burger's vector. Furthermore, consideration of the way in which the originally separate overlapping dislocation loops must have lined up to form the radial boundaries suggested that, initially, even those boundaries which were at right angles to a $[11\bar{2}0]$ direction and, therefore, could have had a simple structure, probably formed from equal numbers of dislocations whose Burger's vector lay 60° to either side of the direction normal to the boundary. In a pure tilt boundary of this type in which none of the dislocations are in pure edge position, the screw components of the two types of dislocations present are of opposite sign and cancel one another. Due to the attraction of the screw components, there would be a strong tendency, if climb of edge components is permitted, for unlike pairs of dislocations to combine, forming a single pure edge dislocation by the reaction

$$a/_3[2\bar{1}\bar{1}0]+a/_3[\bar{1}2\bar{1}0]\rightarrow a/_3[11\bar{2}0].$$

Thus, the boundary would be expected to assume the simple structure. The assumption that small angle boundaries having this ideal structure would have a lower boundary energy than those containing more than one type of dislocation was consistent with the shape assumed by the system of boundaries during collapse. Boundaries which could not have the minimum number of dislocations because they did not lie at right angles to a slip direction tended to shorten or to disappear by combination with other boundaries. Finally, just before the complete disappearance of the system, most of the remaining boundaries lay in the preferred directions. The screw segments of the original dislocation loops had presumably been eliminated by reactions of the above type. Rather than forming part of a complete loop, each dislocation segment then must have ended at a node. Fig. 4 shows such a system of boundaries in the final stages. On heating to 400°C, the last picture of Fig. 1 shows that the cleavage plane was again just as mirror flat as it had been before the indentation had been made. The dislocation loops had, in effect, completely collapsed, resulting in 100 pct

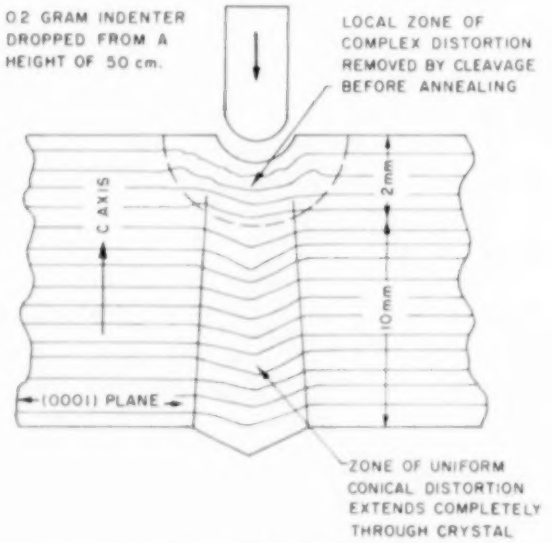
0.2 GRAM INDENTER DROPPED FROM A HEIGHT OF 50 cm.
LOCAL ZONE OF COMPLEX DISTORTION REMOVED BY CLEAVAGE BEFORE ANNEALING
C AXIS
2mm
10mm
(0001) PLANE
ZONE OF UNIFORM CONICAL DISTORTION EXTENDS COMPLETELY THROUGH CRYSTAL

Fig. 2—Diagram plots method of making indentations. Impact is directed along c-axis of the crystal.

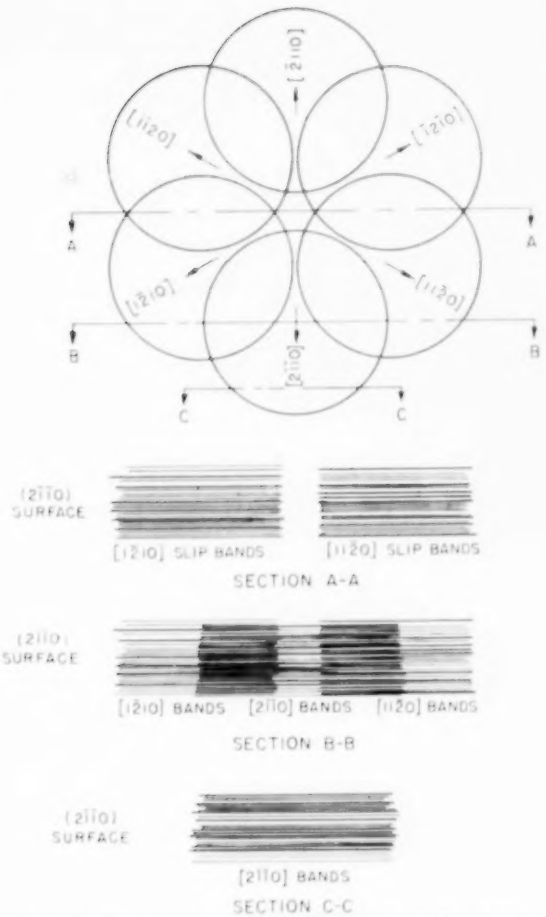

Fig. 3—The mode of deformation in an indentation is illustrated.

strain recovery of the 2.5 pct local plastic deformation.

The following predictions of dislocation theory are illustrated by the experimental observations: 1—*dislocation line tension* which must supply much of the driving force causing collapse of the loops, 2—*stability of a vertical wall of dislocations* even when

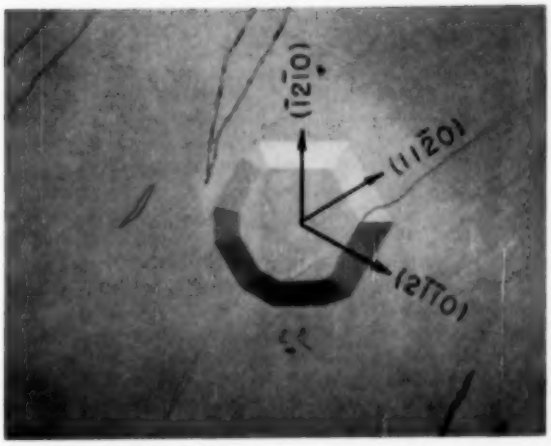

Fig. 4—Micrograph shows final stage in the disappearance of an indentation during annealing. The most stable boundaries are those at right angles to directions of the type [2110]. X50. Area reduced approximately 10 pct for reproduction.

all of the dislocations in the boundary must be of mixed edge and screw character, 3—*decrease in energy of the system when two boundaries* combine to form a single boundary whose angle is the sum of those of its components, 4—*lower energy of a pure edge dislocation boundary* as compared to a boundary of the same angle containing dislocations of more than one Burger's vector, 5—*climb of edge dislocations* at high temperature, 6—*mobility of simple dislocation boundaries* by motion of their component dislocations in their respective slip planes, 7—*formation of dislocation nodes* at which the sum of the Burger's vectors of the three joining dislocations equals zero, 8—*mobility of dislocation nodes* when all three dislocations lie in the same slip plane, and 9—*annihilation of dislocations during annealing* by joining of positive and negative segments.

Discussion of this paper, if any, will appear in JOURNAL OF METALS, November 1956, and in AIME Metals Branch *Transactions*, Vol. **206**, 1956.

Reference

1 D. C. Jillson: Trans. AIME (1950) 188, p. 1009; JOURNAL OF METALS (August 1950).

High Speed Quenching Dilatometer

by F. E. Martin and R. H. Raring

A high speed gas quenching dilatometer useful in studying phase transformations in low alloy steels is described. Changes in specimen length are measured by means of an electrical micrometer tube. The maximum instantaneous cooling rate is approximately 5000°F per sec; the maximum average cooling rate from 1650° to 950°F is approximately 2900°F per sec. Data for steels of 0.11 pct and 0.67 pct C content are included.

F. E. MARTIN is Graduate Student, Dept. of Physics, University of Illinois, Urbana, Ill., and R. H. RARING is associated with NACA, Washington.

Discussion of this paper, TP 4063E, may be sent, 2 copies, to AIME by Apr. 1, 1956. Manuscript, Feb. 4, 1955. Philadelphia Meeting, October 1955.

KNOWLEDGE of phase transformations as they occur in an alloy under conditions of continuous cooling affords valuable insight into its properties. The transformation characteristics during continuous cooling of steels of high hardenability, which decompose entirely to martensite at fairly slow cool-

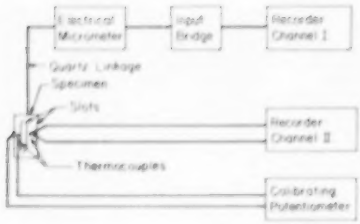

Fig. 1—Diagram blocks parts of dilatometer.

ing rates, can be studied with relative ease. But steels of low and intermediate hardenability, which represent the bulk of our commercial steels, have high critical cooling rates. For such steels, apparatus for the determination of transformation diagrams for continuous cooling must, therefore, be fast acting.

Early studies of transformations in steels undergoing rapid cooling were made by considering irregularities in time-temperature curves caused by evolution of heat on change of phase. Considerable work has since been done by this thermal arrest method.[1] Chevenard,[2] in a study of transformations made with a differential recording dilatometer, reported high cooling rates for hydrogen quenching of steel wire specimens. The method employed in recording temperatures, though ingenious, was based on many assumptions and did not give results in accord with modern studies.

More recently, Christenson, Nelson, and Jackson[3] developed a dilatometer in which length changes were measured by means of an electrical micrometer tube and an oscillograph. They reported studies of transformations in low alloy steels at cooling rates up to 900°F per sec. Cottrell[4, 5] has recently reported dilatometric work at average cooling rates to transformation, up to 260°F per sec. Modern dilatometers used for lower cooling rates have also been described.[6, 7]

The present dilatometer, in which the electrical micrometer tube is employed as the element sensitive to length change, has made available maximum quenching rates of approximately 5000°F per sec. It is therefore capable of yielding data in the little explored field of continuous cooling transformations in low alloy steels.

Apparatus and Procedure

In Fig. 1 is shown a block diagram of the dilatometer. The specimen used, as shown in Fig. 2, is a thin walled cylindrical shell, 0.700 in. long, with 0.400 and 0.375 in. OD and ID, respectively, copper-plated to prevent decarburization during the thermal cycle. Three slots ½ in. long and ⅛ in. wide, spaced at equal intervals around the circumference of the specimen, permit access of gas to its internal as well as external surface and thus reduce lateral thermal gradients during quenching. Preliminary work indicated that no undesirable results are obtained because of slotting the specimens.

The specimen is mounted on a quartz supporting tube. A quartz *T*-rod, with the top of the *T* in contact with the upper specimen edge, extends down through the tube and transmits increments in specimen length to the projecting arm of the electrical micrometer tube. The *T*-rod is held against the upper specimen edge and the lower specimen edge is held against the quartz tube by the spring shown; spring tension may be adjusted as required.

A simplified diagram of the electrical micrometer tube[8] and control and bridge circuits used with it in recording length changes are given in Fig. 3.* Motion

* An RCA tube, type 5734, available for general purchase, can be used, with circuit modifications, as an electrical micrometer tube.

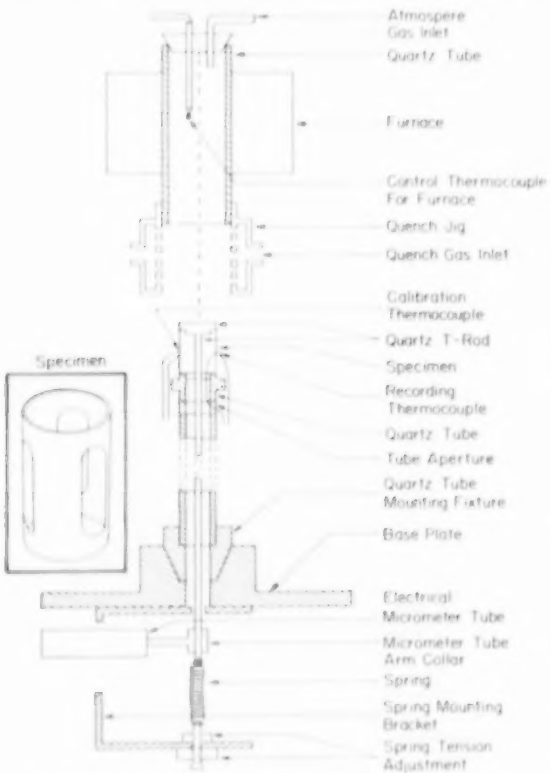

Fig. 2—Diagram gives schematic presentation of dilatometer.

of the projecting arm, mounted on an elastic diaphragm which constitutes the left wall of the micrometer tube as shown, shifts the position of the plates, *P* and *P*, relative to the filament, *F*, and yields a change in current proportional to the displacement of the arm. The corresponding bridge voltage is amplified and recorded by one channel of a magnetic oscillograph.

For the temperature determinations, thermocouples of number 28 gauge chromel and alumel wires individually spot-welded to the specimen surface are used. Because of sizable lateral temperature gradients in the specimen during fast quenching, to be discussed later, both wires are welded to the outer surface when the temperature at the beginning of a transformation is sought, whereas in following progress of transformation a split thermocouple, with one wire welded to the inner specimen surface and the other to the outer, is used. Thermocouple wires from the calibrating potentiometer are welded to the outer specimen surface.

The recording thermocouple is connected directly to the input circuit of a dc amplifier, the output of which is recorded by a second channel of the magnetic oscillograph. The two channel amplifier-oscillograph responds well to frequencies as great as 100 cycles per second. Input impedance of each amplifier is ten megohms. Currents in the thermocouple circuit described are inappreciable.

The resistance furnace and quench jig form an integral unit that can be rapidly raised from or

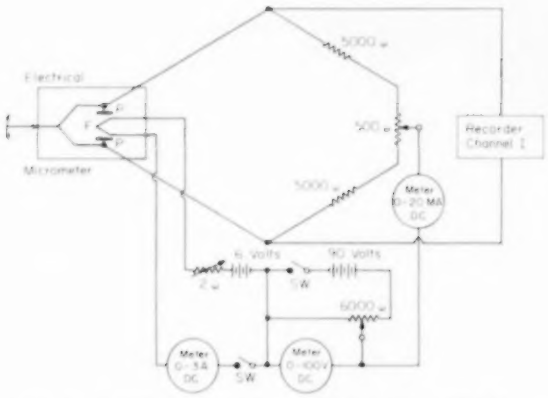

Fig. 3—Diagram shows circuit for electrical micrometer tube.

lowered around the specimen, Fig. 4. Automatic temperature control is employed with the furnace, which can be held within a few degrees of the desired maximum temperature. In Fig. 4 the control thermocouple is shown in position in the furnace; when the furnace is lowered into the specimen heating position the control couple is close to the upper specimen edge.

Helium gas of high purity is used as the quenching medium except when the specimen is cooled slowly by exposure to the atmosphere. It is also used as atmosphere gas to prevent oxidation of the specimen during heating. Pressure indication provided by a manometer is needed in reproducing the lower cooling rates; valve gauge indications suffice for the higher rates. A purification train is used to remove traces of moisture and oxygen in the helium used during the heating cycle.

In making a run, the furnace is preheated to the desired temperature, adjustment of gas fixtures is made, and the furnace is lowered into the specimen heating position. The specimen reaches its maximum temperature in about 1½ min and is held at temperature long enough to ensure that it has all transformed to austenite. The furnace and quench jig assembly is then rapidly shifted to the quench position. To expose the specimen, the assembly is raised to the position shown in Fig. 4.

During a run, initial, maximum, and final specimen temperatures are read with the calibrating potentiometer to establish fixed points on the temperature record. A micrometer screw is used to calibrate the dilation recording equipment.

Results

Temperature vs time and length change vs temperature curves typical of those obtained with the dilatometer are shown in Fig. 5, A and B. The data were obtained for an annealed 0.11 pct C, 0.99 pct Mn, 0.24 pct Si steel.

The fast quench referred to in Fig. 5 was one with helium gas at the maximum pressure now employed.

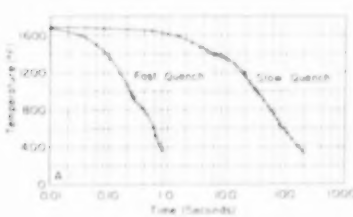

Fig. 5A—Chart gives cooling curves for 0.11 pct C, 0.99 pct Mn steel, with both fast and slow quenches represented.

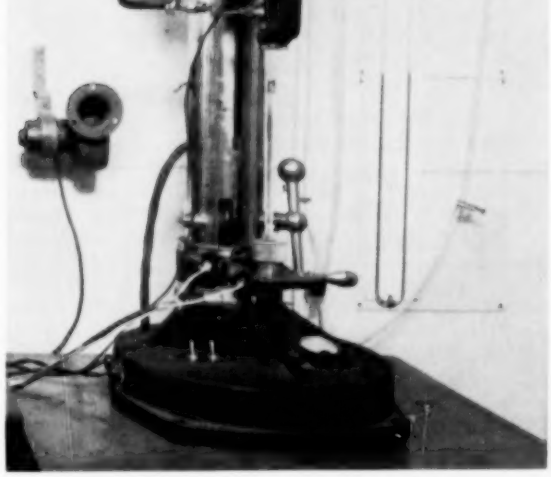

Fig. 4—Photograph of dilatometer is shown.

The approximate maximum cooling rate was 5000°F per sec and the average rate from the beginning of gas quenching to the arrest of cooling (at 0.26 sec) corresponding to transformation was approximately 2900°F per sec. The dilatometric value for the transformation temperature, i.e., the temperature of the first break in linearity in the length change vs temperature curve, is 945°F. Agreement of the initial temperature of thermal arrest read from the time-temperature curve, 922°F, with the dilatometric transformation temperature is considered good.

The slow quench referred to in Fig. 5 was obtained by exposing the specimen to the atmosphere. The maximum cooling rate was approximately 80°F per sec, and the approximate average cooling rate from beginning of cooling until transformation was 50°F per sec. The transformation temperature corresponding to the first significant deviation from linearity in the length change curve is 1390°; that corresponding to initial arrest of cooling is 1397°F.

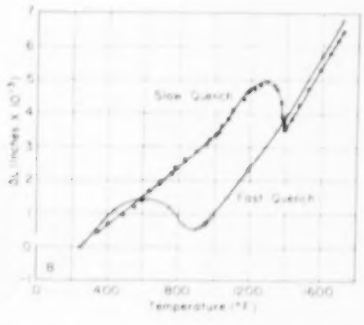

Fig. 5B—Chart gives length change vs temperature curves for 0.11 pct C, 0.99 pct Mn steel, with both fast and slow quenches represented.

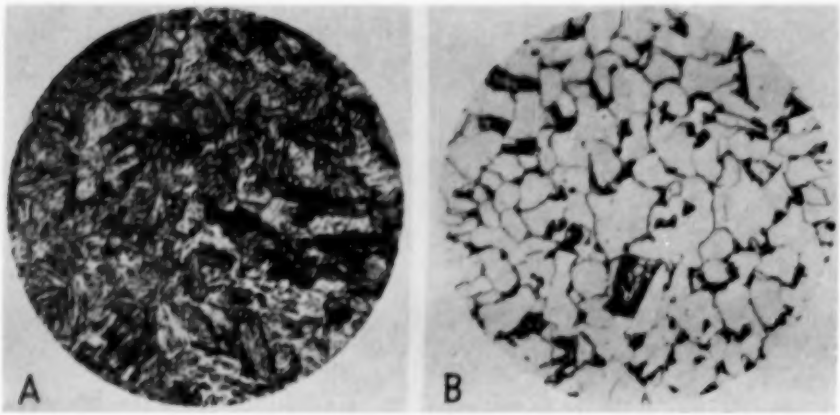

Fig. 6—Microstructures of 0.11 pct C, 0.99 pct Mn steel show results for *A*, fast quench and *B*, slow quench. X750. Area reduced approximately 25 pct for reproduction.

Fig. 6A shows the acicular structure of the fast-cooled specimen. The ferrite and carbide aggregates of the air-cooled specimen are shown in Fig. 6B.

An indication of accuracy of dilatometric data is afforded by expansion data. The average of two values of the coefficient of linear expansion obtained on heating annealed specimens of the 0.11 pct C steel through the temperature range 86° to 1200°F was 7.8×10^{-6} per °F (14.2×10^{-6} per °C); a literature value for annealed SAE 1010 steel in the range 32° to 1292°F is 8.3×10^{-6} per °F (15.0×10^{-6} per °C).[9]

Further indication of accuracy of dilatometric data is given by comparing M_s determined with the dilatometer (with the recording couple on the outer specimen surface) and a value obtained metallographically by the quench and temper method.[10] For three runs with quenched specimens of a 0.67 pct C, 0.99 pct Mn, 0.22 pct Si steel, dilatometric values were 453°, 466°, and 504°F, for an average value of 474°F. Metallographically, martensite was found in traces at 487° and in appreciable quantity at 480°F. Thus, the average value found dilatometrically for M_s is in good agreement with the metallographic value. In general, as in this case, average values of transformation temperatures determined from several runs are believed established to approximately ±30°F.

For the same 0.67 pct C steel, data as to progress of the martensite transformation with cooling were obtained from dilatometric results by a method of proportionality already described in the literature.[11] Comparable metallographic data were obtained by the quench and temper method.[10]

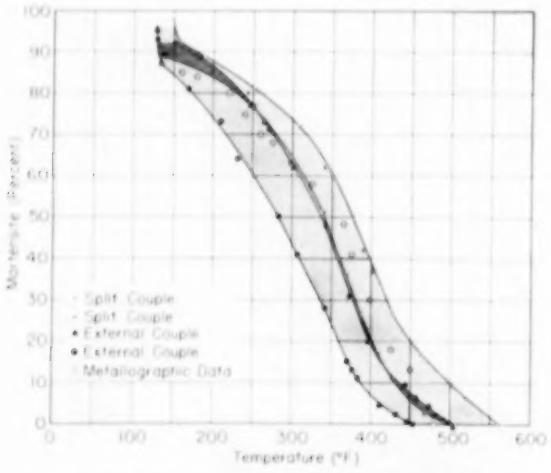

Fig. 7—Chart plots martensite transformation data for 0.67 pct C, 0.99 pct Mn steel.

Fig. 7 shows ranges of percentages of martensite vs temperature curves, as influenced by thermocouple placement. The ranges have been defined by plotting these curves for the runs yielding highest and lowest M_s for each couple position. Thus, for the runs for external couple placement already noted, curves for those yielding M_s points of 453° and 504°F are plotted. The area between these curves is shaded vertically. From runs for split couple placement, yielding M_s points from 503° to 563°F, curves for the highest and lowest value of M_s are plotted. The area between the curves is shaded horizontally. Horizontally and vertically shaded areas are those in which ranges overlap. Corresponding metallographic data are also plotted in Fig. 7.

Dilatometric data in Fig. 7 are for fast quenching (maximum instantaneous quench rates vary from 2200° to 2500°F per sec for the runs). A sizable lateral temperature gradient across each specimen, induced by the fast quenching, is believed to account for failure of the two bands to coincide. Temperature measurements on specimens during fast quenching confirm existence of a gradient of the right magnitude to account for observed differences. Because of the gradient, the temperature of the outer shell of the specimen, read by an externally placed thermocouple, should be lower than the average temperature, read by a split couple, for a given percentage of transformation throughout the specimen; however, the outer shell temperature should correspond well with the initial transformation temperature determined metallographically, since transformation begins in the outer, cooler specimen layer. As expected, the average dilatometric value found for M_s for external couple placement, 474°, does correspond well with M_s found metallographically, 480°F. Hence, an external couple is used to indicate initial transformation temperature in any case where a sizable lateral temperature gradient may exist by virtue of rapid cooling.

The metallographic data showing percentage of transformation for the intermediate stage of cooling below M_s, Fig. 7, show better agreement with split couple dilatometric data than with those for an external couple. For this reason a split couple is used in obtaining data on progress of transformation at this stage of cooling.

Because of difficulties in determining high percentages of martensite accurately by the method of lineal analysis used in the metallographic work,[10] and because the calculated percentage of transformation obtained from the dilatometric data assumes 100 pct transformation on cooling to room temperature (a small amount of austenite appears to be retained at room temperature), agreement of all data indicated in the low temperature region of Fig. 7 is considered satisfactory.

Summary

A gas quenching dilatometer using an electrical micrometer tube has been described. A thin walled, slotted cylindrical shell of material under test is used as a specimen. The instrument can be used in determining transformation temperatures for maximum cooling rates as great as 5000°F per sec. Used with proper precautions, it is believed to give satisfactory results for transformation progress for cooling rates up to 2800°F per sec, and may do so for still greater cooling rates. Thus, it may be used in studying transformations in low alloy steels. Data obtained for 0.11 and 0.67 pct C low alloy steels considered satisfactory.

Acknowledgments

The authors wish to express indebtedness to A. L. Christenson and E. C. Nelson, formerly of Naval Research Laboratory, for the design and assembly of the high speed quenching dilatometer from which present equipment has evolved. They wish to thank H. E. Stauss, J. E. Dinger and W. S. Pellini, all of this Laboratory, for their suggestions and interest.

Discussion of this paper, if any, will appear in JOURNAL OF METALS, November 1956, and in AIME Metals Branch *Transactions*, Vol. **206**, 1956.

References

[1] A. B. Greninger: The Martensite Thermal Arrest in Iron-Carbon Alloys and Plain Carbon Steels. *Trans.* ASM (1942) **30**, p. 1.

[2] P. Chevenard: Mécanisme de la Trempe des Aciers au Carbone. *Revue de Métallurgie* (1919) **16**, p. 17.

[3] A. L. Christenson, E. C. Nelson, and C. E. Jackson: A High-Speed Dilatometer and the Transformational Behavior of Six Steels in Cooling. *Trans.* AIME (1945) **162**, p. 606.

[4] C. L. M. Cottrell: Assessment of Weldability by Rapid Dilatation Tests. *Journal* Iron and Steel Inst. (1953) **174**, p. 17.

[5] C. L. M. Cottrell: Effect of Hydrogen on the Continuous-Cooling Transformation Diagram for a Manganese-Molybdenum Steel. *Journal* Iron and Steel Inst. (1954) **176**, p. 273.

[6] R. W. Dayton and G. M. Foley: Capacitive Micrometer. *Electronics* (1946) **19**, p. 106.

[7] E. J. Vanderman: Microformer Dilatometer. *Review of Scientific Instruments* (1951) **22**, p. 757.

[8] R. Gunn: A Convenient Electrical Micrometer and Its Use in Mechanical Measurements. *Journal of Applied Mechanics* (1940) **7A**, p. 49.

[9] *Metals Handbook*. (1948) 7th Ed., p. 309. Cleveland. ASM.

[10] A. B. Greninger and A. B. Troiano: Kinetics of the Austenite to Martensite Transformation in Steel. *Trans.* ASM (1940) **28**, p. 537.

[11] S. G. Fletcher and M. Cohen: The Dimensional Stability of Steel. *Trans.* ASM (1945) **34**, p. 227.

[12] M. Cohen: The Martensite Transformation. *Phase Transformation in Solids*. (1951) p. 605. New York. John Wiley and Sons Inc.

Tensile Creep of High Purity Aluminum

As part of a program to determine the deformation characteristics of pure metals, the tensile creep properties of high purity aluminum (99.994 pct Al) have been determined using a constant stress loading. The effects of prior annealing temperature, stress, and temperature were studied. These data have been examined on the basis of present-day theories. None of the methods was found to give an accurate representation of the data over all conditions studied. The structures of several specimens after creep were examined by optical and X-ray metallography. Marked changes in the grain size were found and it was substantiated that the magnitude of these changes was greatly influenced by the applied stress (or creep strain). The changes in fiber texture which occur on creep deformation are shown to be consistent with those observed on deformation at lower temperatures.

by R. W. Guard and W. R. Hibbard, Jr.

UNDERSTANDING the properties of new materials under different experimental conditions must be based on considerable knowledge of the mechanisms involved in plastic flow and how to control them. Tension and creep tests have been carried out on a number of pure metals in order to document their deformation characteristics.[1, 2] It is hoped that a comparison of these data with theory will indicate those areas where work on mechanisms and their relation to metallurgical variables may be most fruitful.

R. W. GUARD, Junior Member AIME, and W. R. HIBBARD, JR., Member AIME, are Research Associate and Manager, Alloy Studies Research, respectively, Research Laboratory, General Electric Co., Schenectady.

Discussion of this paper, TP 4070E, may be sent, 2 copies, to AIME by Apr. 1, 1956. Manuscript, Feb. 17, 1955. Philadelphia Meeting, October 1955.

Since aluminum has often been used for studying the qualitative aspects of creep behavior, it was chosen for detailed study. The effects of annealing temperature, stress, and test temperature on the constant stress creep behavior were studied. Although most of the tests were made above one half the absolute melting temperature, a few tests were made at lower temperatures to give qualitative comparisons. Some specimens were examined metallographically and by X-ray diffraction techniques after creep. Since only a limited number of specimens could be made from the available material, no effort was made to study detailed changes in subgrain structure or other metallographic features.

Servi and Grant[3] and Dushman et al.[4] have previously published studies of high temperature creep of high purity aluminum. In both cases, a great deal of emphasis was placed on the minimum creep rate.

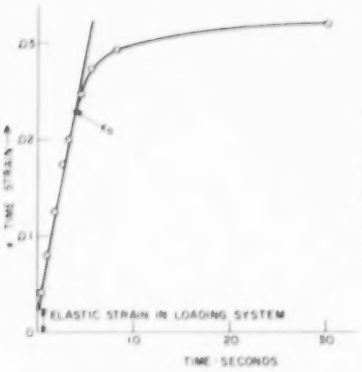

Fig. 1—Early part of the creep curve (typical curve) is plotted.

Servi and Grant[7] point out differences in fracturing behavior at high and low temperatures. Dushman et al.[4] analyze their results by the application of chemical rate process theory, which puts the emphasis on the *steady state* aspects of creep behavior. In the present work an attempt was made to study the entire curve, at least to strains of 0.20. The premise adopted was that a general description of creep behavior would be more useful than one dealing with a special part of the creep curve.

The results of Sherby and Dorn[6] could not be compared to the present data since they were obtained on a constant load rather than a constant stress apparatus. However, their method of analyzing the data was applied to the present data, as discussed later.

Experimental Technique

The high purity aluminum (99.994 pct Al) was obtained from Aluminum Co. of America through the Bureau of Standards. The analysis of the material and its processing history are given in Table I.

In order to obtain a range of grain sizes, specimens were cold drawn from 0.5 in. rods to 0.030 in. wire and annealed at each of a series of temperatures (250°, 300°, 350°, 400°, 450°, and 500°C) for 1 hr. Metallographic examination showed that recrystallization was not complete for the 250°C annealed material and that the material annealed at 500°C had too few grains per cross section (2 to 4) for accurate results. The creep tests were therefore made only on the material from the four intermediate annealing temperatures. The grain sizes obtained are given in Table I.

The creep tests were made at constant stress using a loading lever of the type described by Fullman, Carreker and Fisher.[5] This lever maintains a constant stress by causing the point of application of the load to move toward the fulcrum in proportion to the elongation. Its construction assumes a constant volume and a change in diameter proportional to the elongation during deformation. The specimens were 0.030 in. diam wire, gripped on a five in. gauge length. A ten g preload (less than 1 pct of the total load) was applied before the test to set all link-

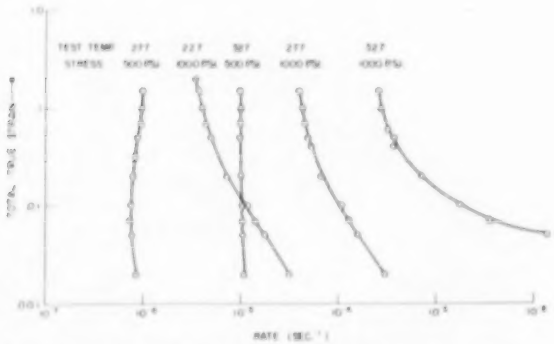

Fig. 2—Chart plots variation of creep rate with strain. All specimens were annealed for 1 hr at 350°C.

Table I. Material and Processing History

As-received material—Round (3/8 in. diam) cut from notch bar and swaged and drawn cold to 0.030 in. diam.

Annealed 1 hr at 300°, 350°, 400°, 450°C; giving average grain diameters of 0.021, 0.037, 0.047 and 0.065 mm, respectively.

Chemical analysis: 0.002 pct C, 0.003 pct Fe, <0.0002 pct Mn, <0.001 pct P, <0.006 pct S. All other elements, faint trace or less. Balance, 99.994 pct Al.

ages. A long seven-winding resistance furnace was used, which provided an eight to ten in. central zone with a temperature constant within ±2°C. Temperature cycling was kept to about ±1°C over long periods by use of an anticipator. In order to minimize heat losses from the end and ambient temperature effects, the upper pull rod was a hollow quartz tube. The Pt—Pt-Rh thermocouple was placed on the upper grip at the end of the specimen. The extension was measured from the motion of the outer end of the lever arm with a lever magnification of 2.5:1.

For recording the strain, a device similar to that of Dushman et al.[4] was used. This apparatus measures the relative motion of two finely ruled grids, one attached to the end of the lever arm, the other fixed. This motion is measured by recording the cyclic change in intensity of a light beam passed through the two grid system as the grid lines move in and out of registry. An ac recorder was added to the circuit used by Dushman to record the rapid extension at the beginning of the test. With this equipment, using grids ruled at 100 lines per in., the minimum measurable strain is 0.0004 in. per in. The minimum strain rate measurable with accuracy is approximately 10^{-4} sec^{-1}. The maximum rate obtainable is limited by the loading rate to 5×10^{-2} sec^{-1}.

Table II. Test Conditions

Anneal	Stress	Test Temperature* 227°C	277°C	327°C	377°C
300°C	500	-	x	x	x
	1000	-	x	x	x
	1500	-	x	x	-
350°	500	-	x	x	-
	1000	x	x	x	-
400°	500	-	x	x	x
	1000	-	x	x	x
	1500	x	x	x	-
	2000	x	x	-	-
450°	500	-	x	x	x
	1000	x	x	x	x
	1500	x	x	-	-

* x's indicate that tests were made at these temperatures.

In order to provide a sound basis for examining present theories, tests were made over as wide a range of stresses and temperatures as possible with the equipment. A few tests were made at temperatures above that of the prior anneal with the in-

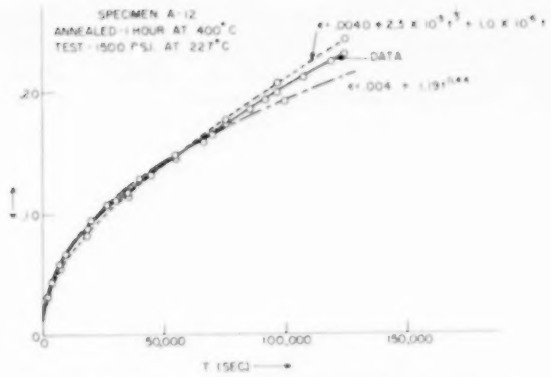

Fig. 3—Chart shows typical fit of the equations of Andrade[14, 15] and Hazlett and Parker[16] to a creep strain-time curve.

tention of examining the effects of an unstable grain size. The conditions under which the elevated temperature creep tests were made are indicated by the x's in Table II.

A number of the specimens were examined metallographically after testing in creep to large strains (0.30). In addition, the preferred orientation or fiber texture before and after creep deformation was examined on two specimens by X-ray techniques.

Results

Structural Observations—Metallographic examination of a number of specimens after large creep strains showed that marked growth of the original grains had occurred. From the results of this examination, shown in Table III, several conclusions were drawn:

1—None of the grain sizes was stable during creep tests, even at temperatures 150°C below the original annealing temperature.

Table III. Grain Size After Creep Test as Function of Test Conditions, Average Grain Diameter in Mm

Original Diameter	Prior Anneal	500 Psi, 277°C	500 Psi, 327°C	500 Psi, 377°C	1000 Psi, 277°C	1500 Psi, 277°C	2000 Psi, 277°C
0.021	300°C	0.106	0.113	0.140	-	-	-
0.047	400°C	0.121	0.138	-	0.111	0.107	0.099
0.065	450°C	-	0.223	-	-	-	-

2—The test temperature, original grain size, and time of test were all factors in determining the final grain size after test.

One of the original objectives of the program was to study the effects of annealing temperature, particularly as it affects the grain size. In view of the changes in grain size which occur during the test it does not seem proper to discuss differences in behavior with respect to the original grain size. Examination of the differences in creep behavior of specimens having different original grain sizes tested under the same conditions of stress and temperature lead to the following conclusions:

1—The effect of annealing temperature on the creep curve is a function of the test conditions.

2—At the lowest test temperatures and stresses the strain on loading increases with increasing annealing temperature. The effect tends to reverse with increasing temperature.

3—The strain hardening rate, as indicated by the rate of change of the creep rate with strain, increases with increasing annealing temperature.

On the basis of these observations, it might be concluded that the stability of the structure established by a prior anneal is more important in determining the creep behavior than is the initial structure of the annealed sample. It is not possible to ascribe the differences in strain hardening rate for the different original grain sizes to any particular mechanism.

In order to determine whether the grain growth is affected by the presence of the stress, a separate set of tests was made, in which duplicate unstressed samples were loaded with creep specimens. The microstructures after strains of approximately 0.30 were compared, and the results in Table IV show the marked effect of creep strain (or stress) on grain growth. This observation agrees qualitatively with those of Chang and Grant[7] and McLean[8] on boundary migration during creep.

Several specimens which had been tested to large strains (0.30) were also examined by X-ray diffraction techniques for preferred orientation. The data,

Table IV. Effect of Stress on Grain Growth During the Test*

Stress, Psi	Test Temperature, °C	Average Grain Diameter, Mm		Time of Test, Sec
1000	327	Stressed	0.095	907
		Unstressed	0.067	
1000	277	Stressed	0.086	5,904
		Unstressed	0.069	

* Material was annealed for 1 hr at 425°C. Average grain diameter is 0.060 mm.

while insufficient for definite conclusions, show several interesting indications. The texture of the specimen before testing is essentially the annealing texture for aluminum wire, although the films are somewhat spotty because of the fairly large grain size. Most grains have a <111> orientation with some <100> and a few <112>. After deforming 30 pct in creep, the texture changes toward the deformation texture. The <112> portion completely disappears. Those grains of the <111> orientation *fragment* severely and increase in amount, although it is difficult to be sure exactly how much, since the ring becomes diffuse in that region; the grains in <100> orientation remain as sharp single points.

A preliminary interpretation of these observations may be made as follows: The retention of frag-

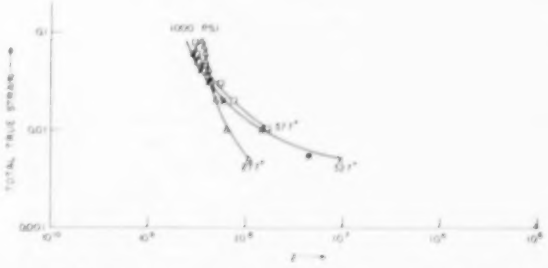

Fig. 4—Chart shows correlation of creep data using Zener-Hollomon parameter $Z = (\dot{\varepsilon}e^{\Delta H/RT})$. $\Delta H/R$ = 15,100 cal. All specimens were annealed for 1 hr at 300°C.

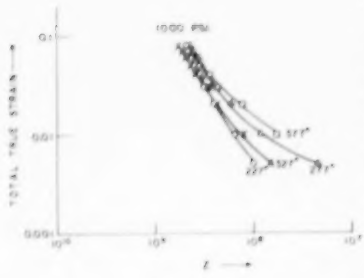

Fig. 5—Chart shows correlation of creep data using Zener-Hollomon parameter $Z = (\dot{\epsilon}e^{-\Delta H/RT})$. $\Delta H/R = 15{,}100$ cal. All specimens were annealed for 1 hr at 450°C.

mented grains in the <111> fiber orientation is consistent with the analysis of Hibbard and Yen.[9] Under tensile flow where the circular cross section is maintained, the operation of the six symmetrical slip systems about the <111> axis will permit deformation without a gross change in orientation, but with a considerable slip leading to *fragmentation*. The retention of the <100> orientation without *fragmentation* suggests that these grains are not subject to severe deformation, but persist as a result of elastic anisotropy which will promote the growth of grains having the lowest elastic modulus, i.e., the largest elastic strain for a given stress. In the case of aluminum the elastic modulus is lowest in the <100> direction.[10] The disappearance of the <112> orientation is consistent with the observation that it fits neither of these criteria.

Nature of the Creep Curve

A number of different methods of analyzing creep curves were tried and none proved to be entirely satisfactory. The results and discussion which follow are therefore written to point out where each of the methods tried proved inadequate.

With the apparatus used it is possible to study the beginning of the creep curve in some detail. Fig. 1 shows a typical example of the first minute of a creep curve. The first part of the curve is linear and represents the plastic and elastic extension during loading. The rate during this portion of the curve is limited by the maximum rate of loading possible with the equipment. The strain occurring on loading (defined as ϵ_o) is reasonably uniform for duplicate specimens.

Mathematical Analysis—In describing high temperature creep curves, many different equations have been suggested and many papers written examining one or another of these in some detail. Cottrell[11] has discussed these equations and shows that all of them are derivable from an equation of the type

$$\dot{\epsilon} = C\epsilon^n \qquad [1]$$

where n assumes values from -1 to 0. Logarithmic plots of strain rate vs strain for our data show that in the range of strains, stresses, and temperatures the exponent n is rarely constant during a test, Fig. 2. The exponent n generally decreases with increasing strain and decreasing temperature and stress.

The constants have been determined which give the best fit of our data for two of the most common equations. Examples of the typical results of the application of the equations to our data are shown in Fig. 3. Neither shows exact agreement over all regions of strain.

Often the creep curves have been divided into two stages, primary or transient and secondary or steady state. It appears impossible to make any such division of our data. For this reason, any of the methods used to analyze *steady state* creep could not be applied. Tests made on other materials known to have a stable grain size also fail to show any prolonged *constant rate* for strains less than 0.20.

Activation Energy Analysis—The proposal of Sherby et al.[12] which applies the activation process concept to the whole creep curve could be examined. This analysis has been done for all of the tests in the stress range 500 psi to 1500 psi, using the Zener-Hollomon[13] parameter

$$Z = \dot{\epsilon}e^{-\Delta H/RT}. \qquad [2]$$

Figs. 4 and 5 show some of these results. Several points of interest are evident from this analysis. First, while the deviations of tests at different temperatures are small from a practical standpoint, they are greater than specimen to specimen variation, especially at low strains. Second, the degree of fit is not a very sensitive function of the activation energy chosen. Third, these statements are true for only a small range of temperatures and stresses.

Because of the large deviations which occur at low strains, plots of logarithm of the strain rate vs $1/T$ were made for a number of strains. The results in Fig. 6 show that the value of ΔH obtained is a function of strain. The variation of ΔH with strain is greater for the material having the least stable grain size (i.e., that material annealed at 300°C). It can be concluded that while both methods of analysis serve as a good approximation to creep behavior, neither method provides the unifying principle needed to analyze creep behavior under a wide range of conditions on a number of different materials. The reasons for this lie in the lack of quantitative understanding of the structural changes which are going on during a creep test and the relation of these changes to the mechanical properties.

Summary

High purity (99.994 pct) aluminum was tested in creep at a constant stress over a wide range of temperatures (above 0.5 of the melting point) and stresses. The strain-time curves could not be analyzed satisfactorily over the complete range of strain by any existing equation or method of analysis, although several gave reasonable agreement over limited ranges. It appeared unjustifiable to separate the curves into transient and steady state components or primary and secondary stages.

The validity of an activation energy for creep, ΔH, independent of strain, temperature, and stress is questioned because of deviations somewhat larger than testing error. Modification of the concept to

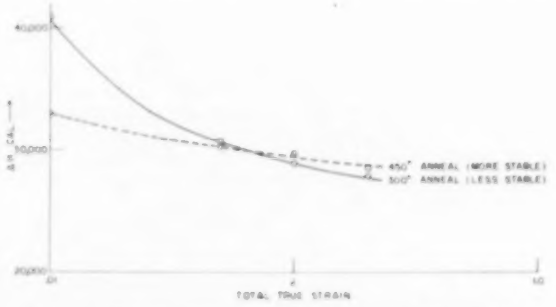

Fig. 6—Chart plots variation of apparent activation energy with strain [ΔH in equation $\dot{\epsilon} = f(\dot{\epsilon}e^{\Delta H/RT})$].

allow ΔH to be a function of strain improves the agreement quite a bit. More detailed data would be necessary to prove that this is valid.

Part of the complexity of the behavior in these experiments may be related to the observed instability of the grain size. Marked grain growth occurs during the test and is greatly influenced by the presence of the stress. X-ray diffraction studies of several crept specimens show some changes in the detail of preferred orientation. The fragmentation of diffraction spots seems to be confined to grains of certain orientations while others remain relatively unfragmented. In addition, grains having certain orientations disappear entirely. Whether these changes occur as a result of grain growth or rotation induced by deformation is not known.

These results indicate that a general description of creep behavior will require a quantitative understanding of the structural changes which take place during creep. Boundary migration, subgrain formation, and growth and similar processes must play important roles. A detailed study of these structural effects on the mechanical properties would assist us in predicting creep behavior quantitatively.

Acknowledgments

The authors wish to acknowledge the assistance of E. A. Smith, who performed the creep tests, and of M. V. Doyle and E. Saacke, who did most of the routine mathematical analysis. All of them have made many useful suggestions relating to their jobs. Discussions with R. P. Carreker, who originally built the apparatus and has conducted many creep tests, have proven very fruitful. Our thanks also to J. I. Hoffman of the Bureau of Standards, who supplied the high purity aluminum.

The work on which this report is based was supported by the Aeronautical Research Laboratory of the Wright Air Development Center under Air Force Contract No. AF 33(616)-2120.

Discussion of this paper, if any, will appear in JOURNAL OF METALS, November 1956, and in AIME Metals Branch *Transactions*, Vol. **206**, 1956.

References

[1] R. P. Carreker: Plastic Flow of Platinum Wires. *Journal of Applied Physics* (1950) **21**, pp. 1289-1296.

[2] R. P. Carreker and W. R. Hibbard, Jr.: Tensile Deformation of High-purity Copper as a Function of Temperature, Strain Rate and Grain Size. *Acta Metallurgica* (1953) **1**, p. 654.

[3] I. S. Servi and N. J. Grant: Creep and Stress Rupture Behavior of Aluminum as a Function of Purity. *Trans.* AIME (1951) **191**, pp. 909-916; JOURNAL OF METALS (October 1951).

[4] S. Dushman, L. W. Dunbar, and H. Huthsteiner: Creep of Metals. *Journal of Applied Physics* (1944) **15**, pp. 108-124.

[5] O. D. Sherby and J. E. Dorn: Creep Correlations in Solid Solutions of Aluminum. *Trans.* AIME (1952) **194**, pp. 959-964; JOURNAL OF METALS (September 1952).

[6] R. L. Fullman, R. P. Carreker, Jr., and J. C. Fisher: Simple Devices for Approximating Constant Stress During Tensile Creep Tests. *Trans.* AIME (1953) **197**, p. 657; JOURNAL OF METALS (May 1953).

[7] H. C. Chang and N. J. Grant: Grain Boundary Sliding and Migration and Intercrystalline Failure under Creep Conditions. *Trans.* AIME (1953) **197**, pp. 305-312; JOURNAL OF METALS (February 1953).

[8] D. McLean: Note on Boundary Migration During Creep. *Nature* (1953) No. 4372, p. 301.

[9] W. R. Hibbard, Jr. and M. K. Yen: Wire Textures of Copper and Its Binary Alpha Solid Solution Alloys with Aluminum, Nickel and Zinc. *Trans.* AIME (1948) **175**, p. 126; METALS TECHNOLOGY (February 1948).

[10] E. Schmid and W. Boas: *Kristallplastizitat*. (1935). Berlin. J. Springer.

[11] A. H. Cottrell: The Time Laws of Creep. *Journal of Mechanics and Physics of Solids* (1952) **1**, pp. 53-63.

[12] O. D. Sherby, R. L. Ott, and J. E. Dorn: Creep Correlations in Metals at Elevated Temperatures. *Trans.* AIME (1954) **200**, pp. 71-79; JOURNAL OF METALS (January 1954).

[13] C. Zener and J. H. Hollomon: Plastic Flow and Rupture in Metals. *Trans.* ASM (1944) **33**, pp. 163-235.

[14] E. N. da C. Andrade: On the Viscose Flow of Metals and Allied Phenomena. *Proceedings* Royal Soc., London (1910) **A84**, pp. 1-12.

[15] E. N. da C. Andrade: The Flow of Metals under a Large Constant Stress. *Proceedings* Royal Soc., London (1914) **A90**, pp. 329-342.

[16] T. H. Hazlett and E. R. Parker: The Nature of the Creep Curve. *Trans.* AIME (1953) **197**, pp. 318-323; JOURNAL OF METALS (February 1953).

Diffusion in Liquid Lead

The diffusion of lead and of trace amounts of bismuth in liquid lead have been investigated by the capillary method, using RaD and RaE as tracers. The results are compared with existing theories of diffusion in liquids, the agreement with theory being fair. The heat of activation for self-diffusion in lead is found experimentally to be close to the corresponding activation energy obtained from viscosity data. The pioneer data of Groh and von Hevesi for the self-diffusion of liquid lead, using ThB as a tracer, fit in with the present results.

by S. J. Rothman and L. D. Hall

S. J. ROTHMAN, Junior Member AIME, formerly Graduate Student, Physical Metallurgy, School of Mineral Sciences, Stanford University, Stanford, Calif., is now associated with Argonne National Laboratory, Lemont, Ill., and L. D. HALL, formerly Assistant Professor of Physical Metallurgy, School of Mineral Sciences, Stanford University, is now associated with Stanford Research Institute, Stanford, Calif.

Discussion of this paper, TP 4067E, may be sent, 2 copies, to AIME by Apr. 1, 1956. Manuscript, Mar. 7, 1955. Philadelphia Meeting, October 1955.

This paper is based on a portion of a thesis by S. J. Rothman submitted, in partial fulfillment of the requirements for the degree of Doctor of Philosophy in Metallurgical Engineering, to the School of Mineral Sciences of Stanford University.

COMPARED with the volume of effort expended on solid state diffusion, there has been little attention paid to diffusion in liquid metals. A review of experimental work in this field, covering most of the studies up to 1951, was given by Jost.[1] More recent papers include those by Hoffman[2] on self-diffusion in mercury, Morgan and Kitchener[3] and Stark, Shchilishchev, and Kazachkev[4] on the diffusion of various elements in liquid iron, and Grace and Derge[5] on the diffusion of bismuth in bismuth-lead alloys.

The need for more experimental data to aid in the evaluation of existing theories prompted the

present study. Theories of diffusion, the predictions of which can be checked experimentally, have been proposed by Einstein,[4] Eyring,[7] and Peter.[8] These theories all consider the diffusion process from the standpoint of viscous properties, and all predict heats of activation for diffusion which are essentially equal to the heats of activation for viscosity. As pointed out by Hoffman,[2] this has been found to be approximately true for water and for mercury. The same has been found by Meyer and Nachtrieb[9] for liquid sodium and by Haycock, Alder, and Hildebrand for the diffusion of I, in CCl_4.[10] It was considered of interest, therefore, to ascertain whether it is also the case for lead. The Stokes-Einstein equation,[4] derived on the basis of hydrodynamic theory, in which it is assumed that the diffusing particles are very large compared with the *particle size* of the medium gives

$$D = kT/6\pi r\eta \qquad [1]$$

where k is the Boltzmann constant, r is the radius of the diffusing particle and η is the viscosity of the medium. Eyring's equation[7] contains three parameters λ, in the place of r, but has the same form and for monatomic liquids can be reduced to

$$D = kT/2\pi\eta . \qquad [2]$$

The variation of D with T, according to these equations, will be determined principally by the variation of η, and thus in the case of self-diffusion, as pointed out by Eyring,[7] the free energies of activation for diffusion and for viscous flow should be equal. If this is so, the heats of activation should also be approximately equal for the two processes. Eyring further derives the expression

$$D = e\lambda^2 \frac{kT}{h} \exp \frac{\Delta S}{R} \exp - \frac{E}{RT} \qquad [3]$$

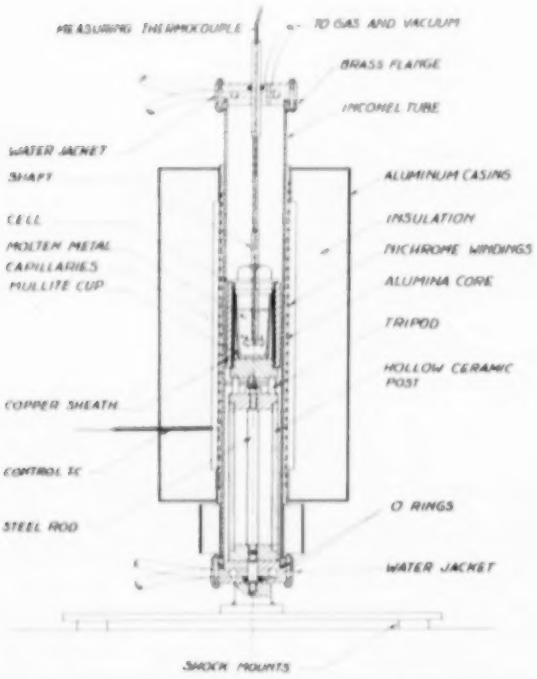

Fig. 1—Diagram shows a cross sectional view of diffusion cell and furnace.

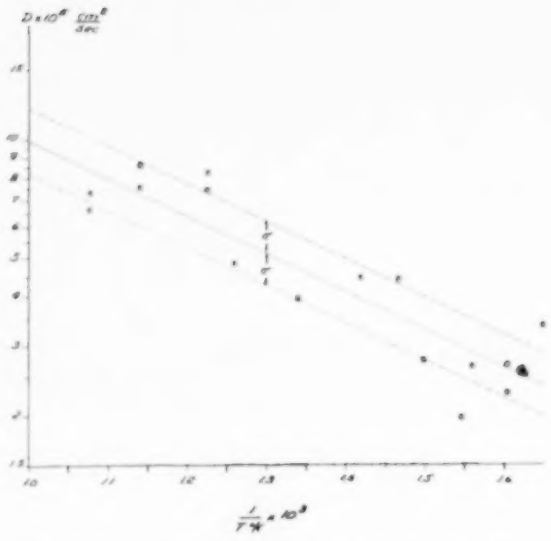

Fig. 2—Lines and data points show results for the self-diffusion of liquid lead. Encircled triangle represents data of Groh and von Hevesi,[12] who used ThB as a tracer.

which is to be identified with the experimentally observed relation

$$D = A \exp - \frac{\Delta H}{RT}$$

with $E = \Delta H$. Peter's equation for D is[8]

$$D = 5.17\text{x}10^{-10^3} (\Delta V)^{\frac{2}{3}} (E/RT)^{\frac{5}{3}} \exp (-E/RT) \qquad [4]$$

where ν is the vibration frequency, ΔV is the volume change on melting per mol, and $E = \Delta H$.

Experimental Procedure

Preliminary attempts were made to use the shear cell technique,[11] which was originally developed for use at room temperature. The effort was eventually abandoned, when it was found impossible to obtain reproducible results by this method. It was felt that the large scatter encountered was probably due to convection, because of the large (7 mm) diameter of the specimens, and recourse was had, therefore, to the capillary method, by which the data presented herein were obtained.

In the capillary method[12] the material studied, which contains a uniform concentration of radioactive tracer, fills a capillary which is open at one end. In the process of diffusion, material diffuses out of the capillary into a reservoir of inert material, which can be considered infinite in extent.

Fig. 1 shows a cross sectional view of the diffusion cell and furnace. The furnace rested on a shock-mounted plate which in turn rested on a heavy, shock-mounted table. During the initial installation of equipment, a seismometer was used to detect the nature and severity of any external sources of vibration. It was found that the only measurable disturbances arose from shock rather than from forced vibrations. Hence, rubber mounts were used.

A Nichrome-wound gastight vertical Inconel tube furnace with water cooled ends was used. The windings were more closely spaced at the ends than at the middle, to compensate for end losses. By means

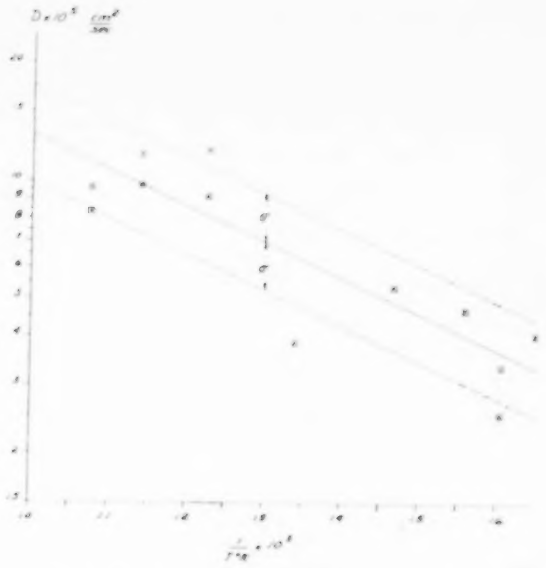

Fig. 3—Experimental results of the diffusion of lead with trace amounts of bismuth are plotted.

of taps at various points of the windings, sections of the heating element could be shunted out, and temperature gradients thus minimized. A chromel-alumel control thermocouple was placed close to the windings; the specimen temperature was measured with a central couple, also chromel-alumel, using a Leeds and Northrup No. 8662 portable precision potentiometer. The control circuit used a Tag-Celectray controller, a Powerstat autotransformer, and a large variable carbon resistor for regulating the *on* and *off* currents.

The capillaries were either Vycor or Pyrex, about 1 cm long and of the following bores: 1.24, 1.30, 1.53, or 1.63 mm. One end was sealed off to form a flat bottom; the capillary was then filled, and the open end ground flat on a travelling belt.

Radioactive lead and bismuth (Ra*D* in secular equilibrium with Ra*E*) were obtained as $Pb(NO_3)_2$ from Atomic Energy Products Ltd., Ottawa, Ontario. The Ra*D* was electrodeposited and diluted with Tadanac 99.999 pct pure Pb. This procedure produced a lead alloy containing less than 0.0008 pct Bi, as determined by Harvey's method.[14] A filled capillary counted approximately 1,000 to 10,000 counts per min. A scintillation counter was used to detect the Ra*D*, while the Ra*E* was detected with a Geiger-Muller tube.

In the counting procedure used, the samples were counted immediately after the diffusion runs, in order to distinguish between Ra*D* (lead) and Ra*E* (bismuth). The procedure was based on the decay schemes of Ra*D* and Ra*E*. Ra*D*, with a half-life of 22 years, emits a 0.025 mev β and a 0.047 mev γ, decaying to Ra*E*. Ra*E*, with a half-life of 5 days, emits chiefly a 1.17 mev β, decaying to Ra*F*, which decays to stable Pb^{206} by the emission of α radiation and a very small amount of γ radiation.

The scintillation counter used to detect the γ radiation of Ra*D* had a very low efficiency for β radiation. In addition, there was always sufficient aluminum between the crystal and the specimen to absorb any β's present. The scintillation counter thus counted essentially only the γ radiation of Ra*D*. In order to establish the fact that the Geiger-Muller tube counted only the 1.17 mev β radiation of Ra*E*, a count was made with an aluminum absorber of about 0.196 cm (0.5 g per cm^2) interposed between tube and specimen. Under these conditions, the total count dropped to the background level of the counter, although this thickness of absorber reduces the γ intensity by only 20 pct. Therefore, the Geiger-Muller counter counted only β radiation. Further tests with thin aluminum foil showed that the 0.025 mev β from the Ra*D* was absorbed in the window of the Geiger-Muller counter.

Using the formulas for the concentration of the first daughter[15] in a chain disintegration and substituting the decay constants of Ra*D* and Ra*E*, it is easily shown that if the specimen is counted 3 hr after the end of the diffusion run, the amount of Ra*E* formed after the diffusion is about 1 pct of the Ra*E* present, so that the concentration of Ra*E* is substantially independent of the concentration of Ra*D*. Similar calculations will also show that the γ radiation from Ra*F*, the daughter of Ra*E*, is negligible.

All diffusion runs were made under about 3 lb gage pressure of helium. A fresh metal bath (700 to 800 g Pb) was used for each run. After the lead in the bath had melted, the capillaries were lowered so that the open end was just above the bath. When thermal equilibrium had been reached, they were completely submerged. The bath was agitated every 5 min by twirling the shaft which held the capillaries.

Continuous agitation was also tried, and the results evaluated by slit-counting the specimens. In this process a sheet of lead, ¼ in. thick, is placed between the sample and the counter. The lead has a 1 mm wide slit in it. This slit is moved parallel to the direction of diffusion, and can thus be used to find c as a function of x. It was found that the concentration profile along the capillary was, within the experimental error, unaffected by the continuous agitation of the bath. This same slit-counting system was used to show that the radioactive isotopes were uniformly distributed along the capillary.

Mathematics

Diffusion under the conditions described obeys Fick's law:

$$\frac{\partial c}{\partial t} = \frac{\partial^2 c}{\partial x^2} \qquad [5]$$

with initial and boundary conditions

$$\frac{\partial c}{\partial x}(x \to 0) = 0; t \geq 0 \qquad [6]$$

$$c(l) = 0; t > 0 \qquad [7]$$

$$c(x) = c_o, 0 \leq x \leq l, t = 0 \qquad [8]$$

$$c(x, t) = 0 \text{ elsewhere} \qquad [9]$$

where the axis of the capillary is the x axis, with origin at the sealed end, and the length of the capillary is l.

The solution of Eq. 5 with the given initial and boundary conditions, Eqs. 6 through 9, is, after integration,[16]

$$\frac{C}{C_o} = \frac{8}{\pi^2} \sum_{n=1}^{\infty} \frac{1}{(2n-1)^2} \exp - \left(\frac{2n-1}{2}\right)^2 \left(\frac{\pi}{l}\right)^2 Dt \qquad [10]$$

where C and C_0 are the total amounts of tracer present in the capillary after and before diffusion, respectively. If $\frac{\pi^2}{8}\frac{C}{C_0}$ is less than 0.700, the series can be cut off after the first term without appreciable error.

Experimental Results

The results are tabulated in Table I and plotted in Figs. 2 and 3. The values show that the diffusion coefficient is independent of t, l, and capillary diameter.

The results can be fitted by the following equations:

Self-diffusion in lead

$$D = (9.15 \pm 0.30) \times 10^{-4} \exp(-4450 \pm 330/RT) \text{ cm}^2 \text{ per sec.} \quad [11]$$

Diffusion of bismuth in lead

$$D = (9.63 \pm 0.50) \times 10^{-4} \exp(-4070 \pm 546/RT) \text{ cm}^2 \text{ per sec.} \quad [12]$$

Table I. Diffusion in Lead

T, °K	t, Sec	l, Cm	Capillary Diameter, Mm	D, Cm² per Sec x 10⁵ Lead	Bismuth
606 ± 0.5	1500	0.844	1.24	3.33	4.52
624 ± 0.5	9000	0.938	1.24	2.69	2.51
624 ± 0.5	9000	0.890	1.53	2.28	3.39
645.5 ± 1	8880	0.812	1.24	1.93	—
642 ± 0.5	1800	0.766	1.24	2.65	4.70
671 ± 1	3840	0.913	1.24	2.76	—
682 ± 0.5	1800	0.892	1.24	4.42	5.32
704.5 ± 1	3180	0.928	1.24	4.44	—
746 ± 0.5	4500	0.829	1.24	3.97	3.88
794 ± 0.5	3240	0.650	1.30	4.84	—
816.5 ± 0.5	1860	0.815	1.63	8.24	12.0
816.5 ± 0.5	1860	0.813	1.30	7.45	9.13
877.5 ± 0.5	1794	0.830	1.30	8.55	11.7
877.5 ± 0.5	1794	0.675	1.63	7.52	9.79
930 ± 0.5	2040	0.809	1.30	7.32	9.60
930 ± 0.5	2040	0.818	1.30	6.64	8.34

The scatter in the data is probably due chiefly to errors in the measurement of the quantities used to calculate D. Principal sources of error were in the degree of filling the capillaries, in measurements of the length, l, in deviations from the boundary condition (Ib),[17] and in disturbances resulting from freezing. In systems which must be frozen from the liquid state in order to make measurements, errors are inevitably introduced by the changes which occur at the freezing point.

In view of the scatter, the results were subjected to statistical analysis[18] to see whether the differences in the parameters (activation energies and pre-exponential factors) between the cases described by Eqs. 11 and 12 were significant. First, it is assumed that a relation of the form $D = D_0 \exp(-\Delta H/RT)$ holds, as used in Eqs. 11 and 12. This relation is then written in logarithmic form, $Y = A + bX$, where $Y = \ln D$, $A = \ln D_0$, $b = -\Delta H/R$, and $X = 1/T$. The analysis is based on the additional assumptions: 1—The error in X is negligible, see Table I, and 2—The errors in Y are normally distributed, i.e., for each X value there is a normal population of Y values. The second assumption is perhaps open to question, but can be neither proved nor disproved.

The activation energies for the diffusion of lead and of trace amounts of bismuth, respectively, in lead, are not significantly different at the 50 pct level, whereas the D_0 values are significantly different at the 99 pct level. That is, if the ΔH values for the two diffusing entities were actually equal, a calculated difference of the magnitude indicated by comparison of Eqs. 11 and 12 would be found more than 50 times out of 100 measurements, whereas if the D_0 values were actually equal, the indicated difference would be found in only 1 out of 100 measurements.

Discussion

Table II gives comparative values for heats of activation for self-diffusion and viscosity of lead.

The heats of activation for self-diffusion were obtained from the slopes of plots of ln D vs $1/T$, while those for viscosity were obtained from the slopes of plots of ln (η/T) vs $1/T$. For the purpose of such a comparison, this is equivalent to obtaining the heats of activation for diffusion from a plot of ln D/T vs $1/T$ and those for viscosity from plots of ln η vs $1/T$.

Table II. Heats of Activation, Cal per G-Atom

ΔH, Diffusion	ΔH, Viscosity
4450 ± 330	4000 ± 192*
—	2370 ± 21†

* Data from ref. 20.
† Data from ref. 19.

The data are too scattered to show which of these suppositions is correct. The agreement with the Sauerwald data is good; with the newer data of Fisher and Phillips, not as good. However, the latter were determined over a rather narrow range of temperature.

Peter's equation, Eq. 4, permits the calculation of D_0 if the parameters can be estimated. Using his data for $(\Delta V)^s$ and evaluating ν as in his paper, $D_0 = 2.75 \times 10^{-2}$ is obtained, which is some 30 times the value obtained experimentally.

Table III. Radii of the Diffusing Particle at 350°C in Angstroms

Eyring Equation		Stokes-Einstein Equation	
Viscosity Data from Ref. 20	Viscosity Data from Ref. 19	Viscosity Data from Ref. 20	Viscosity Data from Ref. 19
6.73	7.12	0.715	0.757

The radius of the diffusing particle can be calculated from either the Stokes-Einstein equation, Eq. 1, or the Eyring equation, Eq. 2. These values are shown in Table III. One-half the distance to the first peak on the radial distribution curve at 375°C is 1.70A.[21] The Goldschmidt radii are[22] lead, 1.74Å and Pb^{++}, 1.32A. Thus the agreement between experimentally determined atomic radii and calculated

Table IV. Temperature Dependence of the Atomic Radius of Lead, in Angstroms

T, °C	Radius, Using Einstein Equation and Viscosity Data from Ref. 20	Radius, Using Einstein Equation and Viscosity Data from Ref. 19	One-Half the Cube Root of the Volume per Atom[23]
400	0.643	0.655	1.60
850	0.56	0.40	1.63

ones is better when the Stokes-Einstein equation is used than when the Eyring equation is used, as was found by Hoffman[5] and Haycock et al.[20] The data are

not accurate enough to draw conclusions regarding the entity of the diffusing particle.

The atomic radius can be expected to increase slightly with the temperature, the increase being of the same order as the increase in the molar volume. This expectation is not borne out by the authors' data, as shown in Table IV.

Work on diffusion in the Pb-Bi system has been done by Grace and Derge.[5] Their data are compared with the authors' in Table V.

Table V. Comparison of the Present Data With That of Grace and Derge[5]

Pct Bismuth in the Capillary Before Diffusion	D_0, Cm² per Sec	H Cal per Mol
0.0008	9.15×10^{-4}	4450
1.73[5]	2.0×10^{-4}	1730
52.7[5]	4.1	9500
100[5]	6.5	8150

Summary

The diffusion of the radioactive tracers Ra*D* (lead) and Ra*E* (bismuth) in liquid lead has been studied in the temperature range 606° to 930°K. The heats of activation have been calculated as 4450 and 4070 cal per g atom respectively. The results have been compared with the predictions of several theories of diffusion, with varying degrees of agreement.

Acknowledgments

This work was supported by the Office of Ordnance Research, U. S. Army. The authors are deeply indebted to A. Newton, who built or helped to build most of the equipment. The aid of M. Volpe, E. Bryan, R. Hunnicutt, T. Hikido, and O. Vieira on various phases of the work is gratefully acknowledged.

Discussion of this paper, if any, will appear in JOURNAL OF METALS, November 1956, and in AIME Metals Branch *Transactions*, Vol. **206**, 1956.

References

[1] W. Jost: *Diffusion in Solids, Liquids and Gases.* (1952) p. 479. New York. Academic Press.
[2] R. E. Hoffmann: *Journal of Chemical Physics* (1952) **20**, p. 1567.
[3] D. W. Morgan and J. A. Kitchener: *Trans.* Faraday Soc. (1954) **50**, p. 51.
[4] B. V. Stark, E. V. Shchilishchev, and E. A. Kazachev: *Izvestiia Akad. Nauk SSSR*, Otdel. Tekh. Nauk (1951) **11**, p. 1689.
[5] R. Grace and G. Derge: *Trans.* AIME (1955) **203**, p. 839; JOURNAL OF METALS (July 1955).
[6] A. Einstein: *Annalen der Physik* (1905) **17**, p. 549.
[7] S. Glasstone, K. Laidler, and H. Eyring: *The Theory of Rate Processes.* (1941) p. 477 ff. New York. McGraw-Hill Book Co. Inc.
[8] S. Peter: *Ztsch. für Naturforschung* (1954) **9a**, p. 98.
[9] R. Meyer and N. Nachtrieb: *Journal of Chemical Physics* (1955) **23**, p. 405.
[10] E. Haycock, B. Alder, and J. Hildebrand: *Journal of Chemical Physics* (1953) **21**, p. 1601.
[11] J. Schumeister: Sitzungsber. *Wiener Akad. des Wissenschaft, II* (1879) **79**, p. 603.
[12] J. S. Anderson and K. Saddington: *Journal* Chemical Soc., London (1949) p. S381.
[13] J. Groh and G. von Hevesi: *Annalen der Physik* (1920) **63**, p. 85.
[14] C. E. Harvey: *A Method of Semi-Quantitative Spectrographic Analysis.* (1947) pp. 13-14, 137. Glendale, Calif. Applied Research Laboratories.
[15] D. Halliday: *Introductory Nuclear Physics.* (1950) p. 35. New York. J. Wiley and Sons.
[16] R. V. Churchill: *Fourier Series and Boundary Value Problems.* (1943) p. 109. New York. McGraw-Hill Book Co. Inc.
[17] S. J. Rothman: Doctorate dissertation, Stanford University (1954).
[18] A. Hald: *Statistical Theory with Engineering Applications.* (1952) p. 522 ff. New York. J. Wiley and Sons.
[19] H. J. Fisher and A. Phillips: *Trans.* AIME (1954) **200**, p. 1060; JOURNAL OF METALS (September 1954).
[20] A. Bienias and F. Sauerwald: *Ztsch. für Anorg. Allgem. Chemie* (1927) **161**, p. 51; H. Esser, F. Greis, and W. Bunghardt: *Arch. Eisenhüttenwesen* (1934) **7**, p. 385. Given in *The Handbook of Chemistry and Physics.* (1949) 31st Ed., p. 1759. Cleveland. The Chemical Rubber Publishing Co.
[21] R. Glocker and H. Hendus: *Annalen der Physik* (1943) **43**, p. 513.
[22] E. T. Wherry: *Amer. Mineralogist* (1929) **14**, p. 54; *The Handbook of Chemistry and Physics.* (1949) 31st Ed., p. 2680. Cleveland. The Chemical Rubber Publishing Co.
[23] A. L. Day, R. B. Sosman, and J. C. Hostetter: *Amer. Journal of Science* (1914) **37**, p. 1; *The Handbook of Chemistry and Physics.* (1949) 31st Ed., p. 1712. Cleveland. The Chemical Rubber Publishing Co.

Effects of Alloying Elements on the Electrical Properties of Manganin-Type Alloys

Relationships between the compositions of specially prepared manganin-type alloys and some of their electrical properties have been established. Empirical equations, based upon the electronic configurations of the alloying elements, are given which describe the resistivity, temperature coefficient, peak temperature, and thermoelectric power of Cu-Mn-Ni-Fe alloys at approximately room temperature. Calculations based upon these relationships are correlated with experimental data.

by D. D. Pollock and D. I. Finch

SECURING suitable alloys for the construction of stable resistors, for use in precise electrical measuring devices, has been important ever since the art of electrical measurement was begun. German silver, Pt-Ag, and Platinoid are examples of some of the alloys in early use. These early alloys were unsatisfactory for one or more of the following reasons: 1—insufficient stability of electrical properties with time, 2—poor reproducibility of electrical characteristics from melt to melt, 3—excessive temperature coefficients of resistance, and 4—excessive cost.

Weston[1] introduced the Cu-Mn-Fe and Cu-Mn-Ni-Fe alloys of the type now generally known as manganins. His patents are believed to represent the first disclosure of any alloy with a negative temperature coefficient of resistance. After this work, the German company, Isabellenhutte, in conjunction with Feussner and St. Lindeck,[2,3] produced alloys of

D. D. POLLOCK and D. I. FINCH, Members AIME, are Research Metallurgist and Chief, respectively, Metallurgical Div., Research and Development Dept., Leeds and Northrup Co., Philadelphia.

Discussion of this paper, TP 4080E, may be sent, 2 copies, to AIME by Apr. 1, 1956. Manuscript, Mar. 11, 1955. Philadelphia Meeting, October 1955.

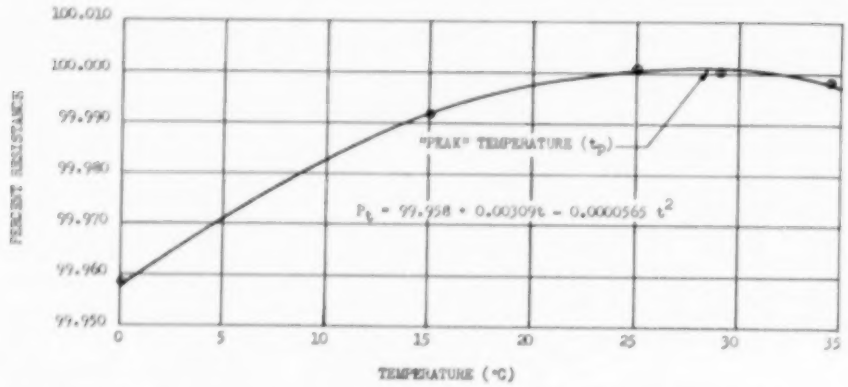

Fig. 1—Chart plots typical resistance-temperature curve for a commercially available manganin.

this type. The Isabellenhutte was the only source of manganin up to and including World War I.

Bash,[4] in an effort to make the American instrument industry independent of the German source, produced the first acceptable manganin to be made in this country. Pilling[5] studied some of the electrical properties of this general family of alloys. Higher purity alloys of this system were later investigated by Dean and Anderson.[6]

Manganin has become almost universally adopted for use as a resistance material in electrical instrumentation because of its important electrical and mechanical properties. The mechanical properties of this alloy type are such that it is suitable for cold drawing down to very fine wire sizes.

Perhaps the most significant property of manganin is its unusually high degree of stability of resistance with time, when it is suitably heat treated and protected. This property permits the manufacture of very accurate and stable standards of resistance for use in precision measuring equipment.

The resistivity of commercial manganin is moderately high (about 48 microhm-cm at room temperature) and its temperature coefficient in the neighborhood of room temperature is very low. An important characteristic of the resistance-temperature curve of manganin is that it is parabolic with the maximum occurring between 25° and 50°C (the so-called peak temperature). It is desirable that this maximum be close to the operating temperature of the instrument in which the manganin is being used. When this is the case, normal changes in ambient temperature will result in only very small changes in the calibration of the instrument. Also, the smaller the departure of the resistance-temperature relationship from linearity the more useful is the alloy.

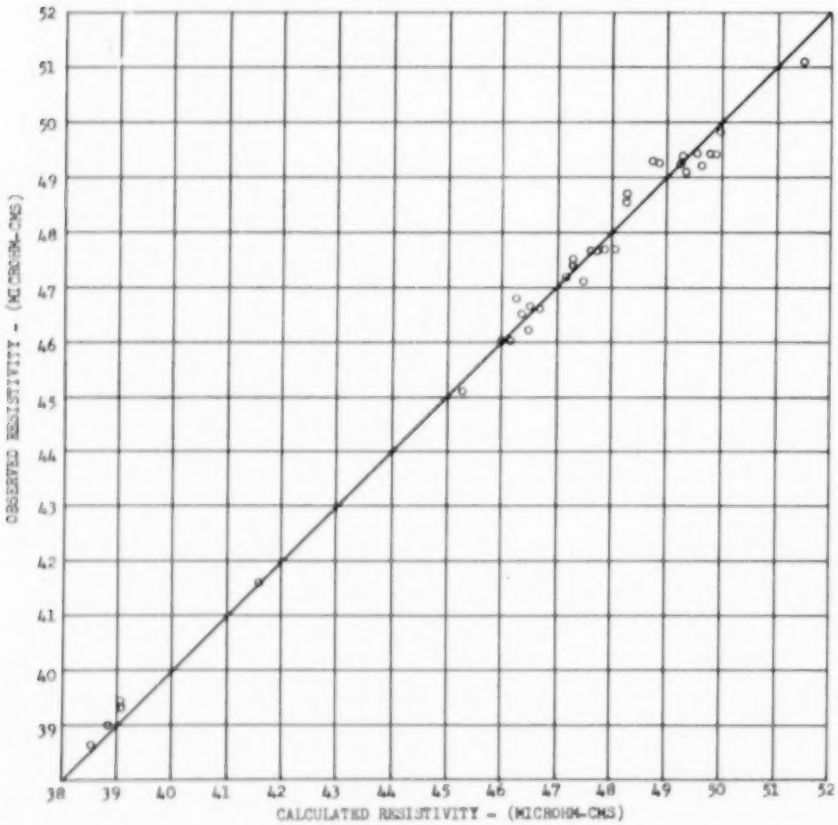

Fig. 2—Chart shows agreement between calculated and observed resistivities for Cu-Mn-Ni-Fe alloys.

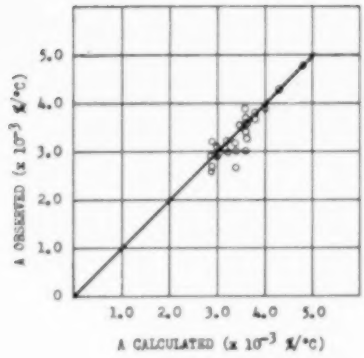

Fig. 3—Chart shows agreement between calculated and observed values for the constant *A* for Cu-Mn-Ni-Fe alloys.

Fig. 1 shows a typical resistance-temperature curve for the best commercially available manganin.

Another important property is that the thermoelectric power of manganin against copper is very low (approximately 1.5 μv per °C maximum between 0° and 50°C). This is significant in that it reduces parasitic emfs, generated by small temperature differences within an instrument, to a negligible quantity.

No other commercially available resistance alloy possesses all of these properties to the degree manifested by manganin. However, its electrical characteristics are readily influenced by its thermal and mechanical history, its surface condition and its chemical composition. Its resistance to corrosion under ordinary atmospheric conditions is only fair. Normal practice requires that enamelling or other surface protection be used to prevent tarnishing. Small changes in any one of these factors result in relatively large effects upon the electrical properties of the alloy. Thomas[7] cites some of these effects.

Table I. Analyses of the Raw Materials Used in the Melting of the Cu-Mn-Ni-Fe Alloys

Element	Copper Rod, Pct	Electrolytic Manganese, Pct	Electrolytic Nickel Shot, Pct	Armco Iron, Pct	Cu-Mg Master, Pct
Pb	0.002				
Fe	0.005	0.001	0.053 to 0.061	Balance	0.3
Al	0.001				
Ni	0.002		Balance	0.021	
Si	0.003		0.023 to 0.035	0.003	0.1
Ag	0.001				
V	0.0002				
Cu	Balance			0.069	Balance
N		0.015			
C		0.004		0.013	
S		0.013		0.027	
Mn		Balance		0.088	
Co			0.24 to 0.32		
P				0.007	
Cr				0.01	
Mg					20.5
Ca					0.01

Preparation of Alloys

A study was undertaken to determine the existence of consistent empirical relationships between the compositions of specially prepared manganin-type alloys and some of their electrical properties.

All of the alloys studied were made from OFHC copper rod, electrolytic manganese cathode chip, electrolytic nickel shot and low copper Armco iron. A Cu-Mg master alloy was used for deoxidation. Alloy compositions are given in Table I.

These materials were carefully weighed out into three pound heats and melted in a high frequency

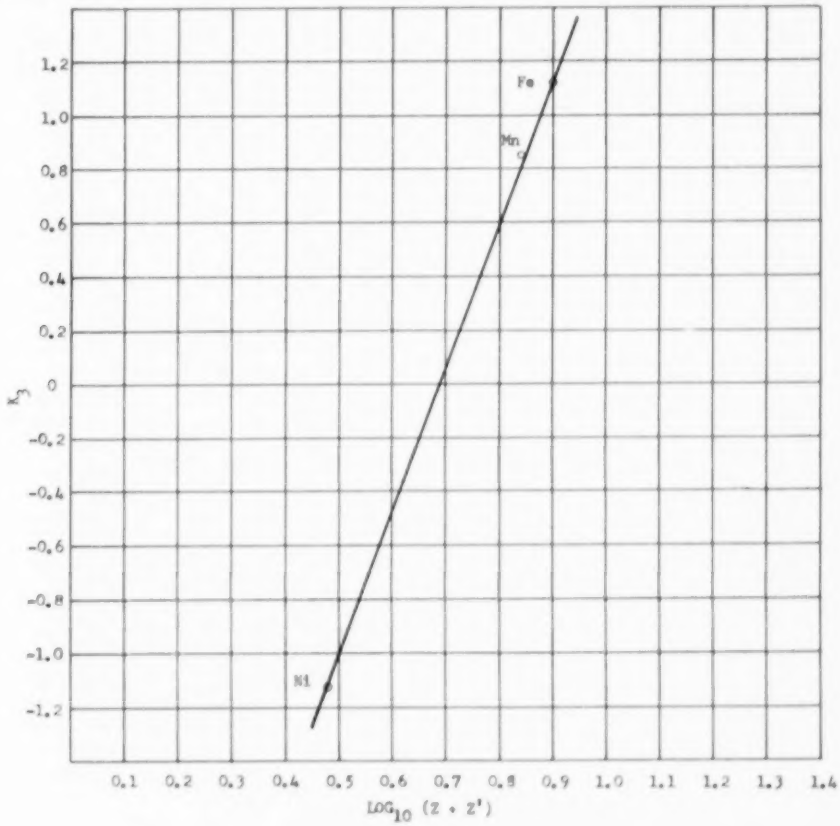

Fig. 4—Chart shows dependence of K_3 on electronic configuration for Cu-Mn-Ni-Fe alloys.

Table II. Experimental Data for Cu-Mn-Ni-Fe Alloys

Atomic Pct							
Mn	Ni	Fe	t_c, °C	$A \times 10^{-4}$, Pct per °C	$-B \times 10^{-6}$, Pct per °C²	$\Delta E/\Delta t$, μv per °C	ρ_m, Microhm-Cm
13.93	4.50	0.345	27.8	2.91	5.23	−1.67	45.14
14.01	4.66	0.311	27.3	2.98	5.45	−1.47	47.68
14.40	4.52	0.337	28.1	2.64	4.70	−1.36	48.64
15.27	4.50	0.288	28.9	3.01	5.21	−1.17	51.11
15.93	4.49	0.312	27.9	3.14	5.65	−1.00	53.01
15.25	6.	0.341	37.2	4.84	6.50	+0.56	46.46
15.24	0.534	0.258	36.9	4.30	5.84	+0.42	46.25
14.88	1.03	0.299	33.4	4.63	6.94	+0.07	46.80
15.10	1.59	0.236	34.6	3.65	5.28	−0.09	47.18
14.89	2.09	0.325	32.4	3.86	5.96	−0.31	47.71
14.89	2.12	0.285	31.7	3.73	5.92	−0.32	47.16
14.78	2.53	0.286	31.7	3.43	5.41	−0.58	47.66
14.66	3.16	0.239	29.5	3.55	6.02	−0.76	—
14.49	4.10	0.288	27.4	3.09	5.65	−1.33	—
14.53	4.18	0.346	30.7	2.87	4.67	−1.05	47.26
14.52	5.13	0.315	29.0	2.67	4.61	−1.44	—
14.41	4.50	0.092	37.9	3.91	5.16	−0.96	47.50
14.59	4.31	0.049	38.4	3.56	4.63	−0.95	47.75
14.43	4.55	0.149	35.7	3.04	4.26	−1.14	48.64
14.42	4.44	0.175	33.2	2.92	4.40	−1.25	48.51
14.75	4.35	0.222	31.5	3.15	5.01	−1.20	48.99
14.73	4.44	0.267	29.4	3.24	5.51	−1.23	49.19
14.72	4.28	0.336	27.2	3.13	5.61	−1.31	49.38
14.70	4.31	0.347	28.1	3.22	5.73	−1.20	49.42
14.72	4.31	0.511	26.9	2.90	5.01	−1.28	49.81
14.33	4.45	0.797	29.5	2.53	4.33	−1.29	49.23
14.42	4.48	0.904	31.4	2.72	4.35	−1.27	49.24
14.27	4.52	1.15	30.4	2.93	4.81	−1.31	49.21
14.50	4.59	2.25	41.7	4.04	4.84	−1.29	49.42
11.46	4.66	0.034	62.0	3.94	3.21	—	39.37
11.45	4.44	0.048	54.9	3.73	3.40	—	39.03
13.40	6.33	0.026	37.3	3.33	4.47	−1.93	46.57
13.15	6.38	0.021	38.3	3.04	3.97	−1.96	46.07
11.19	4.62	0.093	50.2	3.24	3.23	−1.92	38.60
11.49	4.62	0.119	45.4	3.21	3.59	−1.83	39.59
12.22	4.53	0.116	41.1	3.04	3.74	−1.60	41.64
13.87	4.04	0.238	31.9	2.77	4.34	−1.33	46.55
14.10	4.21	0.217	29.8	3.01	5.02	−1.30	47.38

induction furnace. Magnesia crucibles, backed with flake graphite, were used. The melts were covered with a mixture consisting of 50 pct lime, 25 pct silica and 25 pct fluorspar.

The alloys were cast in a preheated, split graphite pig-mold. The ingots were 22 in. long, ⅜ in. wide and 1 in. deep. A ⅜ in. x ⅜ in. section, of appropriate length, was slit from the bottom portion of each ingot. This was pickled in a 1-1 solution HNO_3-H_2O, and cold rolled down to approximately 0.1 in. x 0.1 in. The *square* wires were annealed at 790°C for 1 hr, in a dissociated ammonia atmosphere. They were then cooled slowly to room temperature, under the protective furnace atmosphere. Next, the wires were cold drawn to 0.0808 in. diam. The finished wires were annealed at 570°C for 1 hr. in a dissociated ammonia atmosphere and then cooled in the same manner as after the first anneal. This procedure was followed in producing all of the wire specimens studied.

Experimental Procedure

The finished wire size of 0.0808 in. diam was chosen for the sake of convenience in making self-supporting test specimens, thus eliminating any extraneous effects which might have been introduced by winding smaller diameter wire on spools or forms. The following tests were performed on the finished wires.

Chemical Analysis—Manganese was determined by premium gravimetric methods. Nickel and iron were determined by means of arc type spectrographic analysis. The principle impurities are silicon and magnesium. The maximum amounts of these elements are 0.004 and 0.008 wt pct, respectively. Other *impurities* are less than 0.001 pct each. Table II presents the mean values computed from at least four determinations of each constituent.

Electrical Characteristics—*Thermal EMF Against Copper:* The thermal emf of each alloy against copper was determined for a single sample from each melt. Copper was chosen as the base because it represents the standard state for the alloy and because it is commonly used as *leads* to resistors. The wire specimen was straightened and then cleaned with ethyl alcohol. It was reannealed in the same way as the finished wires to assure that any residual stress would be at a minimum level. Preliminary work had shown that the presence of small amounts of stress had the effect of decreasing the thermal emf against copper.

The manganin specimen was soldered to a copper wire which was selected for its close conformity with the National Bureau of Standards values[5] for the emf of copper against platinum. A standard set of copper leads was then soldered to the cold junctions of the couple thus formed. These joints were maintained in finely shaved melting ice during the test. The emf of the couple was checked at four temperatures between 15° and 50°C. This temperature range was selected because it includes the temperatures which resistors may normally be expected to encounter. A known source of emf was *bucked against* the output of the couple until a null balance was reached. The data were then expressed in terms of *μv per °C* as shown in Table II. These data have a limit of error of less than ±0.2 pct.

Resistivity: Three specimens of each alloy sample were carefully straightened, cleaned with ethyl alcohol and annealed as noted above.

A simple fixture was prepared for the resistance measurements on the wire specimens so that the conditions of test would be reproducible. The distance between the potential points is 6.452 cm at 25.0°C. The length was so chosen that a resistance reading of slightly less than 0.01 ohm would be obtained. This value was selected so that an available adjustable 0.01 ohm standard resistor could be used with nearly its entire length in the Kelvin bridge circuit in order to secure the maximum accuracy of setting. A suitable ratio box was used to complete

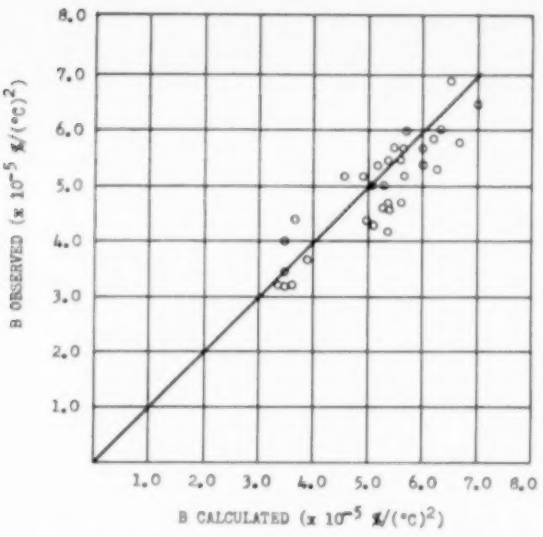

Fig. 5—Chart shows agreement between calculated and observed values for the constant *B* for Cu-Mn-Ni-Fe alloys.

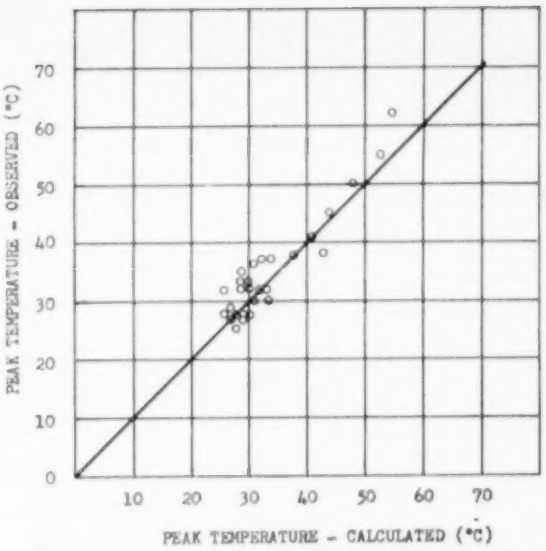

Fig. 6—Chart shows agreement between calculated and observed peak temperatures for Cu-Mn-Ni-Fe alloys.

the apparatus. The limit of error of resistance readings made by this method was less than ±0.04 pct.

The specimens were placed in the fixture and the assembly was immersed in a constant temperature oil bath at 25.0°±0.03°C, and the resistance measured. Ten measurements of the diameter of each specimen, between the potential points, were made with a micrometer with a least count of 0.0001 in. The resistivity at 25°C was then calculated. The overall error introduced by the above sources is less than ±0.5 pct.

Resistance-Temperature Relationship: Three open spiral bifilar wound coils, whose nominal resistance was 0.1 ohm, were made from each alloy. These were completely fabricated and adjusted prior to heat treatment. The coils were then annealed in a dissociated ammonia atmosphere as described.

It is well known that the curve shape of this class of alloys is readily influenced by their surface condition.[7] In order to avoid any undesirable effects and to secure reproducible surfaces, the surfaces of the specimens were etched under rigorously controlled conditions and then stress relieved at 180°C for 24 hr in a vacuum.

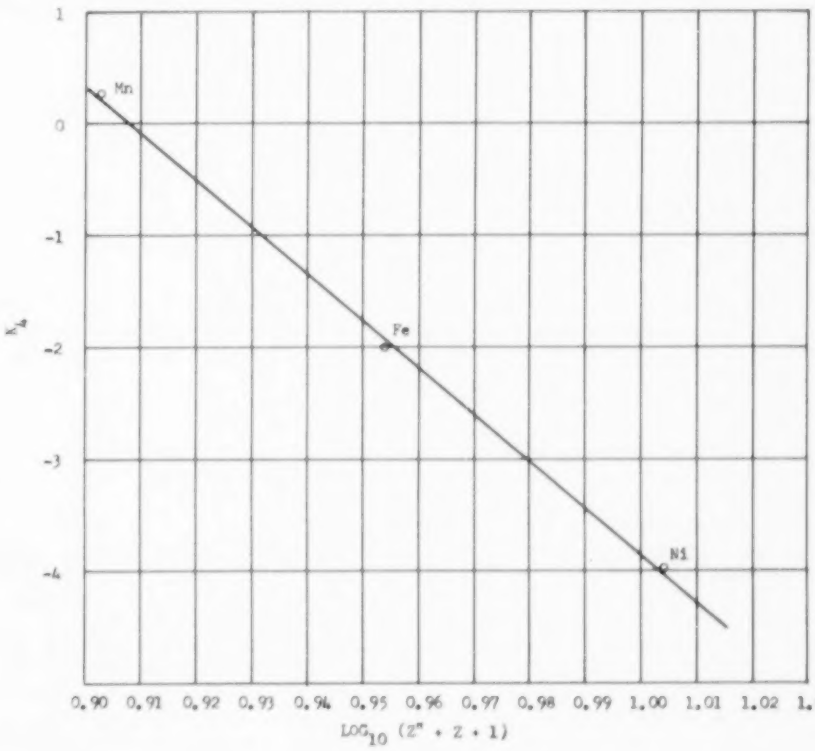

Fig. 7—Chart shows dependence of K_i on electronic configuration for Cu-Mn-Ni-Fe alloys.

The coils were then measured in constant temperature oil baths at four different temperatures between 15° and 40°C. Each of these temperatures was maintained within ±0.03°C in specially constructed baths. A Kelvin percent bridge, accurate to ±0.0003 pct, was used for this group of measurements. Equations were fitted to the resistance-temperature data.[9] None of the experimentally determined values depart from the computed curves by more than +0.001 pct. The equations are of the form

$$P_t = P_{t_0} + AT + Bt^2 \qquad [1]$$

where P_t is the resistance at t°C, expressed in percentage of a given standard resistance, P_{t_0} is this percentage at 0°C and A and B are constants for a given composition when it has been treated as noted in the foregoing.

Interpretation of Data

Binary Alloy Studies—Preliminary experiments were conducted on alloys of the Cu-Mn, Cu-Ni, and Cu-Fe binary systems. The experimental data are given in Table III. This was done to verify Linde's work.[10] It was found that the average change in electrical resistivity closely followed his empirical formula as modified by Robinson and Dorn:[11]

$$\Delta\rho = [K_s + K_v (Z_s - Z_v)^2]C \qquad [2]$$

where $\Delta\rho$ is the increase in resistivity, Z_s the valence of the solute, Z_v the valence of the solvent, C the atomic percent of solute and K_s and K_v are constants for the periodic group to which the solute element belongs.

Good agreement with Linde's work was obtained for the values (average change in resistivity per atomic percent of solute element) for manganese and nickel. The average effect of manganese additions was determined to be 2.91 microhm-cm per atomic pct and that of nickel to be 1.19 microhm-cm per atomic pct. These quantities were used to calculate the values of the constants in Eq. 2. It was found that this equation best described the experimental data when an ionic charge of −2 electrons was assigned to manganese and −1½ electrons assigned to nickel. The constant K_s was thus found to be 2.29 and K_v to be 0.62.

In metals, the valence electrons are not bound to specific atoms; they move freely throughout the lattice. Their *orbits* are sufficiently far from the ion-core of any one atom so that the fields of other cores may instantaneously contain them. Thus the valence electrons may not be identified with any given metallic atoms. This resonant bonding is considered to be the typical metallic type of bond. Many properties of metals are explained by this model. Fractional valences (or ionic charges) of metals are consistent with this picture, since an average number of electrons, in association with a given atom, may be approximated.

The average effect of iron additions was found to be 5.79 microhm-cm per atomic pct. This value is considerably lower than that reported by Linde. The difference may be explained by the differences in the techniques used to prepare the test specimens. The limited solid solubility of iron in copper was noted by Linde. He quenched the specimens rapidly in order to retain the iron in solution. However, this resulted in a highly stressed, metastable structure. No evaluation was made of the effect of these stresses upon the change in resistivity. The effect of iron upon the resistivity of copper, as reported by Linde, is too large by an amount equal to the contribution made by the lattice distortion induced by the excess iron and by the quenching stresses. The same comments hold for his effects of cobalt as reported.

If an ionic charge of −2½ electrons is assigned to iron and substituted into Eq. 2, the effect of iron is calculated to be 5.77 microhm-cm per atomic pct. This is in good agreement with the experimental average value of 5.79. Hibbard[12] noted the deviations in the effects of the transition elements and Robinson and Dorn[11] have shown the ionic charge on aluminum to be approximately −2½ electrons.

The tests on the binary systems also included temperature coefficient measurements. These data were found to obey Matthiessen's rule within narrow limits. The constant predicted by this rule, based upon measurements made on the copper used in these alloys, is 6.49×10^{-6}. However, as was expected, it was found that the experimentally obtained values for the binary alloys were slightly different from this and from each other. These variations are caused by small differences in the impurity contents of the individual alloy systems. The constant which best fits the data for the Cu-Mn alloys is 6.25×10^{-6}, for the Cu-Ni series 7.14×10^{-6}, and for the Cu-Fe family 6.62×10^{-6}. The value for the Cu-Mn alloys is close to that obtained from the data of Smith and Palmer.[13]

The approximate value of 6.67×10^{-6} from the work of Hansen, Johnson, and Parks[14] is in good agreement with the above data. The experimental data for the binary systems are shown in Table III.

Cu-Mn-Ni-Fe Alloys—The experimental data for these alloys are given in Table II. The modified Linde relationship for resistivity changes is known to be valid for dilute solid solutions. A check was made to determine the applicability of this equation to the relatively concentrated solid solutions represented by this more complex alloy system. It was found that the resistivity of the Cu-Mn-Ni-Fe alloys could be computed from the sum of the effects that the individual elements manifested as binary alloys.

Table III. Experimental Data for Binary Alloys of Copper

Atomic Pct Alloying Element	ρ_{25}, Microhm-Cm	$\Delta\rho$, Microhm-Cm	Average $\Delta\rho/C$, Microhm-Cm per Atomic Pct	Temperature Coefficient of Resistance, 25°C Reference Temperature, Ohms per Ohm per °C, 15° to 40°C
99.86 Cu	1.760	—	—	0.00369
0.553 Mn	3.376	1.616	2.92	0.00181
5.276 Mn	17.242	15.482	2.93	0.00036
7.744 Mn	24.467	22.707	2.93	0.00027
11.292 Mn	34.212	32.452	2.87	0.00018
15.788 Mn	47.538	45.778	2.90	0.00010
1.029 Ni	2.989	1.229	1.19	0.00239
2.012 Ni	4.159	2.399	1.19	0.00213
3.101 Ni	5.459	3.700	1.19	0.00126
4.327 Ni	6.848	5.088	1.17	0.00100
5.286 Ni	8.043	6.283	1.18	0.00089
0.115 Fe	2.493	0.734	6.38	0.00242
0.291 Fe	3.273	1.513	5.20	0.00220

These calculated resistivities are in good agreement with the experimentally determined resistivities. The accuracy of this relationship is shown in Fig. 2.

It was found that the constant A in Eq. 1 could be well described by the sum of the temperature co-

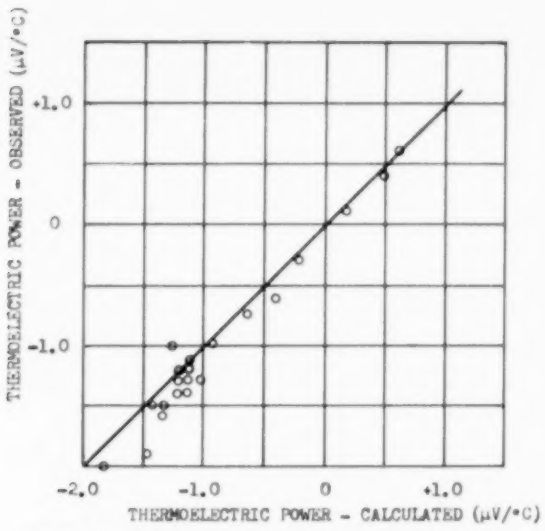

Fig. 8—Chart shows agreement between calculated and observed thermoelectric power for Cu-Mn-Ni-Fe alloys.

efficients that the individual components would have demonstrated as binary alloys of copper. The effects of nickel and iron for concentrations less than 0.2 atomic pct in the Cu-Mn-Ni-Fe matrix are more accurately given by 5.0×10^{-6}. The larger values for nickel and iron (7.14×10^{-6} and 6.62×10^{-6}) obtained from the binary systems give a good representation for the more concentrated solutions. The agreement, shown in Fig. 3, obtained between the experimental and calculated values of this constant shows the degree of accuracy of this relationship.

The constant B for Eq. 1 is a function of the electronic effects of the solute atoms present in the copper. The individual effects of the alloying elements may be expressed by the empirically derived relationship

$$\Delta B = (Z_s - Z_c)^2 \left(\frac{R}{r} - 1\right) K_s C \,. \qquad [3]$$

ΔB may be considered as a function of the intensity of the scattering effect and the interaction, or overlapping, effect of the incomplete d-shells of the solute atoms. The scattering may be expressed approximately by the quantity $(Z_s - Z_c)^2$. The overlapping for these elements in copper may be given by $\left(\frac{R}{r} - 1\right) K_s$. R is half of the internuclear distance and r is the radius of the incomplete inner shell. The ratio of R/r relates atomic separation with the incomplete d-shell radius. Bozorth[18] uses this ratio for overlap as a criterion of the energy of magnetization for metals of the iron group. The constant K_s, for a given solute atom in copper, is a function of the number of valence electrons, Z, and the number of unfilled positions, Z', in the incomplete d-shells. The values of K_s for manganese, iron, and nickel are shown as functions of these parameters in Fig. 4. The mutual interaction of both of these effects (scattering and overlapping) would appear to explain the behavior of the constant B. The correlation of the experimental and the calculated values for B are given in Fig. 5. The data used to calculate B are given in Table IV. The values for R/r, in this table, were taken from calculations performed by Slater.[18]

Table IV. Data for Computation of B

Element	K_s, Experimental*	R/r†	$\Delta B/C$,‡ Calculated
Mn	+0.85	1.47	+0.40
Fe	−1.11	1.63	+2.80
Ni	−1.17	1.97	−0.28

* K_s = Pct resistance /(°C)² (ionic charge difference)² atomic pct.
† R/r = Atomic radius/d-shell radius.
‡ $\Delta B/C$ = Pct resistance /(°C)² atomic pct.

The importance of knowing the constants A and B resides in the fact that they may be used to determine the peak temperature (t_p, the maximum point

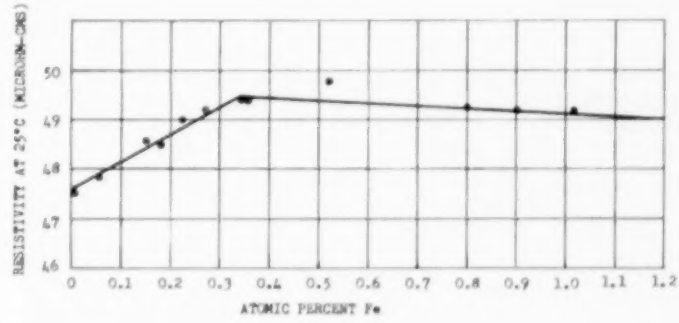

Fig. 9a—Chart plots resistivity as a function of iron content in copper containing 14.5 atomic pct Mn and 4.4 atomic pct Ni. Note that continuity ceases at about 0.35 pct Fe.

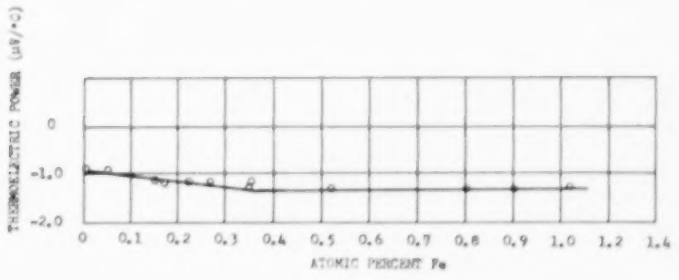

Fig. 9b—Chart plots thermoelectric power as a function of iron content in copper containing 14.5 atomic pct Mn and 4.4 atomic pct Ni. Note that discontinuity occurs at about 0.35 pct Fe.

of Eq. 1) and the temperature coefficient. The peak temperature is given by

$$tp = \frac{A}{2B} \qquad [4]$$

and the temperature coefficient by

$$\frac{dR}{dt} = A + 2Bt. \qquad [5]$$

Fig. 6 shows the order of reliability of these computations.

The thermoelectric power of the Cu-Mn-Ni-Fe alloys is given by the empirically derived relationship

$$\frac{\Delta E}{\Delta t} = \frac{1}{2} \sum \frac{K_i \Delta \rho_i}{Z_i}. \qquad [6]$$

Thermoelectric power may be considered as a function of the conduction electrons of the solute atoms, the scattering cross sections, and the electronic energy level variations. The quantity Z_i represents the effective electron density resulting from the solute atoms. An approximation of the scattering cross section resulting from the effects of the solute atoms is contained in $\Delta\rho_i$. Also included in $\Delta\rho_i$ are the scattering effects of phonons and imperfections. It is thought that the constant K_i provides a measure of the *s-d* electron interactions. Eq. 6 thus accounts for the principle variables and provides a good first order approximation of the thermoelectric power.

The constant K_i is apparently related to the electronic configurations of the constituent elements. Here it appears that the number of 3*d* electrons, Z'', plays an important role. This is shown graphically in Fig. 7. The observed thermoelectric power is shown correlated with the calculated values in Fig. 8.

The limit of solid solubility of iron in copper containing approximately 14.5 atomic pct Mn and 4.4 atomic pct Ni is very close to 0.35 atomic pct. This is shown graphically by means of resistivity and thermoelectric measurements in Figs. 9a and 9b.

The electrical properties of Cu-Mn-Ni-Fe alloys are sensitive to small variations in chemical composition. Small errors in chemical analysis thus result in significant deviations between calculated and observed electrical properties. It is believed that better correlations of the calculated with the observed data would have been obtained if more precise analyses had been available.

Summary

1—Fractional ionic charges of $-1\frac{1}{2}$ electrons for nickel and $-2\frac{1}{2}$ electrons for iron accurately describe the electrical properties of solid solutions of these elements in copper. An ionic charge of -2 electrons accounts for electrical effects of manganese in copper.

2—Empirical relationships, based upon the electronic configurations of the alloying elements, are given which describe the resistivity, temperature coefficient, peak temperature, and thermoelectric power of Cu-Mn-Ni-Fe alloys at approximately room temperature.

3—These relationships may be used to predict the electrical properties of a given Cu-Mn-Ni-Fe alloy, or to design alloys which will possess desired sets of electrical characteristics.

Acknowledgments

The authors wish to acknowledge the work of G. V. Porter in melting and fabricating the alloy wires. They are also indebted to P. H. Dike and G. A. Perley for their valuable criticisms of the manuscript. Grateful acknowledgment is made to the Leeds and Northrup Co. for permission to publish this paper.

Discussion of this paper, if any, will appear in JOURNAL OF METALS, November 1956, and in AIME Metals Branch *Transactions*, Vol. **206**, 1956.

References

[1] E. Weston: U. S. Patent Nos. 381,304 and 381,305, superseded by reissue Patent Nos. 10,944 and 10,945.

[2] K. Feussner and St. Lindeck: Metal Alloys for Electrical Resistances. *Ztsch. für Instrumentenkunde* (1889) **9**, p. 233.

[3] K. Feussner: The Construction of the Electrical Standard Resistances of the P.T.R. *Ztsch. für Instrumentenkunde* (1890) **10**, p. 6.

[4] F. E. Bash: The Manufacture and Electrical Properties of Manganin. *Trans.* AIME (1919) **155**, p. 1717.

[5] N. B. Pilling: Some Electrical Properties of Cu-Ni-Mn Alloys. *Trans.* Electrochemical Soc. (1925) **48**, p. 171.

[6] R. S. Dean and C. T. Anderson: The Alloys of Manganese-Nickel and Copper. *Trans.* ASM (1941) **29**, p. 899.

[7] J. L. Thomas: Precision Resistors and Their Measurement. *Circular 470* National Bureau of Standards (1948) p. 2.

[8] W. F. Roeser and A. I. Dahl: Reference Tables for Iron-Constantan and Copper-Constantan Thermocouples. Research Paper No. RP 1080. *Journal of Research* National Bureau of Standards (1938) **20**, p. 337.

[9] J. Lipka: *Graphical and Mechanical Computation*. (1918) p. 145. New York. J. Wiley and Sons.

[10] J. O. Linde: Elektrische Eigenshaften Verdunnter Mischkristallegierungen III. *Annalen der Physik* (1923) **14**, p. 219.

[11] A. T. Robinson and J. E. Dorn: Effects of Alloying Elements on the Electrical Resistivity of Aluminum Alloys. *Trans.* AIME (1951) **191**, p. 457; JOURNAL OF METALS (June 1951).

[12] W. R. Hibbard, Jr.: Electrical Resistivity of Dilute Binary Terminal Solid Solutions. *Trans.* AIME (1954) **200**, p. 594; JOURNAL OF METALS (May 1954).

[13] C. S. Smith and E. W. Palmer: Thermal and Electrical Conductivities of Copper Alloys. *Trans.* AIME (1935) **117**, p. 225.

[14] M. Hansen, W. R. Johnson, and J. M. Parks: Correlation between Electrical Conductivity and Temperature Coefficient of Resistance of Solid-Solution Alloys. *Trans.* AIME (1951) **191**, p. 1184; JOURNAL OF METALS (December 1951).

[15] J. C. Slater: Atomic Shielding Constants. *Physical Review* (1930) **36**, p. 57.

[16] R. M. Bozorth: *Ferromagnetism*. (1951) p. 444. New York. D. Van Nostrand Co.

Technical Note

Occurrence of Chi Phase in a 16 Pct Cr-15 Pct Ni-7 Pct Mn-6 Pct Mo Alloy

by John Birtalan and R. A. Bloom

CONSIDERABLE interest has been shown in recent years toward determining the crystal structure, mode of formation, and chemical composition of the χ phase, designated as such by Andrews,[1] who was the first to establish its presence in Fe-Cr-Ni-Mo alloys. Later work[2] by the same author has shown that the occurrence of χ depends on the presence of some molybdenum in the alloy. The phase, which appears to be identical or very similar to α manganese, has a body-centered-cubic structure and is closely related to σ phase. Koh[3] observed a similarity in composition between χ and σ and speculated as to whether χ might be an ordered structure of σ which is known to have a tetragonal crystal

J. BIRTALAN and R. A. BLOOM are Research Metallurgists, Timken Roller Bearing Co., Canton, Ohio.

TN 295E. Manuscript, May 13, 1955.

structure. More recent work by Kasper,[4] using an alloy of pure χ phase, has shown the structure to be an ordered α manganese type, and from valency and atom size considerations suggests the formation of χ to be governed primarily by atom size factors. Some information concerning the formation of χ in similar alloy systems is available.[5-7]

In a recent paper[8] published by this laboratory, a routine X-ray diffraction examination was made of a specimen to determine a phase present which could not be ascertained from a metallographic study. A micrograph of the sample appears as Fig. 14 of ref. 8. The steel in this case was a modified 16 pct Cr-25 pct Ni-6 pct Mo alloy in which 6 pct Mn was used to replace 10 pct Ni. The treatment consisted of solution quench from 2150°F, cold upset 90 pct, and aged for 1000 hr at 1500°F. An X-ray diffraction pattern, using the direct measurement technique, was made by means of a General Electric XRD3 unit using chromium radiation with a vanadium foil filter. The treated specimen was given a standard metallographic polish followed by an electrolytic $FeCl_3$ etch. The diffraction peaks obtained identified the two phase structure to consist of austenite and χ phase. The measured interplanar and intensity values, covering a range of 2θ values from 55° to 160°, agreed very well with those published by Andrews.

In order to obtain further lattice parameter measurements of the phase, the sample was subjected to an electrolytic separation treatment. The separation technique used was a modification of the Klinger and Koch[9] method; the solution consisted of a flowing buffered anolyte containing 5 pct sodium citrate and 1 pct NaCNS with a Cu_2SO_4 catholyte at a current density of 2.5 to 3 amp per sq in. at 4 to 6 v, with the current being periodically reversed.

The Debye-Scherrer powder pattern made from the extracted residue gave diffraction lines identical to those obtained by direct measurement on the solid sample. The completeness of the extraction technique was indicated by the absence of diffraction lines for phases other than χ.

The lattice parameter values obtained by direct measurement and film techniques were 8.905 and 8.907A, respectively. The value reported by Andrews[2] for an alloy containing 5 pct Mo was 8.904A (reported as 8.886kX). Koh[3] found that for his various alloy systems the value varied from 8.89 to 8.92A, while Kasper[4] reported 8.920A for his alloy which contained 27 pct Mo.

The extracted residue was submitted to an outside laboratory for spectrochemical analysis which was reported as follows: 62.0 pct Fe, 0.18 pct Si, 2.8 pct Mn, 2.5 pct Mo, 12.0 pct Ni, and 20.0 pct Cr.

The values presented here are somewhat different from those reported by Koh,[3] Andrews,[10] and Vacher[7] on the chemical composition of their extracted residues of χ. Andrews, in his discussion,[10] points out the fact that other elements, namely silicon and nickel, can replace molybdenum in the lattice structure. What effects the replacement of various alloying elements such as silicon, nickel, and manganese, etc., for molybdenum in the lattice has on the phase boundaries of χ in the basic Fe-Cr-Ni ternary diagram cannot be forecast from the information now available.

References

[1] K. W. Andrews: A New Intermetallic Phase In Alloy Steels. *Nature* (1949) No. 4180, p. 1015.

[2] K. W. Andrews and P. E. Brookes: Chi Phase In Alloy Steels. *Metal Treatment and Drop Forging* (1951) pp. 301-311.

[3] P. H. Koh: Occurrence of Chi-Phase In Molybdenum-Bearing Stainless Steels. *Trans.* AIME (1953) 197, pp. 339-343; JOURNAL OF METALS (February 1953).

[4] J. S. Kasper: The Ordering Of Atoms In The Chi Phase Of The Iron-Chromium-Molybdenum System. *Acta Metallurgica* (1954) 2, pp. 456-461.

[5] J. G. McMullin, S. F. Reiter, and D. G. Ebeling: Equilibrium Structures In Fe-Cr-Mo Alloys. *Trans.* ASM (1954) 46, pp. 799-806.

[6] F. L. Ver Snyder and H. J. Beattie, Jr.: The Laves And Chi Phases In A Modified 12 Cr Stainless Alloy. *Trans.* ASM (1955) 47, pp. 211-225.

[7] H. C. Vacher and C. J. Bechtoldt: Delta Ferrite-Austenite Reactions And The Formation Of Carbide, Sigma and Chi-Phases In 18 Chromium-8 Nickel-3.5 Molybdenum Steels. *Journal of Research* (1954) 53, pp. 67-76.

[8] W. E. Ellis and Martin Fleischmann: The Substitution Of Manganese For Nickel In 16-25-6 Alloy. *Trans.* ASM (1954) 46, pp. 1039-1055.

[9] P. Klinger and W. Koch: *Contribution to Metallurgical Analysis.* (1949) Dusseldorf, Stahleisen m.b.H.

[10] K. W. Andrews: Discussion of ref. 5. *Trans.* ASM (1954) 46, pp. 808-810.

Titanium-Rich Corner of the Ti-Al-V System

The titanium-rich corner of the system Ti-Al-V has been studied to determine the phase relationships in the temperature interval 600° to 1200°C. Metallographic examination of long time isothermally annealed specimens was the principal method of investigation.

by J. J. Rausch, F. A. Crossley, and H. D. Kessler

TWENTY-SIX alloys in the region 1 to 22 pct Al and 2 to 11 pct V, and the temperature range 600° to 1200°C, were studied as part of a program on phase relationships and transformation processes of titanium alloy systems.

J. J. RAUSCH and F. A. CROSSLEY, Junior Members AIME, are Assistant Metallurgist and Research Metallurgist, respectively, Nonferrous Metals Research, Armour Research Foundation, Chicago, and H. D. KESSLER, Member AIME, is Supervisor, Metallurgical Div., Titanium Metals Corp. of America, Henderson, Nevada.

Discussion of this paper, TP 4083E, may be sent, 2 copies, to AIME by Apr. 1, 1956. Manuscript, Feb. 28, 1955. Philadelphia Meeting, October 1955.

Experimental Procedure

Preparation of Alloys—Materials used in the preparation of alloys were high purity Bureau of Mines sponge titanium (103 Bhn), 99.7 pct pure V chips obtained from the Electro Metallurgical Div., Union Carbide and Carbon Corp., and 99.71 pct pure Al in the form of granulated shot from Aluminum Co. of America.

The alloy ingots, weighing 15 g, were melted in a nonconsumable tungsten electrode arc furnace un-

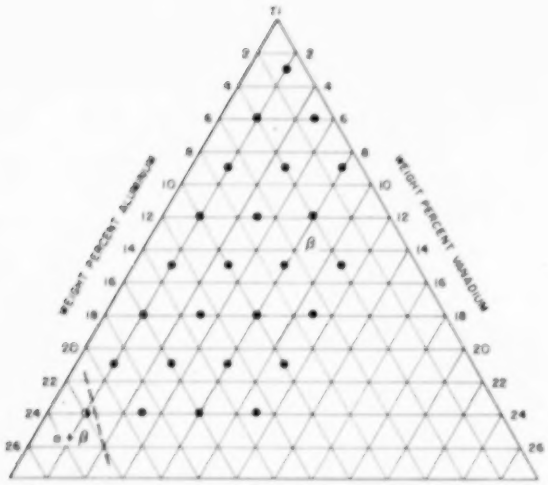

Fig. 1—Chart shows partial isothermal section of Ti-Al-V system at 1200°C. Closed circle represents one phase; divided circle, two phase.

Fig. 2—Chart shows partial isothermal section of Ti-Al-V system at 1100°C. Open and closed circle each represents one phase; divided circle, two phase.

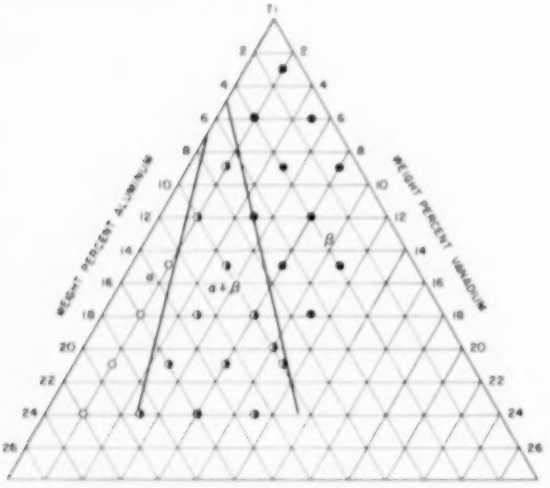

Fig. 3—Chart plots partial isothermal section of Ti-Al-V system at 1000°C. Closed and open circle each represents one phase; divided circle, two phase.

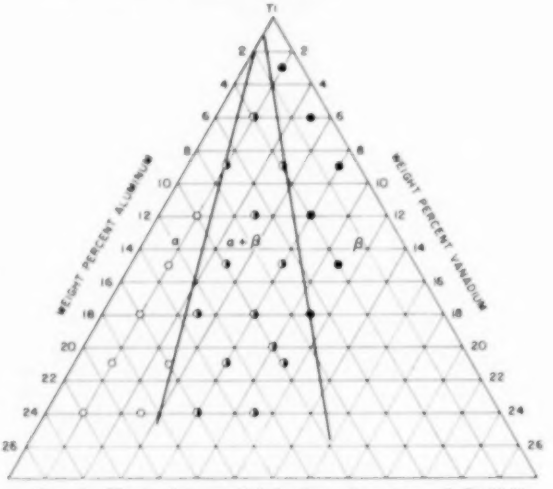

Fig. 4—Chart plots partial isothermal section of Ti-Al-V system at 900°C. Closed and open circle each represents one phase; divided circle, two phase.

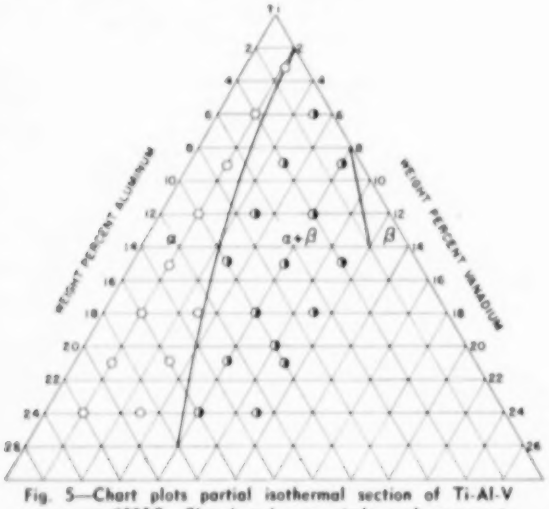

Fig. 5—Chart plots partial isothermal section of Ti-Al-V system at 800°C. Closed and open circle each represents one phase; divided circle, two phase.

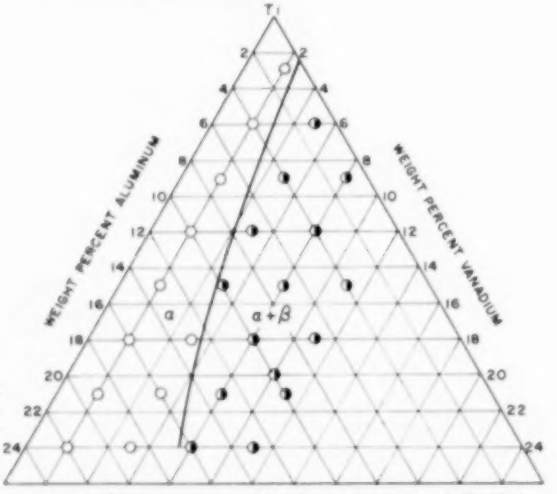

Fig. 6—Chart plots partial isothermal section of Ti-Al-V system at 700°C. Open circle represents one phase; divided circle, two phase.

Table I. Annealing Schedule for Alloys Investigated

Temperature, °C	Time
1200	24 hr
1100	24 hr
1000	48 hr
900	72 hr
800	1 week
700	2 weeks
600	1 month

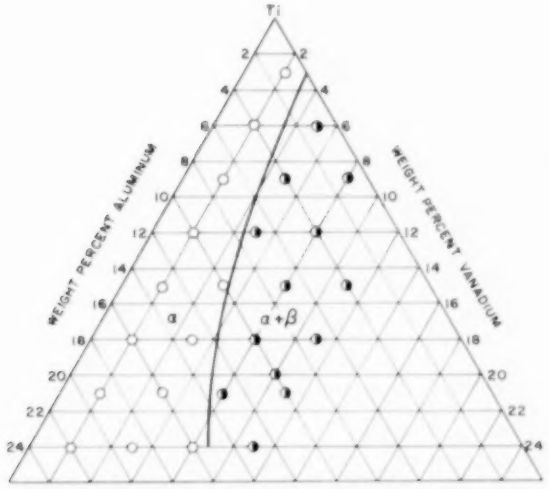

Fig. 7—Chart plots partial isothermal section of Ti-Al-V system at 600°C. Open circle represents one phase; divided circle, two phase.

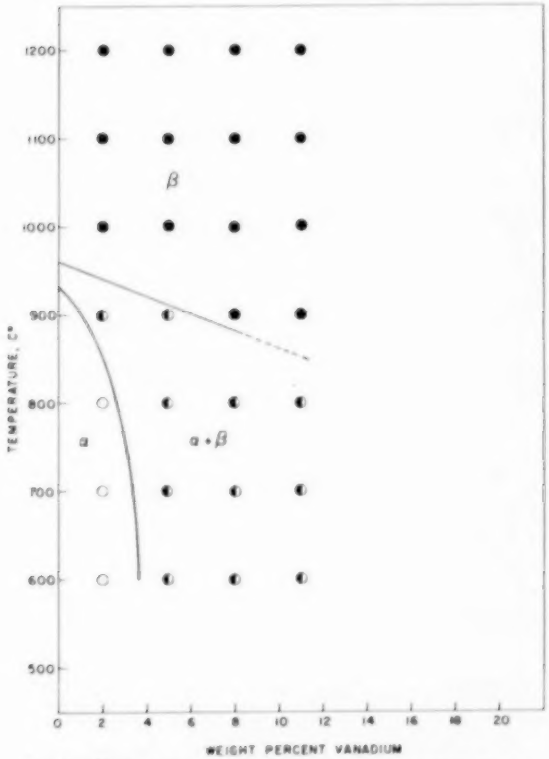

Fig. 8—Chart plots vertical section of Ti-Al-V system at 4 pct Al. Closed circle represents β; divided circle, α plus β; and open circle, α.

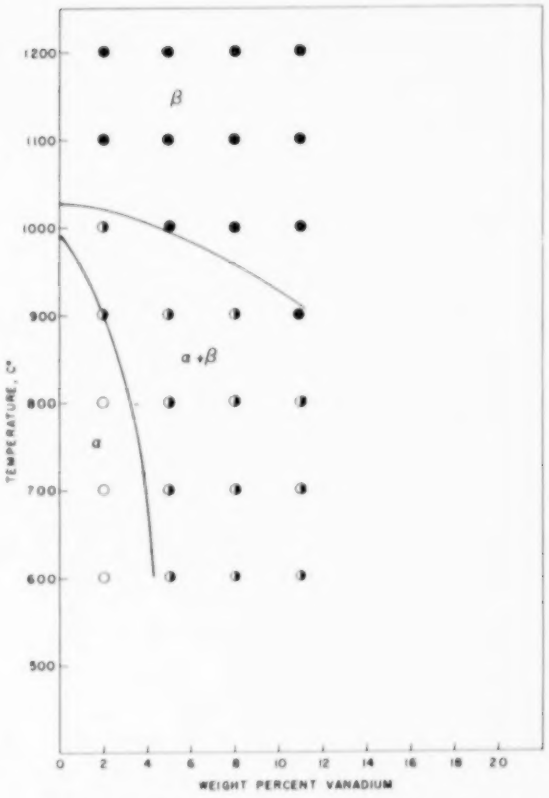

Fig. 9—Chart plots vertical section of Ti-Al-V system at 7 pct Al. Closed circle represents β; divided circle, α plus β; and open circle, α.

der a slightly positive pressure of helium. Detailed descriptions of melting techniques have been previously reported.[1] The alloy charges and resultant ingots were weighed to the nearest 1/10 mg and negligible weight losses were found.

Annealing Treatments—Samples annealed at temperatures from 600° to 1100°C were sealed in evacuated Vycor bulbs. Samples annealed at 1200°C were sealed in quartz bulbs under a partial pressure of argon. Cold deformation prior to annealing was not possible for the majority of the alloys in this investigation. This was not of great consequence since it is felt that annealing times were of sufficient duration for equilibrium to be reached. The annealing schedule appears in Table I.

Equilibrating anneals of specimens at temperatures below 1000°C were preceded by a 1 hr homogenization treatment at this temperature, followed by a furnace cool to the desired equilibrium temperature. This heat treatment was employed to eliminate coring found in the as-cast microstructures of alloys containing more than 7 pct Al and those containing more than 8 pct V.

Results and Discussion

The Ti-Al phase diagram reported by Bumps et al.[2] and the Ti-V phase diagram reported by Adenstedt et al.[3] were used to extend the phase boundaries determined by the ternary data to the binary axes of the partial isothermal sections. Although the binary systems were based on investigations in which iodide titanium was used, it is felt that the sponge used in the current investigation was

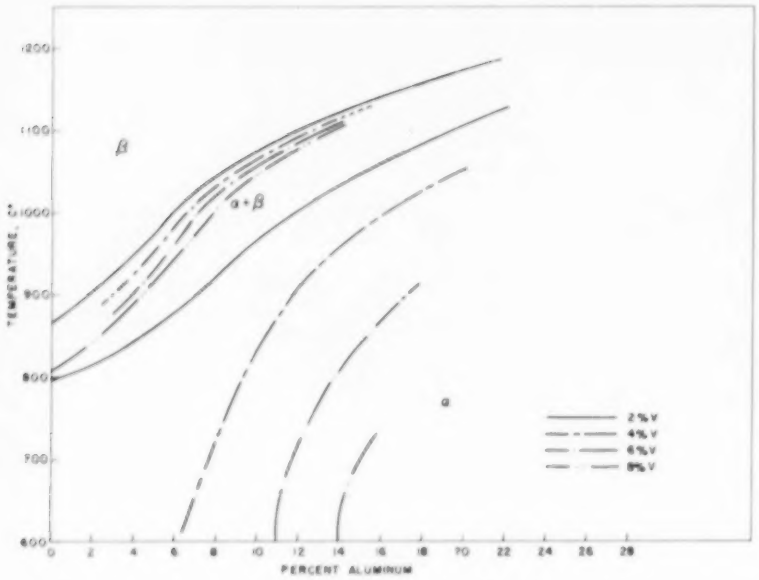

Fig. 10—Chart plots vertical sections of Ti-Al-V system at constant vanadium contents.

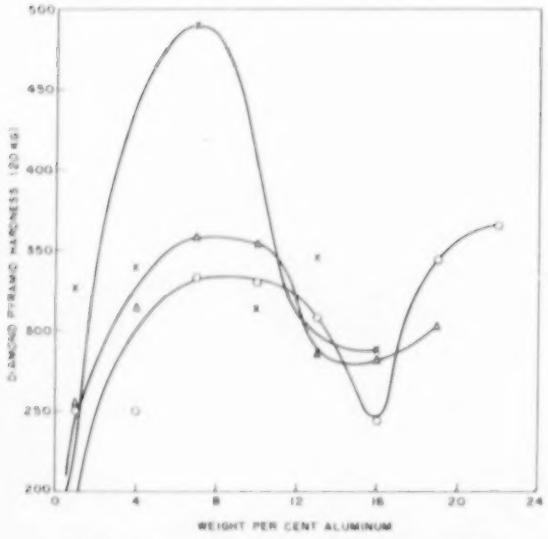

Fig. 11—Chart plots hardness of Ti-Al-V alloys at constant vanadium contents, water quenched from 1000°C. Circle represents 2 pct V; triangle, 5 pct V; and cross, 8 pct V.

of sufficient purity to make the error inherent in such extension small.

Seven isothermal sections were made at 100°C intervals from 1200° to 600°C. These are presented in Figs. 1 to 7. The isothermal sections show that increasing the aluminum content expands the α field at a given temperature. Fig. 7 shows that increasing the aluminum content of Ti-Al-V alloys from 4 to 7 pct increases the solubility of vanadium in α from approximately 3.5 to 4.5 pct at 600°C.

Vertical sections at both constant aluminum and constant vanadium contents are shown in Figs. 8 to 10. The addition of vanadium to Ti-Al alloys has little effect on the $\beta/\alpha + \beta$ boundary, as may be seen in Fig. 10. Raising the vanadium content from 2 to 8 pct lowers the $\beta/\alpha + \beta$ boundary approximately 60°C at the 2 pct Al level, and approximately 40°C at the 8 pct Al level.

The hardness of alloys water quenched from 1000°C is plotted vs aluminum content in Fig. 11. The curves show that minima occur at about 16 pct Al, independent of the vanadium content. The same phenomenon has also been observed in Ti-Al-O, N, C systems.[1] Although most of the alloys shown in the figure were in the $\alpha + \beta$ field when quenched, the fact that the most pronounced dip in the curve occurred for 2 pct V alloys was proof that the minima were due to softening of the α phase. The last four points in the curve for 2 pct V alloys were entirely in the α field when quenched. It was possible that this softening was associated with the restoration of ductility at aluminum contents in the vicinity of 16 pct. To investigate this possibility, three 100 g buttons of this composition were made using high purity sponge (103 Bhn) and aluminum shot. An 800°C anneal for 92 hr followed by water quenching showed the hardness of this alloy to be 260 Dph. This compared favorably to the minima obtained for the ternary alloys. The alloy showed no room temperature ductility in this condition. Attempts to cold press and cold roll resulted in brittle failure. Hot rolling at temperatures up to 1050°C also resulted in cracking after one or two passes. Since practical ductility does not appear to be a virtue of this alloy no further work was done.

Acknowledgment

The authors are indebted to the Materials Laboratory, Wright Air Development Center, sponsors of the research described, for permission to publish this paper.

Discussion of this paper, if any, will appear in JOURNAL OF METALS, November 1956, and in AIME Metals Branch *Transactions*, Vol. **206**, 1956.

References

[1] M. Hansen, H. D. Kessler, and D. J. McPherson: The Titanium-Silicon System. *Trans.* ASM (1952) **44**, pp. 518-538.

[2] E. S. Bumps, H. D. Kessler, and M. Hansen: Titanium-Aluminum System. *Trans.* AIME (1952) **194**, pp. 609-614; JOURNAL OF METALS (June 1952).

[3] H. K. Adenstedt, J. R. Pequignot, and J. M. Raymer: The Titanium-Vanadium System. *Trans.* ASM (1952) **44**, pp. 990-1003.

[4] R. J. Van Thyne and H. D. Kessler: Influence of Oxygen, Nitrogen and Carbon on the Phase Relationships of the Ti-Al System. *Trans.* AIME (1954) **200**, pp. 193-199; JOURNAL OF METALS (February 1954).

Technical Note

Density Distribution in Metal Powder Compacts

by G. C. Kuczynski and I. Zaplatynskyj

SINCE the excellent studies of metal powder compaction executed by Kamm, Steinberg, and Wulff,[1,2] no work on the subject has appeared in the technical literature. Kamm et al. were the first to investigate quantitatively the distribution of density in a powder compact, as a function of pressure, height and diameter of the die, powder particle size, etc. For this purpose they devised a very ingenious method. They inserted a thin lead grid into a die and then filled the die with powder. During cold pressing, the lead grid moved downward. Due to its deformability it followed closely the downward descent of the adjacent powder. The die was then radiographed and, from the deformations of the grid openings measured on the radiographs, the density in the vicinity of each opening was evaluated. Their findings led them to the conclusion that the friction on the side walls of the die is a major controlling factor of the density distribution inside the cold pressed powder compacts.

However, it is difficult to conduct tests similar to those of Kamm, Steinberg, and Wulff in a processing plant laboratory, which usually lacks the necessary expensive radiographic equipment. The purpose of this note is to describe a method which makes it possible to determine the density distribution in green powder compacts with the same accuracy as the lead-grid method but which is far simpler and faster and requires only standard laboratory equipment. Instead of using a lead grid, the hardness at selected points of the sectioned compact is determined. If the relationship between hardness and density is known the density distribution is readily obtained. This relationship is easily found from measuring hardness and densities of thin compacts. In such compacts the density, for all practical purposes, is constant throughout.

The method was tested on a Plast nickel powder, grade F1A-A20, kindly supplied by Plast Metals Co. Thin compacts (height to diameter ratio 0.2) were pressed in a single action cylindrical die at various pressures. The density of the compacts was determined by weighing and by measuring the height and diameter with a micrometer. Subsequently the RH hardness was determined. Up to ten readings were taken on each specimen. The difference in hardness readings on each compact was never greater than three corresponding to about 0.1 g per cu cm uncertainty in density. By varying the compaction pressure of the samples, a whole scale of densities was obtained allowing construction of a set of density-hardness calibration curves. To test the method several compacts of different height were pressed under varying pressures. Die walls were always well lubricated. After pressing, the compacts were mounted in bakelite and halved by grinding, and hardness readings taken along the diameters of the specimens. The distance between adjacent indentations was about 2.5 mm.

After hardness readings were translated into densities, *contour maps* of densities of the compacts were prepared. One of them is reproduced in Fig. 1. The areas encompassed by the curves are labeled with numbers representing the density in g per cu cm of those regions. In Fig. 2 the same results are replotted to emphasize the radial density changes at various depths. The results thus obtained confirm the findings of Kamm, Steinberg, and Wulff[1,2] mentioned previously. They are recapitulated here briefly.

1—The densest part of a compact pressed from one side is at the outer circumference at the top and the least dense part at the bottom, at the outer circumference. Figs. 1 and 2 show this clearly.

2—The density near the cylindrical surfaces of the compact decreases uniformly with height from top to bottom.

3—The density variation increases with the height to diameter ratio.

References

[1] R. Kamm, M. A. Steinberg, and J. Wulff: *Trans. AIME* (1947) 171, p. 439; METALS TECHNOLOGY (February 1947).
[2] R. Kamm, M. A. Steinberg, and J. Wulff: *Trans. AIME* (1949) 180, p. 694; METALS TECHNOLOGY (December 1948).

G. C. KUCZYNSKI and I. ZAPLATYNSKYJ are associated with Dept. of Metallurgy, University of Notre Dame, Notre Dame, Indiana.
TN 300E. Manuscript, June 30, 1955.

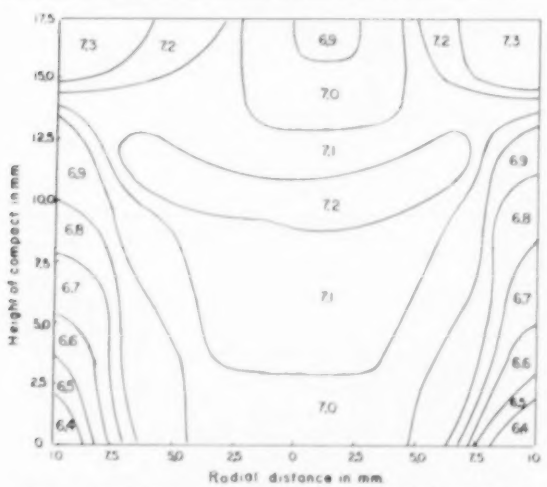

Fig. 1—Distribution of densities in a green nickel compact pressed at 46 psi is charted. Die diameter *D* is 0.79 in.; *h/D*, 0.87.

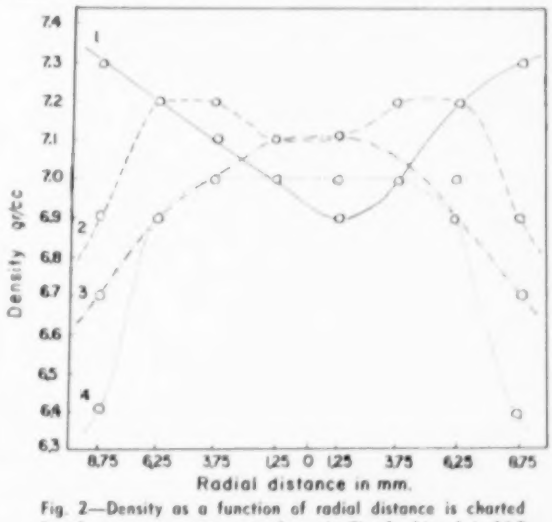

Fig. 2—Density as a function of radial distance is charted for the same compact as is shown in Fig. 1. Line 1 is 16.0 mm; line 2, 11.0 mm; line 3, 6.0 mm; and line 4, 2.0 mm from the bottom of the die.

Technical Note

Production of High Nitrogen Steels

by V. F. Zackay, E. R. Morgan, and J. C. Shyne

NITROGEN used as an alloying element in steel has received increased attention in recent years. Its merit as an austenite stabilizer and hot strengthener has long been recognized, particularly by European investigators.[1]

Recent work[2] indicates that nitrogen contents of ½ pct or more allow the addition of several percent of ferrite-forming hot strengtheners, such as molybdenum, without subsequent austenite decomposition at elevated temperatures. The room temperature properties of such alloys are characterized by high yield and tensile strengths with excellent ductility, even after cold working, as shown in Tables I and II. The 1350°F creep-rupture properties of Cr-Mn-Mo-N steels are comparable to those of commercial alloys such as Timken's 16-25-6, containing 16 pct Cr, 25 pct Ni, and 6 pct Mo, as shown in Table III.

Cr-Mn steel containing ½ pct N must be made under pressure if ingot gassing is to be avoided. However, there are difficulties attendant to this practice. Pressure melting restricts the ingot size, and the equipment required is costlier and more complicated than comparable air melting facilities. An effort was made, therefore, to determine more economical methods of adding nitrogen.

The pressures generated in centrifugal casting usually range from 5 to 10 atm and are sufficient to prevent the gassing of high nitrogen Cr-Mn steels. A centrifugal casting was made of an alloy containing 16 pct Cr, 18 pct Mn, 2 pct Mo, and 0.73 pct N. A disk, 8 in. diam and 1½ in. thick, was cast at 1000 rpm. It has been calculated that a pressure of 9 atm was developed at the periphery of the disk at this speed. Metallographic inspection of specimens taken from the disk revealed no gas holes or other defects. The elevated temperature properties of radial and circumferential specimens taken from this casting are given in Table IV. The creep-rupture life of this cast nickel-free austenitic steel was equivalent to that of the wrought Cr-Mn-Mo-N steels.

Although centrifugal casting appears to lend itself to the manufacture of high nitrogen austenitic steels, its applicability is limited to relatively small sizes.

A process applicable to the production of large ingots of high nitrogen steels is suggested by low carbon rimming steel practice. Gas holes formed during ingot solidification are not detrimental so long as they weld shut during hot rolling. An economic advantage of gassing ingots is the increased ingot-to-slab yield, especially if the ingots are mechanically capped. Also, it is probable that higher nitrogen levels can be achieved with mechanically capped ingots than with hot-topped ingots.

A series of gassy heats was made under both atmospheric and higher pressures, as indicated in Table V. Several of the air melted ingots were mechanically capped by chilling the molten ingot tops with a steel plate. The ingots were allowed to freeze in steel molds without hot-tops unless otherwise indicated.

A comparison of Table III with Table V shows no significant difference in the creep-rupture properties of the gassy and the nongassy ingots after hot working nor between the gassy ingots produced under different conditions.

V. F. ZACKAY, E. R. MORGAN, Junior Members AIME, and J. C. SHYNE are associated with Metallurgy Dept., Scientific Laboratory, Ford Motor Co., Dearborn.

TN 323E. Manuscript, Oct. 20, 1955.

References

[1] F. Rapatz: Application of Stainless and Heat Resisting Steels Alloyed with Nitrogen. *Stahl und Eisen* (1941) 61, pp. 1073-1078.
[2] V. F. Zackay, J. F. Carlson, and P. L. Jackson: High Nitrogen Austenitic Cr-Mn Steels. *Trans.* ASM (1955) 48, pp. 509-523.

Table I. Room Temperature Tensile Tests of Wrought Cr-Mn-Mo-N Steels Water Quenched from 2150°F

Nominal Composition in Pct	Tensile Test Data		
	Yield Strength, Psi	Tensile Strength, Psi	Elongation, Pct
16 Cr-14 Mn-2 Mo-0.5 N	61,400	119,000	70
16 Cr-14 Mn-2 Mo-0.5 N	59,100	121,250	68
16 Cr-14 Mn-2 Mo-0.6 N	61,500	120,000	65
17 Cr-13 Mn-2.5 Mo-0.75 N	75,000	140,000	50

Table II. Tensile Properties of Cold Worked Austenitic Steels

Nominal Composition	Type				
	301	302	CM*	Cr, Mn, N	Cr, Mn, N
Pct Cr	17	18	16	16	17
Pct Ni	7	9	1	—	—
Pct Mn	—	—	15	14	13
Pct Mo	—	—	—	2	2.5
Pct N	—	—	—	0.6	0.75
Cold Work, Pct	40	60	40	33	25
Yield Strength, Psi	150,000	180,000	145,000	183,000	176,000
Tensile Strength, Psi	200,000	195,000	185,000	207,000	205,000
Elongation, Pct	10	3	5	13	11.5

* CM represents commercial Cr-Mn steel.

Table III. Creep-Rupture Properties of Wrought Cr-Mn-Mo-N Steels Water Quenched from 2150°F

Nominal Composition in Pct	100 Hr Rupture Life in Psi at 1350°F
16 Cr-13 Mn-3 Mo-½ N	28,000
16 Cr-14 Mn-2 Mo-½ N	26,000
16 Cr-25 Ni-6 Mo	27,000

Table IV. Creep-Rupture Life of Centrifugally Cast Cr-Mn-Mo-N Steel Water Quenched from 2150°F

16 Pct Cr-18 Pct Mn-2 Pct Mo-0.73 Pct N*, Nominal Composition	100 Hr Rupture Life in Psi at 1350°F
Radial Test Specimen	28,000
Circumferential Test Specimen	28,000

* Percentage given is actual nitrogen value.

Table V. Creep-Rupture Life of Wrought Cr-Mn-Mo-N Austenitic Steels Water Quenched from 2150°F

Nominal Composition* in Pct	Casting Condition	100 Hr Rupture Life at 1350°F, Psi
15 Cr-16 Mn-4 Mo-0.50 N	Gassy, pressure melt	25,000
16 Cr-15 Mn-3 Mo-1 Ni-1 Si-0.46 N	Gassy, pressure melt	26,000
16 Cr-12 Mn-2 Mo-0.60 N	Gassy, pressure melt	29,000
16 Cr-16 Mn-2 Mo-0.62 N	Gassy, air melt	29,000
16 Cr-16 Mn-2 Mo-0.61 N	Gassy, air melt	26,000
16 Cr-14 Mn-2 Mo-0.55 N	Gassy, mechanically capped	26,000
16 Cr-14 Mn-2 Mo-0.56 N	Gassy, mechanically capped	26,000

* Percentages given are in actual nitrogen values.

Appreciation is gratefully acknowledged to the following organizations whose support has helped to make possible AIME's extensive publications program of metallurgical research:

Allis-Chalmers Mfg. Co.
Aluminum Co. of America
American Brake Shoe Co.
American Cast Iron Pipe Co.
American Iron & Steel Institute
American Metal Co. Ltd.
American Metallurgical Products Co.
American Smelting & Refining Co.
American Zinc, Lead & Smelting Co.
Anaconda Co.
Battelle Memorial Institute
Bridgeport Brass Co.
Budd Co.
Bunker Hill & Sullivan Mining & Concentrating Co.
Calumet & Hecla, Inc.
Cerro de Pasco Corp.
Clevite Corp.
Climax Molybdenum Co.
Consolidated Coppermines Corp.
Consolidated Mining & Smelting Co. of Canada Ltd.
Copper Range Co.
Cornell Aeronautical Laboratory, Inc.
Crane Co.
Cyprus Mines Corp.
Dow Chemical Co.
Driver-Harris Co.
Wilbur B. Driver Co.
Eaton Mfg. Co.
Electro Metallurgical Co., div. of Union Carbide & Carbon Corp.
Engineering Foundation
Ford Motor Co.
Freeport Sulphur Co.
General Electric Co.
General Motors Corp.
Handy & Harman
E. F. Houghton & Co.
Howe Sound Co.
Hudson Bay Mining & Smelting Co. Ltd.
International Nickel Co., Inc.
Janney Cylinder Co.
Kennecott Copper Corp.
Leeds & Northrup Co.
Magma Copper Co.
Mallinckrodt Chemical Works
P. R. Mallory & Co., Inc.
Mallory-Sharon Titanium Corp.
Metal Hydrides, Inc.
Miami Copper Co.
Molybdenum Corp. of America
Mueller Brass Co.
National Lead Co.
New Jersey Zinc Co.
Newmont Mining Corp.
Noranda Mines, Ltd.
Owens-Corning Fiberglas Corp.
Phelps Dodge Corp.
Raytheon Mfg. Co.
Rem-Cru Titanium Inc.
Revere Copper & Brass Inc.
Reynolds Metals Co.
Alfred P. Sloan Foundation, Inc.
St. Joseph Lead Co.
Superior Tube Co.
Texas Gulf Sulphur Co.
Titanium Metals Corp. of America
U. S. Smelting, Refining & Mining Co.
Vanadium Corp. of America
S. K. Wellman Co.

SECOND VOLUME

ON

NUCLEAR METALLURGY

All the Papers at a Symposium
Conducted by

INSTITUTE OF METALS DIVISION
AMERICAN INSTITUTE OF MINING AND METALLURGICAL ENGINEERS, INC.

February 20, 1956
(AIME Annual Meeting, Hotel New Yorker, New York)

General Problems in the Application of Materials in Reactor Environments
by R. C. Dalzell, Atomic Energy Commission

The Behavior of Materials in Aggressive Liquid Metals
by D. H. Gurinsky, Brookhaven National Laboratory

Behavior of Materials in Nonaggressive Liquid Metals
by R. F. Koenig and E. G. Brush, General Electric Company

The Application of Materials in Low Temperature Water and Organic Liquid Cooled Reactor
by J. E. Draley and S. Greenberg, Argonne National Laboratory

Structural Materials for Use in the Pressurized Water Power Reactor
by D. M. Wroughton and D. J. DePaul, Westinghouse Electric Corporation

Corrosion of Materials in Fused Hydroxides
by G. P. Smith, Oak Ridge National Laboratory

Price: $3.75
(AIME Members: $2.50)

AIME, 29 W. 39th St., New York 18, N. Y.

Please send me a copy of the Second Volume on Nuclear Metallurgy. Enclosed is Check ☐; Money Order ☐ for $ _____ (AIME members may be billed.)

Name _____

Address _____

City and Zone _____ State _____

Nonmember Foreign Order, Add 50¢ for Mailing.

Purchase your copy at the Registration Desk, Hotel New Yorker, during the Annual Meeting, or use the form at the left to order by mail. (Mail orders will be filled after the Annual Meeting.)

The first volume containing the five papers presented at Nuclear Metallurgy Symposium of the Institute of Metals Division Fall Meeting, Oct. 17, 1955, will also be available at the Registration Desk. (Price to AIME members, $2.50; nonmembers, $3.75.)